WASHINGTON UNIVERSITY
SEVER INSTITUTE OF TECHNOLOGY
DEPARTMENT OF CHEMICAL ENGINEERING

Modeling the Fluid Dynamics of Bubble Column Flows

by

Peng Chen

Prepared under the direction of

Prof. M. P. Duduković

A dissertation presented to the Sever Institute of
Washington University in partial fulfillment
of the requirements for the degree of

DOCTOR OF SCIENCE

May, 2004

Saint Louis, Missouri, USA

WASHINGTON UNIVERSITY
SEVER INSTITUTE OF TECHNOLOGY
DEPARTMENT OF CHEMICAL ENGINEERING

ABSTRACT

Modeling the Fluid Dynamics of Bubble Column Flows

by Peng Chen

ADVISOR: Prof. M. P. Duduković

March, 2004

Saint Louis, Missouri, USA

Bubble column and slurry bubble column reactors are used in numerous industrial applications. In these systems gas sparged through the liquid rises in forms of bubbles of various sizes and provides the energy via interfacial momentum transfer for vigorous mixing of the liquid. The Euler-Euler approach describes the motion of the two-phase mixture in a macroscopic sense, which is preferred for industrial applications. To model the drag force term, which is one of the key closures, most numerical simulations resort to a single particle model with a so-called "mean" bubble size. This assumption is physically unrealistic in churn-turbulent flow regime and results in poor gas holdup prediction and limited capability for interfacial area concentration prediction. Moreover,

the determination of the assumed “mean” bubble size needs a trial-and-error procedure which significantly compromises the prediction capability of Computational Fluid Dynamics (CFD) approach. This research shows that bubble column flows could be better modeled by explicitly accounting for bubble breakup and coalescence with the implementation of Bubble Population Balance Equation (BPBE) into the CFD code. When the breakup rate is increased by an order of magnitude, compared to values predicted by models in the literature, the implementation of BPBE leads to better agreement of CFD prediction with all available data for gas holdup and liquid axial velocity distribution, compared to the simulation based on an estimated constant mean bubble diameter. The choice of currently available bubble breakup and coalescence closures has some but not a significant impact on the simulated results. Quantitative comparisons with the experimental data (Kumar, 1994; Degaleesan, 1997; Chen *et al.*, 1999; Ong, 2003; Shaikh *et al.*, 2003) demonstrate that CFD model coupled with BPBE provides satisfactory mean axial liquid velocity and gas holdup profile for columns operated over a wide range of superficial velocity, operating pressure, physical properties, and column diameter. The bubble Sauter mean diameter and interfacial area per unit volume are also reasonably predicted. For reactor modeling, convective and axial dispersion time scales are predicted correctly, improvement is needed for the radial dispersion time scale which is currently overpredicted.

to my parents and sister

Contents

Tables ..... **vii**

Figures ..... **ix**

Nomenclature ..... **xiv**

Acknowledgments ..... **xviii**

1 Introduction **1**

1.1 Research Motivation 1

1.2 Research Objectives 6

2 Background and CFD models **7**

2.1 Direct Numerical Simulation (DNS) 15

2.2 Euler-Lagrangian Method 19

2.2.1 One-way coupling 20

2.2.2 Two-way coupling 20

2.2.3 Four-way coupling 21

2.3 Euler-Euler (Two-Fluid) Approach 25

2.4 Algebraic Slip Mixture Model (ASMM) 27

2.5 Interfacial Force 30

2.5.1 Drag Force 30

2.5.2 Added/virtual mass force 34

2.5.3 Transversal or Lateral force 36

2.6 Multiphase Turbulence Modeling 42

2.7 Previous Euler-Euler Investigations of Bubble Column Flows 45

3 Background - Population balance equation and bubble breakup and coalescence **52**

3.1 Bubble Population Balance Equation 53
3.2 Bubble Breakup 55
3.2.1 Maximum Stable Bubble Size 56
3.2.2 Number of Daughter Bubbles 60
3.2.3 Breakup Rate and Daughter Bubble Size Probability Density Function (p.d.f.) 61
3.3 Bubble Coalescence 70
3.3.1 Collision Frequency 72
3.3.2 Coalescence Efficiency 76
3.4 Attempts of implementation of the bubble population balance into CFD for investigation of bubble column flows 79

4 Implementation of Bubble Population Balance Equation (BPBE) in Computational Fluid Dynamic (CFD) Models 83

4.1 CFD Model Equations 83
4.2 Bubble Population Balance Equation 88
4.2.1 Breakup and Coalescence Closures 92
4.2.2 Bubble classes tracked 94
4.2.3 Solution Procedure 94
4.3 Boundary and Initial Conditions 96
4.4 Experimental Conditions Simulated 97

5 Numerical Simulation of Bubble Column Flows with Bubble Coalescence and Breakup 100

5.1 Experimental Techniques Used 100
5.2 Two-dimensional Axisymmetric Simulation 103
5.2.1 Summary 122
5.3 Three-Dimensional Simulation 122
5.3.1 Results and Conclusions 151

6 Numerical Tracer and Particle Tracking 153

6.1 Introduction 153

6.2 Computational Models 154
6.3 Numerical Tracer Experiment 154
6.4 Numerical Particle Tracking Experiment 158
6.5 Results and Discussions 161
6.6 Summary 167

7 Conclusions and Recommendations 168

7.1 Conclusions 168
7.2 Recommendations 174

References 177

Vita 191

Tables

2.1 Different Phenomenological Models for Bubble Columns 11

2.2 CFD modeling of multiphase flow in bubble columns. 12

2.3 Dispersed Turbulence Model Equation (in Euler-Euler Model).....44

2.4 Mixture Turbulence Model Equation (in ASMM).....45

3.1 Various forces that act to break up and stabilize the bubble.....55

3.2 Deformation/Stabilization Force Used by Different Models.....60

3.3 Maximum Stable Bubble Size Predictions by Different Models.....60

3.4 Different forms of bubble coalescence efficiency 77

4.1 Euler-Euler model equations.....84

4.2 Algebraic Slip Mixture (ASM) model equations.....86

4.3 Breakup and Coalescence Closures Implemented 93

4.4 Bubble classes tracked in 2D axisymmetric simulation 94

4.5 Bubble classes tracked in 3D simulation 94

4.6 Column size, sparger design, operating conditions and the corresponding mesh parameters in two-dimensional axi-symmetric simulations (liquid phase: water). 97

4.7 Column size, operating conditions and the corresponding computational parameters in three-dimensional simulations.....99

5.1 Implemented breakup and coalescence closures.....104

5.2 Overall liquid continuity for air-water bubble column: D_C = 16.2 cm and U_g = 30.0 cm/s 138

5.3 Physical properties.....149

5.4 Operation condition 150

6.1 Turbulent eddy diffusivity calculation.....161

6.2 Predicted axial eddy diffusivity in bubbly flow.....162

6.3 Predicted axial eddy diffusivity in churn-turbulent flow. 165
6.4 Time scales for convection and dispersion in a 44-cm diameter column operated at U_g=10 cm/s. 166

Figures

1.1 Schematic of a bubble column configuration 2

1.2 Variables affecting bubble-column phenomena and performance 3

1.3 Mechanistic description of buoyancy induced recirculation and turbulent dispersion in a bubble column reactor (from Gupta, 2002) 5

2.1 Two-dimensional volume-of-fluid simulations of the rise trajectories of bubbles (from Krishna and Van Baten, 1999) 16

2.2 Position of the bubbles and streamlines in a vertical cross-section (from Bunner and Tryggvason, 2002)....17

2.3 Photographic representation of a) bubbly and b) churn-turbulent flow regimes in a 2D bubble column. 18

2.4 Schematic of Euler-Lagrangian Method 19

2.5 Computed structure of two-phase gas-liquid flow in a bubble column with an aspect ratio of 11.4. Superficial gas velocity equals 35 mm/s. Both instantaneous bubble positions and liquid velocity fields are shown 30 s after start up, 60 s after start up and 90 s after start up. (Delnoij *et al.*, 1997b)....22

2.6 Bubble column with single bubble plume (from Pfleger *et al.*, 1999). 24

2.7 Drag force for a single bubble 31

2.8 Added/virtual mass force for a single bubble 35

2.9 Schematic representation of lift force: a) The Magnus force without boundary layer transition, b) The Magnus force with laminar boundary layer on one side and turbulent boundary layer on the other side of the bubble, c) The Saffman force, d) the lift force due to bubble deformation (from Tomiyama *et al.*, 1995b) 37

2.10 Illustration of split-lamina lift model showing bubble cleaving for co-linear bubble and flow field velocity vector (from Schrage *et al.*, 2001) 41

2.11 Axial dispersion coefficient of the liquid phase: comparison of experimental data with 2D and 3D Eulerian simulations (from van Baten and Krishna, 2001). 50
3.1 Idealization of bubble column flows (a) Single mean bubble size (b) Reality (c) Local bubble size distribution. 52
3.2 Luo and Svendsen's (1996) breakup model illustration. 63
3.3 Martínez-Bazán *et al.*'s (1999a; 1999b) breakup model illustration. 65
3.4 Typical breakup rate with respect to bubble diameter predicted by Martínez-Bazán *et al.* (1999a) 66
3.5 Dimensionless daughter size distribution (from Lehr and Mewes, 2001). 68
3.6 Breakup determined by (a) surface energy criteria only, b) Both criteria are not satisfied simultaneously thus no breakup, c) Breakup determined by surface energy and energy density criteria (from Hagesaether *et al.*, 2002a)....70
3.7 Bubble coalescence in turbulent flow. 71
3.8 (a) Buoyancy-driven and (b) laminar shear induced collision. 73
3.9 Wake Entrainment 74
4.1 Bubble reassignment to pivots 91
4.2 Overview of solution procedure....95
4.3 Typical numerical mesh for three dimensional simulation. 98
5.1 (a) Schematic diagram of the CARPT experimental setup (from Gupta, 2002) and (b) typical particle trajectory (from Degaleesan, 1997) 101
5.2 Schematic diagram of the CT setup (from Kumar, 1994). 103
5.3 Comparison of the radial profiles of the axial liquid velocity obtained from simulations with experimental data measured by CARPT for (a) 14-cm diameter column operated at U_g = 9.6 cm/s, (b) 19-cm diameter column operated at U_g = 2.0 cm/s (c) 19-cm diameter column operated at U_g = 12.0 cm/s (d) 44-cm diameter column operated at U_g = 2.0 cm/s, (e) a 44-cm diameter column operated at U_g = 10.0 cm/s, P = 1 bar. 109
5.4 Comparison of the radial profiles of the axial liquid velocity obtained from simulations by "tweaked" mean bubble size with experimental data measured by CARPT (P = 1 bar). 111

5.5 Comparison of the radial profiles of the kinetic energy obtained from simulations with experimental data measured by CARPT for (a) 14-cm diameter column operated at U_g = 9.6 cm/s, (b) 19-cm diameter column operated at U_g = 2.0 cm/s (c) 19-cm diameter column operated at U_g = 12.0 cm/s (d) 44-cm diameter column operated at U_g = 2.0 cm/s, (e) a 44-cm diameter column operated at U_g = 10.0 cm/s, P = 1 bar. 115
5.6 Comparison of the radial profiles of the gas holdup obtained from simulations with experimental data measured by CT for a 19-cm diameter column operated at Ug = 12.0 cm/s, P = 1 bar.....116
5.7 Comparison of the radial profiles of the bubble local mean diameter for a 19-cm diameter column operated at U_g = 12.0 cm/s, P = 1 bar. 117
5.8 Comparison of the bubble volume-based p.d.f. for a 44-cm diameter column operated at U_g = 10.0 cm/s, P = 1 bar. 118
5.9 Comparison of the radial profiles of the interfacial area for a 19-cm diameter column operated at (a) U_g = 2.0 cm/s, P = 1 bar (b) U_g = 12.0 cm/s, P = 1 bar.....119
5.10 Centerline mean bubble diameter evolution. 119
5.11 Bubble size distribution evolution along column elevation in (a) 14-cm diameter column operated at U_g = 9.6 cm/s, P = 1 bar (b) 44-cm diameter column operated at U_g = 10 cm/s, P = 1 bar 121
5.12 The instantaneous iso-surfaces of the gas holdup, α, in various bubble columns: (a) α = 0.2, U_g = 10.0 cm/s, (b) α = 0.13, U_g = 14.0 cm/s, (c) α = 0.28, U_g = 30.0 cm/s, P = 1 bar, (d) α = 0.35, U_g = 30.0 cm/s, P = 4 bar, (e) α = 0.44, U_g = 30.0 cm/s, P = 10 bar 123
5.13 Typical simulated gas holdup and liquid axial velocity time series (D_C= 44 cm, U_g = 10.0 cm/s, P = 1 bar).....124
5.14 Comparison of time-averaged (a) axial liquid velocity and (b) gas holdup distribution (D_C= 44 cm, U_g = 10.0 cm/s, P = 1 bar).....125
5.15 Effect of BPBE on the prediction of (a) axial liquid velocity and (b) gas holdup distribution for a 44-cm diameter column operated at Ug = 10.0 cm/s, P = 1 bar. 128
5.16 Time-averaged liquid axial velocity profile evolution.....130

5.17 Velocity vector plot for D_C = 44 cm, U_g = 10.0 cm/s, P = 1 bar (from Degaleesan, 1997).....130
5.18 Time-averaged gas holdup profile evolution.....131
5.19 Comparison of time-averaged gas holdup profile of Air-Therminol-glass beads system.....131
5.20 Comparison of time-averaged and liquid holdup weighted liquid axial velocity profile (D_C = 44 cm, U_g = 10 cm/s, P = 1 bar).....134
5.21 Comparison of time-averaged gas holdup profile (D_C = 16.2 cm, U_g = 30 cm/s, P = 1, 4, and 10 bar).....135
5.22 Comparison of liquid axial velocity profile for air-water bubble column. D_C = 16.2 cm, U_g = 30.0 cm/s, P = 1, 4, 10 bar .(a) Time averaged (b) Time-averaged and liquid holdup weighted.....136
5.23 Cross correlation radial distribution of the liquid holdup and axial velocity, $\overline{-\alpha_l' u_{lz}'}$.....138
5.24 Effect of using the whole population locally on calculating drag and in using local mean bubble size (D_C = 16.2 cm, U_g = 30.0 cm/s, P = 1 bar).....140
5.25 Comparison of the intensity of liquid turbulent (a) normal stress and (b) shear stress obtained from simulations with experimental data for air-water bubble column: Dc = 16.2 cm, Ug = 30.0 cm/s, P = 1 bar. 142
5.26 Comparison of the liquid turbulent kinetic energy obtained from simulations with experimental data for columns of different diameter and operated in the churn turbulent regime.....143
5.27 Time-averaged bubble class holdup profile (D_C = 16.2 cm, U_g = 30.0 cm/s, P = 1 bar).....144
5.28 Effect of operating pressure on medium size bubbles ($d = 6.35\ mm$) 145
5.29 Comparison of the radial profiles of the (a) bubble Sauter mean diameter and (b) interfacial area concentration obtained from simulation with experimental data measured by four-point optical probe for 16.2-cm diameter column operated at U_g = 30.0 cm/s.....146
5.30 Overall bubble classes cumulative holdup.....147

5.31 Bubble classes holdup-based probability distribution 149
5.32 Surface tension effect on bubble holdup-based probability distribution. 150
6.1 Computational mesh system for tracer simulation in bubble columns 157
6.2. Time evolution of the liquid tracer concentration inside a 44-cm diameter column at U_g =10 cm/s. 162
6.3. Time evolution of the gas tracer concentration inside a 44-cm diameter column at U_g = 10 cm/s. 163
6.4. Numerical detector responses for liquid tracer injection at z = 3 cm, in a 44-cm column operated at U_g=10 cm/s. 164
6.5 Comparison of Eddy diffusivity radial profile (D_C = 44 cm, U_g = 10 cm/s, P = 1 bar). 165

Nomenclature

a	Breakup frequency, s^{-1}
b	Coalescence frequency, s^{-1}
c, c_1, c_2, c_f	Dimensionless constant
C	Liquid tracer concentration, mol l^{-1}
c_B	Dimensionless constant
C_D	Drag coefficient, dimensionless
c_f	Increase coefficient of surface area, $c_f = f_{BV}^{2/3} + \left(1 - f_{BV}\right)^{2/3} - 1$
d, D, d', d_B	Bubble diameter, m
D^*	Dimensionless daughter bubble diameter, $D^* = D/D_0$
d_h	Sparger orifice diameter, m
D	Molecular or eddy diffusivity, $m^2\ s^{-1}$
$\langle d \rangle$	Average distance between bubbles, m
d_s	Bubble diameter at the sparger, m
$D^*_{\max}$	Maximum dimensionless daughter bubble diameter
$D^*_{\min}$	Minimum dimensionless daughter bubble diameter
$e, \overline{e}$	Eddy energy level, $N\ m^3$
f	Bubble number density function, m^{-3}
f^*	Daughter bubble p.d.f. function, dimensionless
f_{BV}	Volume fraction of one daughter bubble, dimensionless
$\mathbf{F_{12}}, \mathbf{F}_{exchange}$	Interfacial momentum exchange term, $N\ m^{-3}$
F_d	Energy density criteria function, dimensionless
F_s	Surface energy criteria function, dimensionless
$\mathbf{g}$	Gravity, $m\ s^{-2}$
h	Film thickness between coalescing bubbles, m
k	Wave number, dimensionless
k	Turbulent kinetic energy, $m^2\ s^{-2}$
K_g	Dimensionless constant
L/D	Aspect ratio, dimensionless
L_w	Wake effective length, m
$\mathbf{M_d}$	Drag force per unit volume, $N\ m^{-3}$
m	Mean number of daughter bubbles produced by breakup, dimensionless

m_b	Mass of the bubble, kg
n, N	Number density of bubble or eddy, m^{-3}
N_w	$N_w = We/Fr^{1/2} = \frac{d_o^{1.5} U_{gh} \rho_l g^{0.5}}{\sigma}$
p	Pressure, Pa
P_B	Probability of breakup, dimensionless
P_C	Coalescence efficiency, dimensionless
r	Bubble radius, m
r	Radial position, m
R	Bubble column radius, m
Re	Bubble Reynolds number, dimensionless, $Re = d_b \left\| \mathbf{u_l} - \mathbf{u_g} \right\| \rho_l / \mu_l$
S	Source term, s^{-1}
S	Gas tracer concentration, mol l^{-1}
S_i	Source term, m^{-3} s^{-1}
$\mathbf{u}$	Velocity, m/s
$\mathbf{u'}$	Velocity fluctuation, m/s
$\overline{u}_i, \overline{u}_j$	Bubble velocity in turbulence, m/s
$\overline{u}_{ij}$	Bubble approaching velocity in turbulence, m/s
u_r	Bubble rising velocity, m/s
$u_{D,k}$	Drift velocity, m/s
v, v', v_z	Bubble volume, m^3
U_g	Superficial gas velocity, m/s
U_{gh}	Gas velocity at the sparger holes, m/s
$\overline{\frac{dU_l}{dR}}$	Average liquid axial velocity gradient, 1/s
t	Time, s
t_C	Coalescence time, s
t_I	Bubbles contact time (interaction time), s
V_i^{BOX}	Volume influenced by the wake of a bubble of size d_i
We	Webber number, dimensionless
$\mathbf{x}$	Position vector
x_i	Diameter of i^{th} bubble tracked in BPBE, m
z	Axial position, m

Greek symbols

α	Volume fraction, dimensionless
β	Dimensionless constant
ε	Dissipation rate, m^2/s^3
γ	Fraction that to be reassigned to nearby bubble classes, dimensionless
γ	Virtual mass coefficient, dimensionless
λ	Arriving eddy size, m
Λ	Dimensionless critical diameter, $\Lambda = \left[12\sigma/\left(\beta\rho_l\right)\right]^{3/5} \varepsilon^{-2/5} D_0^{-1}$
μ	Viscosity, kg m^{-1} s^{-1}
$\pi_{i,j}$	Dimensionless
θ	Collision frequency, m^{-3} s^{-1}
ρ	Density, kg/m^3
σ	Surface Tension, kg s^{-2}
τ	Time, s
τ	Stress tensor, Pa
τ_s	Surface restoring pressure, Pa
$\dot{\omega}$	Eddy bombardment frequency, s^{-1}
Ω_B	Breakup rate, m^{-3} s^{-1}
Ω_C	Coalescence rate, m^{-3} s^{-1}
ξ	d_i/d_j *or* λ/d, dimensionless

Subscripts

b	Bubble
c	Continuous phase
d	Dispersed Phase
e	Eddy
exp	Experiment
g	Gas phase index
i, j, k	Bubble class index
k	Phase index
l	Liquid phase index
m	Mixture
max	Maximum
min	Minimum
p	Particle
p	Pressure change
ph	Phase change
r	Reaction

sim	Simulation
t	Turbulent
WE	Wake

Superscripts

B	Buoyancy driven
g	Gas phase index
i	Bubble class index
l	Liquid phase index
LS	Laminar shear
m	Molecular
T	Turbulence
WE	Wake

Acknowledgments

I wish to express my deepest gratitude to my advisor Prof. M. P. Duduković for his guidance, encouragement and constructive criticism. I would like to thank the members of my committee, Prof. M. H. Al-Dahhan, Prof. R. A. Gardner, Prof. P. Biswas, Dr. B. Helgeland-Sannaes of Statoil, Dr. J. Sanyal of Fluent, Inc., and Dr. B. A. Toseland of Air Products and Chemicals, Inc., for investing their valuable time in examining my thesis and providing me with useful comments and suggestions during the coarse of my research.

I also wish to gratefully acknowledge the financial support of the Department of Energy (DE-FG22-95PC95051) and the industrial participants of the CREL consortium, which made this research work possible.

I owe special thanks to Dr. J. Sanyal, Dr. S. Roy, and Dr. M. Rafique. Dr. J. Sanyal has provided information to make the model implementation possible. I greatly appreciate his kindness in agreeing to sit on my thesis committee. Dr. S. Roy has been a close friend with whom I have had a number of useful discussions on experimental validation aspects of this research. Dr. M. Rafique has also been a close friend and colleague with whom I have had ever going discussions that helped me to better focus on my research goals. In addition, I want to thank Dr. Y. Pan, Dr. A. Kemoun, and graduated students of CREL, Dr. Y. Jiang, Dr. P. Gupta, Dr. N. Rados, Dr. A. Rammohan, and Dr. B. C. Ong for sharing their knowledge with me during my early days at CREL, and for numerous discussions and valuable comments thereafter. I would like to thank Dr. Y. Yamashita, B. Shands, and M. Bober for their constant help in matters related to the computational facilities.

I sincerely acknowledge the help and assistance offered by all the past and present members of CREL, including Dr. P. Spicka, J. Xue, S. Bhusarapu, A. Sheikh, H. Luo, J. Guo, and many others. I also wish to thank the secretaries of the Department of Chemical Engineering for their prompt help in numerous administrative issues. I wish to thank the faculty, associates and students of the Department of Chemical Engineering for making my overall graduate school experience enjoyable.

Last, but not the least, my heartfelt gratitude goes to my parents and my sister for their patience and support in these years of my doctoral program.

Peng Chen
Washington University, St. Louis
May, 2004

Chapter 1
Introduction

1.1 Research Motivation

Multiphase reactors are at the heart of chemical industry. Reactions between gas and liquid are frequently encountered in chemical, petrochemical, and biochemical processes. The classification of gas-liquid reactors is based on the dispersed phase nature and, hence, two main groups of such contactors are defined - reactors with dispersed gas phase and reactors with dispersed liquid phase. For a majority of gas-liquid reactions, the interfacial mass transfer resistance is concentrated in the liquid phase, leading to the application of reactors with continuous liquid and dispersed gas phase. In cases where the third solid phase is also present, the choice of the liquid as the continuous phase is understandable regarding the requirements of the highest possible solids hold-up and minimum energy consumption for its dispersion. Bubble column reactors are at the forefront of such applications.

Figure 1.1 shows a typical bubble column, in which gas is sparged in the form of bubbles, using a distributor (sparger), into a medium of liquid or liquid-solid suspensions. Heat exchanger tubes may be inserted into the reactor for cooling/heating the system and maintaining isothermal conditions, especially for highly exothermic/ endothermic reactions. In addition, in some cases the column may be sectionalized using baffles to inhibit liquid backmixing. Gas is typically reactant, liquid is usually product and/or reactant (sometimes inert), while the solid particles are typically catalyst (or product). Bubble columns usually operate with a length to diameter ratio, or aspect ratio, of at least five. Liquid (slurry) is used in either semi-batch (zero liquid throughputs) or continuous

mode (co-current or counter-current with respect to the gas flow), with liquid superficial velocities lower than the gas superficial velocity by at least one order of magnitude. Momentum is transferred from the faster, upward moving, gas phase to the slower liquid (slurry) phases. As a result, it is a flow that is buoyancy driven and gas controls its dynamics. A significant advantage of bubble column reactors is their excellent mixing, comparable to that achieved in agitated reactors but without moving parts (smaller capital and maintenance costs) and with much lower power consumption. These excellent mixing characteristics lead to nearly isothermal operation (good heat transfer) and, together with capabilities of using fine catalyst particles, to good mass transfer and improved production. However such significant back-mixing also results in relatively low conversion for a given reactor volume that if plug flow could be maintained.

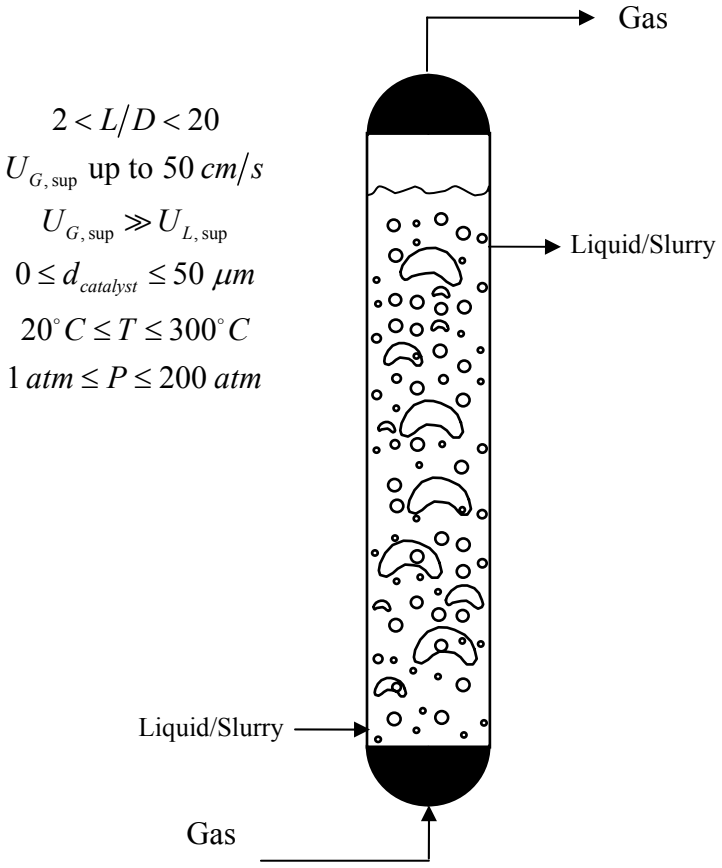

Figure 1.1 Schematic of a bubble column configuration

Bubble column reactors are widely used in Fischer-Tropsch synthesis, in fine chemicals production, in oxidation reactions, in alkylation reactions, for effluent treatment, in coal liquefaction, in fermentation reactions and more recently, in cell cultures, waste water treatment and single cell protein production. The primary advantages of bubble column reactors are easy construction due to no moving parts (which leads to easier maintenance), high interfacial area concentration, good mass/heat transfer rate between gas and liquid phase, and large liquid holdup which is favorable for slow liquid phase reactions (Shah *et al.*, 1982). Figure 1.2 illustrates the phenomena that affect bubble column performance. In design, scale-up and scale-down of such reactors the understanding of the fluid dynamics is a critical issue.

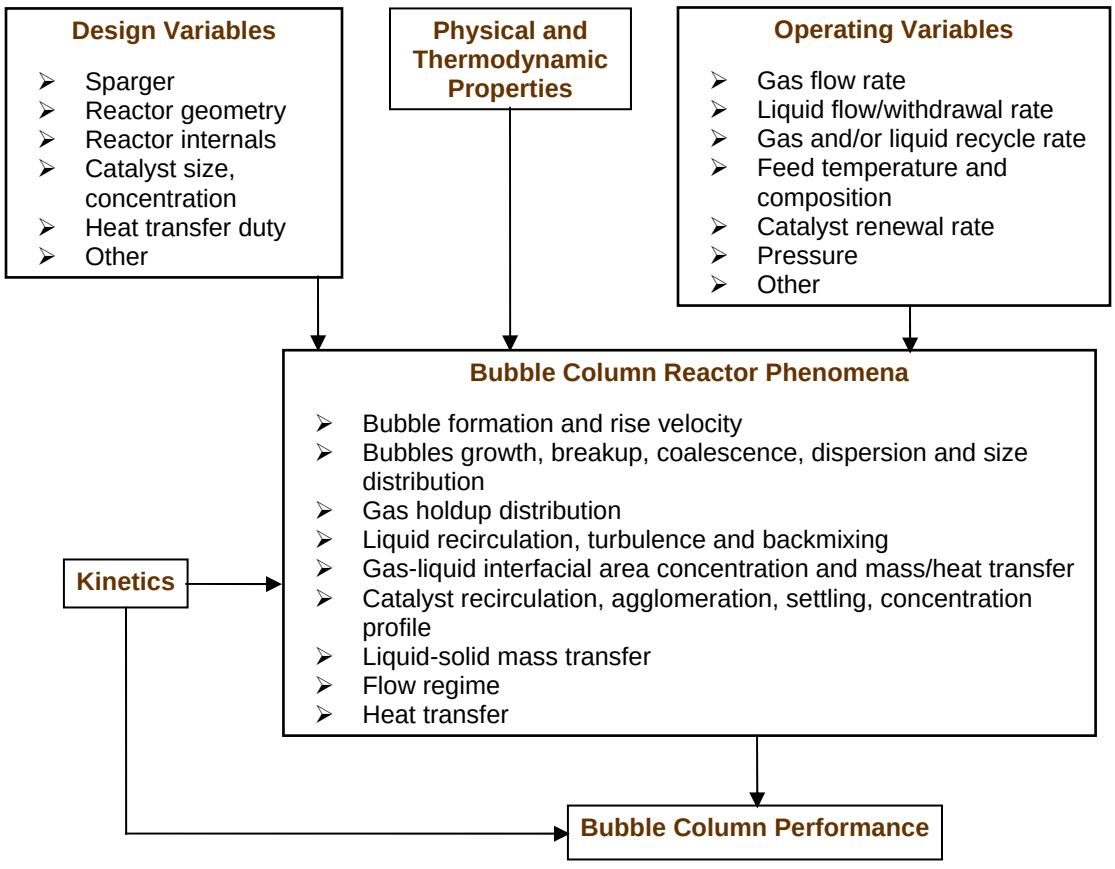

Figure 1.2 Variables affecting bubble-column phenomena and performance

From the industrial point of view, churn-turbulent flow is of most interest as it ensures high volumetric productivity. Yet this flow is poorly understood. An important task is to describe the large scale mixing of the liquid and gas phase in columns operated in the churn-turbulent flow regime. It has been demonstrated that gas holdup radial profile is almost parabolic (Kumar *et al.*, 1997b) with the highest value at the center of the column, and that after one to 1.5 diameters from the sparger such profile becomes height invariant (George *et al.*, 2000; Shollenberger *et al.*, 2000; Ong, 2003) and it drives, in a time-averaged sense, a single cell liquid recirculation (Degaleesan, 1997). Superimposed on this large scale convective motion, caused by the persistent difference in buoyancy forces, is eddy dispersion (Figure 1.3), driven by bubble wakes and meandering pathways, with axial diffusivity exceeding radial by an order of magnitude (Degaleesan, 1997). This experimental evidence, imbedded in phenomenological physically based models has been highly successful in predicting liquid (Degaleesan *et al.*, 1996b) and gas phase mixing (Gupta *et al.*, 2001a). Since such phenomenological models can predict liquid and gas tracer dynamic responses faithfully (Degaleesan *et al.*, 1996b; Gupta *et al.*, 2001a), it is important to examine whether the parameters needed by such models can be computed by Computational Fluid Dynamics (CFD). This requires computation of gas radial holdup distribution, liquid recirculation velocity, eddy diffusivities, mean bubble size and interfacial area per unit volume.

There are different approaches in CFD. For the churn turbulent flow regime only the Euler-Euler k-fluid model or Algebraic Slip Mixture Model (ASMM) seems practical. However, most previous attempts (e.g. Pan and Dudukovic, 2001) utilized an assumed mean bubble size for evaluation of the drag. This assumed size was often adjusted based on attempts to match model predictions to some measured result. Hence, the model was not fully predictive. Moreover, even with 3D simulations holdup profiles were not always predicted well, and interfacial areas were pre-judged by assumption of the bubble size. In addition, in churn-turbulent flow, bubble-bubble interactions result in widely distributed bubble sizes that may be substantially different from the “mean” bubble size assumption. A remedy to this situation can be developed by implementation of the bubble population

balance equation (BPBE) in the Euler-Euler model or in the ASMM. This eliminates the assumption of single constant bubble size and should improve the gas holdup profile prediction. Most importantly, the implementation of BPBE allows one to predict the bubble size distribution locally, and eliminates the trial-and-error procedure regarding the unknown mean bubble diameter mentioned above, while also providing the estimate of the interfacial area concentration locally throughout the column. Therefore, it would substantially increase the capability of CFD modeling on bubble column reactors.

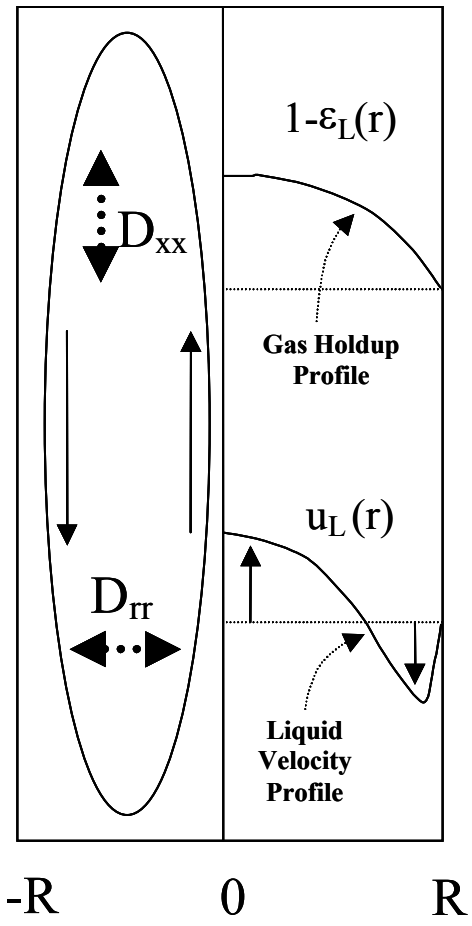

Figure 1.3 Mechanistic description of buoyancy induced recirculation and turbulent dispersion in a bubble column reactor (from Gupta, 2002)

1.2 Research Objectives

The primary objective of this thesis is to advance the understanding of gas-liquid bubble column hydrodynamics in the range of industrially relevant operating conditions. Specifically, three major research goals are:

1) To test the existing bubble breakup and coalescence closures by implementing them into the CFD framework, 2) to improve the prediction of gas holdup profiles and produce an estimation of local interfacial area per unit volume with the help of bubble population balance model, and 3) based on the improved CFD model mentioned above, provide parameters that can be used in a phenomenological model for interpretation of tracer responses in liquid and gas phase and for reactor modeling.

To accomplish these goals, the existing bubble coalescence and breakup models are implemented into the two-fluid model and the ASMM in FLUENT framework. At CREL, the CARPT/CT technique has earlier been used to establish the database for the time averaged gas holdup, liquid velocity and Reynolds stresses for the air-water system. This database is used to validate the closures and improve the gas holdup profile and interfacial area density prediction. Further, the improved two-fluid model is used to provide parameters for the phenomenological model of the bubble column (e.g. Degaleesan *et al.*, 1997; Gupta *et al.*, 2000) by performing numerical particle tracking and numerical tracer experiments.

Chapter 2
Background and CFD models

Bubble column reactors are widely used for Fischer-Tropsch synthesis, in fine chemicals production, in oxidation reactions, and in alkylation reactions, for effluent treatment, in coal liquefaction, in fermentation reactions and more recently, in cell cultures, waste water treatment and single cell proteins production. The primary advantages of bubble column reactors are easy construction due to no moving parts (which leads to easier maintenance), high interfacial area concentration, good mass/heat transfer rate between gas and liquid phase, and large liquid holdup which is favorable for slow liquid phase reactions (Shah *et al.*, 1982). The performance of bubble column reactors depends on gas holdup and liquid velocity distribution, bubble breakup, coalescence and dispersion rate, bubble rise velocity, bubble size distribution, gas-liquid interfacial area distribution, intraphase turbulence, gas-liquid mass/heat transfer coefficients and the extent of liquid phase backmixing (Krishna *et al.*, 1996; Dudukovic *et al.*, 1997).

Fluid dynamical features of bubble column reactors have been investigated for many years and there is a vast body of literature available for different gas-liquid systems, Nevertheless, fundamental features of fluid dynamics in bubble columns, which are essential for reactor design, scale-up and scale-down, are still not fully understood mainly due to the complicated nature of multiphase flow. This lack of understanding of bubble column flows stems from the existence of the multi-time-and-length scales within the column. Although the recent advances in novel techniques have enabled the measurement of the instanteneous large scale phenomena and their subsequent characterization, measurement at relatively small scales under actual operating condition

(e.g. high superficial gas velocity, high pressure, heavy solid loading, etc.), which is critical for the understanding of the buble column flows, is still rare. The main achievements in the experimental investigation of bubble column flows are the measurement of gas holdup, liquid velocity, dispersion, turbulent parameters, mass and heat transport coefficients. Most of the earlier studies focused on the measurement of global hydrodynamic parameters, like overall gas holdup and volumetric mass transfer coefficient (Mashelkar, 1970; Shah *et al.*, 1982; Saxena, 1995). This has changed primarily thanks to the development of new sophisticated experimental techniques like Laser Doppler Anemometry-LDA (Mudde *et al.*, 1997a), Computer Automated Radioactive Particle Tracking-CARPT (Lin *et al.*, 1985; Devanathan *et al.*, 1990; Moslemian *et al.*, 1992; Yang *et al.*, 1993; Larachi *et al.*, 1994; Limtrakul, 1996; Degaleesan, 1997), Particle Image Velocimetry-PIV (Chen and Fan, 1992; Tzeng *et al.*, 1993; Chen *et al.*, 1994), γ-ray Computed Tomography-CT (Kumar *et al.*, 1995; Adkins *et al.*, 1996; Kumar *et al.*, 1997a; Shollenberger *et al.*, 1997), Electrical Impedance Tomography (Dickin *et al.*, 1993), Electrical Capacitance Tomography (Warsito and Fan, 2001) and point optical and conductance probes (Choi and W. K., 1990; Cartellier, 1992; Chabot and De Lasa, 1993; Mudde and Saito, 2001; Xue, 2002). These new techniques made the local quantitative characterization of the fluid dynamics feasible. The review of these experimental investigations is out of the scope of this thesis and therefore is not discussed here.

The modeling investigations involve the mathematical description of transport of chemical species in a given bubble column reactor that includes chemical reaction. Normally, the hydrodynamic description which governs the convective, diffusive and interfacial transport of chemical species and heat in a reactor, is usually modeled separately, and serves as input to the reactor models. According to the “level” of fluid dynamic detail that they incorporate, the various models can be classfied into three groups.

In the first group, the hydrodynamic information is completely lumped into one parameter, which is usually the ratio of the convective and dispersion flux for each phase. Details of how the phases distribute and flow are completely ignored. Among the various mixing models in this group, the most commonly used one is the Axial Dispersion Model (ADM) where an effective axial diffusion is considered as superimposed on the net convective axial flow (Zhao *et al.*, 1987; Schlueter *et al.*, 1992; Schlueter, 1995). Because the ADM is suitable only for modeling of mixing processes in which the flow is not far away from ideal plug flow conditions, the application of such models for recirculation dominated convective flows, such as bubble column operations, is without a firm physical basis and results in poor predictive capabilities. Degaleesan *et al*. (1996a) presented in detail the shortcomings of the ADM applied to liquid and gas tracer data from a pilot-scale slurry-bubble column during liquid phase methanol synthesis at the La Porte Alternate Fuels Development Unit (AFDU). It was shown that the liquid phase dispersion coefficients fitted to the tracer responses, measured at various elevations, did not exhibit a consistent trend, and the values were widely scattered around the estimated means up to ±150%. For gas phase dispersion investigation, although the axial gas dispersion coefficient obtained by fitting tracer data at different detector levels has a standard deviation typically within ±22%, which is not surprising as the gas is closer to plug flow. However, the overall volumetric mass transfer coefficient exhibits a standard deviation of up to ±100%. Moreover, the available correlations for axial dispersion coefficients (with data base acquired at atmospheric pressure operation) underpredict the observed liquid axial dispersion coefficient by 150%, and overpredict the observed gas axial dispersion coefficient by 100% to 360%.

Realizing the shortcomings of the ADM in that it lacks a definitive physical basis, the second group of models were developed to predict the time-averaged fluid dynamic properties of these systems based on some physical picture of the observable fluid dynamic phenomena in bubble column reactors. In these models, the complicated multiphase flow in bubble columns is often treated as an interconnected set of continuous stirred reactors (CSTR), plug flow reactors (PFR), recycle subsystems and dead zones.

Between different regions of these models, convection, back mixing, cross-flow, and mass transfer are accounted for. It is known that the time-averaged liquid recirculation flow patterns in a bubble column reactor are the result of the differences in radial buoyancy forces arising due to the non-uniform distribution of gas phase in the column. It is this physical picture that has formed the basis for most of the phenomenological mechanistic models listed in Table 2.1.

Based on the experimental evidence (e.g. Devanathan *et al.*, 1995), it is clear that, beside the time averaged quantities, the transient behavior of flow is required to provide proper and needed information about the fluid dynamics and transport parameters in bubble columns. The transient information can be obtained from experimental data or available correlations. However, the need for experimental data makes the phenomenological models unsuitable for reactor scale-up and design, while the available correlations can be used confidently only within the conditions used to generate them.

In the third group of models, the appropriate form of the continuity and momentum equations for each phase are solved. These models are referred to as Computational Fluid Dynamic (CFD) models as they incorporate a detailed fluid dynamic description in prediction of scalar transport in a multiphase system. The CFD models can provide either the detailed local hydrodynamic properties as input to the less detailed models (e.g., the Recycle and Cross-Flow Model with Dispersion Model) or the species transport equations can be solved within the CFD framework in a coupled manner. However, in practical reaction systems, this means the solution of additional 20-30 scalar transport equations which is computationally much expensive and sometimes cannot be achieved in a realistic time-frame. Moreover, the highly non-linear reaction rate (scalar source term) could make such scalar transport equation less stable. Therefore, in most current applications CFD bubble column models are mainly used to provide the needed fluid dynamics parameters for simpler models describing species transport.

Table 2.1 Different Phenomenological Models for Bubble Columns

CST = Continuous Stirred Tank, PF = Plug Flow
ADM = Axial Dispersion Model, BM = Back Mixing

Reference	Model Description
Ueyama and Miyauchi, 1979	One of early 1D liquid recirculation models. Liquid velocity profile is matched with universal velocity profile.
Deckwer and Schumpe, 1987, Review Paper	Classification of models according to the state of mixing in different phases (CST, ADM, PF). Multi-cell model for gas (no BM) and liquid (with BM) and mass transport between phases. Cell model with upward moving liquid in a single cell (no BM) and downward moving liquid in multi-cells with BM.
Myers *et al.*, 1987, Slug and Cell Model	Upward moving gas-rich region (slug bubble) is mixing with stagnant gas-lean multi-cells (CST) region.
Anderson and Rice, 1989, Burns and Rice, 1997	1D recirculation models. Averaged radial holdup profile is taken within each of the three relevant regions (core, buffer and wall)
Rice and Geary, 1990, Kumar *et al.*, 1994	1D recirculation model. Radial holdup profile is fitted using power law.
Wilkinson *et al.*, 1993, Liquid Recirculation Model	Liquid flow is divided into two cells, upward and downward moving with axial dispersion and cross-flow between phases.
Kantak *et al.*, 1995	Small bubbles and liquid phase are described using ADM, and large bubbles using PF.
Wang, 1996, Recycle and Cross Flow Model (RCFM)	Two PF liquid zones (up and downward), three PF gas zones (small bubbles moving up and downward and large bubbles moving upward) and four CSTs (2 for top and 2 for bottom mixing of gas and liquid phase). Liquid BM and bubble-bubble interaction are accounted for by cross-flow exchange between up and downward moving fluid. Mass transfer is allowed between phases in the same zone.
Degaleesan *et al.*, 1996b, Recycle and Cross-Flow Model with Dispersion Model	Model similar to the original RCFM with dispersion terms added. The liquid tracer experiments are modeled, so only liquid phase is accounted for.
Degaleesan, 1997, Convective-Diffusion Model	2D convection-diffusion model based on observed liquid recirculation velocity profile applied to simulate slurry system tracer response curve using CARPT obtained values for eddy diffusivities as dispersion coefficients.
Liu *et al.*, 1998	Simplified approach to solution of the shear stress radial profile using 1D recirculation model.
Gupta *et al.*, 2000; Gupta *et al.*, 2001a	Model similar to the 2D convective-diffusion model with a sub-model based on the two-fluid approach for estimation of the gas and liquid phase recirculation, bubble size, volumetric mass transfer coefficient.

The need to establish a rational basis for the interpretation of the interaction of fluid dynamic variables has been the primary motivation for active research in the area of bubble column modeling based on computational fluid dynamics (CFD). During the last several years the dynamic simulation of gas-liquid flow in bubble column reactors has drawn considerable attention of the investigators in the chemical reaction engineering community (Sokolichin and Eigenberger, 1994; Kuipers and Swaaij, 1998; Pan *et al.*, 2000).

The two-phase gas-liquid flow in bubble columns is typically buoyancy driven. A number of CFD modeling studies of two-phase bubble column flows have been performed since the 1980's, when the general advancement in numerical simulation and substantial increase in computational power became available. However, real progress in bubble column CFD modeling has occurred after 1990 (See Table 2.2). Various methods are available for the simulation of dispersed two-phase flows. They range from model-free direct numerical simulations (DNS) to continuum-based models requiring a considerable number of closure relationships.

Table 2.2 CFD modeling of multiphase flow in bubble columns.
E-E: Euler-Euler E-L: Euler-Lagrangian VM: Virtual Mass

Wallis, 1969	One dimensional drift flux model.
Drew *et al.*, 1979	The virtual mass force during the acceleration of a two-phase mixture is studied. The general form of an objective virtual mass acceleration is derived and appropriate experiments are suggested for verification and parameter determination.
Sato *et al.*, 1981a	A theory is proposed which describes the transfer process for momentum and heat in two-phase bubbly flow in channels. A bubble-induced turbulence viscosity is proposed.
Drew, 1983	One of the mostly referred papers on the modeling of two-phase flow. The phase-averaged equations of the two-fluid model are derived thoroughly.
Torvik and Svendsen, 1990	Cylindrical air-water bubble column, 2D axi-symmetric transient simulation, E-E approach, $k-\varepsilon$ model, constant slip, Magnus force, no VM, quantitative comparison with data.

Ranade, 1992	Cylindrical air-water bubble column, 2D axi-symmetric transient simulation, E-E approach, $k-\varepsilon$ model, use pressure gradient to calculate momentum exchange term.
Grienberger and Hofmann, 1992	Cylindrical air-water bubble column, 2D axi-symmetric steady simulation, E-E approach, $k-\varepsilon$ model, constant slip velocity, Magnus force, no VM, quantitative comparison with data.
Webb *et al.*, 1992	2D air-water bubble column, 2D transient simulation, E-L approach, $k-\varepsilon$ model, constant slip velocity.
Svendsen *et al.*, 1992	Cylindrical air-water bubble column, 2D axi-symmetric transient simulation, E-E approach, $k-\varepsilon$ model, single particle drag law, Magnus force, no VM, quantitative comparison with data.
Jakobsen *et al.*, 1993	Cylindrical air-water bubble column, 2D axi-symmetric transient simulation, E-E approach, modified $k-\varepsilon$ model, drag-force, lift force, no VM.
Zhang and Prosperetti, 1994	Averaged equations governing the motion of equal spheres suspended in a potential flow are derived from the equation for the probability distribution.
Sokolichin and Eigenberger, 1994 Becker *et al.*, 1994	2D partially aerated bubble column, 2D transient simulation, E-E approach, laminar, constant slip, VM, Magnus force, qualitative comparison with data.
Lapin and Lübbert, 1994b	2D air-water bubble column, 2D transient simulation, E-L approach, single particle drag law, no VM, qualitative comparison.
Zhang and Prosperetti, 1997	The averaged momentum and energy equations for disperse two phase flows are derived by extending a recently developed ensemble averaging method. The resulting equations have a "two-fluid" form and the closure problem is phrased in terms of quantities that are amenable to direct numerical simulation.
Sokolichin *et al.*, 1997	2D partially aerated bubble column, 2D transient simulation, E-E and E-L approach, laminar, constant slip, no VM, qualitative comparison with data.
Ranade, 1997	Cylindrical air-water bubble column, 2D axi-symmetric steady-state simulation, E-E approach, $k-\varepsilon$ model, radial position dependent inward force and slip velocity, no VM, quantitative comparison with data.
Delnoij *et al.*, 1997a Delnoij *et al.*, 1999 Delnoij *et al.*, 1997b	Dynamic E-L simulation, 2D rectangular system, Aspect ratio studied L/D=1 to 11.4. Two-way coupling i.e. momentum transfer from bubble to liquid and from liquid to bubbles is considered. Drag, VM, lift. Dynamic 3D, E-L simulations, two-way coupling. Dynamic E-L simulation, 2D rectangular system, homogeneous flow regime, bubble-bubble interaction via a collision model, L/D and startup are studied.

Sokolichin and Eigenberger, 1999	2D partially aerated bubble column, 2D and 3D transient simulation, E-E approach, laminar (2D) and $k-\varepsilon$ model (3D), constant slip, no VM, qualitative comparison with data.
Thakre and Joshi, 1999	Cylindrical air-water bubble column, 2D axi-symmetric transient simulation, E-E approach, $k-\varepsilon$ model, constant slip velocity, VM, Magnus force, quantitative comparison with data.
Lain *et al.*, 1999	3D bubble column, 2D axi-symmetric dynamic E-L simulations, modified $k-\varepsilon$ model that accounts for turbulence modifications by the bubbles including wake generated turbulence, two types of drag formulations: rigid sphere, fluid sphere, VM and lift force.
Borchers *et al.*, 1999	2D partially aerated bubble column, 3D transient simulation, E-L approach, $k-\varepsilon$ model, single particle drag model, no VM.
Sanyal *et al.*, 1999	Cylindrical air-water bubble column, 2D axi-symmetric transient simulation, E-E approach, $k-\varepsilon$ model, single particle drag model, no VM, quantitative comparison with data.
Pfleger *et al.*, 1999	Dynamic E-E simulation, air-water system, 2D and 3D rectangular partially aerated system, Laminar and Turbulent (single phase $k-\varepsilon$ model) simulations.
Mudde and Simonin, 1999 Oey *et al.*, 2001 Mudde and Van Den Akker, 2001	2D and 3D rectangular system, dynamic E-E simulation, air-water system, drag force, with VM, no lift force, modified single phase $k-\varepsilon$ model to account for the effect of dispersed phase.
Pan *et al.*, 1999; 2000; Pan and Dudukovic, 2001	Dynamic 2D and 3D simulations, rectangular bubble column, bubbly and churn turbulent flow regimes, E-E model, bubble-induced turbulence, single particle drag model, virtual mass, no lift force, quantitative comparison with data.
Padial *et al.*, 2000	Three-phase flow in conical-bottom draft-tube bubble columns, 3D transient simulation, E-E approach, $k-\varepsilon$ model, single particle drag model, VM, quantitative comparison with data.
Krishna *et al.*, 1999; 2000; 2001a; 2001b van-Baten and Krishna, 2001 Krishna and van Baten, 2001b	Dynamic E-E, 3D cylindrical bubble column, air-water, air-tellus oil, 2D axi-symmetric and 3D simulations, $k-\varepsilon$ model, different single particle drag formulae for 'small' and 'large' bubbles, no VM, no lift force, quantitative comparison with data.
Pfleger and Becker, 2001	Dynamic, 3D, E-E simulations, Cylindrical bubble column, bubbly flow regime, Standard single phase $k-\varepsilon$ model, The effect of bubble induced turbulence is included.
Ranade and Tayalia, 2001	2D-axisymmetric, 2D-rectangular, 3D-cylindrical systems, Dynamic E-E simulation, shallow bubble column (L/D=2), air/water system. Standard single-phase $k-\varepsilon$ model, drag force, no VM, no lift force.

2.1 Direct Numerical Simulation (DNS)

The best way of dealing with the presence of a broad range of spatial and time scales is to resolve them in full spectrum. For bubbly flow, this means to solve the three-dimensional time dependent flow field described by the Navier-Stokes equations both in the carrier fluid and inside the bubbles. DNS is model free and describes the full physics of the flow problem under investigation. Special algorithms are necessary to track the fluid interface and very fine meshing is needed to capture all time and length scales.

The oldest and most popular approach is to capture the front dividing the phases directly on a fixed grid. The Volume-Of-Fluid (VOF) method (Hirt and Nichols, 1981), where a marker function was used to identify each fluid, is the best-known example. A number of developments, including a technique to include surface tension (Brackbill *et al.*, 1992), the use of "level sets" (Sussman *et al.*, 1994), the Constrained Interpolation Profile (CIP) method (Yabe, 1997) and phase field method (Jacqmin, 1999) have increased the accuracy of this approach. For details, one should consult the review by Scardovelli and Zaleski (1999) which provides a list of references concerning the VOF method.

The second approach in front tracking is a method with a separate front marking the interface but a fixed grid, which is only modified near the front to make the grid line follow the interface, is used for the fluid within each phase. The original front tracking method was proposed by Unverdi and Tryggvason (1992). Several improvements and modifications were made during the last decade. Esmaeeli and Tryggvason (1996) simulated the motion of a few hundred two-dimensional bubbles at small Reynolds number, 1-2, and found an inverse energy cascade similar to what is seen in the two-dimensional turbulence. They also looked at another case where the Reynolds number is 20-30 (Esmaeeli and Tryggvason, 1999). Bunner and Tryggvason (1999) used a parallel version of this method to investigate the dynamics of two hundred freely moving three-dimensional bubbles with gas volume fraction up to 6%.

The third approach is a Lagrangian method where the grid follows the fluid (see e.g. Johnson and Tezduyar, 1997) and the fourth approach uses separate, boundary fitted grids for each phase (see e.g. Takagi and Matsumoto, 1996). This last method is the most accurate and computationally expensive. For details, one should consult the review by Crowe *et al.* (1996) that contains a list of references concerning applications of DNS in two phase flows.

DNS can be used to obtain a wealth of information such as bubble motion, dispersion and turbulent statistics as seen by the bubble which enrich the understanding of this two phase flow. It can also be used to test the closures that are needed for the macro-scale models (e.g., two-fluid model). In general, DNS is extensively used in simulation of single bubble (Figure 2.1) or bubble cluster (Figure 2.2) flows in confined small domains, frequently with periodic boundary conditions. Due to the excessive computational cost, DNS is limited to low Reynolds numbers and few bubbles, making it unsuitable for most real applications.

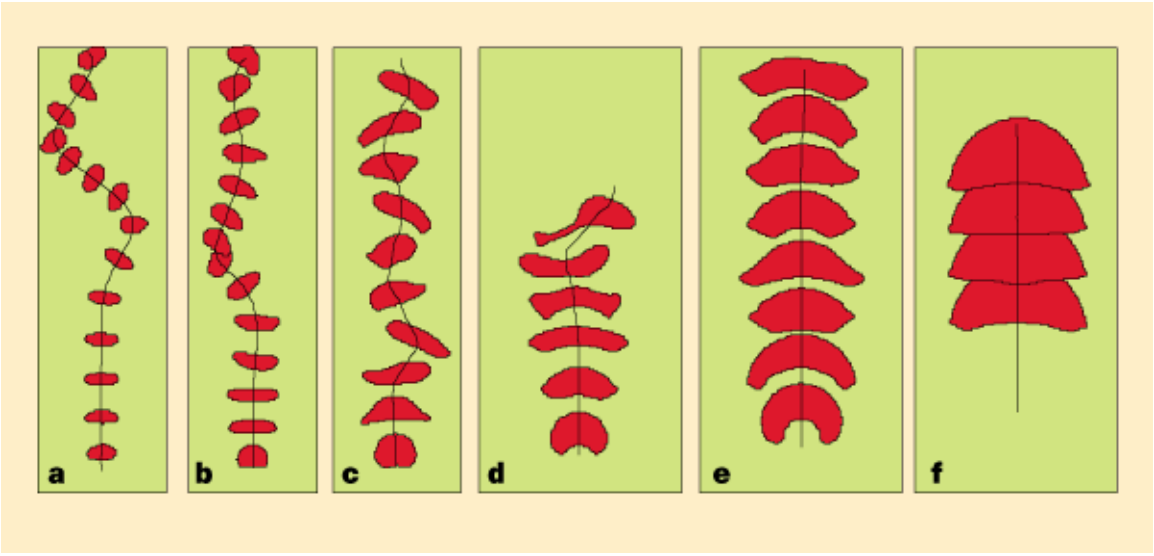

Figure 2.1 Two-dimensional volume-of-fluid simulations of the rise trajectories of bubbles (from Krishna and Van Baten, 1999)

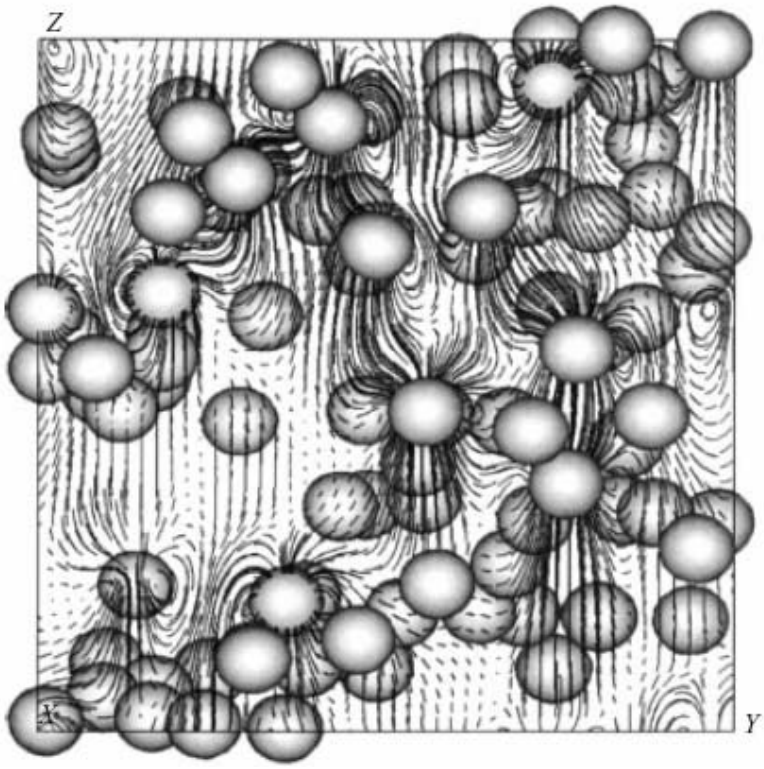

Figure 2.2 Position of the bubbles and streamlines in a vertical cross-section (from Bunner and Tryggvason, 2002).

Our focus is on models that can, at present, simulate the flow in the whole column. Moreover, we are cognizant of the fact that the demands for high volumetric productivity are forcing industrial operations to abandon the bubble flow regime (see Figure 2.3a) and operate increasingly at high gas velocities and high gas holdups (in excess of 30%) in the churn turbulent regime (Figure 2.3b). Figure 2.3, taken in our laboratory in a 2D Plexiglas column with air bubbles sparged through water, illustrates qualitatively the key differences between the two regimes. While in bubbly flow (Figure 2.3a) one indeed has the gas phase in the form of individual bubbles, narrowly distributed around some mean diameter, in churn turbulent flow (Figure 2.3b) also clusters and "large" irregular shape bubbles appear.

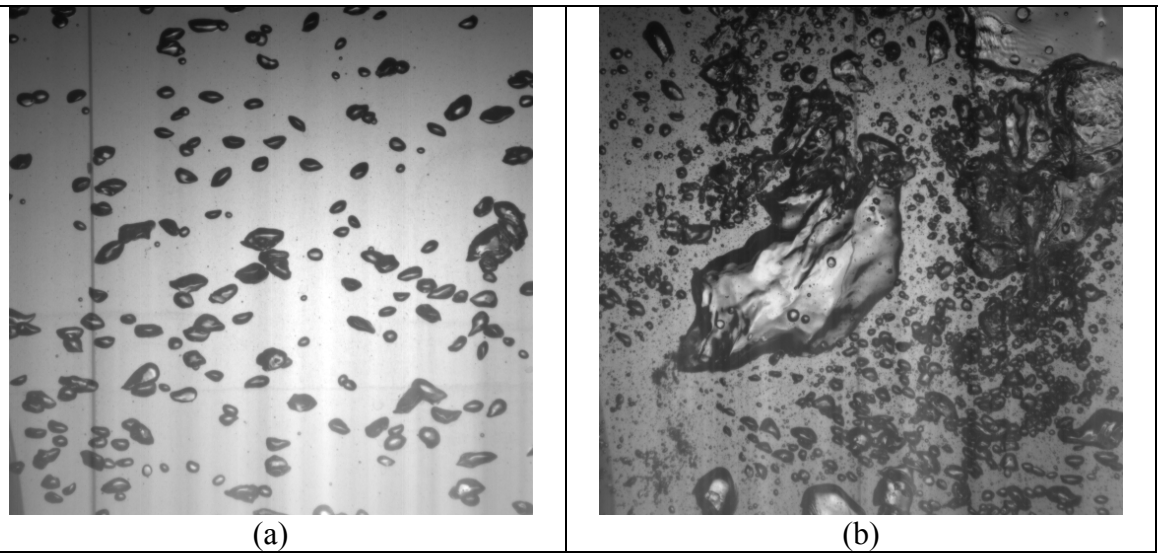

Figure 2.3 Photographic representation of a) bubbly and b) churn-turbulent flow regimes in a 2D bubble column.

To handle the complex gas-liquid flows in practical applications, different averaging techniques, such as ensemble, phase, and time averaging, have been used (Drew *et al.*, 1979; Drew, 1983; Zhang and Prosperetti, 1994; 1997 and Drew and Passmann, 1999), to derive the governing equations. Similarly, numerous studies have been devoted to model the interfacial exchange phenomena (Biesheuvel and Spoelstra, 1989; Drew and Lahey, 1987; Tomiyama *et al.*, 1995a) and turbulence (Abou-Arab, 1986; Elghobashi and Abou-Arab, 1983; Sato *et al.*, 1981a; b and Jakobsen, 1993) in these flows. These fluid dynamic models capable of describing multi-phase flows in the whole column can be divided into Euler-Euler, Euler-Lagrangian or mixture type of models (which is simplified Euler-Euler model) depending on how the dispersed phase is treated.

These approaches have their own advantages and disadvantages and one can choose one of them depending on the flow situation at hand and the desired objectives. In the following sections, we briefly discuss these approaches.

2.2 *Euler-Lagrangian Method*

In this approach, a single set of conservation equations is solved for a continuous phase, while the dispersed phase is instead treated as discrete bubbles or clusters of bubbles and is explicitly tracked by solving an appropriate equation of motion in the Lagrangian frame of reference through the continuous (carrier) phase flow field (Figure 2.4). The interaction between the continuous and the dispersed phase can be taken into account with separate models for drag, lift, virtual mass, and the Basset history forces.

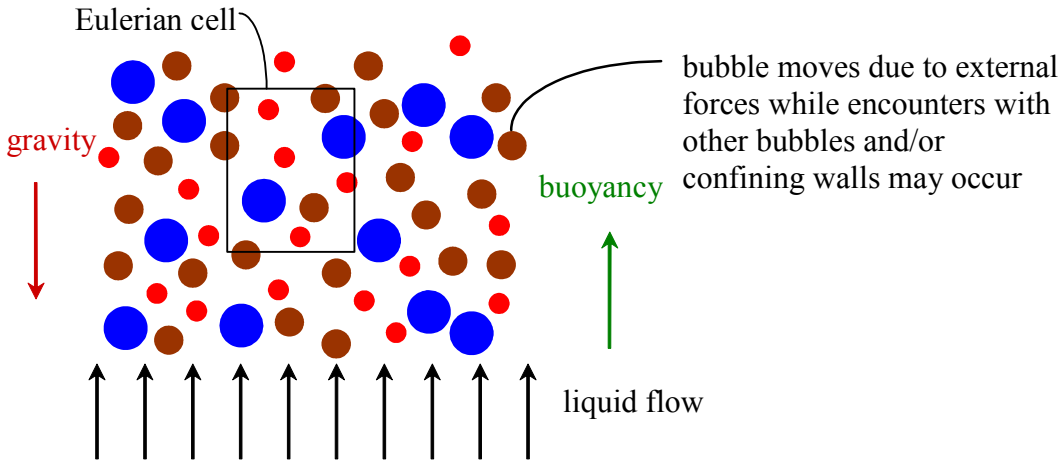

Figure 2.4 Schematic of Euler-Lagrangian Method

For continuous phase, the volume averaged mass and momentum balance equations can be written as:

$$\frac{\partial(\alpha_1\rho_1)}{\partial t}+\nabla\cdot(\alpha_1\rho_1\mathbf{u}_1)=0 \tag{2.1}$$

$$\frac{\partial(\alpha_1\rho_1\mathbf{u}_1)}{\partial t}+\nabla\bullet(\alpha_1\rho_1\mathbf{u}_1\mathbf{u}_1)=-\alpha_1\nabla p+\nabla\bullet\alpha_1\boldsymbol{\tau}_1+\alpha_1\rho_1\mathbf{g}+\mathbf{F}_{12} \tag{2.2}$$

where α_1 , ρ_1 , $\mathbf{u}_1$ are volume fraction, density, and velocity vector of the continuous phase, respectively. p is the pressure, $\boldsymbol{\tau}_1$ is the stress tensor, $\mathbf{g}$ is the acceleration due to gravity. The stress tensor can be defined as:

$$\boldsymbol{\tau}_1 = \mu_1 \left[\nabla \mathbf{u}_1 + \left(\nabla \mathbf{u}_1 \right)^{\mathrm{T}} - \frac{2}{3} \mathbf{I} \left(\nabla \bullet \mathbf{u}_1 \right) \right] \tag{2.3}$$

where μ_1 is the continuous phase molecular viscosity. In Equation (2.2), the term $\mathbf{F}_{12}$ represents the (interfacial) momentum (e.g., drag force, virtual mass, and lift forces) transferred to the continuous phase due to the movement of dispersed phase particles. Depending on the size and concentration of dispersed phase particles, three different levels of coupling between the phases need to be described:

2.2.1 One-way coupling

When dispersed phase particles are very small in size and low in concentration, one-way coupling prevails between the phases (Johansen, 1990; Webb *et al.*, 1992). In this case, it is assumed that the movement of the dispersed phase particles does not change the flow field of the continuous phase (i.e., $\mathbf{F}_{12} = 0$); therefore, the flow field of the continuous phase can be obtained independent of the motion of the dispersed phase particles.

2.2.2 Two-way coupling

For moderate size and/or concentration of particles, a two-way coupling (Lapin and Lübbert, 1994b; Lain *et al.*, 1999; Delnoij *et al.*, 1999) prevails between the phases in which the effects of dispersed phase movement on the continuous phase flow field and vice versa are taken into account (i.e., $\mathbf{F}_{12} \neq 0$).

2.2.3 Four-way coupling

When particle concentration is significantly high, in addition to the two-way coupling, one needs to include the momentum exchange between the particles via particle-particle collisions. This is called four-way coupling (Hoomans *et al.*, 1996; Delnoij *et al.*, 1997b; Hoomans, 2000) and will not be discussed here further as it mainly used in gas-solid or liquid-solid flow investigations.

The motion of gas bubbles can generally be formulated based on Newton's second law as (Johansen, 1990):

$$\frac{d\left(m_b \mathbf{u}_2\right)}{dt} = \mathbf{F_D} + \mathbf{F_V} + \mathbf{F_P} + \mathbf{F_G} + \mathbf{F_B} + \mathbf{F_L} + \mathbf{F_E} \tag{2.4}$$

where m_b and $\mathbf{u}_2$ are the mass and velocity vector of the bubble, respectively. The forces appearing on the right hand side of Equation (2.4) are interfacial and field forces acting on the bubble. $\mathbf{F_D}$, $\mathbf{F_V}$, $\mathbf{F_P}$, $\mathbf{F_G}$, $\mathbf{F_B}$, $\mathbf{F_L}$ and $\mathbf{F_E}$ are the drag force, virtual mass, global pressure force, gravity, Basset history force, transversal lift force and all external field forces except gravity, respectively.

As turbulence description in the continuous phase by either a $k-\varepsilon$ or an RSM model only leads to averaged velocity and turbulence statistics, while the equation of motion requires the instantaneous velocity of the continuous phase at bubble position, some assumptions have to be made to generate the instantaneous values from its mean. Three methods are typically employed in the Euler-Lagrangian approach (Lathouwers, 1999): discrete random walk, continuous random walk and models based on the Langevin equation (make use of a Lagrangian stochastic differential equation to compute the fluctuation and the mean velocity together).

The dynamic modeling of bubble column flows using the Euler-Lagrangian approach has contributed a great deal to the improvement of fundamental understanding of these flows. Many authors (e.g., Johansen *et al.*, 1987; Johansen and Boysan, 1988;

Johansen, 1990; Webb *et al.*, 1992; Lapin and Lübbert, 1994b; Delnoij *et al.*, 1997a; Delnoij *et al.*, 1997b; Delnoij *et al.*, 1997c; Delnoij *et al.*, 1999; Lain *et al.*, 1999; Borchers *et al.*, 1999; Lapin *et al.*, 2001; Lapin *et al.*, 2002) use the Euler-Lagrangian approach to study the dynamics of bubble column flows in 2D and/or 3D systems. All of these studies assume a pseudo-continuous carrier phase flow in which discrete bubbles are tracked by solving their equations of motion. The interactions between the carrier and the discrete phase are taken into account with separate models for drag, lift, virtual mass, buoyancy and the Basset history terms. The turbulence in the carrier fluid is usually modeled using the $k-\varepsilon$ model. Depending upon flow conditions, one-way or two-way coupling between the phases were employed but no bubble breakup or coalescence was considered as only low gas holdup conditions (<3 %) were studied.

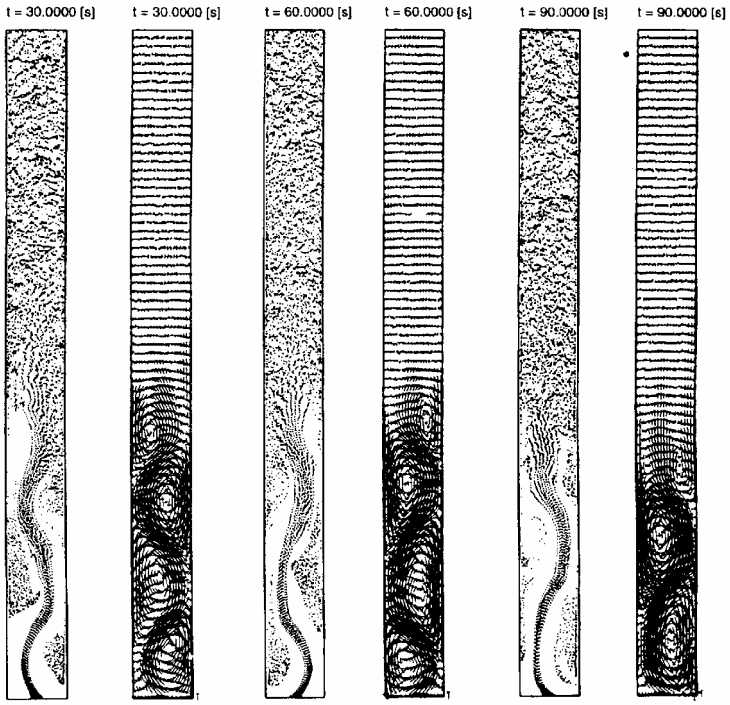

Figure 2.5 Computed structure of two-phase gas-liquid flow in a bubble column with an aspect ratio of 11.4. Superficial gas velocity equals 35 mm/s. Both instantaneous bubble positions and liquid velocity fields are shown 30 s after start up, 60 s after start up and 90 s after start up. (Delnoij *et al.*, 1997b).

Delnoij *et al.* (1997a; 1997b), via 2D simulations of a locally aerated bubble column, found: (a) a transition in the flow pattern from 'cooling tower' mode of circulation ($L/D = 1.0$) to the staggered vortices mode of circulation ($L/D \geq 2.0$), (b) a stationary mode of staggered vortices for $2.0 < L/D < 4.8$ where the vortices do not move downwards along the wall, (c) a dynamic mode of staggered vortices for $4.8 < L/D < 7.7$, where the staggered vortices move downwards and form a meandering bubble plume, and (d) a flow structure consisting of two different regions where in the lower region, the dynamic staggered vortices form a bubble plume while in the upper region bubbles disperse uniformly (i.e., no bubble plume, see Figure 2.5) over the cross section without any vortices for $L/D > 7.7$. Delnoij *et al*. (1999) extended their previous model (Delnoij *et al.*, 1997a) to 3D simulations and obtained the same conclusions as in 2D simulations regarding the absence of the bubble plume in the upper region of the column. However, Chen *et al*. (1989) investigated experimentally two different 2D-rectangular bubble columns (Column A: width=760 mm, depth=50 mm; Column B: width=175 mm, depth=15 mm, both operated at a superficial gas velocity of 0.35 cm/s) the effect of the *L/D* ratio (*L/D* ratio from 0.5 to 11.4) and reported the presence of the bubble plume in the upper region of the column.

Lain *et al.* (1999) presented an experimental and numerical study of the hydrodynamics in a cylindrical bubble column (*L/D* = 65cm/14cm = 4.6) using phase-Doppler anemometry (PDA) and dynamic Euler-Lagrangian simulations coupled with a modified $k-\varepsilon$ model to incorporate the effect of bubbles on the turbulence field. They reported that the bubble size distribution must be considered for predicting the non-isotropy in the fluctuating motion of the bubbles, and that for the prediction of the bubble induced turbulence appropriate source terms, which also account for the wake effects, should be incorporated in the turbulence model.

Recently, Lapin *et al*. (2002) and Michele and Hempel* (2002) studied the effect of the ring-sparger on the hydrodynamics of a bubble column. The experimental observations (Lapin *et al.*, 2001; Michele and Hempel, 2002) confirm the numerical predictions (Lapin *et al.*, 2002; Michele and Hempel, 2002) that the long time-averaged flow pattern in a slender bubble column ($L/D \approx 8$) equipped with a *ring-sparger* exhibits a two-loop behavior in both bubbly flow (Lapin *et al.*, 2002) and churn-turbulent flow regime (Michele and Hempel, 2002). In other words, the mean flow rises close to the wall in the lower part of the column and consequently comes down in the core region, while the flow structure has its usual pattern of up flow in the center and down flow near the walls in the upper region.

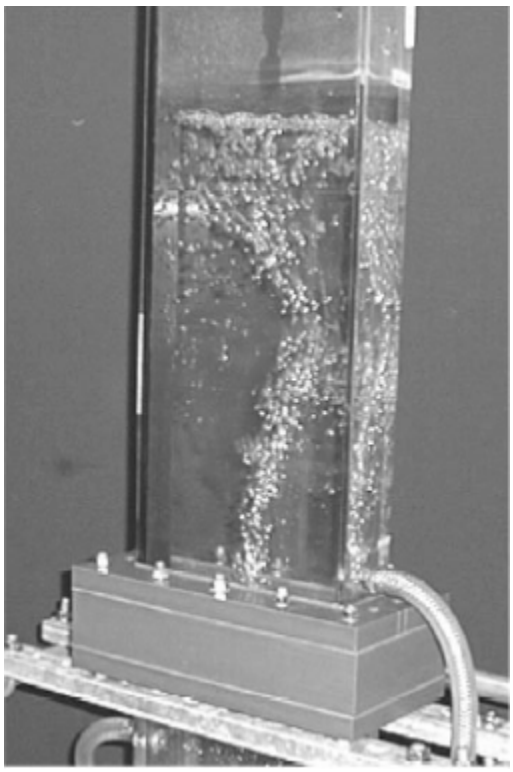

Figure 2.6 Bubble column with single bubble plume (from Pfleger *et al.*, 1999).

* Euler-Euler method was used.

The Euler-Lagrangian method is quite suitable for fundamental investigations since it allows for direct consideration of various effects related to bubble-bubble and bubble-liquid interactions. Another advantage of the Euler-Lagrangian method is that it allows for easy implementation via an extension of an existing single-phase simulation code. Moreover, incorporation of arbitrary distribution of bubble properties is easy. As illustrated earlier, the Euler-Lagrangian method is generally used in investigation of lab-scale bubbly flow (Figure 2.3a) or single bubble plume (Figure 2.6). The applicability of this method is limited to the situations where the gas superficial velocity and gas holdup are relatively low ($\alpha_g < 5\%$) and the number of bubbles is limited to 100,000. The required computational power is not only dictated by the spatial mesh resolution but also by the number of bubbles that are tracked. For dynamic calculations, tracking all bubbles soon becomes infeasible as the gas volume fraction, and the number of bubbles, increases. A possible simplification has been introduced by Lapin and Lübbert (1994b) where instead of following individual bubbles, groups of bubbles with similar characteristics, called clusters, are tracked. Each cluster is characterized by a density function. In their model, the bubble clusters are considered to have a velocity that is the sum of the liquid velocity, the slip velocity, and a random contribution modeled by a Monte Carlo method. They found that no steady-state could be obtained and only the long time average for the liquid flow field exhibited a single circulation zone. However, in churn turbulent flow regime, the bubbles differ in shape and size significantly and they interact, breakup and coalesce frequently, such that the cluster-tracking concept is no longer valid.

2.3 Euler-Euler (Two-Fluid) Approach

In this approach, both the continuous and dispersed phases are considered to be interpenetrating continua. The two-fluid model is developed to describe the motion for each phase in a macroscopic sense. From the mathematical point of view, the macroscopic description of both phases is derived by ensemble averaging the fundamental microscopic conservation equations for each phase, as shown by Drew

(1983) and Drew and Passmann (1999). The flow description consists of differential equations describing the conservation of mass, momentum and energy for each phase separately. The mass balance is given by (in absence of interphase exchange):

$$\frac{\partial\left(\rho_k\alpha_k\right)}{\partial t}+\nabla\bullet\left(\rho_k\alpha_k\mathbf{u}_k\right)=0 \tag{2.5}$$

$$\sum_{k=1}^{N}\alpha_k=1 \tag{2.6}$$

where α, ρ and $\mathbf{u}$ are the volume fraction, the phase density and the velocity of each phase. k is the phase indicator, $k=1$ for the liquid phase and $k=2$ for gas phase. The corresponding momentum equations for the two phases can be written as:

$$\frac{\partial\left(\alpha_k\rho_k\mathbf{u}_k\right)}{\partial t}+\nabla\bullet\left(\alpha_k\rho_k\mathbf{u}_k\mathbf{u}_k\right)=-\alpha_k\nabla p+\nabla\bullet\left(\alpha_k\boldsymbol{\tau}_k\right)+\alpha_k\rho_k\mathbf{g}+\left(-1\right)^k\mathbf{F}_{exchange} \tag{2.7}$$

where k=1 for continuous phase and k=2 for dispersed phase. $\boldsymbol{\tau}$ is the effective stress tensor which contains not only the contributions from viscous effects but also the contributions from the cross-correlations between velocity fluctuations arising from the averaging, $\mathbf{F}_{exchange}$ is the interfacial force, which explicitly contains the mean interaction between the phases and accounts for the effects of two-way coupling, and $\alpha\rho\mathbf{g}$ is the gravity force. Due to the loss of information in the ensemble averaging process, in Equation (2.7) the interfacial momentum exchange term, $\mathbf{F}_{exchange}$, needs to be closed in terms of known variables. Several challenging issues regarding the modeling of averaged equations and closure relations, which have been the active research topic in the field of multiphase flow for many years, still exist. One key question is how to model the inter-phase momentum exchange. This is related to the problem of calculating the force acting on the bubble and taking into account the effect of multi-bubble interaction, large deformable bubbles of the dispersed phase and finite value of gas holdup on these forces. Another unresolved issue is modeling of turbulence in two-phase flow.

In most industrial applications, high gas superficial velocity is used which results in heterogeneous flow regime, i.e., the so-called churn turbulent flows. Under such

conditions Euler-Euler method is usually preferred. As stated above, in the Euler-Euler approach the information regarding the microscopic scale has been lost leading to the closure problem which is the key issue of the Eulerian two-fluid model. One of the main objectives of this work is to take the bubble-bubble interaction effect into account and implement it into the CFD framework to predict the local bubble size (or interfacial area) and improve the gas holdup prediction with the help of the bubble population balance equation.

2.4 Algebraic Slip Mixture Model (ASMM)

Like the Euler-Euler approach, the algebraic slip mixture model assumes the phases to be completely interpenetrating and allows the phases to move at different velocities. However, unlike the Euler-Euler model, the mixture model does not solve the mass and the momentum balance equations for each phase, but only for the mixture phase. The continuity and the momentum equations for the mixture phase, shown below, can be obtained by summing together the corresponding equations for the constituent phases.

$$\frac{\partial \rho_m}{\partial t} + \nabla \bullet \left(\rho_m \mathbf{u}_{\mathrm{m}} \right) = 0 \tag{2.8}$$

$$\frac{\partial \left(\rho_m \mathbf{u}_{\mathrm{m}} \right)}{\partial t} + \nabla \bullet \left(\rho_m \mathbf{u}_{\mathrm{m}} \mathbf{u}_{\mathrm{m}} \right) = -\nabla p + \nabla \bullet \left(\boldsymbol{\tau}_{\mathrm{m}} + \boldsymbol{\tau}_{\mathrm{m}}^{\mathrm{t}} \right) + \nabla \bullet \boldsymbol{\tau}_{\mathrm{Dm}} + \rho_m \mathbf{g} \tag{2.9}$$

where $\rho_m = \sum_{k=1}^{n} \alpha_k \rho_k$ is the mixture density, n is number of phases, $\mathbf{u}_{\mathrm{m}} = \frac{\sum_{k=1}^{n} \alpha_k \rho_k \mathbf{u}_{\mathrm{k}}}{\rho_m}$ is the mass-averaged mixture velocity, $\mu_m = \sum_{k=1}^{n} \alpha_k \mu_k$ is the mixture viscosity, $\mathbf{g}$ is the gravity acceleration, $\boldsymbol{\tau}_{\mathrm{m}}$, $\boldsymbol{\tau}_{\mathrm{m}}^{\mathrm{t}}$, $\boldsymbol{\tau}_{\mathrm{Dm}}$ are the mixture viscose stress, turbulent stress and diffusion stress due to the phase slip, respectively.

$$\boldsymbol{\tau}_m = \mu_m \left(\nabla \mathbf{u}_m + \nabla \mathbf{u}_m^{\mathrm{T}} \right) - \frac{2}{3} \mu_m \nabla \bullet \mathbf{u}_m \mathbf{I} \tag{2.10}$$

$$\boldsymbol{\tau}_m^t = \mu_m^t \left[\left(\nabla \mathbf{u}_m + \nabla \mathbf{u}_m^{\mathrm{T}} \right) - \frac{2}{3} \nabla \bullet \mathbf{u}_m \mathbf{I} \right] - \frac{2}{3} \rho_m k_m \mathbf{I} \tag{2.11}$$

$$\boldsymbol{\tau}_{Dm} = \sum_{k=1}^{m} \alpha_k \rho_k \mathbf{u}_{D,k} \mathbf{u}_{D,k} \tag{2.12}$$

where k_m is the mixture turbulent kinetic energy density and μ_m^t is the mixture turbulent viscosity. The turbulent stress term in the mixture equation is closed by solving the $k-\varepsilon$ model for the mixture phase. In Equation (2.12), $\mathbf{u}_{\mathrm{D,k}} = \mathbf{u}_{\mathrm{k}} - \mathbf{u}_{\mathrm{m}}$ are the drift (diffusion) velocities for liquid ($k = l$) and gas phases ($k = g$) with respect to the mass center, respectively.

The diffusion stress, $\boldsymbol{\tau}_{Dm}$, which originates because of the relative slip between the two phases, requires closure in terms of the diffusion velocity $\mathbf{u}_{\mathrm{D,k}}$ of each phase (or, equivalently, the drift or the slip velocity between the phases). In the ASMM, this is supplied by assuming that the phases are in local equilibrium over short spatial length scales. This implies that the accelerating dispersed phase particles (bubbles) attain the terminal velocity after traveling a distance which is much smaller than the system length scale. In other words, the dispersed phase entity (bubble, particle) always slips with respect to the continuous phase at its terminal Stokes' velocity in the local acceleration field. The form of the slip or relative velocity is given by:

$$\mathbf{u}_{slip,k} = \tau_{12} \mathbf{a} \tag{2.13}$$

where $\mathbf{a}$ is the dispersed phase particle acceleration and τ_{12} is its relaxation time. If the particle/bubble is small compared to the scale of the velocity variations and possesses a low particle Reynolds number, it follows the motion of the fluid. According to Clift *et al.* (1978), a particle follows the fluid motion if its relaxation time τ_{12} is small compared with the hydrodynamic time-scale. In the Stokes regime this condition can be written as

$$\tau_{12} = \frac{\rho_2 d_p^2}{18 \mu_m} << \tau_{hydro} \tag{2.14}$$

where d is the particle (bubble) diameter and τ_{hydro} is the hydrodynamic time scale of the system which can be estimated as

$$\tau_{hydro} = \left| \frac{\mathbf{u}_m}{\partial \mathbf{u}_m / \partial t + \left(\mathbf{u}_m \bullet \nabla\right)\mathbf{u}_m} \right| \tag{2.15}$$

The slip velocity is defined as the velocity of the secondary phase relative to the primary phase velocity:

$$\mathbf{u}_{slip,k} = \mathbf{u}_{k\neq 1} - \mathbf{u}_1 \tag{2.16}$$

The slip velocity and the drift velocity can be connected by the following expression:

$$\mathbf{u}_{D,k} = \mathbf{u}_{slip,k} - \sum_{i=1}^{n} \frac{\alpha_i \rho_i \mathbf{u}_{1i}}{\rho_m} \tag{2.17}$$

and

$$\mathbf{u}_{slip,k} = \frac{\left(\rho_m - \rho_k\right) d_k^2}{18\mu_1 f}\left(\mathbf{g} - \frac{D\mathbf{u}_m}{Dt}\right) \tag{2.18}$$

$$f = \begin{cases} 1 + 0.05Re^{0.687} & Re < 1000 \\ 0.018Re & Re < 1000 \end{cases} \tag{2.19}$$

By solving Equations (2.17) and (2.18), the diffusion velocity $\mathbf{u}_{\mathrm{D,k}}$ of each phase can be obtained, thus the closure for the diffusion stress, $\boldsymbol{\tau}_{Dm}$, is provided.

The diffusion stress term $\boldsymbol{\tau}_{Dm}$ is also the only term in which the phase volume fractions appear explicitly. In order to back out the individual phase velocities and volume fraction, it is necessary to solve a differential equation for volume fraction of the dispersed phase coupled with the solution of the mixture equations. This equation is obtained from the equation of continuity for the dispersed phase.

$$\frac{\partial}{\partial t}\left(\alpha_s \rho_s\right) + \nabla\left(\alpha_s \rho_s \mathbf{u}_{\mathrm{m}}\right) = -\nabla \bullet \left(\alpha_s \rho_s \mathbf{u}_{\mathrm{D,s}}\right) \tag{2.20}$$

It should be noted that in order to apply the mixture model, the bubble has to reach the terminal velocity in a short period of time compared to the time scale characterizing the flow. In reality, however, it has been shown ASMM behaves well far outside its limitations and predict flow field equally well with Euler-Euler model prediction (Sanyal *et al.*, 1999).

2.5 Interfacial Force

The Euler-Lagrangian, the Euler-Euler and the ASMM approaches require additional models to describe the interaction between the continuous and the dispersed phases. The forces acting on a motionless bubble in a stagnant liquid are pressure and gravity. Since there is usually a relative motion between the bubble and liquid, the liquid flow around individual bubbles leads to local variations in pressure producing a shear stress. A bubble surrounded by a flowing liquid is exposed to a number of forces, which act on it through the traction at the gas-liquid interface (Zhang and Prosperetti, 1997; Drew and Passmann, 1999). If the slip velocity is constant, the force acting due to the relative motion is only the frictional drag force. If, however, the motion is non-uniform one needs to extend the concept of the interfacial force to include in addition to the friction drag, the virtual mass and the lateral lift forces. In order to calculate the Basset force, one needs bubble trajectory which is not available in Euler-Euler or ASMM approaches. Moreover, the magnitude of Basset force is about $\left(\rho_l/\rho_g\right)^{0.5}$ times lower than virtual mass force (Chung and Troutt, 1988). Thus Basset force can be neglected in gas-liquid flow.

2.5.1 Drag Force

So far investigations of dispersed gas-liquid flows in bubble columns have been performed by modeling the generalized or total drag force as a linear combination of its various components. This linear combination has widely been used by all researchers.

Drew and Passmann (1999) presented the theoretical analysis of the constitutive relations for the interfacial momentum transfer and showed the validity of the above-mentioned linear combination in the limit of dilute suspensions. But there is no theoretical study proving the applicability of the linear combination to cases where the suspension is dense. All studies reported in the literature, dealing with the modeling of bubbly flow as well as the churn-turbulent flow regimes, use the linear combination. The forces assumed to be important for the dispersed flow in bubble columns are: the steady interfacial drag force, the added/virtual mass force, the transversal lift forces, the Basset force and the interfacial mass transfer rate. These forces are discussed in the following sections.

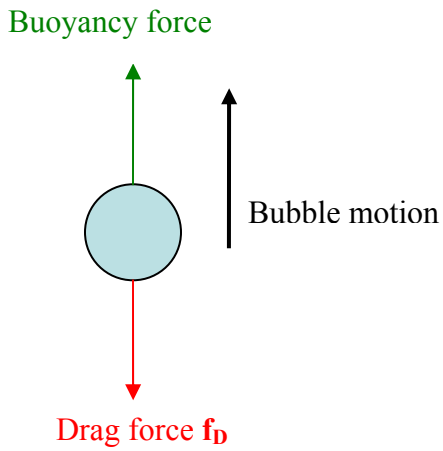

Figure 2.7 Drag force for a single bubble

For a single spherical bubble, rising at steady state, the force balance yields the following drag force $\mathbf{f_D}$ (Figure 2.7).

$$\mathbf{f}_D = C_D\left(\frac{\pi}{4}d_B^2\right)\frac{\rho_1}{2}(\mathbf{u}_2-\mathbf{u}_1)\left|\mathbf{u}_2-\mathbf{u}_1\right| \tag{2.21}$$

where C_D is the drag coefficient, d_B, is the bubble diameter and $(\mathbf{u}_2 - \mathbf{u}_1)$ is the slip velocity. Equation (2.21) assumes that bubbles are spherical in shape. The drag coefficient, C_D , is a function of the particle Reynolds number, defined as $\mathrm{Re} = \dfrac{\rho_1 |\mathbf{u}_2 - \mathbf{u}_1| d_B}{\mu_1}$.

The drag force for a single bubble depends on the size and the shape of the bubble, and the nature of the gas-liquid interface. For a swarm of bubbles, the formulation of the drag force is further complicated by the presence of other surrounding bubbles. If there are N bubbles in a bubble column, then the drag force, based on simple geometric arguments which ignore the effect of bubble-bubble interactions on the surrounding liquid, can be written as:

$$\mathbf{F}_{swarm} = N\mathbf{f}_D = \left(\frac{\pi D^2 H \alpha_2 / 4}{\pi d_B^3 / 6} \right) \mathbf{f}_D \tag{2.22}$$

The drag force per unit volume thus is:

$$\mathbf{F}_D = \frac{\mathbf{F}_{swarm}}{\left(\pi D^2 H/4\right)} = \left(\frac{\alpha_2}{\pi d_B^3/6} \right) \mathbf{f}_D = \frac{3\alpha_2}{4} \left(\frac{\rho_1}{d_B} \right) C_D |\mathbf{u}_2 - \mathbf{u}_1| \left(\mathbf{u}_2 - \mathbf{u}_1 \right) \tag{2.23}$$

where D and H are diameter and height of the control volume considered, respectively. In order to ensure that the interfacial force vanishes at locations where either of the two phases (continuous or dispersed) is present in its pure form, and the model properly solves only the single-phase momentum equations at such locations while recognizing the absence of any other phase, one needs to multiply Equation (2.23) by α_1 , i.e.

$$\mathbf{F}_D = \frac{3\alpha_1\alpha_2}{4} \left(\frac{\rho_1}{d_B} \right) C_D |\mathbf{u}_2 - \mathbf{u}_1| \left(\mathbf{u}_2 - \mathbf{u}_1 \right); \quad \text{such that } \lim_{\alpha_1 \to 0} F_D = 0 = \lim_{\alpha_2 \to 0} F_D \tag{2.24}$$

Equation (2.24) implicitly assumes that bubbles do not interact (absence of bubble coalescence and breakup) with each other but they move rather as independent entities. Moreover, to estimate F_D using Equation (2.24), the knowledge of bubble diameter d_B is

needed. In most of the reported studies (Jakobsen, 1993, Jakobsen *et al.*, 1997, Johansen, 1990, Kuipers and Swaaij, 1998, Lapin and Lübbert, 1994a, Lapin *et al.*, 2002, Oey *et al.*, 2001, Pan *et al.*, 1999, Pfleger *et al.*, 1999, Pfleger and Becker, 2001, Ranade and Van der Akker, 1994, etc.), the value of '*d'* is taken as *'the mean bubble size'*. For bubble columns operated at low gas superficial velocities (< 3 cm/s), where the bubble size distribution remains narrow, the concept of mean bubble size may work. However, at high gas superficial velocities, which is the case in most of the industrial applications, bubble breakup and coalescence phenomena prevail, resulting in a broad distribution of bubble sizes. Approximating the representative bubble size by a single mean bubble size may not be adequate in this case. Therefore, it is necessary to take into consideration the effect of bubble breakup and coalescence phenomena and of bubble size distribution on the hydrodynamics in order to be able to simulate the flow correctly, which is one of the major objectives of this research.

The coefficient C_D appearing in Equations (2.24) is called the drag coefficient. Its value is likely to be different for a single bubble and a bubble swarm. This is because the shape and size of a bubble in a bubble swarm is much different than that of an isolated bubble. Moreover, bubble-bubble interaction and gas holdup may alter the numerical value of the coefficient from that of single bubble as the flow structure of the liquid surrounding a bubble gets modified when the bubble becomes part of the swarm. There are several empirical and semi-empirical correlations available in the literature for the estimation of the drag coefficient C_D, which can be found in the recent review by Rafique *et al.* (2004). In this study, the drag coefficient suggested by Schiller and Naumann (1935) was used, and it can be given as:

$$C_D = \begin{cases} 24\left(1+0.15\,\mathrm{Re}^{0.687}\right)/\mathrm{Re} & \mathrm{Re} \le 1000 \\ 0.44 & \mathrm{Re} > 1000 \end{cases} \tag{2.25}$$

There are several drag coefficient correlations for gas-liquid system (e.g. Ishii and Zuber, 1979; Tsuchiya *et al.*, 1997) developed from single bubble rising in quiescent liquid or in dilute bubbly flows. However, if they are applied to churn-turbulent flow regime, these

correlations significantly overestimate drag coefficient. The drag reduction factor correlation is not yet available and one has to manually adjust this factor or artificially increases the bubble size. For example, when Tsuchiya *et al.*'s (1997) correlation is used to calculate the drag force, the mean bubble size is increased to 3.2 cm to fit the liquid axial velocity profile in a 44-cm diameter air-water column operated at $U_g = 10$ cm/s (Pan and Dudukovic, 2000).

The drag force accounts for the interaction between the liquid and bubbles in a uniform flow field under non-accelerating conditions. If, however, the flow conditions are not uniform, or the flow field surrounding a bubble is accelerating/decelerating, then additional forces act on the bubble, which can be lumped as non-drag forces. These forces are discussed in the following sections.

2.5.2 Added/virtual mass force

When a bubble moves in a liquid field with a non-uniform velocity, it accelerates some of the liquid in its neighborhood. Due to the acceleration induced by the bubble motion, the surrounding liquid experiences an extra force, which is due to the motion in a non-inertial frame of reference, called virtual or added mass force (Figure 2.8). It should be emphasized that although a bubble moving with a constant terminal velocity also accelerates some liquid in its neighborhood but this does not result in a virtual mass force. The concept of the added mass force can be understood by considering the change in the kinetic energy of a fluid surrounding an accelerating sphere. In potential flow the acceleration induces a resisting force on the sphere equal to one-half the mass of the displaced fluid times the acceleration of the sphere. Drew *et al.* (1979) and Drew and Lahey (1987) studied the necessary condition for the requirement of frame indifference of the constitutive equations and, by applying the principle of objectivity, derived the virtual mass force as:

$$\mathbf{F}_v = -\alpha_1 \alpha_2 \rho_1 C_v \frac{D(\mathbf{u}_1 - \mathbf{u}_2)}{Dt} \tag{2.26}$$

The coefficient C_V is the virtual mass coefficient and it corresponds to the volume fraction of liquid that is accelerated with the bubble. This coefficient is generally bubble-shape and gas holdup dependent.

Figure 2.8 Added/virtual mass force for a single bubble

In the case of gas-liquid flows, the influence of the steady state drag force is predominant as compared to the virtual mass force, inclusion of the virtual mass effect is necessary to predict correct hydrodynamics (Mudde and Simonin, 1999). Mudde and Simonin (1999), via 3D simulations using the $k-\varepsilon$ model, showed that the use of only drag force as an interfacial momentum exchange source resulted in an under-prediction of the amplitude and frequency of the bubble plume oscillations. However, when the drag and the virtual mass forces were used together, the values of the amplitude and the time period are satisfactorily comparable with the experimental observations. Recently, using a different code than Mudde and Simonin (1999), Oey *et al.* (2003) investigated the influence of interfacial closures and numerics on the hydrodynamics of the same bubble column, but they could not reproduce the results of Mudde and Simonin (1999). However,

they found the right magnitude of the oscillations of meandering plume without using the virtual mass.

In this work, the virtual mass force was neglected in our CFD simulation because of two reasons: 1) virtual mass was neglected by most authors or found to be negligible in Euler-Euler simulation, and 2) in the churn-turbulent flow regime, large bubbles do not have a closed wake and the concept of added mass is not applicable (Krishna *et al.*, 2001b).

2.5.3 Transversal or Lateral force

The physical phenomena giving rise to a transversal or lift force on a single bubble in liquids can roughly be divided into three groups. The Magnus lift force, originally described by Magnus (1853), is due to bubble rotation in a uniform flow field. Swanson (1961) attributed the origin of this force to an asymmetric pressure distribution around the bubble caused by the bubble rotation, as depicted schematically in Figure 2.9.

It was observed that the lift force on a sphere could act in the opposite direction of the standard Magnus force at high Reynolds numbers due to the transition from laminar to turbulent boundary layers on two sides of the sphere as shown in Figure 2.9b (Krahn, 1956; Taneda, 1957). A second lift force, the Saffman force, acts on non-rotating bodies due to shear in the continuous phase flow pattern as depicted in Figure 2.9c (Saffman, 1965; Stone, 2000). Saffman (1965) showed that at low Reynolds numbers, unless the rotating speed of the particle was much larger than the rate of shear, the lateral force due to shear would be an order of magnitude larger than the force due to rotation. At intermediate to high Reynolds numbers, as in bubble column flows, only very idealized models of these forces, based on potential theory, have been presented (Kariysaki, 1987).

The tendency for bubbles to deform under various flow conditions allows for yet another lift force as depicted in Figure 2.9d. Kariysaki (1987) observed a lift force on deformable particles of the opposite sign to that on rigid spheres under linear shear flow.

Similarly, Sankaranarayanan and Sundaresan (2002) performed lattice Boltzmann simulations of bubbly suspension consisting of deformable ellipsoidal bubbles and found a sign reversal. In a paper by Tomiyama *et al.* (1995b), this force was expressed as a transversal force caused by a slanted wake behind a distorted bubble in a shear field.

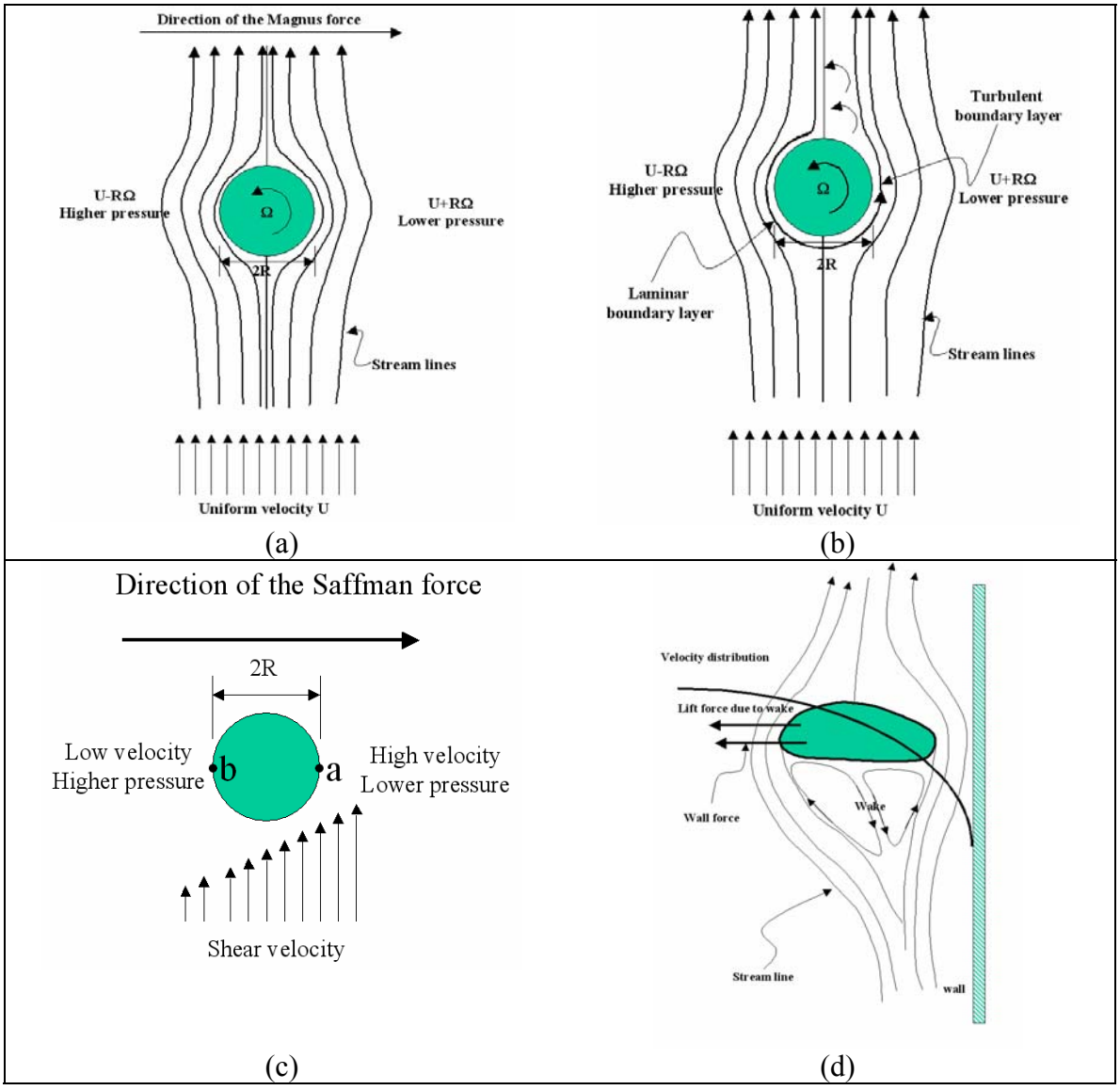

Figure 2.9 Schematic representation of lift force: a) The Magnus force without boundary layer transition, b) The Magnus force with laminar boundary layer on one side and turbulent boundary layer on the other side of the bubble, c) The Saffman force, d) the lift force due to bubble deformation (from Tomiyama *et al.*, 1995b)

2.5.3.1 Magnus force

The Magnus force is purely related to the transversal force acting on rotating bodies. Placed in a uniform flow field, the particle rotation results in an increase in the velocity on one side and a decrease on the other side. This gives rise to an asymmetric pressure distribution around the particle. Rubinow and Keller (1961) showed that a spinning sphere moving in a viscous fluid experiences a force orthogonal to its direction of motion, a lift force. They studied the flow about a sphere of radius r_2, spinning with an angular velocity Ω and moving through an unbounded stationary fluid with a velocity u_2. For small values of the particle Reynolds number (<1), they found that the sphere would experience a lift force given by:

$$\mathbf{F}_L = \pi \rho_1 r_2^3 \Omega \times \mathbf{u}_2 \tag{2.27}$$

This force acts in the same direction as the classical Magnus force.

In a heterogeneous (churn-turbulent) regime, gas bubbles appear to move towards the column center while rising upwards. Tzeng *et al.* (1993) observed such motion of bubbles away from walls. According to Svendsen *et al.* (1992), this radial force arises due to a number of phenomena such as bubble rotation around its own axis (Magnus lift force), relative gas-liquid velocity and a liquid velocity gradient, viscous and turbulent shear gradients around the bubbles, radial pressure gradients, bubble shape changes, wake phenomena and coalescence tendency. There have been a number of investigations (Krahn, 1956; Taneda, 1957; Swanson, 1961; Svendsen *et al.*, 1992; Tzeng *et al.*, 1993) regarding the origin of this force. Swanson (1961) attributed this force to an asymmetric pressure distribution around the bubble created by the interaction of the bubble motion with the flow field. He concluded that the transversal force on bubbles acts towards the regions of high speed if the bubble moves against the liquid flow or moves with the flow but slower than the flow. The force acts towards the low speed regions if the bubble moves with the flow and faster than the flow. However, as already mentioned, Taneda (1957) observed experimentally that in certain ranges of Reynolds number and rotation speed, rotating spheres in a uniform flow field experience a lift force having a direction

opposite to that of the Magnus force. It was concluded that this effect could be explained by a transition of the boundary layer from laminar to turbulent. Both the direction and the magnitude of this force depend on the local flow conditions such that using mean values of the force coefficient may be highly misleading.

2.5.3.2 Saffman force

As described by Lahey (1990) and Jakobsen (1993), a non rotating particle experiences a similar lateral force when placed in a shear flow field. A rigid sphere in shear flow experiences forces that move the particle normal to the flow direction. The Magnus force is thus not the only mechanism responsible for lateral movement of particles. Saffman (1965) computed the lift force on a particle in shear flow. He showed that at low Reynolds numbers, unless the rotating speed of the particle was much larger than the rate of shear, the lateral force due to shear is an order of magnitude larger than the force due to rotation.

The transverse lift force on a spherical gas bubble created by gradients in relative velocity across the bubble diameter was derived by Thomas *et al.* (1983).

$$\mathbf{F}_L = \alpha_1 \alpha_2 \rho_1 C_L \left(\mathbf{u}_1 - \mathbf{u}_2\right) \times \left(\nabla \times \mathbf{u}_1\right) \tag{2.28}$$

Thomas *et al.* (1983), Drew (1983), Drew and Lahey (1987) and Drew and Passmann (1999) assigned the force coefficient as C_L = 0.5 for spherical particles in potential flow. However, the value varies, and for viscous flow, Lahey (1990) reports values as small as 0.01. Sankaranarayanan and Sundaresan (2002) investigated, through Lattice Boltzmann simulation, the lift force in bubbly suspensions and reports the lift force coefficient is not only related to the bubble diameter, but also the shear stress in which the bubble is immerged. Moreover, negative lift force coefficient is found for large bubbles and in strong shear fields. Tomiyama *et al.* (2002) analyzed, both experimentally and through Euler-Lagrange simulations, the transverse migration of single bubbles in

simple shear flows. They found that the lift coefficient C_L for small bubbles (0-4 mm) is a function of bubble Reynolds number *Re*, whereas the coefficient for larger bubbles correlates well with a modified Eötvös number which employs the maximum horizontal dimension of a deformed bubble as a characteristic length. It should be noted that Equation (2.28) implicitly assumes that the bubble velocity vector and the flow field velocity vector are collinear. However, in general three-dimensional flow fields, these may not be collinear. Schrage *et al.* (2001) have derived analytically a generalized form of the lift force for three-dimensional flow fields. Their study assumes a time-independent inviscid flow field surrounding a bubble and conceptually cleaves the bubble into two halves along the plane of the impinging flow field velocity (see Figure 2.10), such that each half-bubble resides in a flow field of a slightly different velocity. In their analysis, the presence of the bubble in the flow field is conceptualized as a small perturbation to the far-field flow dynamics.

Schrage *et al.* (2001) integrated the Euler equation to derive the pressure field for a constant Bernoulli function. The lift force acting on a bubble is calculated by the imbalance of kinetic energy and convective potential of the respective halves and it is shown that the lift force acts from lower velocity regions towards higher velocity regions (from the lower half towards the upper half in Figure 2.10).

It should be noted that, in the Euler-Euler framework, both Magnus and Saffman forces attain an identical mathematical form so that respective coefficients become additive. Most of the researchers (Torvik, 1990; Svendsen *et al.*, 1992; Becker *et al.*, 1994; Sokolichin and Eigenberger, 1994; Lain *et al.*, 1999; Jakobsen, 2001) used C_L~0.5.

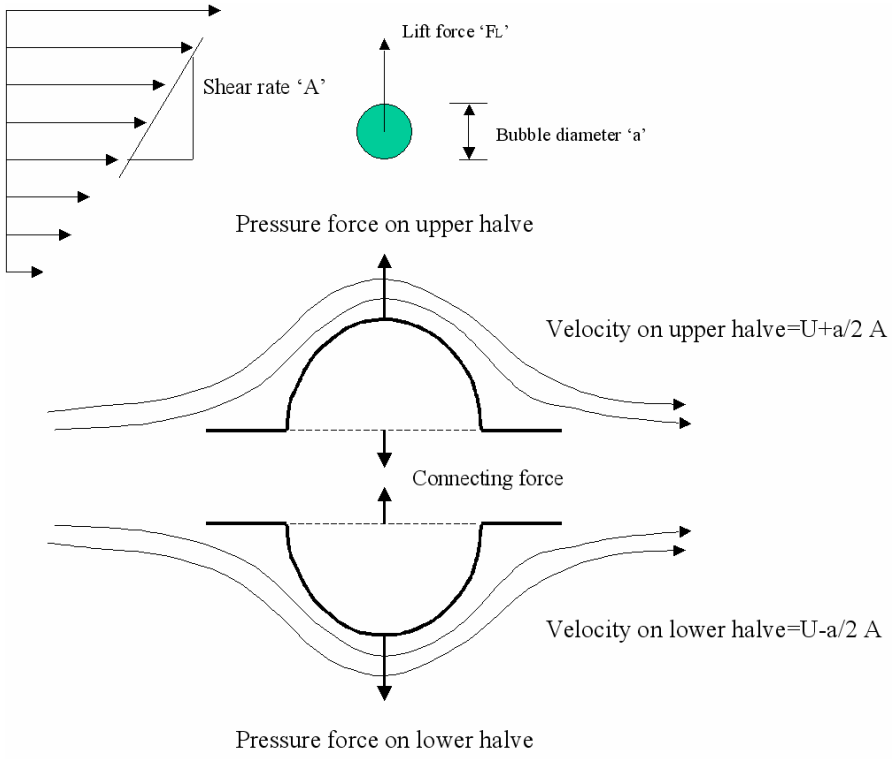

Figure 2.10 Illustration of split-lamina lift model showing bubble cleaving for co-linear bubble and flow field velocity vector (from Schrage *et al.*, 2001)

In the case of 2D simulations, two types of methodologies are usually applied. In the first case, all the derivatives in the third direction appearing in the conservation equations are identically set to zero and the equations are solved in 2D space (say x-y plane). In the second case, an arbitrary unit length in the third direction is assumed and the derivatives with respect to the third direction are retained in the conservation equations. In the first approach, the lift force as represented by Equation (2.28) becomes meaningless as the vorticity vector that is pointing out of the 2D-plane is set to zero as well. For such situations, Ranade (1997) proposed the following formulation for 2D simulations,

$$F_{w12r} = K_{wl}\frac{\rho_1\alpha_1\alpha_2}{d}\left(u_{slip}^{axial}\right)^2\left[\frac{2r/R}{1+r/R}\right];\ K_{wl}=0.15 \tag{2.29}$$

where u_{slip}^{axial} is the axial component of the slip velocity, and ν_t is the turbulent viscosity.

The force F_{w12r} acts on the bubble found in the zones near the walls where on one side of the bubble there is lower velocity (due to the presence of wall) as compared to the other side. This velocity difference generates a pressure difference across the bubble, as a result of which the bubble moves away from the wall towards the zones of lower pressure. It should be noted that the bracketed quantity in Equation (2.29) tends to zero as '*r*' approaches zero (center of the column) while it is equal to one for $r = R$ (column walls).

In this study, the lift force is neglected as most authors did. The main reason is that the lift force due to bubble deformation in strong shear flow fields, which is the most important and relevant lateral force in gas-liquid flow, has not been well modeled and is not available even for single bubble. Another reason is the lift force is less important in magnitude than the drag force. However, it should be noted that lift force component in the horizontal plane may not be negligible in large velocity gradient region.

2.6 Multiphase Turbulence Modeling

Typically, all fluctuations are filtered out by applying different averaging techniques i.e., Reynolds averaging, leaving a semi-empirical analysis of the mean turbulent quantities intended to describe all scales of motion lumped together in a single model. Most of the published research has employed this approach with the goal being to obtain sufficient information about mean turbulent quantities in a simple and efficient way.

As stated earlier, the continuity and the momentum balance equations (Equations (2.5) and (2.7)) are derived using ensemble-averaging. Therefore, the velocity vector $\mathbf{u}_k$ appearing in these equations represents an average velocity field and the phase-holdup α_k is a continuous function in the interval [0, 1]. The effect of fluctuations smaller than the scales of averaging appears as unclosed parts in the stress-tensor and the interfacial momentum exchange terms. Inherently the Euler-Euler model represents the scales larger

than the length and time scales employed by the ensemble-averaging, therefore, it does not contain all hydrodynamic scales present in the flow field, but rather the effects of these scales in an averaged sense. In principle, there is no need to apply any further averaging, such as Reynolds averaging, to model the turbulence while simulating a flow process. However, in industrial equipment simulations, the computational domain can become very large, and one may only be interested in very large scales. Then intermediate length and time scales can be defined, which are larger than the scales involved in ensemble averaging but still substantially smaller than the large hydrodynamic scales. Reynolds averaging practice is used to resolve only these very large scales.

The resulting ensemble plus Reynolds averaged equations, in addition to proper means, contain further unknown covariance or correlation terms that have to be modeled separately leading to the closure problem once again. It should be noted that the unknown covariance terms thus appearing, contain fluctuations with respect to ensemble-averaged mean flow field, which does not have its counterpart in single-phase flow problems. Therefore, the closure problem is even more complicated. For details, one should consult the recent review by Rafique *et al.* (2004).

In this work for Euler-Euler model, turbulence in the liquid phase is modeled through a set of modified $k-\varepsilon$ equations with extra terms that account for interphase turbulent momentum transfer (Launder and Spalding, 1974; Elghobashi and Abou-Arab, 1983). For the dispersed gas phase, turbulence closure is effected through correlations from the theory of dispersion of discrete particles by homogeneous turbulence (Tchen, 1947). The model equations are listed in Table 2.3. In ASMM, the turbulent stress term in the mixture equation is closed by solving a k-ε model for the mixture phase. The model equations are listed in Table 2.4. The $k-\varepsilon$ model is available in FLUENT.

Table 2.3 Dispersed Turbulence Model Equation (in Euler-Euler Model)

Turbulence in the Continuous Phase

$$\alpha_l \rho_l \mathbf{u}_l' \mathbf{u}_l' = -\frac{2}{3}\left(\rho_l k_l + \rho_l \mu_{t,l} \nabla \bullet \mathbf{U}_l\right)\mathbf{I} + \rho_l \mu_{t,l}\left(\nabla \bullet \mathbf{U}_l + \nabla \bullet \mathbf{U}_l^T\right)$$ (**U** is phase weighted velocity)

$$\mu_{t,l} = \rho_l C_\mu \frac{k_l^2}{\varepsilon_l}$$

$$\frac{\partial}{\partial t}\left(\alpha_l \rho_l k_l\right) + \nabla \bullet \left(\alpha_l \rho_l \mathbf{U}_l k_l\right) = \nabla \bullet \left(\alpha_l \frac{\mu_{t,l}}{\sigma_k} \nabla k_l\right) + \alpha_l G_{k,l} - \alpha_l \rho_l \varepsilon_l + \alpha_l \rho_l \prod_{k_l}$$

$$\frac{\partial}{\partial t}\left(\alpha_l \rho_l \varepsilon_l\right) + \nabla \bullet \left(\alpha_l \rho_l \mathbf{U}_l \varepsilon_l\right) = \nabla \bullet \left(\alpha_l \frac{\mu_{t,l}}{\sigma_\varepsilon} \nabla \varepsilon_l\right) + \alpha_l \frac{\varepsilon_l}{k_l}\left(C_{1\varepsilon} G_{k,l} - C_{2\varepsilon} \rho_l \varepsilon_l\right) + \alpha_l \rho_l \prod_{\varepsilon_l}$$

$$G_{k,l} = \frac{1}{2}\mu_{t,l}\left[\nabla \mathbf{U}_l + \left(\nabla \mathbf{U}_l\right)^T\right]^2$$

$\prod_{k_l} = \sum_{p=1}^{M} \frac{K_{gl}}{\alpha_l \rho_l}\left[k_{gl} - 2k_l + \left(\mathbf{u}_g - \mathbf{u}_l\right) \bullet \mathbf{u}_{dr}\right]$, M is the number of secondary phase

$$\prod_{\varepsilon_l} = C_{3\varepsilon} \frac{\varepsilon_l}{k_l} \prod_{k_l}$$

$$K_{gl} = \frac{3\alpha_l \alpha_g}{4}\left(\frac{\rho_l}{d_b}\right) C_D \left|\mathbf{u}_g - \mathbf{u}_l\right|$$

Turbulence in the Dispersed Phase

$$\tau_{F,gl} = \alpha_l \rho_l K_{gl}^{-1}\left(\frac{\rho_g}{\rho_l} + C_V\right)$$

$$\tau_{t,gl} = \frac{\tau_{t,l}}{\sqrt{\left(1 + C_\beta \xi^2\right)}}$$

$$\xi = \frac{\left|\mathbf{u}_g - \mathbf{u}_l\right| \tau_{t,l}}{L_{t,l}}$$

$C_\beta = 1.8 - 1.35\cos^2\theta$, θ is the angle between the gas velocity and the slip velocity.

$$\eta_{gl} = \frac{\tau_{t,gl}}{\tau_{F,gl}}$$

$$k_g = k_l\left(\frac{b^2 + \eta_{gl}}{1 + \eta_{gl}}\right)$$

$$k_{gl} = 2k_l\left(\frac{b + \eta_{gl}}{1 + \eta_{gl}}\right)$$

$$D_g = D_l = D_{t,gl} = \frac{1}{3} k_{gl} \tau_{t,gl}$$ $$b = \left(1 + C_V\right)\left(\frac{\rho_g}{\rho_l} + C_V\right)^{-1}, C_V = 0.5$$
Interphase Turbulent Momentum Transfer
$$K_{gl}\left(\mathbf{u}_g - \mathbf{u}_l\right) = K_{gl}\left(\mathbf{U}_g - \mathbf{U}_l\right) - K_{gl}\mathbf{u}_{dr}$$ $$\mathbf{u}_{dr} = -\left(\frac{D_g}{\sigma_{gl}\alpha_g}\nabla\alpha_g - \frac{D_l}{\sigma_{gl}\alpha_l}\nabla\alpha_l\right)$$
Model Constants
$C_\mu = 0.09, C_{1\varepsilon} = 1.44, C_{2\varepsilon} = 1.92, C_{3\varepsilon} = 1.20, \sigma_k = 1.00, \sigma_e = 1.30, \sigma_{gl} = 0.75$

Table 2.4 Mixture Turbulence Model Equation (in ASMM)

$$\frac{\partial}{\partial t}\left(\rho_m k_m\right) + \nabla\bullet\left(\rho_m \mathbf{u}_m k_m\right) = \nabla\bullet\left(\frac{\mu_{t,m}}{\sigma_k}\nabla k_m\right) + G_{k,m} - \rho_m \varepsilon_m$$ $$\frac{\partial}{\partial t}\left(\rho_m \varepsilon_m\right) + \nabla\bullet\left(\rho_m \mathbf{u}_m \varepsilon_m\right) = \nabla\bullet\left(\frac{\mu_{t,m}}{\sigma_\varepsilon}\nabla\varepsilon_m\right) + \frac{\varepsilon_m}{k_m}\left(C_{1\varepsilon}G_{k,m} - C_{2\varepsilon}\rho_m\varepsilon_m\right)$$ $$\mu_{t,m} = \rho_m C_\mu \frac{k_m^2}{\varepsilon_m}$$ $$G_{k,l} = \frac{1}{2}\mu_{t,m}\left[\nabla\mathbf{u}_m + \left(\nabla\mathbf{u}_m\right)^T\right]^2$$ $$C_\mu = 0.09, C_{1\varepsilon} = 1.44, C_{2\varepsilon} = 1.92, \sigma_k = 1.00, \sigma_e = 1.30$$

2.7 Previous Euler-Euler Investigations of Bubble Column Flows

There have been numerous studies since 1990 in using the Euler-Euler approach to model the hydrodynamics of lab-scale as well as pilot-scale bubble columns operated from the bubble flow to churn-turbulent flow regime (e.g., Torvik, 1990; Torvik and Svendsen, 1990; Ranade, 1992; 1997; Grienberger and Hofmann, 1992; Svendsen *et al.*, 1992; Jakobsen *et al.*, 1993; Sokolichin and Eigenberger, 1994; 1999; Becker *et al.*, 1994; Sokolichin *et al.*, 1997; Thakre and Joshi, 1999; Sanyal *et al.*, 1999; Pfleger *et al.*, 1999; Mudde and Simonin, 1999; Oey *et al.*, 2001; Pan *et al.*, 1999; 2000; Pan and Dudukovic, 2001; Padial *et al.*, 2000; Krishna *et al.*, 1999; Krishna *et al.*, 2000; van-Baten and

Krishna, 2001; Krishna and van Baten, 2001b; Krishna *et al.*, 2001a; Krishna *et al.*, 2001b; Pfleger and Becker, 2001 and Ranade and Tayalia, 2001).

Some of these studies do not use a turbulence model in the Euler-Euler implementation (Sokolichin and Eigenberger, 1994; 1999 and Pfleger *et al.*, 1999). They found that if only the molecular viscosity of the carrier fluid is increased 100 times (Sokolichin and Eigenberger, 1994), a good agreement between the computed results and experimental data can be obtained for bubbly flow in the air-water system. Without increasing the viscosity, however, the dynamic behavior can be resolved in 2D simulations, but the grid independent solution cannot be obtained (Sokolichin and Eigenberger, 1999). Pfleger *et al.* (1999) have shown that the results obtained by 3D dynamic simulations without a turbulence model exhibit a chaotic behavior, which is contrary to the experimental observation where harmonic oscillations are observed. These observations suggest that the prediction of local turbulent viscosity is one of the key issue of the two-fluid model.

Most of the studies, which use turbulence models to incorporate the turbulence induced by the dispersed phase, assume the turbulence to be the property of the continuous phase and model it using the k-ε model for the liquid phase (Torvik, 1990, Torvik and Svendsen, 1990, Jakobsen *et al.*, 1993, Sokolichin and Eigenberger, 1994, Sokolichin *et al.*, 1997, Sokolichin and Eigenberger, 1999, Pfleger *et al.*, 1999, Sanyal *et al.*, 1999, Mudde and Simonin, 1999, Krishna *et al.*, 1999, Krishna *et al.*, 2000, van-Baten and Krishna, 2001, Krishna and van Baten, 2001b, Krishna *et al.*, 2001a, Krishna *et al.*, 2001b, Ranade and Tayalia, 2001 and Pfleger and Becker, 2001).

Sokolichin and Eigenberger (1994) have shown, through 2D simulation of partially aerated 2D bubble column (i.e., column width and height are much larger than its depth) operated in bubbly flow regime, that the use of the single-phase $k-\varepsilon$ model predicts much higher viscosity (5-10 times higher as compared to full 3D simulation). This is an artifact of inappropriate characteristic turbulence length scale, and results in dampening of the transient characteristics of the flow. This conclusion was also

confirmed by Mudde and Simonin (1999) and Pfleger *et al.* (1999). Nevertheless, unlike studies which do not use a turbulence model, a grid independent solution can be obtained on a relatively coarse mesh by using the $k-\varepsilon$ turbulence model.

Sokolichin and Eigenberger (1999), in the case of 3D simulations using the single-phase $k-\varepsilon$ model, have obtained a good agreement with experiments. This leads to the conclusion that the 2D column depth effects, which are neglected in the 2D simulations, have a strong influence on the simulation. Pfleger *et al.* (1999), by comparing 2D and 3D simulations of a rectangular bubble column, concluded that in 2D simulations, the length scale used by the $k-\varepsilon$ model is equal to the column width, while in 3D simulations, it is equal to the column depth. Due to the much smaller length scale, the $k-\varepsilon$ model in 3D simulation predicts much smaller viscosity and the predicted hydrodynamics is in better agreement with the experimental observations. Hence, Pfleger *et al*. (1999) suggest that the column depth must be resolved meticulously to obtain accurate hydrodynamics. Mudde and Simonin (1999) performed 3D simulations using the $k-\varepsilon$ model and have shown that when only drag force was used as an interfacial momentum source, the amplitude and time period of the oscillations were under-predicted. However, when the drag and the virtual mass forces were used together, the values of the amplitude and the time period were quite comparable with the experimental observations. The importance of the virtual mass in momentum exchange closures is not reported by other authors (e.g., Pfleger *et al.*, 1999, Buwa and Ranade, 2002).

Sanyal *et al.* (1999) performed 2D axi-symmetric simulations of a 19-cm diameter cylindrical bubble column (air-water system at atmospheric pressure), operated in typical bubbly flow (U_g = 2 *cm/s*) and churn turbulent flow (U_g = 12 *cm/s*) regimes. The numerical simulations were performed using the Algebraic Slip Mixture Model (ASMM), and the Euler-Euler model. The results are compared with experimental data using CT and CARPT and a reasonably good quantitative agreement is obtained between the experimental data and simulation for the time-averaged gas holdup, axial liquid velocity

distribution, and the kinetic energy distribution. They concluded that both the Euler-Euler model and ASMM predict reality equally well within engineering accuracy.

Pan *et al.* (1999; 2000) used the dynamic Euler-Euler approach with the bubble-induced turbulence model (Sato *et al.*, 1981a; b), including drag and virtual mass forces, to simulate a 2D rectangular bubble column operating in bubbly flow regime. The computed time-averaged axial velocity profiles and turbulent quantities were compared with experimental data of Mudde *et al.* (1997b), and found in reasonable agreement. Contrary to Pfleger *et al*. (1999), who emphasized the importance of resolving the third direction properly and advocated the need for full 3D simulation for 2D bubble column to acquire accurate fluid dynamic data, Pan *et al.* (1999; 2000) only performed 2D simulations and still captured all the essential fluid dynamic features. The main difference between Pfleger *et al.* (1999) and Pan *et al.* (1999; 2000), other than the simulation dimension (3D vs. 2D), is the use of different turbulence models, i.e. the $k-\varepsilon$ model in the former case and the bubble induced turbulence model in the later cases. As mentioned earlier, the characteristic length scale used by the $k-\varepsilon$ model is about the smallest length of the geometry involved, which is the column depth in 2D column. In 2D simulation, the column depth is assumed to be infinite such that the correct characteristic length scale cannot be used, which turns out to over-predict the turbulent viscosity by 5-10 times. However, the bubble induced turbulence model, due to the right *input* of the characteristic length scale through the assumed bubble size, predicts the flow dynamic characteristics correctly. Once an appropriate bubble size is selected, the bubble induced turbulence model can predict a correct magnitude of turbulent viscosity and other hydrodynamic properties at least in the bubbly flow regime. One may argue that the success of bubble induced turbulence may just be a coincidence. However, in bubbly flow regime, it is the bubble induced turbulence, rather than the shear induced turbulence ($k-\varepsilon$ model), that dominates. In churn-turbulent flow regime, the domination of the bubble induced turbulence may not be true any more. However, as illustrated by Pan and Dudukoviċ (2001), the use of bubble-induced turbulence model (Sato *et al.*, 1981a; b),

including drag and virtual mass forces, can predict well a wide range of cylindrical bubble column operations in bubbly flow and churn-turbulent flow regime.

Krishna and co-workers (Krishna *et al.*, 1999; Krishna *et al.*, 2000; van-Baten and Krishna, 2001; Krishna and van Baten, 2001b; Krishna *et al.*, 2001a; Krishna *et al.*, 2001b) published a number of 2D-axisymmetric and 3D simulations based on the two-bubble class concept, which suggests that in the heterogeneous regime, the whole bubble size distribution consists of two classes: 'small bubbles' and 'large bubbles'. The large bubbles usually occupy the central region of the column and travel with a velocity greater than the small bubbles, which occupy the regions near the walls. Both bubble classes interact with the continuous phase via drag force only, which differs for the small bubbles and the large bubbles. However, Krishna and coworkers ignore the mutual interaction between the two bubble classes, thus both bubble classes are treated as separate phases, i.e., the flow field in a bubble column can be regarded as consisting of three phases: liquid phase, small bubble phase and large bubble phase.

Krishna *et al.* (1999) performed experiments and 2D-axisymmetric simulations, which show that all velocity profiles collapse to a single one if plotted as the normalized velocity as a function of normalized radial distance. Krishna *et al*. (2000) reconfirmed the widely accepted point of view that azimuthally and time-averaged radial distribution of liquid phase axial velocity can be well predicted by 2D axi-symmetric simulation and due to imposition of axi-symmetric constraint, the 2D axi-symmetric simulations cannot predict an accurate radial distribution of the gas holdup. The results from the 3D simulations do show an improvement, which is also confirmed by Ranade and Tayalia (2001), in the prediction of gas holdup but the use of single 'mean bubble size' still fails to lead to good and reliable holdup profile prediction. Krishna *et al*. (2000) also suggest that the concept of 'two-bubble classes' is indeed a right direction but not sufficient to be able to predict the gas holdup profile accurately.

Krishna *et al.* (2001a) use 2D axi-symmetric simulations to analyze the effect of bubble column diameter on the hydrodynamics of bubble columns. They found that the

overall gas holdup decreases with increase in column diameter due to the increase in the strength of the liquid circulation with increase in column diameter, which accelerates the bubbles traveling upwards in the central core. The qualitative trend agrees with Zehner's (1989) correlation, but the quantitative comparison shows that there is at least 50-90% discrepancy between the computed and experimental results.

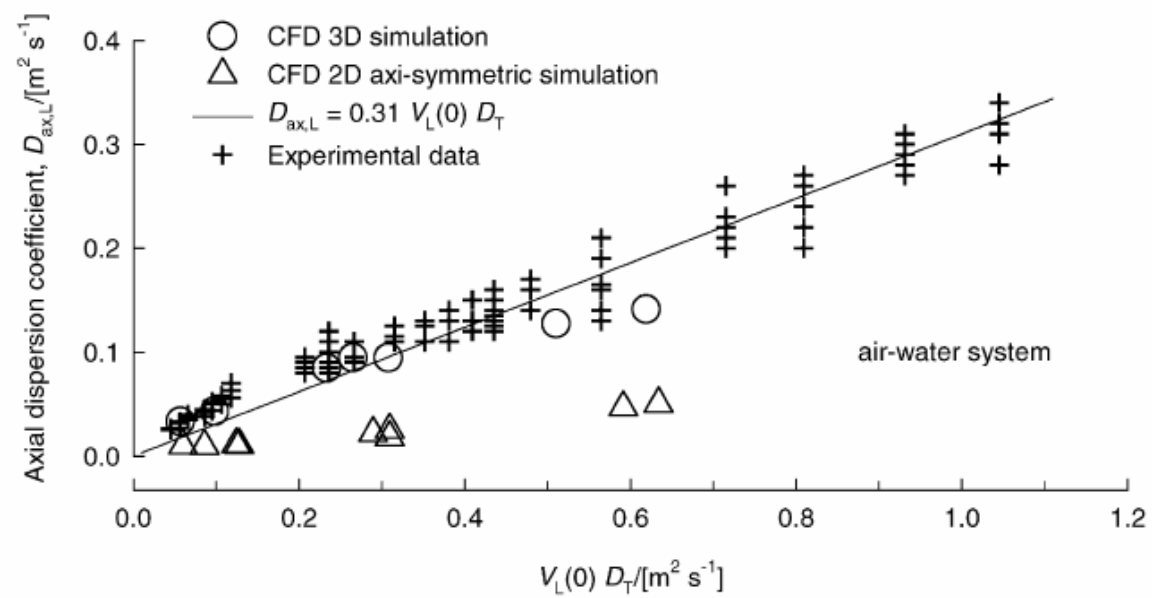

Figure 2.11 Axial dispersion coefficient of the liquid phase: comparison of experimental data with 2D and 3D Eulerian simulations (from van Baten and Krishna, 2001).

Van Baten and Krishna (2001) found a good agreement between the computed velocity profiles and centerline velocity obtained from 3D simulation and their experimental data (Krishna *et al.*, 1999). They also investigated liquid phase axial dispersion coefficient and the effect of physical properties of interacting fluids (air/water and air/Tellus oil) by 3D numerical tracer simulations and obtained reasonably good comparison with experimental data (Krishna *et al.*, 1999). It was found that the prediction of the liquid phase axial dispersion coefficient via 2D simulation is about one order of magnitude lower than the experimental observations (Figure 2.11). The authors also investigated the gas phase axial dispersion coefficient via 3D simulation. They

found that the computed dispersion coefficient of the large bubbles was significantly lower (up to 40%), and that of the small bubbles was almost the same as that of the liquid phase, which suggests the entrainment of the small bubbles by the liquid phase.

Pfleger and Becker (2001) used, for a 3D-cylindrical bubble column simulation, a modified $k-\varepsilon$ model in the liquid phase, which incorporates an additional production term in $k-$ and $\varepsilon-$ equations to include the influence of the dispersed phase,. They concluded that the single phase $k-\varepsilon$ model is better in describing the instantaneous large-scale flow structures and the prediction of the local and overall gas holdup than the modified $k-\varepsilon$ model. However, the incorporation of additional terms shows a positive impact on the prediction of the velocity profiles and corresponding time-series but it deteriorates the local and over-all holdup prediction. Moreover, it was observed that as the grid size decreases, the agreement between predicted long time-averaged gas holdup and experimental data improves while that between the axial velocity and experimental data deteriorates (the velocity profiles become flatter). The reasons for such phenomena have to be investigated further.

Chapter 3
Background - Population balance equation and bubble breakup and coalescence

In most of today's CFD calculations of dispersed two phase gas-liquid flows, the local bubble size distribution is not included. Currently used closures for the interfacial momentum transfer terms basically rely on the empirical correlations for single mean bubble size. The bubbles are assumed to have the same size and shape (Figure 3.1a), whereas in reality a wide spectrum of bubble sizes exists (Figure 3.1b), possibly varying from one point to another due to bubble-bubble interactions, phase change and pressure changes. Therefore, the use of a single bubble size correlation may not be appropriate beyond the narrow range of operating conditions and geometries over which it was determined. Instead, the local bubble size distribution information (Figure 3.1c) is needed.

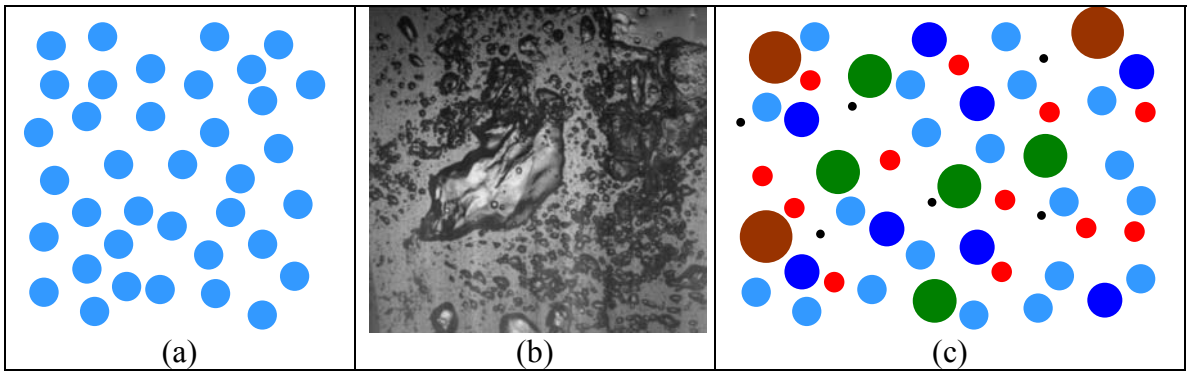

Figure 3.1 Idealization of bubble column flows (a) Single mean bubble size (b) Reality (c) Local bubble size distribution.

The uncertainty in bubble column design, scale-up and scale-down arises from the lack of fundamental understanding of the hydrodynamics and rate processes which govern bubble size and thus interfacial area per unit volume. The local bubble size distribution depends on the balance of coalescence and break-up rate in the column as well as on pressure change, phase change and gas-liquid mass transfer. Because of the incomplete understanding of the physical mechanisms that lead to break-up and coalescence, and the considerable difficulty in obtaining reliable data, especially at high gas flow rates and holdups, no broadly applicable model for these processes in turbulent two phase gas-liquid systems has yet been fully developed.

3.1 Bubble Population Balance Equation

In bubble column reactors, the initial bubble size is determined by the formation of bubbles at the sparger. However, the initial bubble size may not be stable due to turbulence, interfacial instability, wake entrainment, size dependent rise velocity difference and shear layer induced velocity difference. In all these cases, the bubble size is further changed by a break-up and/or coalescence mechanism. In the presence of chemical reactions, in addition to break-up and coalescence, mass transfer should also be considered. Phase change and pressure change may also need to be taken into account.

Since the interfacial area concentration changes with the variation in the bubble number density due to coalescence and break-up, it is important to be able to predict the local bubble surface density. Analogous to the Boltzmann's transport equation, a population balance model can be used to provide a statistical formulation in describing the dispersed phase in multiphase flow. Generally, the population balance equation can be expressed as:

$$\frac{\partial}{\partial t} f\left(\mathbf{x}, v, t\right) + \nabla \cdot \left(\mathbf{u_b}\left(\mathbf{x}, v, t\right) f\left(\mathbf{x}, v, t\right)\right) = S\left(\mathbf{x}, v, t\right) \tag{3.1}$$

In this equation $f(\mathbf{x},v,t)$ is the bubble number density function, which is assumed to be continuous, and specifies the probable number density of bubbles at a given time t, in the spatial range d$\mathbf{x}$ about a position $\mathbf{x}$, with bubble volumes between v and $v+dv$. $\mathbf{u_b}(\mathbf{x},v,t)$ is the local velocity of bubble volumes between v and $v+dv$ at time t. $S(\mathbf{x},v,t)$ is the source term which can be expressed as:

$$\begin{aligned} S(\vec{x},v,t) &= \frac{1}{2}\int_0^v a(v-v',v')f(\vec{x},v-v',t)\,f(\vec{x},v',t)\,dv' \\ &-f(\vec{x},v,t)\int_0^\infty a(v,v')f(\vec{x},v',t)\,dv' \\ &+\int_v^\infty m(v')b(v')P(v,v')\,f(\vec{x},v',t)\,dv' \\ &-b(v)f(\vec{x},v,t)+S_{ph}+S_p+S_r+\cdots \end{aligned} \tag{3.2}$$

In Equation (3.2) the first term is the birth rate of bubbles of volume v due to coalescence of bubbles of volume $v-v'$ and v', the second term is the death rate of bubbles of volume v due to coalescence with the other bubbles, the third term is the birth rate of bubbles of volume v due to breakup of bubbles which volume larger than v, and the fourth term is the death rate of bubble of volume v due to breakup into smaller bubbles. In addition, S_{ph}, S_p and S_r are the bubble source/sink terms due to phase change, pressure change and reaction, respectively; $a(v,v')$ is the coalescence rate between bubbles of volume v and v', $b(v)$ is the breakup rate of bubbles of volume v, $m(v')$ is the mean number of daughter bubbles produced by breakup of a parent bubble of volume v' and $P(v,v')$ is the p.d.f. of daughter bubbles produced upon breakup of a parent bubble with volume v'. It is clear that the source term needs to be closed by modeling the bubble breakup and coalescence. It is noteworthy that there are many studies available in the open literature focusing on the breakup/coalescence of droplets in the liquid-liquid dispersion. These studies do not lie in the scope of this work, therefore, in the following sections we will discuss *only* the models pertinent to gas-liquid dispersion.

3.2 Bubble Breakup

The bubbles in turbulent dispersion are not only exposed to a turbulent field, but are also subject to both inertial and viscous forces. Moreover, the gas-liquid interface is also subject to Rayleigh-Taylor and Kelvin-Helmholtz instability due to the difference in density and velocity of the gas and liquid phase. The most important force in stabilizing the bubble is the surface tension. In addition, a centrifugal force, induced by internal circulation of the gas in a bubble, can suppress the disturbances at the gas-liquid interface and act as a stabilizing force. On the other hand, such a centrifugal force can also disintegrate the bubble as it increases with an increase in bubble size. The bubble breaks up when the centrifugal force exceeds the surface tension force, especially at high pressures when gas density is high. The fate of a bubble is determined by the breakup/deformation force and the stabilization/restoration force (Table 3.1). Since the bubbles are much larger than the microscale of turbulence (Shinnar, 1961; Narsimhan *et al.*, 1979), the viscous force can be neglected.

Table 3.1 Various forces that act to break up and stabilize the bubble.

Breakup/Deformation Force	**Stabilization/Restoration Force**
Turbulence stress/Eddy bombardment	**Surface tension**
Inertial force (negligible)	Liquid acceleration along the bubble surface
Viscous force	
Kelvin-Helmholtz instability	
Rayleigh-Taylor instability	
Centrifugal force induced by gas internal circulation	

Much of the published literature on bubble break-up in turbulent flow is derived from Hinze (1955) which assumes that the bubble break-up occurs through bubble interactions with turbulent eddies. Only the eddies which are approximately equal to the size of the bubble can break the bubble, since larger eddies have the tendency to transport

the bubble rather than break it, while very small eddies do not contain sufficient energy to break the bubble.

From Equation (3.2), it is clear that for a complete bubble breakup model, the number of daughter bubbles produced upon breakup of a parent bubble, the daughter bubble size probability density function (p.d.f.) and breakup rate need to be provided. In addition, when a bubble exceeds a critical value, the bubble interface becomes unstable and breakup is likely to occur. Therefore, the bubble breakup can be related to the maximum attainable size (Kocamustafaogullari and Ishii, 1995) and a complete bubble breakup model, should also include the maximum stable bubble size (which gives a threshold below which a bubble will not be breakable in a given turbulent flow field). As already stated such a complete breakup model must also specify the number of daughter bubbles generated upon breakup from a given parent bubble under given turbulent flow field, the p.d.f. of daughter bubbles (which is the probability distribution of daughter bubbles upon breakup from a parent bubble) and the breakup rate (which gives the number of bubbles of given size that break per unit volume per unit time) must be provided.

3.2.1 Maximum Stable Bubble Size

In turbulent flow, bubble breakup is caused by fluctuating eddies resulting in the pressure variation along the bubble surface. When a bubble size exceeds a critical value, at which the breakup/deformation mechanism and the stabilization/restoration mechanism reach equilibrium, the bubble interface becomes unstable and break-up is likely to occur. Different expressions have been proposed to estimate the maximum stable bubble size, $d_{\max}$, that a bubble can attain in a given flow field. One should note that the maximum stable bubble size is not equal to the maximum (possible) bubble size in a given system.

Martínez-Bazán *et al.* (1999a), based on Kolmogorov's concept, suggested the following maximum stable bubble size in turbulent flows, which compared well with their experimental data.

$$d_{\max} = \left(\frac{12\sigma}{\beta \rho_l} \right)^{3/5} \varepsilon^{-2/5} \tag{3.3}$$

where ε is the local energy dissipation rate per unit volume, σ is the surface tension, ρ_c is liquid phase density, and the constant $\beta = 8.2$ was provided by Batchelor (1956) and used by Martínez-Bazán *et al.* (1999a). In this model, only the dominant forces, turbulence stress and surface tension, are considered.

Lin *et al.* (1998) showed that Hinze's (1955) method under-predicts the maximum stable bubble size and cannot predict the observed effect of pressure on bubble size. Grace *et al.* (1978) applied the Rayleigh-Taylor instability theory by considering the time available for the disturbance to grow and the time required for the disturbance to grow to an adequate amplitude that causes breakup. Batchelor (1987) pointed out that the observed maximum stable size air bubbles in water were considerably larger than that predicted by the model of Grace *et al.* (1978). Batchelor (1987) further took into account the stabilizing effects of the liquid acceleration along the bubble surface and the non-constant growth rate of the disturbance. In his model, the information regarding the disturbances is required for the prediction of the maximum stable bubble size.

Kitscha and Kocamustafaogullari (1989) applied the Kelvin-Helmholtz instability theory to model the breakup of large bubbles in liquids, using the same concept as Grace *et al.* (1978). Wilkinson and van Dierendonck (1990) applied the critical wavelength to explain the maximum stable bubble size in high-pressure bubble columns. Their results showed that the critical wavelength decreases with an increase in pressure and therefore bubbles are easier to disintegrate by the disturbances at higher pressure. However, the critical wavelength is not necessarily equivalent to the maximum stable bubble size and their approach alone cannot quantify the pressure effect on bubble size.

All the models mentioned above neglected the effect of the internal circulation of the gas in a bubble. Due to the continuity of the tangential velocity in the gas and liquid phases, the internal circulation velocity is of the same order of magnitude as the bubble rise velocity. A centrifugal force is induced by this circulation, pointing outwards to the bubble surface, which can suppress the disturbances at the gas-liquid interface and act as a stabilizing force. This force may be another reason that explains the underestimation of $d_{\max}$ by the model of Grace *et al.* (1978), besides the arguments discussed by Batchelor (1987). On the other hand, such a centrifugal force can also disintegrate the bubble as it increases with an increase in bubble size. The bubble breaks up when the centrifugal force exceeds the surface tension force, especially at high pressures when gas density is high.

Levich (1962) recognized the importance of internal gas circulation, assumed the centrifugal force to be equal to the dynamic pressure induced by the gas moving at the bubble rise velocity, u_b, and proposed a simple expression to calculate the maximum stable bubble size:

$$d_{\max} \approx \frac{3.63\sigma}{u_b^2 \sqrt[3]{\rho_l^2 \rho_g}} \tag{3.4}$$

where ρ_g is gas phase density. Equation (3.4) shows a significant effect of pressure on the maximum stable bubble size which is qualitatively in the right direction; however, it severely under-predicts the maximum stable bubble size in churn-turbulent flow regime. Moreover, the surrounding turbulence effect on the bubbles is not taken into account.

Luo *et al.* (1999) proposed a model which accounts for the internal circulation of the gas in a bubble by using the force balance between the centrifugal force and the surface tension force. They consider a single large bubble rising in a stagnant liquid at a velocity of u_b, without any disturbance on the gas-liquid interface. The internal circulation model provides an estimation of the upper limit on the maximum stable bubble size, since the external stresses in the liquid phase are neglected. In actual bubble

columns or slurry bubble columns, especially in churn-turbulent flow where the liquid phase turbulence intensity is high, the observed maximum stable bubble size should be smaller than the predictions. Based on their model, the maximum stable bubble size rising in liquids can be expressed as:

$$d_{\max} \approx 2.53\sqrt{\frac{\sigma}{g\rho_g}} \tag{3.5}$$

where g is gravity acceleration.

Lehr and Mewes (2001) suggested another formula following the idea of Levich (1962) and Luo and Svendsen (1996):

$$d_{\max} = 2^{1/5}\frac{\sigma^{3/5}}{\rho_l^{3/5}\varepsilon^{2/5}} \tag{3.6}$$

Table 3.2 lists the deformation/restoration forces considered in different models. Table 3.3 lists the maximum stable bubble size computed by three different models in an air-water system at atmospheric pressure and at superficial gas velocity of 2 and 14 cm/sec, typically bubbly flow and churn turbulent flow, respectively. The dissipation rate was calculated by Bhavaraju *et al.'s* (1978) model. Luo *et al.* (1999) provide an estimation of the upper limit on the maximum stable bubble size, since the external stresses in the liquid phase are neglected. Thus it significantly overestimates the maximum stable bubble size, and the predicted value is independent of underlying turbulence intensity. Martínez-Bazán *et al.* (1999a) and Lehr and Mewes (2001) model predictions are almost identical and seem reasonable.

Table 3.2 Deformation/Stabilization Force Used by Different Models

	Deformation Force	**Stabilization Force**
Levich, 1962	Internal gas circulation	Surface tension
Grace *et al.*, 1978	Rayleigh-Taylor instability	Surface tension
Batchelor, 1987	Rayleigh-Taylor instability	Internal gas circulation, surface tension
Kitscha and Kocamustafaogullari, 1989	Kelvin-Helmholtz instability	Surface tension
Martínez-Bazán *et al.*, 1999a	Turbulent stress	Surface tension
Luo *et al.*, 1999	Internal gas circulation	Surface tension
Lehr and Mewes, 2001	Turbulent stress	Surface tension

Table 3.3 Maximum Stable Bubble Size Predictions by Different Models

	U_g= 2 cm/sec, ε = 0.19 m^2/s^3	U_g= 14 cm/sec, ε = 1.3 m^2/s^3
Levich, 1962[*]	$d_{max} = 15.3\ mm$	$d_{max} = 2.4\ mm$
Martínez-Bazán *et al.*, 1999a	$d_{max} = 7.8\ mm$	$d_{max} = 3.6\ mm$
Luo *et al.*, 1999	$d_{max} = 196\ mm$	$d_{max} = 196\ mm$
Lehr and Mewes, 2001	$d_{max} = 7.3\ mm$	$d_{max} = 3.4\ mm$

3.2.2 Number of Daughter Bubbles

The parameter $m(v')$ in Equation (3.2) denotes the average number of daughter particles produced by break-up of a parent particle of volume v_0. The assumption of binary breakage has been widely used by many authors (e.g., Hesketh *et al.*, 1991; Nambiar *et al.*, 1992; Luo and Svendsen, 1996, Martínez-Bazán *et al.*, 1999b, Lehr and Mewes, 2001). The experimental results of Hesketh *et al.* (1991) support this assumption, while Prince *et al.* (1989) noted that bubble break-up is often accompanied by the production of two primary bubbles and a number of small fragments. Incorporation of

[*] Bubble rise velocity is estimated as u_b = 40cm/s for U_g= 2 cm/sec, and u_b = 100 cm/s for U_g= 14 cm/sec

this observation, rather than binary breakup, is expected to significantly change the number of smaller bubbles and the interfacial area concentration predicted by the transport equation. However, such a model has not been proposed yet. Binary breakup is assumed in this work.

3.2.3 Breakup Rate and Daughter Bubble Size Probability Density Function (p.d.f.)

For gas-liquid dispersed turbulent flow, the kinetic energy carried by the turbulent eddies plays a dominant role in the break-up process. The imbalance between the kinetic energy and the surface energy is used to define the break-up rate.

Lee *et al.* (1987a) developed a bubble breakup model based on the work of Narsimhan *et al.* (1979) using dimensional analysis to obtain an expression for the average frequency of eddies, Λ, arriving at a drop (bubble) surface, which results in the following breakup rate $\Omega_B\left(d_i\right)$:

$$\Omega_B\left(d_i\right) = c_1 n_i \left(\frac{\varepsilon}{d_i^2}\right)^{1/3} \left[1 - \int_0^1 F\left(\frac{c_2 \sigma}{\rho_g \varepsilon^{2/3} d_i^{5/3} \phi^{11/3}}\right) d\phi\right] \quad \left(m^{-3} s^{-1}\right) \tag{3.7}$$

where $F(\ )$ is the cumulative chi-square distribution function, n_i is the bubble density with diameter d_i. This bubble breakup rate model is independent of the density of the liquid phase, which is contrary to the experimental observations (Bhavaraju *et al.*, 1978).

Based on the energy of the eddy and the surface tension force on the bubble, Prince and Blanch (1990) proposed a model for breakup rate shown below:

$$\Omega_B\left(d_i\right) = \sum_e \left\{\theta_{ie} \exp\left[-\left(u_{ci}^2 / u_{te}^2\right)\right]\right\} \quad \left(m^{-3} s^{-1}\right) \tag{3.8}$$

with $\theta_{ie} = \frac{\pi}{16} n_i n_e \left(d_i + d_e\right)^2 \left(u_{ti}^2 + u_{te}^2\right)^{1/2}$; $\frac{dN(k)}{dk} = \frac{0.1 k^2}{\rho_l}$; $u_{ci} = 2.15\left(\frac{\sigma}{d_i}\right)^{\frac{1}{2}}$; $u_t = 1.4 \varepsilon^{\frac{1}{3}} d^{\frac{1}{3}}$.

where n_e is the eddy density of size d_e, $N(k)$ is the number of eddies of wave number k per mass of fluid. u_{ci} is the critical velocity of an eddy necessary to break a bubble of diameter d_i, u_{te} is the turbulent velocity of an eddy of diameter d_e, θ_{ie} is the collision rate of bubbles with eddies of the appropriate size. Lee *et al.* (1987a) and Prince and Blanch (1990)'s model are incomplete as they do not provide the daughter bubble size p.d.f.

The daughter particle size probability density function (p.d.f.) was first introduced by Valentas *et al.* (1966) to describe the size distribution of daughter drops or bubbles. So far, four approaches have been used for daughter particle size p.d.f. modeling: statistical models (Valentas *et al.*, 1966; Coulaloglou and Tavlarides, 1977; Lee *et al.*, 1987b; Chatzi *et al.*, 1989; Chatzi and Kiparissides, 1992; Novikov and Dommermuth, 1997), phenomenological model based on surface energy consideration (Tsouris and Tavlarides, 1994; Luo and Svendsen, 1996), phenomenological model based on turbulence stress and surface tension consideration (Martínez-Bazán *et al.*, 1999b), and hybrid models based on a combination of the first and second approaches (Konno *et al.*, 1983; Cohen, 1991).

Almost all the statistical and hybrid models have the same deficiency in that the daughter particle size p.d.f. is basically independent of the turbulent energy of the underlying turbulence. Konno *et al.*'s (1983) model even does not depend on the parent bubble size. These two results are contrary to experimental observation. The shape of the daughter particle size p.d.f. is a source of dispute also because the daughter particle size p.d.f. obtained by the phenomenological model, based on surface energy consideration, is sharply different from the other three mentioned above. Therefore, more experimental and theoretical investigations are needed to understand the physics involved.

Based on the theory of isotropic turbulence, Luo and Svendsen (1996) proposed a breakup criteria in which the breakup probability is proportional to the difference between the energy carried by the arriving eddies and the increase in surface energy due

to a breakup (Figure 3.2). The bombarding frequency of the eddies of size λ on bubbles of size d can be expressed as

$$\dot{\omega}_{B,\lambda}(d) = c(1-\alpha) n_i (\varepsilon d)^{1/3} \frac{(\lambda + d)^2 d^{11/3}}{\lambda^{11/3}} \quad \left(s^{-1}\right) \tag{3.9}$$

where α is the local gas holdup. The probability of breakup into bubble with a given fraction of f_{BV} upon such bombarding was given as

$$P_B(v : v f_{BV}, \lambda) = \exp\left(-\frac{12 c_f \sigma d^2}{\rho_c \beta \varepsilon^{2/3} \lambda^{11/3}}\right) \tag{3.10}$$

where v is the volume of the parent bubble of size d, c_f is defined as the ratio of increased surface area with respect to the surface area of parent bubble (i.e., $c_f = f_{BV}^{2/3} + (1 - f_{BV})^{2/3} - 1$), and $\beta = 2.05$ are derived from isotropic turbulence theory.

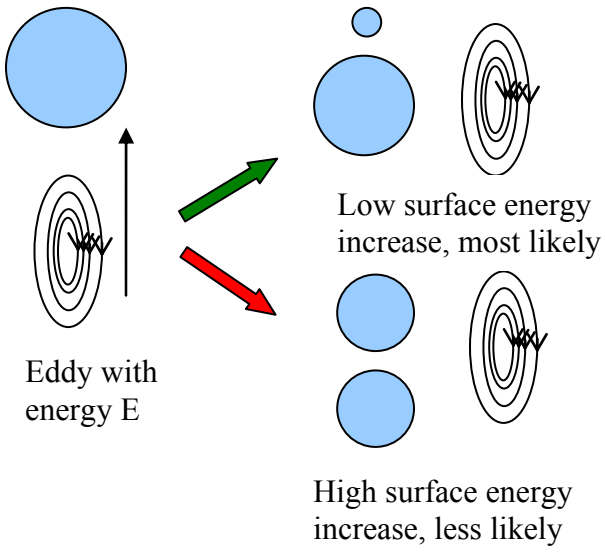

Figure 3.2 Luo and Svendsen's (1996) breakup model illustration.

According to Lee *et al.* (1987a), and also suggested by Luo and Svendsen (1996), only eddies which have a length scale comparable to the bubble diameter can cause

breakup while eddies of a larger scale will just give the bubble a translational velocity. Thus, the authors proposed the following phenomenological model for bubble breakup rate:

$$\begin{aligned}\Omega_B\left(v \to vf_{BV}\right) &= \int_{\lambda_{\min}}^{d} P_B\left(v : vf_{BV}, \lambda\right)\dot{\omega}_{B,\lambda}\left(v\right)d\lambda \\ &= c\left(1-\alpha\right)n\left(\frac{\varepsilon}{d^2}\right)^{1/3}\int_{\xi_{\min}}^{1}\frac{\left(1+\xi\right)^2}{\xi^{11/3}}\exp\left(-\frac{12c_f\sigma}{\beta\rho_c\varepsilon^{2/3}d^{5/3}\xi^{11/3}}\right)d\xi\end{aligned} \tag{3.11}$$

where $\Omega_B\left(v \to vf_{BV}\right)$ is the breakup rate per unit volume of continuous phase (m^{-3} s^{-1}) of a parent bubble with volume v into a daughter bubble with volume vf_{BV}. Here f_{BV} is the volume fraction of one daughter bubble, $c \approx 0.923$, $\xi = \lambda/d$, and λ is the arriving eddy size. Unlike other models, this model predicts the breakup rate for original bubbles of a given size at a given combination of the daughter bubble sizes and, thus, does not need a predefined daughter bubble size distribution. The daughter bubble size distribution is a result that can be calculated directly from the model.

According to Luo and Svendsen's (1996) model, more energy is required for binary equal-sized break-up than for unequal-sized break-up (Figure 3.2) because more interfacial area is generated (Nambiar *et al.*, 1992). Therefore, the possibility of splitting a fraction of bubbles of size d from parent bubble of size d' should be inversely proportional to $d^2 + \left(d'^3 - d^3\right)^{2/3} - d'^2$, so that the daughter bubble size p.d.f. should be U-shaped. This assumption is in line with the experimental observation for bubble and drop break-up in turbulent pipe flow where unequal size breakup was found more likely (Hesketh *et al.*, 1991). However, Luo and Svendsen's (1996) model also predicts that all the bubbles of size greater than the turbulence inertial subrange tend to breakup, and the possibility of tearing a tiny part off the parent bubble is the highest, which is not supported by observation of Hesketh *et al.* (1991).

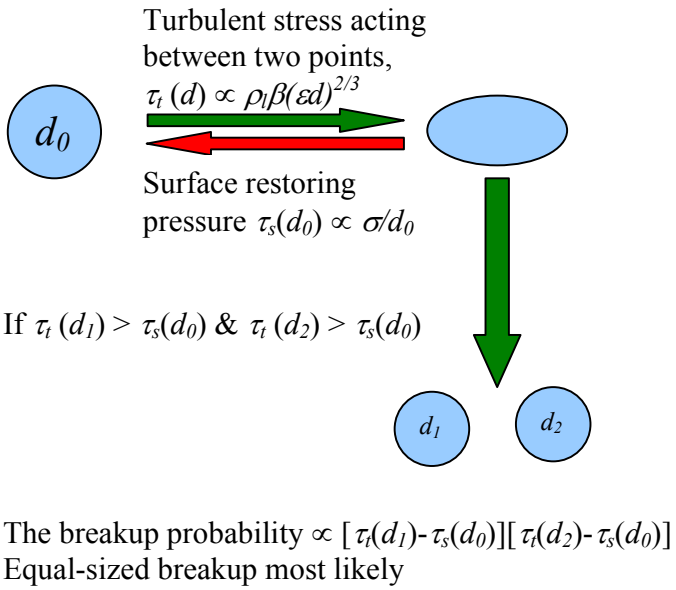

Figure 3.3 Martínez-Bazán *et al.*'s (1999a; 1999b) breakup model illustration.

Martínez-Bazán *et al.* (1999a; 1999b) investigated the breakup of bubbles injected into a fully developed turbulent flow, and proposed a phenomenological model based on turbulence stress and surface tension analysis for daughter bubbles distribution (Figure 3.3). As the bubble residence time within the breakup region is very short, neither buoyancy effect nor the dynamics of bubble oscillation play any role in their experiment. The bubble breakup rate is verified with their experimental data:

$$\Omega_B\left(d_i\right) = K_g n_i \frac{\sqrt{\beta\left(\varepsilon d_i\right)^{2/3} - 12\sigma/\left(\rho_l d_i\right)}}{d_i} \tag{3.12}$$

where $K_g = 0.25$ was found experimentally by Martínez-Bazán *et al.* (1999a). In this model, there are two distinct breakup regimes dependent on bubble size as illustrated in Figure 3.4. The breakup rate is zero for bubbles of size $d \le d_{\max}$, and it increases rapidly for bubbles larger than the maximum stable bubble size. However, it is important to note that the breakup rate, after reaching a maximum at $d_{g\max} = 1.63 d_{\max}$, decreases with

bubble size. In the limit of very large bubbles, $d/d_{\max} \gg 1$, the surface tension forces become very small and the breakup rate can be approximated by

$$\Omega_B\left(d_i\right) \propto \varepsilon^{1/3} d_i^{-2/3} \tag{3.13}$$

This breakup regime, where bubble breakup rate decreases with bubble diameter increase is found experimentally by Martínez-Bazán *et al.* (1999a). On the other hand, for small bubbles of size smaller than $d_{g\max}$, but comparable to the critical diameter $d_{\max}$, the breakup rate can be written as:

$$\Omega_B\left(d_i\right) \propto \left(\frac{\sigma}{\rho_l}\right)^{-2/3} \varepsilon^{3/5} \sqrt{\frac{d_i}{d_c} - 1} \tag{3.14}$$

The breakup rate of bubbles smaller than $d_{g\max}$ increases rapidly with the bubble size. This is the regime in which most investigations have been conducted because they were employed in turbine mixers, where small drop (bubble) diameters are present.

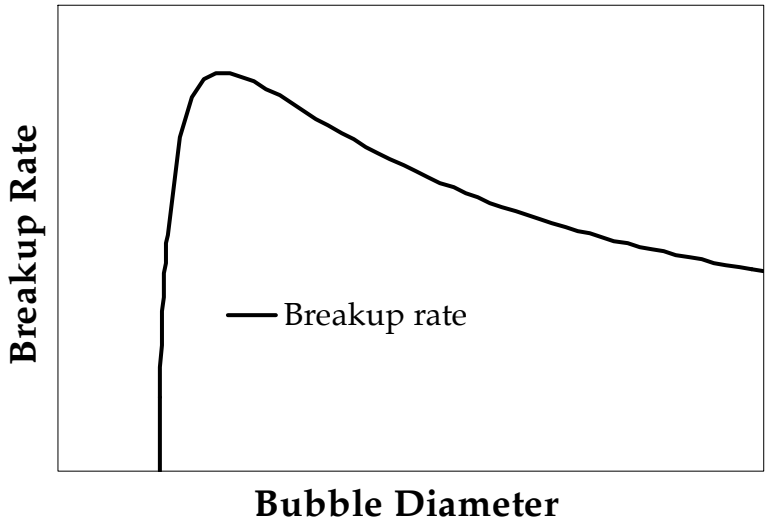

Figure 3.4 Typical breakup rate with respect to bubble diameter predicted by Martínez-Bazán *et al.* (1999a)

Based on Martínez-Bazán *et al.*'s (1999a; 1999b) model, the possibility of splitting a fraction of bubbles of size D from the parent bubble of size D' is proportional to the difference in the turbulence stress acting between the two points separated by the distance D and the confinement pressure due to the surface tension of the parent bubble. This produces an inverted U-shaped ($\cap$-shaped) daughter particle distribution function and can be expressed as:

$$f^*\left(D^*\right)=\frac{\left[D^{*2/3}-\Lambda^{5/3}\right]\left[\left(1-D^{*3}\right)^{2/9}-\Lambda^{5/3}\right]}{\int_{D^*_{\min}}^{D^*_{\max}}\left[D^{*2/3}-\Lambda^{5/3}\right]\left[\left(1-D^{*3}\right)^{2/9}-\Lambda^{5/3}\right]d\left(D^*\right)} \tag{3.15}$$

where D^* is dimensionless diameter of the daughter bubble with respect to parent bubble, $D^*=D/D_0$. The model predictions compared very well with their own downstream measured evolution of the cumulative volume bubble size distribution. Obviously, the shape of daughter bubble p.d.f. needs to be verified against carefully designed experiments to determine which type of p.d.f. prevails.

Lehr and Mewes (2001) suggested another formula, following the idea of Levich (1962) and Luo and Svendsen (1996), for bubble breakup rate of bubble size v into bubbles of size v_z and $\left(v-v_z\right)$:

$$\Omega_B\left(v\rightarrow v_z\right)=1.5\left(1-\alpha_g\right)n\frac{\rho_l^{11/5}\varepsilon^{9/5}}{\sigma^{11/5}}\frac{\hat{v}^{1/3}}{\hat{v}_z^{4/3}}\left(\min\left(\hat{v}_z^{7/6},\frac{1}{\hat{v}_z^{7/9}}\right)-\frac{1}{\hat{v}_z^{7/9}}\right) \tag{3.16}$$

with $\hat{v}=v\frac{6}{\pi}\frac{\rho_l^{9/5}\varepsilon^{6/5}}{\sigma^{9/5}}$ and $\hat{v}_z=v_z\frac{6}{\pi}\frac{\rho_l^{9/5}\varepsilon^{6/5}}{\sigma^{9/5}}$. This equation is valid for bubbles larger than the maximum stable bubble which is provided by Equation (3.6). Similar to the model of Luo and Svendsen (1996), this model predicts the breakup rate for original bubbles of a given size at a given combination of the daughter bubble sizes (Figure 3.5) and thus does not need a predefined daughter bubble size distribution. The daughter bubble size distribution is a result that can be calculated directly from the model.

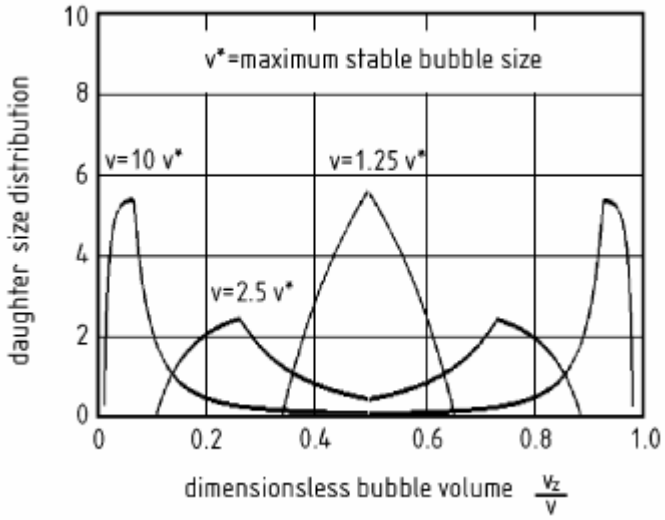

Figure 3.5 Dimensionless daughter size distribution (from Lehr and Mewes, 2001).

Hagesaether *et al.* (2002a) expanded and refined the breakup model of Luo and Svendsen (1996). The assumption, which is suggested by Lee *et al.* (1987a) and Luo and Svendsen (1996), that eddies of a larger scale will just give the bubble a translational velocity whereas eddies of similar scale may break up bubbles, is removed. Instead, eddies of all scales are considered to be able to breakup a bubble. In addition to the aforementioned surface energy criteria suggested by Luo and Svendsen (1996), Hagesaether *et al.* (2002a) argued that the energy density of the daughter bubbles, which is the surface energy divided by the volume of the daughter bubbles, must be lower or equal to the energy density of the arriving eddies which cause the breakup (Figure 3.6). The bombarding frequency of the eddies of size λ on bubbles of size d is the same as Equation (3.9). For a given collision between bubbles of size d_i (or volume v_i) and eddies of size λ_j and energy level $e(\lambda_j)$, the breakup probability distribution can be expressed in terms of a normalized product of two functions related to the two breakup criteria:

$$P_B\left(v_i \rightarrow v_k, \lambda_j, e_l\right) = \overline{F_s F_d} \tag{3.17}$$

where

$$F_s\left(d_i, d_k\right) = \max\left[e\left(\lambda_j\right) - \pi\sigma d_i^2 \left[\frac{d_k^2}{d_i^2} + \left(1 - \frac{d_k^3}{d_i^3} \right)^{2/3} - 1 \right], 0 \right] \text{ (surface criterion)} \quad (3.18)$$

$$F_d\left(d_k\right) = \max\left[\frac{e\left(\lambda_j\right)}{\frac{4}{3}\pi\left(\lambda_j/2\right)^3} - 6\sigma/d_k, 0 \right] \text{ (energy density criterion)} \quad (3.19)$$

where d_i is parent bubble diameter and d_k is daughter bubble diameter. One should note that the energy level, $e\left(\lambda_j\right)$, of a given arriving eddy is not equal to the mean energy level, $\overline{e}\left(\lambda_j\right)$, of such eddy of size of size λ_i. It must be determined by energy probability function distribution.

According to the energy density criteria, arriving eddy with higher energy density is needed to breakup a small bubble, or tear a tiny part off the parent bubble. Thus, these scenario are less likely (e.g., Figure 3.6c) compared with Luo and Svendsen's (1996) model prediction. The inherent weaknesses in Luo and Svendsen's (1996) model regarding the breakup rate for small bubbles and small daughter bubbles fragments are thus removed. However, the numerical implementation of this model is significantly more expensive than other breakup models as double integral is needed for all the possible eddies classes (sizes) *and* all energy levels for certain size of eddy. Therefore, Hagesaether *et al.*'s (2002a) breakup model is not implemented in this work.

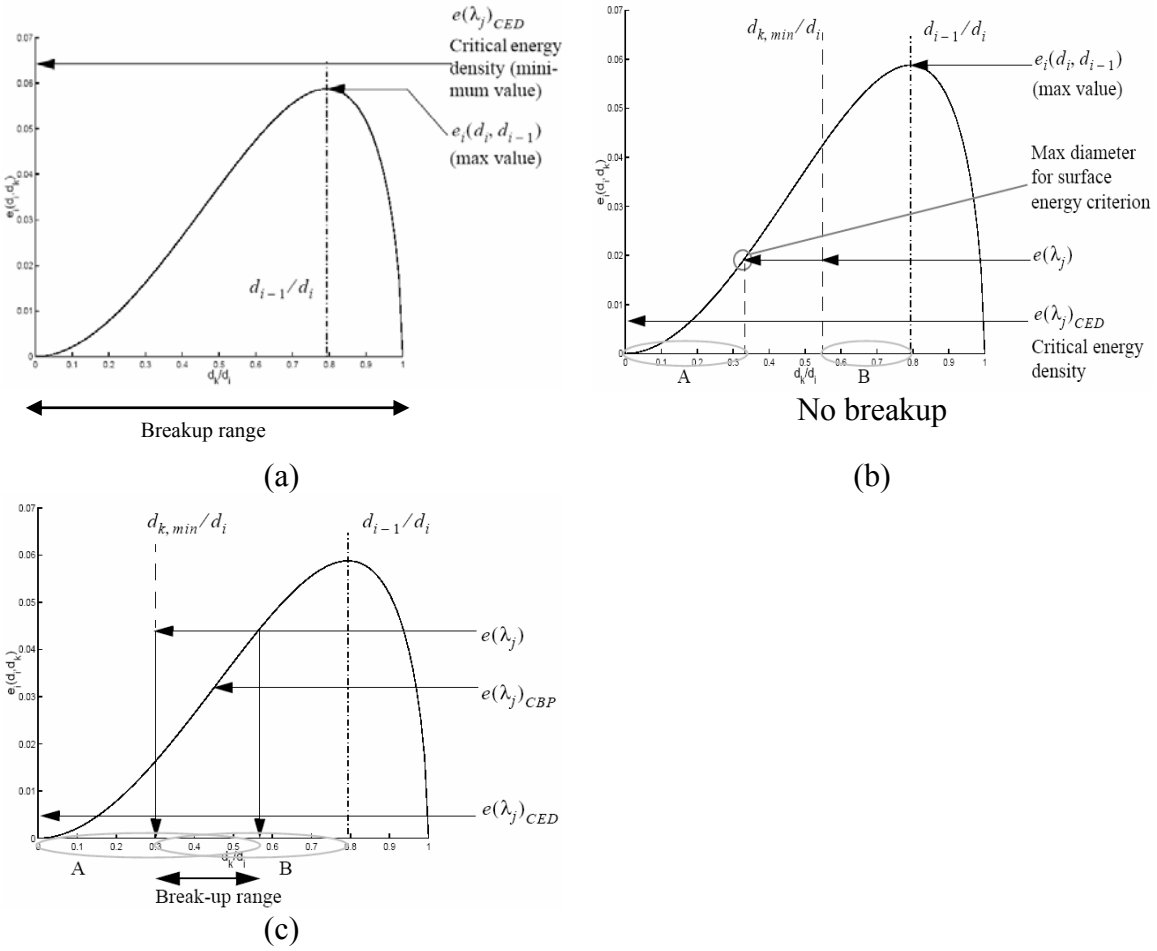

Figure 3.6 Breakup determined by (a) surface energy criteria only, b) Both criteria are not satisfied simultaneously thus no breakup, c) Breakup determined by surface energy and energy density criteria (from Hagesaether *et al.*, 2002a).

3.3 Bubble Coalescence

The coalescence of two bubbles in turbulent flow is usually considered to occur in three steps. First, the bubbles collide, then the surface of the colliding bubbles flattens against each other trapping a small amount of liquid between them. Since the collision of three or more bubbles at the same time has a very small probability, only binary collision is normally considered in coalescence models.

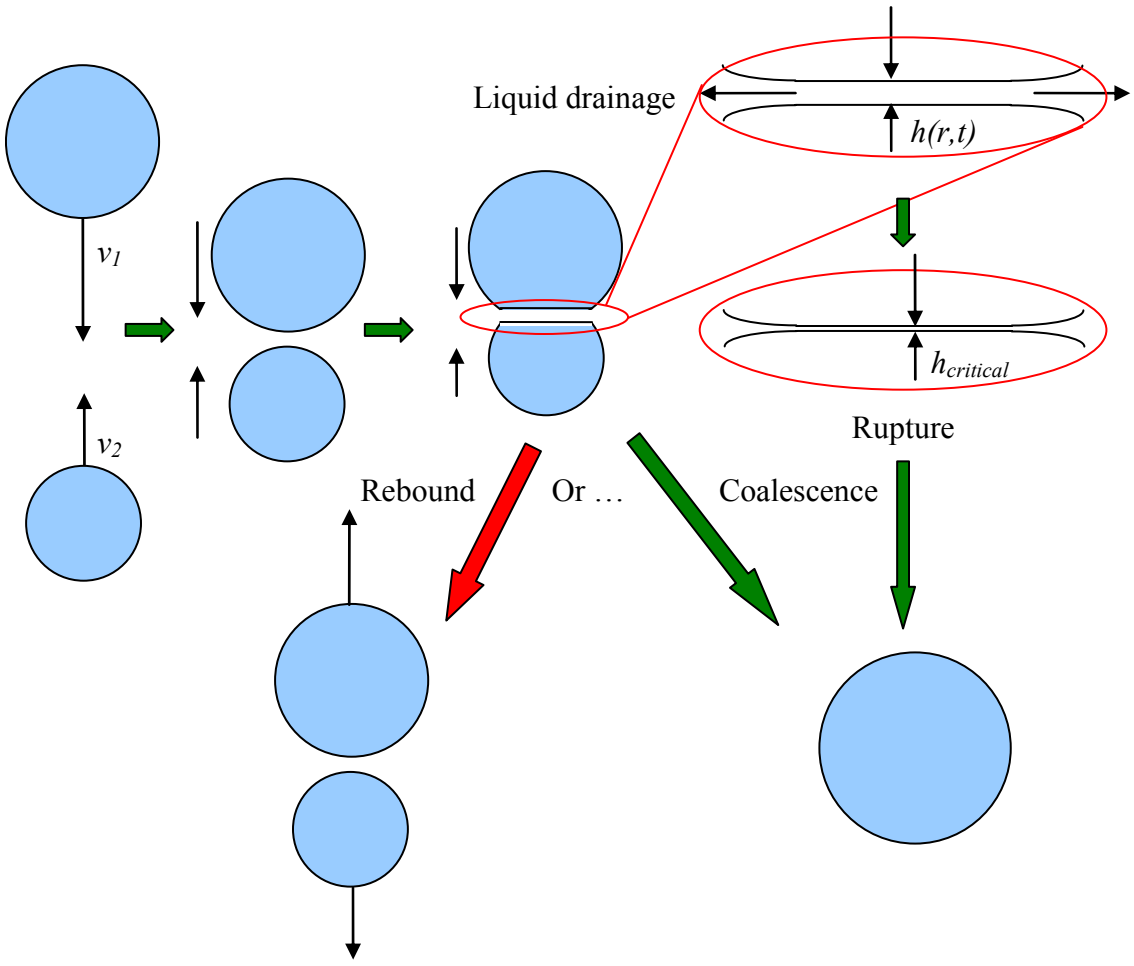

Figure 3.7 Bubble coalescence in turbulent flow.

Coalescence may not result from each collision, and thus coalescence efficiency was introduced by many investigators. The most popular model for the coalescence efficiency is the film-thinning model (e.g., Kirkpatrick and Lockett, 1974, Prince and Blanch, 1990, Luo, 1993). In this type of model, when the bubbles approach faster, they tend to bounce back without coalescence due to the limitation on the film drainage rate governed by the surface tension (Figure 3.7).Two bubbles will coalesce provided they remain in contact for a period of time sufficient for the liquid film between them to thin

out to the critical value necessary for rupture. The coalescence rate, Ω_C, for bubbles of size of d_i and d_j, can be expressed as

$$\Omega_C\left(d_i, d_j\right) = \theta_{ij} P_C \quad \left(m^{-3}s^{-1}\right) \tag{3.20}$$

where θ_{ij} is the collision frequency and P_C is the coalescence efficiency.

3.3.1 Collision Frequency

Collision may occur due to a variety of mechanisms. One is the random motion of bubbles due to turbulence (Figure 3.7). Saffman and Turner (1956) proposed a collision frequency model which only takes turbulent collision into account:

$$\theta_{ij} = \frac{\pi}{4}\left(d_i + d_j\right)^2 n_i n_j \left(\varepsilon d_i\right)^{1/3}\left[1+\left(d_i/d_j\right)^{-2/3}\right]^{1/2} \quad \left(m^{-3}s^{-1}\right) \tag{3.21}$$

where θ_{ij} is the collision frequency between bubbles with diameter of d_i and d_j, n_i and n_j is bubble number density (m^{-3}), ε is local turbulent dissipation rate ($m^2 s^{-3}$). This expression for the collision frequency of bubbles or drops has been verified by Kuboi *et al.* (1972) using the experimental results for the collisions of equal-sized drops in benzene-water and cyclohexanone-water systems and has been used by many authors (e.g. Lee *et al.*, 1987a; Luo, 1993; Tsouris and Tavlarides, 1994).

In addition to turbulence, bubbles of different sizes have different rise velocities that may lead to collision (Figure 3.8a). Also bubbles located in a region of relatively high liquid velocity may collide with bubbles in a slower section of the velocity field (Figure 3.8b). It is assumed that collisions from these various mechanisms are cumulative. In support of this, Swift and Friedlander (1964) reported the cumulative collision of aerosol particles from Brownian motion and laminar shear. Prince and Blanch (1990) proposed a collision frequency model based on the summation of the turbulent collision rate, buoyancy-driven collision rate and laminar shear collision rate as follows:

$$\theta_{ij} = \theta_{ij}^{T} + \theta_{ij}^{B} + \theta_{ij}^{LS} \tag{3.22}$$

$$\theta_{ij}^{T} = 0.089\pi n_i n_j \left(d_i + d_j\right)^2 \varepsilon^{1/3} \left(d_i^{2/3} + d_j^{2/3}\right)^{1/2} \tag{3.23}$$

$$\theta_{ij}^{B} = \frac{\pi}{16} n_i n_j \left(d_i + d_j\right)^2 \left(u_{ri} - u_{rj}\right) \tag{3.24}$$

$$\theta_{ij}^{LS} = \frac{1}{6} n_i n_j \left(d_i + d_j\right)^3 \left(\overline{\frac{dU_l}{dR}}\right) \tag{3.25}$$

where θ_{ij} is the collision frequency, θ_{ij}^{T}, θ_{ij}^{B} and θ_{ij}^{LS} are the turbulent, buoyancy driven and laminar shear collision frequencies, respectively. $\overline{\frac{dU_l}{dR}}$ is average liquid axial velocity gradient and u_r is the bubble rising velocity which is given by Clift *et al.* (1978):

$$u_r = \sqrt{\frac{2.14\sigma}{\rho_l d_b} + 0.505 g d_b} \tag{3.26}$$

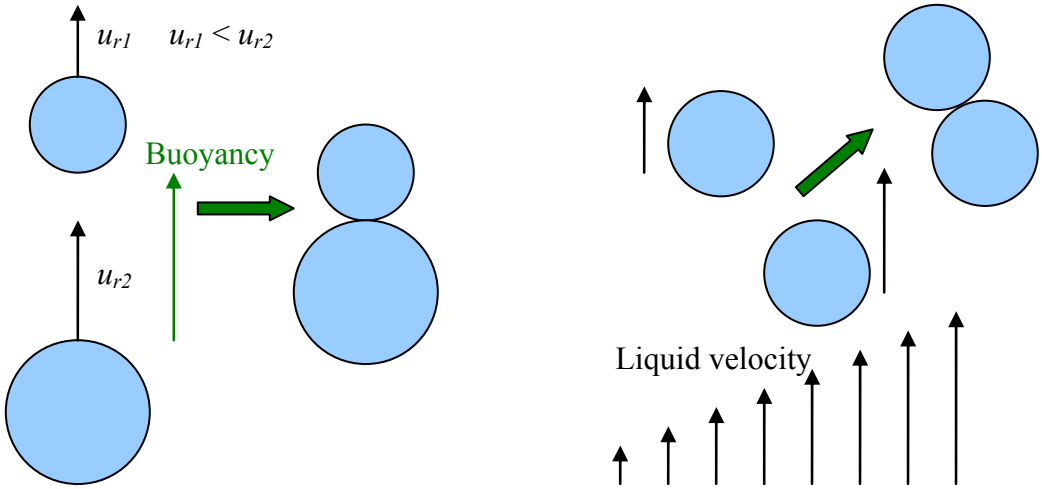

Figure 3.8 (a) Buoyancy-driven and (b) laminar shear induced collision.

Lehr and Mewes (2001) suggested another expression for collision frequency following Prince and Blanch's (1990) model which take the turbulence and buoyancy driven induced collision into account:

$$\theta_{ij} = \frac{\pi}{4}\left(d_i + d_j\right)^2 n_i n_j \left(\max\left(\sqrt{2}\left(\varepsilon\sqrt{d_i d_j}\right)^{1/3}, \left|u_{ri} - u_{rj}\right| \right) \right) \tag{3.27}$$

If a bubble enters another bubble's wake (Figure 3.9), it will usually overtake the leading bubble in an inline collision that may result in coalescence (see Otake *et al.*, 1977, Bilicki and Kestin, 1987, Stewart, 1995, Wu *et al.*, 1998, Colella *et al.*, 1999). Although there are many observations of the wake effects, all of which showed that the wake effect is very important for coalescence, the wake-induced collision models are rare.

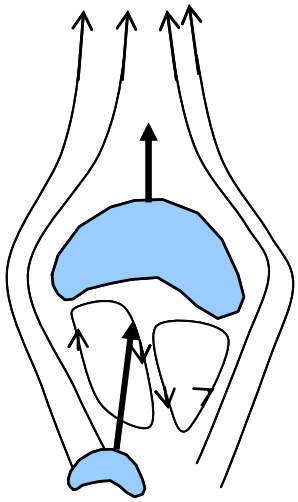

Figure 3.9 Wake Entrainment

Wu *et al.* (1998) defined the effective wake volume, V_m, in which the bubbles that follow may collide with the leading one, as the projected bubble area multiplied by the effective length, L_w, which is 5-7 times the bubble diameter in an air-water system (Tsuchiya *et al.*, 1989, Miyahara *et al.*, 1991, Stewart, 1995). By assuming the wake structure of the leading bubble to be the same as that of a solid sphere, Wu *et al.* (1998)

present the following collision frequency due to wake entrainment (bubble of size d_i is the leading bubble):

$$\theta_{ij}^{WE} = C_{WE} d_i^2 \frac{u_r(d_i)}{L_w/d_i - 1/2}\left[\left(\frac{L_w}{d_i/2}\right)^{1/3} - 1\right] n_i n_j \tag{3.28}$$

where C_{WE} is an adjustable parameter, u_r is the terminal velocity of a bubble of diameter d_i relative to the liquid which is given by:

$$u_r = \left(\frac{d_i g}{3C_D}\frac{\rho_l - \rho_g}{\rho_l}\right)^{1/2} \tag{3.29}$$

where g is gravity acceleration, C_D is drag coefficient which is given by:

$$C_D = 24\frac{1 + 0.1Re_D^{0.75}}{Re_D} \quad and \quad Re_D = (1-\alpha)\frac{\rho_l u_r d_i}{\mu_l} \tag{3.30}$$

where μ_l is the viscosity of liquid phase.

Colella *et al.* (1999) proposed a similar expression for the wake induced collision frequency:

$$\theta_{ij}^{WE} = n_i n_j u_{ij}^{rel} \frac{V_i^{BOX}}{\langle d \rangle} \tag{3.31}$$

where V_i^{BOX} is the volume influenced by the wake of a bubble of size d_i, u_{ij}^{rel} is the relative velocity between the two colliding bubbles and $\langle d \rangle$ is the average distance between bubbles in the considered system. The relative velocity between the leading bubble and the trailing bubble and V_i^{BOX} are given by Nevers and Wu (1971). However, the authors did not mention how to estimate the average distance between bubbles.

Most authors use turbulence-induced collision only, partly because the wake-induced collision, especially the wake-induced coalescence efficiency, is not well

understood. As far as the order of magnitude is concerned, the wake and turbulence induced collision are of the same order, while the laminar shear induced collision is less important. The buoyancy-driven collision is an inline collision, and when the leading bubble collides with the trailing bubble, the trailing bubble is in the wake of the leading bubble. Hence, the velocity difference between the two bubbles cannot be calculated by the free rising velocity difference as suggested by Clift *et al.* (1978). In summary, in turbulent flow there are only two important collision mechanisms: the wake entrainment and turbulence. The difficulty is that the knowledge of the wake-induced coalescence efficiency is essentially non-existent at present. One can either assume that the wake-induced coalescence efficiency is the same as the turbulence-induced coalescence efficiency so that the summation of these two collision frequency can then be used to calculate the coalescence efficiency (Hibiki and Ishii, 2000), or one can consider only the turbulence-induced collision as the existing coalescence efficiency models are based on turbulence induced coalescence (Luo, 1993). We will use the latter approach in this work because the coalescence rate is mainly determined by the coalescence efficiency.

3.3.2 Coalescence Efficiency

Up to now, the coalescence efficiency models were mainly based on the phenomenological analysis. According to coalescence theory (Ross *et al.*, 1978; Chesters, 1991), coalescence will more likely to occur upon a collision of two bubbles if the contact time (interaction time), t_I, exceeds the coalescence time, t_C, required for drainage of the liquid film between them to a critical rupture thickness. Coulaloglou and Tavlarides (1977) suggested the following expression in liquid droplet coalescence rate investigation.

$$P_C = \exp\left(-\frac{t_C}{t_I}\right) \tag{3.32}$$

This basic concept has been adopted by many authors in gas-liquid system (e.g., Prince and Blanch, 1990; Luo, 1993), but various authors used different estimates for

interaction and coalescence times. Common assumptions used by many authors (e.g., Prince and Blanch, 1990; Luo, 1993; Chesters, 1991) are: 1) the interaction time, t_I, is proportional to the characteristic lifetime of an eddy of size equal to the sum of the sizes of the approaching bubbles which can be estimated as $t_I \propto d^{2/3}\varepsilon^{-1/3}$, and 2) that the coalescence time, t_C , can be estimated from the film drainage model and $t_C \propto \rho_c^{1/2} d^{3/2}\sigma^{-1/2}$. Then the coalescence efficiency can be estimated as $P_C \propto \exp\left(\rho_c^{1/2} d^{5/6}\sigma^{-1/2}\varepsilon^{1/3}\right)$. Table 3.4 lists several forms of the bubble coalescence efficiency. Obviously, these are empirical relationships. However, one may use them when more fundamental knowledge of the coalescence efficiency is lacking.

Table 3.4 Different forms of bubble coalescence efficiency

Lee *et al.*, 1987a	$P_C\left(d_i,d_j\right)=\exp\left[-c\varepsilon^{1/3}\left(d_i+d_j\right)^{-2/3}t_C\right]$ $t_C=\left(\frac{R}{4}\right)\left(\rho_c d/2\sigma\right)^{1/2}\ln\left(h_0/h_f\right)+24\pi^2 M\sigma\mu h_f^5 A_h^{-2}$
Prince and Blanch, 1990	$P_C\left(r_i,r_j\right)=\exp\left[-\left(\frac{r_{ij}^3\rho_c}{16\sigma}\right)^{1/2}\varepsilon^{1/3}r_{ij}^{-2/3}\ln\frac{h_0}{h_f}\right],\ r_{ij}=\frac{1}{2}\left(\frac{1}{r_i}+\frac{1}{r_j}\right)^{-1}$
Chesters, 1991	$P_C=\exp\left[-c\left(\frac{We}{2}\right)^{1/2}\right],\ We=\frac{\rho_c\left(\varepsilon d\right)^{2/3}d}{2\sigma}$
Luo, 1993	$P_C\left(d_i,d_j\right)=\exp\left\{-c\frac{\left[0.75\left(1+\xi_{ij}^2\right)\left(1+\xi_{ij}^3\right)\right]^{1/2}}{\left(\rho_d/\rho_c+\gamma\right)^{1/2}\left(1+\xi_{ij}\right)^3}We_{ij}^{1/2}\right\},$ $We=\frac{\rho_c d_i\bar{u}_{ij}^2}{\sigma},\ \xi_{ij}=d_i/d_j,\ \bar{u}_{ij}=\left(\bar{u}_i^2+\bar{u}_j^2\right)^{1/2}=\bar{u}_i\left(1+\xi_{ij}^{-2/3}\right)^{1/2},$ $\bar{u}_i=\beta^{1/2}\left(\varepsilon d_i\right)^{1/2},\beta=1.69$

Experiments (Doubliez, 1991; Duineveld, 1994) with individual bubbles show that small bubbles and small approach velocities lead to higher coalescence efficiency. Thus, for two colliding bubbles with given diameters the coalescence efficiency depends

on the relative velocity of approach. This velocity depends on the angle at which the two bubbles collide. Lehr and Mewes (2001) assume that the relative probability is equal for all steradians. Thus, the coalescence efficiency can be written as:

$$P_C\left(d_i, d_j\right) = \min\left(\frac{u_{crit}}{u'}, 1\right) \tag{3.33}$$

where $u_{crit} = \sqrt{\frac{We_{crit}\sigma}{\rho_l d_{eq}}}$, $u' = \max\left(\sqrt{2}\left(\varepsilon\sqrt{d_i d_j}\right)^{1/3}, \left|\mathbf{u}_i - \mathbf{u}_j\right|\right)$ and $d_{eq} = 2\left(\frac{1}{d_i} + \frac{1}{d_j}\right)^{-1}$. From the experimental results (Doubliez, 1991; Duineveld, 1994), $We_{crit} = 0.06$ is obtained for pure liquids.

The computed coalescence efficiency from models derived from gas-liquid dispersion experiments (Prince and Blanch, 1990; Chesters, 1991; Luo, 1993; Lehr and Mewes, 2001) are of the same order of magnitude (e.g., for $d_i = d_j = 5$ mm, $\varepsilon = 1$ m^2/s^3, $P_C = 0.1$~0.2).

It should be noted that the although the buoyancy driven and laminar shear *collision frequencies* may be superimposed on turbulence induce collision frequency (Prince and Blanch, 1990) because the bubble relative velocity can be superimposed, the turbulent induced *coalescence efficiency model* may not be applied to buoyancy driven and laminar shear collision events. If the Equation (3.32) can still be used, coalescence time scale does not change, and interaction time scale can be estimated as $t_I \propto d/u_{ij}$, then the coalescence rate, can be estimated as

$$P_C\left(d_i, d_j\right) \propto n_i n_j \left(d_i + d_j\right)^2 u_{ij} \exp\left(-\rho_c^{1/2}\left(d_i + d_j\right)^{1/2} \sigma^{-1/2} u_{ij}\right) \tag{3.34}$$

where u_{ij} is the bubble approach velocity. Thus if buoyancy driven and laminar shear collision are superimposed on turbulence induced collision rate (u_{ij} increases), the *coalescence rate* could decrease. Most authors only account for the turbulence-induced coalescence and adjust the parameters in their models. We also use the turbulence-

induced coalescence closure in this work. Thus the collision between bubbles with different velocity will be neglected.

3.4 Attempts of implementation of the bubble population balance into CFD for investigation of bubble column flows

The population balance equation is widely used in the chemical engineering community in crystallization, coagulation, emulsion, precipitation, liquid-liquid extraction, aerosol formation, grinding, and granulation. Most of these modeling investigations are focused on the kernel development and computational method, without taking into account complicated, or simplified, convection.

In gas-liquid flow, convection is important and cannot be neglected. The implementation of interfacial area density transport equation in the investigation of heat transfer in *one dimensional* pipe flow is an active field in nuclear engineering (e.g., Hibiki *et al.*, 2003; Ishii *et al.*, 2003). While this is a good start in the investigation of multiphase flows in the heat exchange tubes, the one dimensional assumption is not valid in bubble column flows.

Several attempts of implementation of the bubble population balance in the bubble column flow simulations were made. The authors mainly focused on either investigation of the breakup and coalescence model, using simplified one-dimensional flow field and estimated turbulence property (e.g., Colella *et al.*, 1999; Hagesaether *et al.*, 2000; 2002b), or on the numerical method for solving the population balance equation. (e.g. Campos and Lage, 2003). These investigations are in line with the methods mentioned above (i.e., one dimensional).

Lo (1998) used a single gas phase velocity field for all the bubble groups (multi group, two-fluid model). Olmas *et al.* (2001) implemented the population balance equation in an Euler-Euler code (CFX 4.3), using the single-phase $k-\varepsilon$ model for the

turbulence in the liquid phase, the breakup model by Luo and Svendsen (1996) and the coalescence model by Prince and Blanch (1990). The authors studied the flow field in a 2D-axisymmetic bubble column (10 cm diameter), operated at different superficial gas velocities (0.5-9.6 cm/s) and compared the computed axial liquid velocity, local gas holdup and bubble size distribution with the experimental data obtained by using the laser Doppler velocimetry, optical probe, and photography respectively (although the use of LDV and photography in high superficial gas velocity is questionable). Olmas *et al.* (2001) used 10 bubbles classes and assumed that all bubbles move with the same speed. By modifying the drag formulation to include the turbulence dispersion, which is a function of turbulent kinetic energy, and the liquid holdup gradient, they obtained the following modified drag formula:

$$\mathbf{F}_D = \frac{3\alpha_2}{4}\left(\frac{\rho_l}{d_B}\right) C_D \left|\mathbf{u}_g - \mathbf{u}_l\right|\left(\mathbf{u}_g - \mathbf{u}_l\right) - C_{TD}\rho_l k \nabla \alpha_1 \tag{3.35}$$

where $C_{TD} = 0.1$. The extra term in Equation (3.35) is essentially a lateral dispersion force. Olmos *et al.* (2001) focused on the bubbly flow and transition flow regime, while this study focused on churn-turbulent flow regime, which is of industrial interest. The overall gas holdup is not predicted well beyond U_g > 8 cm/s (Olmas *et al.*, 2001). Moreover, it is difficult to draw conclusions on whether BPBE is needed from Olmos *et al.*'s (2001) work for a number of reasons. The use of LDV in cylindrical bubble column at gas holdup higher than 10% is questionable, as it is out of the upper limit of LDV measurement. Thus the liquid velocity profile comparison is questionable for all except at superficial gas velocity equal to 1.7 cm/s. For similar reason, the photography determined bubble size distribution is also questionable. In addition, the improvement on the gas holdup prediction with BPBE is marginal as the flow is in the bubbly and transient flow regime, where breakup and coalescence is relatively weak. The predicted gas holdup profiles were in better agreement with data (e.g., the maximum gas holdup appears in the center) due to the modified drag force formula compared to 2D axi-symmetric simulations performed by other authors. However, compared to other authors' (e.g., Krishna *et al.*, 1999) 2D axi-symmetric simulations, the predicted liquid axial

velocity profiles were worse. Besides, the gas holdup is over-predicted and flatter than experimental data, which indicates further tuning of the recommended value $C_{TD} = 0.1$ may be necessary.

Lehr and Mewes (2001) assumed equilibrium between the coalescence and break-up processes, which reduces the population balance model to a single transport equation. In bubble columns, however, the assumption of equilibrium may not be applicable because of significant influence of convection. This transport equation was implemented into three dimensional Euler-Euler framework to simulate a uniformly aerated cylindrical bubble column 0.29 m in diameter and 4.425 m in height operated at $U_g = 2.0\ cm/s$ superficial gas velocity. Several breakup and coalescence models (Levich, 1962; Prince and Blanch, 1990; Luo and Svendsen, 1996) and experimental observations (Doubliez, 1991; Duineveld, 1994) were used to derive a simplified rate kernel for this transport equation (source term). These reported rate kernels are independent of the bubble volume, which is contrary to experimental observations. In addition to the spiral motion and recirculating structures, Lehr and Mewes (2001) also indicate that the scale of the computed eddies seems to be comparable to the column diameter. The time averaged gas holdup and velocity profile well predicted the experimental data of Yao *et al.* (1991). However, Lehr and Mewes (2001) found the bubble size distribution to be bimodal, which has never been reported for the bubbly flow regime ($U_g = 2.0\ cm/s$). It is possible that this result is an artifact of the oversimplified breakup/coalescence rate kernel and it suggests that multi-group bubble population balance equation may be necessary.

Buwa and Ranade (2002) investigated, experimentally and numerically, a rectangular bubble column, with 0.2 m width × 1.2 m height × 0.05 m depth. The superficial air velocity was low and varied from 0.16 to 0.83 cm/s. In addition to reconfirm the main findings of Pfleger *et al.* (1999) and Becker *et al.* (1999), Buwa and Ranade (2002) also incorporated a single transport equation suggested by Lehr and Mewes (2001) to investigate the effect of sparger design. Their findings indicate, at least

in the bubbly flow regime, the importance of bubble size since the influence of sparger may be represented solely by the selection of appropriate bubble size. However, different ways of representing the gas sparger in the computational model was not found to have any significant influence on predicted plume oscillation time. These results indicate that the bubble size and bubble size distribution play an important role in determining the dynamics of gas-liquid flows in bubble columns, which is in line with the suggestion of Krishna *et al*. (2000). Buwa and Ranade (2002) further implemented the breakup and coalescence kernels suggested by Lehr and Mewes (2001) and tracked 5 different group of bubbles (0.5 – 5 mm). The preliminary computed bubble distribution agrees reasonably well with their experimental data.

The previous implementations mostly focused on the bubbly flow, where bubble breakup and coalescence are not important. In this work, we will systematically investigate the influence of the BPBE on the CFD simulation of bubbly and churn-turbulent flow and quantitative comparison will be performed with experimental data whenever possible.

Chapter 4
Implementation of Bubble Population Balance Equation (BPBE) in Computational Fluid Dynamic (CFD) Models

4.1 CFD Model Equations

In the present work, the flow in bubble columns was modeled using the Eulerian multiphase model, as well as the Algebraic Slip Mixture Model (ASMM). These models have been reviewed in Chapter 2. The model equations and closures used are listed in Table 4.1 and Table 4.2, respectively.

The widely used drag formulation does not take the elevated pressure into account. Krishna and van Baten (2001a) proposed in the drag formulation as density correction factor, the ratio of gas density at operating and atmospheric pressure, $\rho_g / \rho_{g,1atm}$. However, the introduction of such correction factor significantly over-predicted the overall gas holdup at higher superficial velocity and higher pressure (e.g., $U_g = 30\ \ cm/s, P = 0.6\ MPa$). For that reason, the density correction factor is reduced in this study to $\left(\rho_g / \rho_{g,1atm}\right)^{0.25}$. In the Euler-Euler model, turbulence in the liquid phase is modeled through a set of modified *k*-ε equations with extra terms that include interphase turbulent momentum transfer (Launder and Spalding, 1974; Elghobashi and Abou-Arab, 1983). For the dispersed gas phase, turbulence closure is effected through correlations from the theory of dispersion of discrete particles by homogeneous turbulence (Tchen,

1947). In ASMM, the turbulent stress term in the mixture equation is closed by solving a k-ε model for the mixture phase.

Table 4.1 Euler-Euler model equations

Continuity Equation
$\frac{\partial \alpha_k}{\partial t} + \nabla \bullet \left(\alpha_k \mathbf{u}_k \right) = 0$ Liquid phase: $k = l$; Gas phase: $k = g$.
Momentum Equation
$\frac{\partial \alpha_k \rho_k \mathbf{u}_k}{\partial t} + \nabla \bullet \left(\alpha_k \rho_k \mathbf{u}_k \mathbf{u}_k \right) = -\alpha_k \nabla p + \alpha_k \rho_k \mathbf{g} \pm \mathbf{M}_d + \nabla . \left(\alpha_k \boldsymbol{\tau}_k \right) + \nabla \bullet \left(\alpha_k \rho_k \mathbf{u}_k' \mathbf{u}_k' \right)$
$\boldsymbol{\tau}_k = \mu_k \left(\nabla \mathbf{u}_k + \nabla \mathbf{u}_k^{\mathrm{T}} \right) - \frac{2}{3} \mu_k \nabla \bullet \mathbf{u}_k \mathbf{I}$
Closure for Drag
$\mathbf{M}_d = \frac{3}{4} \alpha_g \alpha_l \frac{\rho_l}{d_b} C_D \left(\rho_g / \rho_{g,1atm} \right)^{0.25} \left\| \mathbf{u}_l - \mathbf{u}_g \right\| \left(\mathbf{u}_l - \mathbf{u}_g \right)$
$C_D = \begin{cases} 24\left(1 + 0.15\,\mathrm{Re}^{0.687}\right)/\mathrm{Re} & \mathrm{Re} \le 1000 \\ 0.44 & \mathrm{Re} > 1000 \end{cases}$, $\mathrm{Re} = \frac{d_b \left\| \mathbf{u}_l - \mathbf{u}_g \right\| \rho_l}{\mu_l}$
(Schiller and Naumann, 1935)
Turbulence in the Continuous Phase
$\alpha_l \rho_l \mathbf{u}_l' \mathbf{u}_l' = -\frac{2}{3} \left(\rho_l k_l + \rho_l \mu_{t,l} \nabla \bullet \mathbf{U}_l \right) \mathbf{I} + \rho_l \mu_{t,l} \left(\nabla \bullet \mathbf{U}_l + \nabla \bullet \mathbf{U}_l^T \right)$ ($\mathbf{U}$ is phase weighted velocity)
$\mu_{t,l} = \rho_l C_\mu \frac{k_l^2}{\varepsilon_l}$
$\frac{\partial}{\partial t} \left(\alpha_l \rho_l k_l \right) + \nabla \bullet \left(\alpha_l \rho_l \mathbf{U}_l k_l \right) = \nabla \bullet \left(\alpha_l \frac{\mu_{t,l}}{\sigma_k} \nabla k_l \right) + \alpha_l G_{k,l} - \alpha_l \rho_l \varepsilon_l + \alpha_l \rho_l \prod_{k_l}$
$\frac{\partial}{\partial t} \left(\alpha_l \rho_l \varepsilon_l \right) + \nabla \bullet \left(\alpha_l \rho_l \mathbf{U}_l \varepsilon_l \right) = \nabla \bullet \left(\alpha_l \frac{\mu_{t,l}}{\sigma_\varepsilon} \nabla \varepsilon_l \right) + \alpha_l \frac{\varepsilon_l}{k_l} \left(C_{1\varepsilon} G_{k,l} - C_{2\varepsilon} \rho_l \varepsilon_l \right) + \alpha_l \rho_l \prod_{\varepsilon_l}$
$G_{k,l} = \frac{1}{2} \mu_{t,l} \left[\nabla \mathbf{U}_l + \left(\nabla \mathbf{U}_l \right)^T \right]^2$
$\prod_{k_l} = \sum_{p=1}^{M} \frac{K_{gl}}{\alpha_l \rho_l} \left[k_{gl} - 2k_l + \left(\mathbf{u}_g - \mathbf{u}_l \right) \bullet \mathbf{u}_{dr} \right]$, M is the number of secondary phase
$\prod_{\varepsilon_l} = C_{3\varepsilon} \frac{\varepsilon_l}{k_l} \prod_{k_l}$, $K_{gl} = \frac{3 \alpha_l \alpha_g}{4} \left(\frac{\rho_l}{d_b} \right) C_D \left\| \mathbf{u}_g - \mathbf{u}_l \right\|$

Turbulence in the Dispersed Phase

$$\tau_{F,gl} = \alpha_l \rho_l K_{gl}^{-1} \left(\frac{\rho_g}{\rho_l} + C_V \right)$$

$$\tau_{t,gl} = \frac{\tau_{t,l}}{\sqrt{\left(1 + C_\beta \xi^2\right)}}$$

$$\xi = \frac{\left|\mathbf{u}_g - \mathbf{u}_l\right| \tau_{t,l}}{L_{t,l}}$$

$C_\beta = 1.8 - 1.35\cos^2\theta$, θ is the angle between the gas velocity and the slip velocity.

$$\eta_{gl} = \frac{\tau_{t,gl}}{\tau_{F,gl}}$$

$$k_g = k_l \left(\frac{b^2 + \eta_{gl}}{1 + \eta_{gl}} \right)$$

$$k_{gl} = 2k_l \left(\frac{b + \eta_{gl}}{1 + \eta_{gl}} \right)$$

$$D_g = D_l = D_{t,gl} = \frac{1}{3} k_{gl} \tau_{t,gl}$$

$$b = \left(1 + C_V\right) \left(\frac{\rho_g}{\rho_l} + C_V \right)^{-1}, C_V = 0.5$$

Interphase Turbulent Momentum Transfer

$$K_{gl}\left(\mathbf{u}_g - \mathbf{u}_l\right) = K_{gl}\left(\mathbf{U}_g - \mathbf{U}_l\right) - K_{gl}\mathbf{u}_{dr}$$

$$\mathbf{u}_{dr} = -\left(\frac{D_g}{\sigma_{gl}\alpha_g} \nabla \alpha_g - \frac{D_l}{\sigma_{gl}\alpha_l} \nabla \alpha_l \right)$$

Model Constants

$$C_\mu = 0.09, C_{1\varepsilon} = 1.44, C_{2\varepsilon} = 1.92, C_{3\varepsilon} = 1.20, \sigma_k = 1.00, \sigma_e = 1.30, \sigma_{gl} = 0.75$$

Table 4.2 Algebraic Slip Mixture (ASM) model equations

Continuity and Momentum Equation

$$\frac{\partial \rho_m}{\partial t} + \nabla \bullet \left(\rho_m \mathbf{u}_{\mathrm{m}} \right) = 0$$

$$\frac{\partial \left(\rho_m \mathbf{u}_{\mathrm{m}} \right)}{\partial t} + \nabla \bullet \left(\rho_m \mathbf{u}_{\mathrm{m}} \mathbf{u}_{\mathrm{m}} \right) = -\nabla p + \nabla \bullet \left(\boldsymbol{\tau}_{\mathrm{m}} + \boldsymbol{\tau}_{\mathrm{m}}^{\mathrm{t}} \right) + \nabla \bullet \boldsymbol{\tau}_{\mathrm{Dm}} + \rho_m \mathbf{g}$$

$$\rho_m = \sum_{k=1}^{n} \alpha_k \rho_k, \mathbf{u}_{\mathrm{m}} = \frac{\sum_{k=1}^{n} \alpha_k \rho_k \mathbf{u}_{\mathrm{k}}}{\rho_m}, \mu_m = \sum_{k=1}^{n} \alpha_k \mu_k$$

$$\boldsymbol{\tau}_m = \mu_m \left(\nabla \mathbf{u}_m + \nabla \mathbf{u}_m^{\mathrm{T}} \right) - \frac{2}{3} \mu_m \nabla \bullet \mathbf{u}_m \mathbf{I}$$

$$\boldsymbol{\tau}_m^t = \mu_m^t \left[\left(\nabla \mathbf{u}_m + \nabla \mathbf{u}_m^{\mathrm{T}} \right) - \frac{2}{3} \nabla \bullet \mathbf{u}_m \mathbf{I} \right] - \frac{2}{3} \rho_m k_m \mathbf{I}$$

$$\boldsymbol{\tau}_{Dm} = \sum_{k=1}^{m} \alpha_k \rho_k \mathbf{u}_{D,k} \mathbf{u}_{D,k}$$

$$\mathbf{u}_{\mathrm{D,k}} = \mathbf{u}_{\mathrm{k}} - \mathbf{u}_{\mathrm{m}}$$

$$\mathbf{u}_{k,c} \equiv \mathbf{u}_{slip,k} = \mathbf{u}_k - \mathbf{u}_c$$

$$\mathbf{u}_{D,k} = \mathbf{u}_{k,c} - \sum_{i=1}^{n} \frac{\alpha_i \rho_i \mathbf{u}_{i,c}}{\rho_m}$$

$$\frac{\partial}{\partial t} \left(\alpha_s \rho_s \right) + \nabla \left(\alpha_s \rho_s \mathbf{u}_{\mathrm{m}} \right) = -\nabla \bullet \left(\alpha_s \rho_s \mathbf{u}_{\mathrm{D,s}} \right)$$

Slip Velocity and Turbulent Stress Term

$$\mathbf{u}_{k,c} = \frac{\left(\rho_m - \rho_k \right) d_k^2}{18 \mu_c f} \left(g - \frac{D \mathbf{u}_m}{Dt} \right), \; f = \begin{cases} 1 + 0.05 Re^{0.687} & Re < 1000 \\ 0.018 Re & Re < 1000 \end{cases}$$

$$\frac{\partial}{\partial t} \left(\rho_m k_m \right) + \nabla \bullet \left(\rho_m \mathbf{u}_m k_m \right) = \nabla \bullet \left(\frac{\mu_{t,m}}{\sigma_k} \nabla k_m \right) + G_{k,m} - \rho_m \varepsilon_m$$

$$\frac{\partial}{\partial t} \left(\rho_m \varepsilon_m \right) + \nabla \bullet \left(\rho_m \mathbf{u}_m \varepsilon_m \right) = \nabla \bullet \left(\frac{\mu_{t,m}}{\sigma_\varepsilon} \nabla \varepsilon_m \right) + \frac{\varepsilon_m}{k_m} \left(C_{1\varepsilon} G_{k,m} - C_{2\varepsilon} \rho_m \varepsilon_m \right)$$

$$\mu_{t,m} = \rho_m C_\mu \frac{k_m^2}{\varepsilon_m}$$

$$G_{k,l} = \frac{1}{2} \mu_{t,m} \left[\nabla \mathbf{u}_m + \left(\nabla \mathbf{u}_m \right)^T \right]^2$$

$$C_\mu = 0.09, C_{1\varepsilon} = 1.44, C_{2\varepsilon} = 1.92, \sigma_k = 1.00, \sigma_e = 1.30$$

The local bubble diameter is an important needed input parameter for the simulation. In the past it was either estimated from former experience or by a trial-and error method, or it was calculated from available mean bubble diameter correlations. This is mostly done because modeling different sizes of bubbles as individual phases leads to high computational cost and has numerical convergence problems. Such approach is still plausible in bubbly flow because bubble-bubble interactions are weak and the bubble sizes are narrowly distributed. However, in churn-turbulent flow, where most industrial applications lie, bubble-bubble interactions result in widely distributed bubble sizes that may be substantially different from the "mean" bubble size assumption. In addition, in order to generate a simulation result that resembles available data, the "mean" bubble size is customarily adjusted by a trial-and-error procedure and the value so chosen often is far from reality.

There is a need, when evaluating the performance of existing bubble column reactors and when designing new ones in churn-turbulent flow, to assess the gas holdup radial distribution, because it drives liquid recirculation, and local interfacial area concentration distribution, because it is essential to mass transfer. Engineering level of accuracy is needed. Based on extensive studies by many authors, we know that the two-fluid model based codes (e.g. FLUENT, CFX, CFDLIB, etc.) that utilize the mean bubble size concept cannot predict well the observed gas holdup radial profiles even in 3D simulation, in spite of claims of partial success to the contrary (Krishna *et al.*, 2000; Pan and Dudukovic, 2001), while the predicted velocity profiles and overall gas holdup estimates are pretty good. Moreover, available estimates of the local interfacial area are based on the predicted local gas holdup and assumed mean bubble size and are likely in error. One of the reasons for the mismatch of the holdup profile prediction and data could be that the current simulations use the so-called "mean" bubble size assumption, which does not hold well in the churn-turbulent flow regime. To remedy this situation, the implementation of the bubble population balance model (BPBE) in the Euler-Euler model or ASMM is needed. This eliminates the need to assume a single constant bubble size and possibly may improve the gas holdup profile prediction. Most importantly, the

implementation of BPBE allows one to predict the bubble size distribution locally, and eliminates the trial-and-error procedure regarding the unknown mean bubble diameter mentioned above, while providing the capability of predicting the interfacial area concentration locally throughout the column. In this work we will obtain it via the bubble population balance equation which is reviewed in Chapter 3.

4.2 Bubble Population Balance Equation

Bubble Population Balance Equation (BPBE) and breakup and coalescence closures have been reviewed in Chapter 3. There is no analytical solution for BPBE expressed by Equation (4.1) except for a few cases, thus the gas phase needs to be discretized into n subclasses according to bubble size, and be solved separately.

$$\frac{\partial}{\partial t} f\left(\mathbf{x}, v, t\right) + \nabla \cdot \left(\mathbf{u_b}\left(\mathbf{x}, v, t\right) f\left(\mathbf{x}, v, t\right)\right) = S\left(\mathbf{x}, v, t\right) \tag{4.1}$$

In the present implementation of BPBE in the two-fluid model, all the bubbles are assumed to move at identical velocity which equals the local ensemble averaged gas phase velocity, $\mathbf{u_g}$, obtained from the solution of the two-fluid model. In other words, it is assumed that $\mathbf{u}_{\mathrm{bi}} = \mathbf{u}_{\mathrm{g}}$ for all bubble classes. From two-fluid model equations, one can theoretically solve the continuity and momentum equation for N gas phases (N equals to the number of distinct bubble sizes to be tracked) and the liquid phase. However, it is very difficult, if not impossible, to get a large number of highly non-linear momentum equations to converge in a realistic period of time (e.g., $2\left(N+1\right)$ equations in 2D and $3\left(N+1\right)$ in 3D). To circumvent the problem of solving momentum equations for $N+1$ separate phases, only the continuity and momentum equation for two phases (gas and liquid) are solved as shown below. The gas phase is discretized into *n* subclasses according to bubble size (Ramkrishna, 2000). The number density based population balance equation for the i^{th} bubble class can be written as

$$\frac{\partial}{\partial t} n_i + \nabla \cdot \left(\mathbf{u_{bi}} n_i \right) = S_i \tag{4.2}$$

One can also derive the volume fraction based population balance equation for the i^{th} bubble class

$$\frac{\partial}{\partial t} \alpha_i + \nabla \cdot \left(\mathbf{u_{bi}} \alpha_i \right) = S_i^{'} \tag{4.3}$$

where n_i is i^{th} bubble class local number density, α_i is i^{th} bubble class local holdup and $\mathbf{u_{bi}}$ is i^{th} bubble local velocity vector. Reaction and phase change are neglected in the present work and the source term due to pressure change is neglected as well. Therefore, the source term S_i or $S_i^{'}$ is only due to breakup and coalescence of bubbles and its closures have been reviewed in Chapter 3. It should be noted that there are many breakup and coalescence models for liquid-liquid dispersion, which may not be applicable for gas-liquid systems. Besides, breakup models that do not specify the daughter bubble p.d.f. cannot be used. In this work, we used pertinent available breakup and coalescence closures for gas-liquid systems.

Either Equation (4.2) or (4.3) is solved along with the two-fluid model in a sequential manner to obtain for each bubble class its local number density n_i. The local mean bubble size, which is needed to calculate the drag force, is given as

$$d_b = \frac{\sum_{i=1}^{N} n_i d_i^3}{\sum_{i=1}^{N} n_i d_i^2} \tag{4.4}$$

In is intrinsic inconsistent to apply pseudo-Euler-Lagrangian approach (because bubble classes are not treated as discrete entities) for discretized bubble population balance equation in two-fluid model framework as the following equations has to be satisfied simultaneously if each bubble class are considered as different “phase” based on continuity and momentum equation.

$$\sum_{i=1}^{N} \alpha_i \mathbf{u}_{\mathrm{bi}} = \alpha_g \mathbf{u}_{\mathrm{g}} \tag{4.5}$$

$$\sum_{i=1}^{N} \alpha_i \mathbf{u}_{\mathrm{bi}} \mathbf{u}_{\mathrm{bi}} = \alpha_g \mathbf{u}_{\mathrm{g}} \mathbf{u}_{\mathrm{g}} \tag{4.6}$$

Equation (4.5) and (4.6) can be satisfied at the same time if and only if $\mathbf{u}_{\mathrm{bi}} = \mathbf{u}_{\mathrm{g}}$.

The aforementioned strategy can also be applied to the implementation of BPBE in the ASMM. However, contrary to the two-fluid model, only one momentum equation (the mixture momentum equation) needs to be solved in the ASMM. Therefore the aforementioned divergence challenge does not exist, and the simplification, that all the bubbles are assumed to move at identical velocity, is not necessary. One can solve the flow field for $N+1$ phases in the ASMM by the following modification of the volume fraction equation for the secondary phases:

$$\frac{\partial}{\partial t}\left(\alpha_i \rho_s\right) + \nabla\left(\alpha_i \rho_s \mathbf{u}_{\mathrm{m}}\right) = -\nabla \bullet \left(\alpha_i \rho_s \mathbf{u}_{\mathrm{D,i}}\right) + \rho_s S_i^{'} \tag{4.7}$$

Thus, different bubble class velocities are calculated (i.e., the velocities of different size bubble classes are different based on their size). All three implementations described above: 1) BPBE in two-fluid model with velocities of all bubbles assumed to be locally equal to gas phase ensemble local averaged velocity; 2) BPBE in ASMM with velocities of all bubbles assumed to be locally equal to gas phase ensemble local averaged velocity (ASMM, SV); and 3) BPBE in ASMM with N gas phases (i.e., N bubble classes) and one liquid phase such that different size bubbles have different local velocity calculated from ASMM (ASMM, DV), are executed and discussed in this work.

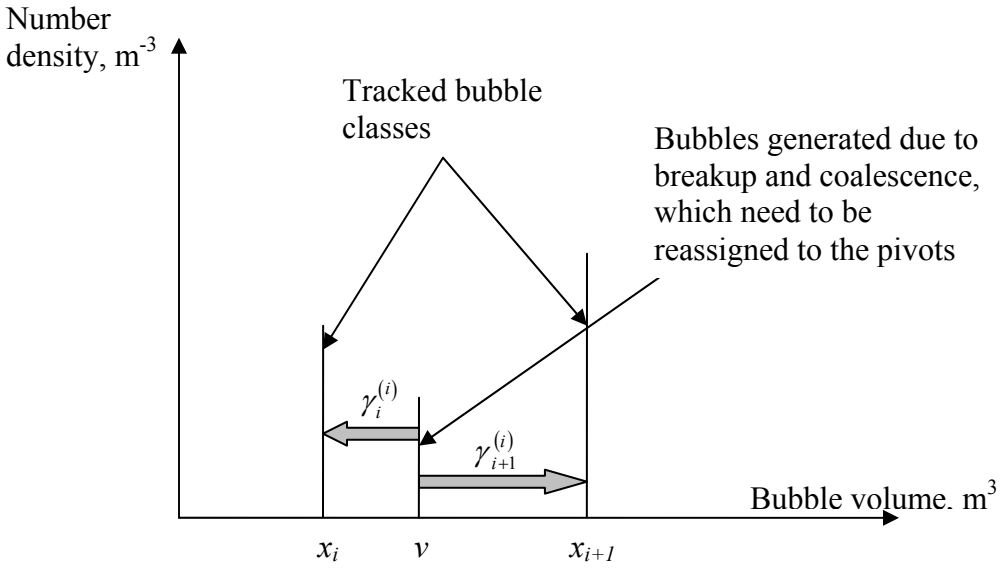

Figure 4.1 Bubble reassignment to pivots

The basic idea, in discretizating the bubble population balance equation, is that bubbles in a size range, say R_i, are assigned to a pivotal size x_i. However, breakup and coalescence processes may produce bubbles that are *between* such pivotal sizes (except in the case of a uniform linear grid, i.e., $x_i = iv_{min}$) and must be reassigned to the pivots (see Figure 4.1). The reassignment must be done carefully to preserve the accurate calculation of the selected moments of the *p.d.f.* Kumar and Ramkrishna (1996a) proposed the following way to preserve any selected moments. For $x_i \le v < x_{i+1}$, let the fraction of bubbles of size v assigned to x_i be denoted by $\gamma_i^{(i)}$, and a fraction of $\gamma_{i+1}^{(i)}$ be assigned to size x_{i+1}. The reassignment will preserve the r^{th} moment provided:

$$\gamma_i^{(i)}(v)\,x_i^r + \gamma_{i+1}^{(i)}(v)\,x_{i+1}^r = v^r, \quad \text{for } r = r_1, r_2 \tag{4.8}$$

These two equations above (i.e. Equation (4.8) for $r = r_1$ and $r = r_2$) yield a unique solution for the quantity $\gamma_i^{(i)}(v)$. In the present work, r was set to 0 and 1 to preserve the

mass balance and the number balance, respectively, during the reassignment process. Then, the source term for Equation (4.2) may be written as

$$S_i\left(\vec{x},t\right)=\sum_{x_{i-1}\le\left(x_j+x_k\right)\le x_i}^{j\ge k}\left(1-\frac{1}{2}\delta_{jk}\right)\left[\gamma_i^{(i-1)}\left(x_j+x_k\right)a\left(x_k,x_j\right)N_jN_k\right]$$
$$+\sum_{x_i\le\left(x_j+x_k\right)\le x_{i+1}}^{j\ge k}\left(1-\frac{1}{2}\delta_{jk}\right)\left[\gamma_i^{(i)}\left(x_j+x_k\right)a\left(x_k,x_j\right)N_jN_k\right] \tag{4.9}$$
$$-N_i\sum_{j=0}^{M}a\left(x_i,x_j\right)N_j+\sum_{j=i}^{M}N_jm\left(x_j\right)b\left(x_j\right)\pi_{i,j}-b\left(x_i\right)N_i$$

where $\pi_{i,j}=\int_{x_{i-1}}^{x_i}\gamma_i^{(i-1)}\left(v\right)P\left(v,x_j\right)dv+\int_{x_i}^{x_{i+1}}\gamma_i^{(i)}\left(v\right)P\left(v,x_j\right)dv$ and N_i (m^{-3}) is the number density of i^{th} bubble class.

It should be noted that the aforementioned reassignment process is to make it possible for the discrete equations to be internally consistent for the selected moments. It cannot, however, resolve the inherent numerical diffusion errors. More advanced BPBE solving technique/algorithms, such as moving pivot, are desirable.

4.2.1 Breakup and Coalescence Closures

The breakup and coalescence closures have been reviewed in Chapter 3. The closures implemented in this work are listed in Table 4.3. Ω_B is bubble breakup rate , Ω_B is bubble coalescence rate, θ_{ij} is bubble collision rate and P_C is bubble coalescence efficiency. All the nomenclatures in Table 4.3 have been given in Chapter 3.

Table 4.3 Breakup and Coalescence Closures Implemented

Breakup Closure Ω_B $(m^{-3}\,s^{-1})$	
Luo and Svendsen, 1996	$\Omega_B\left(v_i : vf_{BV}\right) = c_B\left(1-\alpha_g\right) n_i \left(\frac{\varepsilon}{d^2}\right)^{1/3} \int_{\xi_{\min}}^{1} \frac{\left(1+\xi\right)^2}{\xi^{11/3}} \exp\left(-\frac{12 c_f \sigma}{\beta \rho_c \varepsilon^{2/3} d^{5/3} \xi^{11/3}}\right)$ $c_f = f_{BV}^{2/3} + \left(1-f_{BV}\right)^{2/3} - 1,\ C_B \approx 0.923$
Martínez-Bazán *et al.*, 1999a; b	$\Omega_B\left(\varepsilon, d_i\right) = K_g n_i \frac{\sqrt{\beta\left(\varepsilon d_i\right)^{2/3} - 12\sigma/\left(\rho_c d_i\right)}}{d_i}$ $f^*\left(D^*\right) = \frac{\left[D^{*2/3} - \Lambda^{5/3}\right]\left[\left(1-D^{*3}\right)^{2/9} - \Lambda^{5/3}\right]}{\int_{D^*_{\min}}^{D^*_{\max}} \left[D^{*2/3} - \Lambda^{5/3}\right]\left[\left(1-D^{*3}\right)^{2/9} - \Lambda^{5/3}\right] d\left(D^*\right)}$ $\beta = 8.2,\ K_g = 0.25,\ D^* = D/D_0$
Coalescence Closure $\Omega_C = \theta_{ij} P_C\ (m^{-3}\,s^{-1})$	
Chesters, 1991	$\theta_{ij} = \frac{\pi}{4}\left(d_i + d_j\right)^2 n_i n_j \left(\varepsilon d_i\right)^{1/3} \left[1 + \left(d_i/d_j\right)^{-2/3}\right]^{1/2};$ $P_C = \exp\left[-c\left(\frac{We}{2}\right)^{1/2}\right],\ We = \frac{\rho_c \left(\varepsilon d\right)^{2/3} d}{2\sigma}$
Prince and Blanch, 1990	$\theta_{ij} = 0.089\pi n_i n_j \left(d_{bi} + d_{bj}\right)^2 \varepsilon^{1/3} \left(d_{bi}^{2/3} + d_{bj}^{2/3}\right)^{1/2};$ $P_C\left(r_i, r_j\right) = \exp\left[-\frac{\left(\frac{r_{ij}^3 \rho_c}{16\sigma}\right)^{1/2} \varepsilon^{1/3} \ln\frac{h_0}{h_f}}{r_{ij}^{2/3}}\right];\ r_{ij} = \frac{1}{2}\left(\frac{1}{r_i} + \frac{1}{r_j}\right)^{-1};$
Luo, 1993	$\theta_{ij} = \frac{\pi}{4}\left(d_i + d_j\right)^2 n_i n_j \left(\varepsilon d_i\right)^{1/3} \left[1 + \left(d_i/d_j\right)^{-2/3}\right]^{1/2};$ $P_C\left(d_i, d_j\right) = \exp\left\{-c\frac{\left[0.75\left(1+\xi_{ij}^2\right)\left(1+\xi_{ij}^3\right)\right]^{1/2}}{\left(\rho_d/\rho_c + \gamma\right)^{1/2}\left(1+\xi_{ij}\right)^3} We_{ij}^{1/2}\right\}$ $We_{ij} = \frac{\rho_c d_i \bar{u}_{ij}^2}{\sigma}, \xi_{ij} = d_i/d_j, \bar{u}_{ij} = \bar{u}_i\left(1+\xi_{ij}^{-2/3}\right), \bar{u}_i = \beta^{1/2}\left(\varepsilon d_i\right)^{1/2}$

4.2.2 Bubble classes tracked

In our two-dimensional axi-symmetric simulation bubbles from 1.0 mm to 32.0 mm in diameter are divided into 16 classes such that $v_i = 2v_{i-1}$ (see Table 4.4).

Table 4.4 Bubble classes tracked in 2D axisymmetric simulation

Class index	1	2	3	4	5	6	7	8
Bubble diameter (mm)	1.00	1.26	1.60	2.00	2.50	3.20	4.00	5.04
Class index	9	10	11	12	13	14	15	16
Bubble diameter (mm)	6.35	8.00	10.08	12.70	16.00	20.16	25.40	32.00

In the three-dimensional simulation, bubbles from 1.0 mm to 40.0 mm diameter are divided into 9 classes. (see Table 4.5).

Table 4.5 Bubble classes tracked in 3D simulation

Class index	1	2	3	4	5	6	7	8	9
Bubble diameter (mm)	1.00	1.60	2.50	4.00	6.35	10.08	16.00	25.40	40.00

4.2.3 Solution Procedure

The segregate solver (i.e., governing equations are solved sequentially rather than simultaneously/coupled together) is used to solve the flow field equations. Because the governing equations are non-linear and coupled, several iterations of the solution loop must be performed before a converged solution is obtained for a given time step. Each iteration consists of steps illustrated in Figure 4.2 and are outlined below.

1. Fluid properties are updated, based on the current solution. If the calculation has just begun, the fluid properties will be updated based on the initialized solution, or the solution at the previous time step.

2. The momentum and continuity equations are solved, using Phase Coupled SIMPLE (PC-SIMPLE) algorithm (Vasquez and Ivanov, 2000) in the Euler-Euler model, and SIMPLEC algorithm (Van Doormal and Raithby, 1984) in ASMM, for the pressure-velocity coupling.

3. Equations for scalars such as turbulence quantities (e.g., kinetic energy and dissipation rate), species concentration, and bubble population distribution are solved using the previously updated values of the other variables. The information such as local bubble size distribution and turbulent viscosity are used in the next iteration.

4. A check for convergence of the equation set is made.

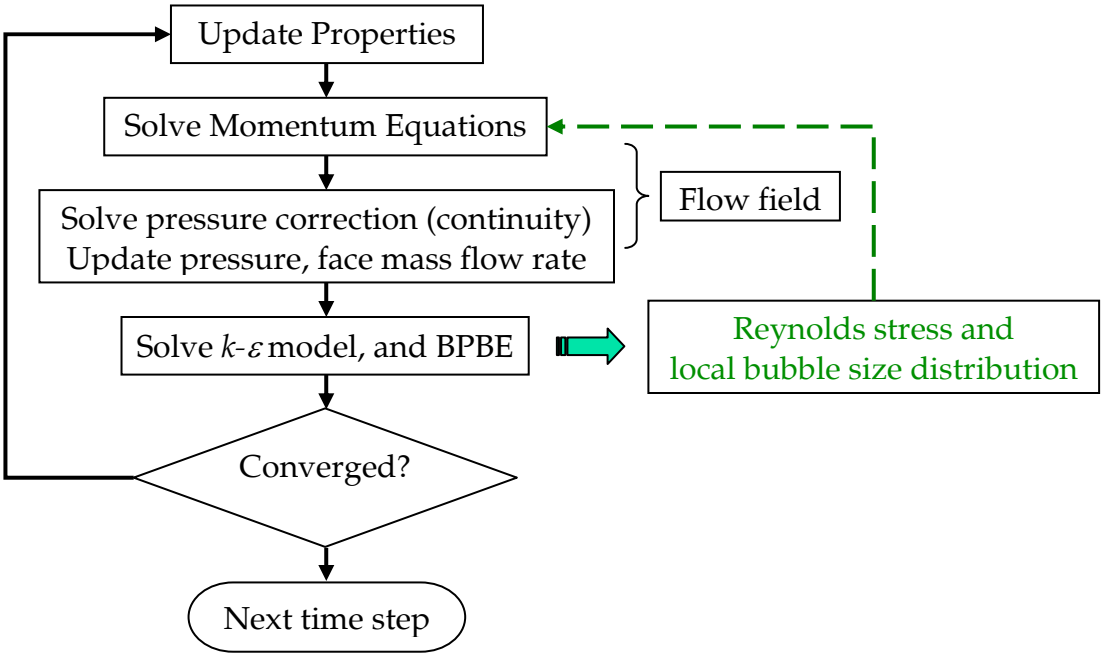

Figure 4.2 Overview of solution procedure

4.3 Boundary and Initial Conditions

Initially the column is filled with liquid (or slurry which is considered pseudo homogeneous), i.e., $\alpha_l = 1;\ \alpha_g = 0,$ up to the level that matches the static liquid height in the experiment. Above this level, the initial condition is $\alpha_l = 0;\ \alpha_g = 1$. To prevent liquid escape from the column (since no net liquid flow is used), the computational domain in the axial direction is about 100% and 50% to 80% higher than the static liquid height for two-dimensional and three-dimensional simulation, respectively. The gas is introduced at the bottom of the column where only the gas phase is allowed to pass through. Since it is impossible (and it is not necessary) to resolve the gas injectors used in the experiments (e.g., 0.33-1.32 mm diameter holes on the perforated plate) with the currently employed mesh, the gas feed is introduced uniformly over the bottom plane in the simulation, i.e., $\alpha_g = 1,\ u_g = U_g,\ u_l = 0$ at $z = 0$. No-slip condition is used at the column wall. Finally the pressure condition, i.e. the operation pressure p, is imposed on the top of the column.

The bubble diameter at the sparger (i.e., boundary condition for BPBE) is assumed to be uniform and is calculated from Miyahara's *et al.* (1983) correlation, which can be written as:

$$d_s = f\left(N_w\right)\Big/\left(g\rho_l/\sigma d_h\right)^{1/3} \tag{4.10}$$

where

$$f\left(N_w\right) = 2.9 \qquad N_w \le 1$$
$$f\left(N_w\right) = 2.9N_w^{-0.188} \qquad 1 < N_w \le 2$$
$$f\left(N_w\right) = 1.8N_w^{0.5} \qquad 2 < N_w \le 4$$
$$f\left(N_w\right) = 3.6 \qquad 4 < N_w$$
$$N_w = We/Fr^{1/2} = \frac{d_o^{1.5}U_{gh}\rho_l g^{0.5}}{\sigma}$$

The initial bubble diameter in the column (i.e., initial condition for BPBE) is assumed to be equal to the bubble diameter formed at the sparger. The initial condition

for BPBE has no effect on the simulation as long as the simulated flow field reaches pseudo-steady state.

4.4 Experimental Conditions Simulated

In order to allow a quantitative comparison with experimental data, we set the conditions for the two-dimensional axi-symmetric simulations as those used in the experiments of Kumar (1994), Degaleesan (1997) and Chen *et al.* (1999), and the conditions for the three-dimensional simulations as those used in the experiments of Chen *et al.* (1999), Ong (2003) and Shaikh (2003). The column size, operating conditions, sparger details which are needed to calculate bubble diameter at the distributor, and the corresponding mesh parameters used for two-dimensional axi-symmetric and three-dimensional simulations are listed in Table 4.6 and Table 4.7, respectively.

Table 4.6 Column size, sparger design, operating conditions and the corresponding mesh parameters in two-dimensional axi-symmetric simulations (liquid phase: water).

Column diameter D_c (cm)	Superficial gas velocity U_g (cm/s)	Static liquid height (cm)	Measured dynamic height (cm)	Sparger information		Δr (cm)	Δz (cm)
				porosity	Size of holes (mm)		
14	9.6	98	123	0.05%	0.4	0.37	1.0
19	2	104	115	0.05%	0.33	0.5	1.0
	12	96	124	0.05%	0.33	0.5	1.0
44	2	179	193	0.077%	0.7	0.5	1.0
	10	176	218	0.077%	0.7	0.5	1.0

Figure 4.3 shows a typical mesh system used for a cylindrical column in three-dimensional simulation. FLUENT 6 uses an unstructured mesh system consisting of hexahedral, tetrahedral, pyramid, and wedge cells. In the axial direction (z-direction), the grid is uniform. The grid sizes for each simulation are listed in Table 4.7.

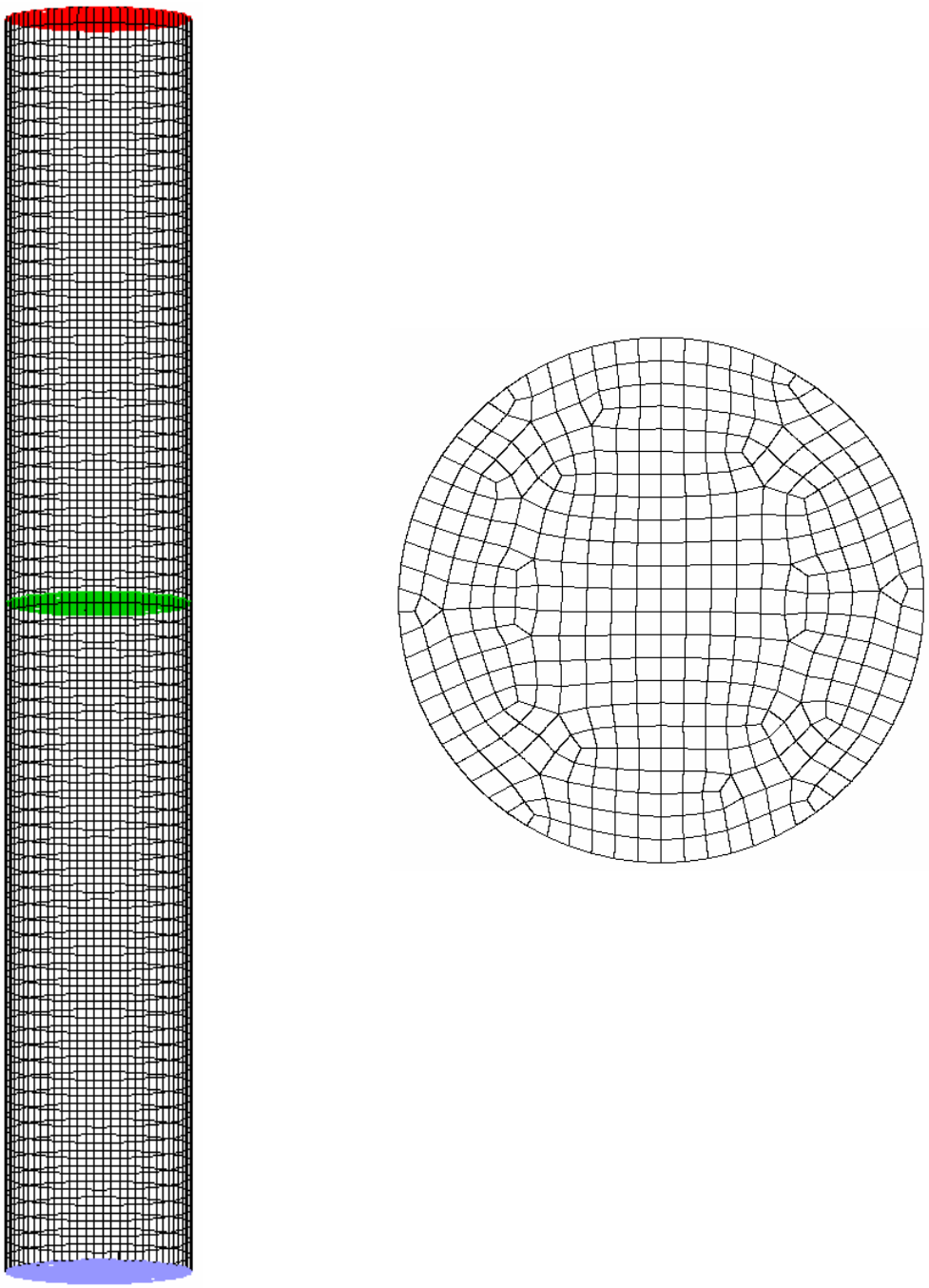

Figure 4.3 Typical numerical mesh for three dimensional simulation.

Table 4.7 Column size, operating conditions and the corresponding computational parameters in three-dimensional simulations.

D_c cm	U_g cm/s	System	P bar	Overall Gas holdup			Sparger information		Δx Δy (cm)	Δz (cm)
				Exp.	Sim.	Error %	porosity	Hole size (mm)		
16.2	8	Air-Therminol	1	0.157	0.165	5.1	0.05%	1.32	1.0	2.0
	14	Air-Therminol	1	0.229	0.218	-4.8	0.05%	1.32	1.0	2.0
16.2	30	Air-Water	1	0.267	0.284	6.4	0.15%	1.25	1.0	2.0
	30	Air-Water	4	0.326	0.325	-0.3	0.15%	1.25	1.0	2.0
	30	Air-Water	10	0.427	0.437	2.3	1.0%	1.25	1.0	2.0
44	10	Air-Water	1	0.191	0.162	-15.2	0.077%	0.7	2.0	3.0

Chapter 5
Numerical Simulation of Bubble Column Flows with Bubble Coalescence and Breakup

5.1 Experimental Techniques Used

At the Chemical Reaction Engineering Laboratory, Washington University in St. Louis, the unique CARPT-CT facilities allow non-invasive monitoring of the velocity and holdup profiles of two phases in opaque multiphase reactors on a single platform (Devanathan *et al.*, 1990; Yang *et al.*, 1992; Kumar *et al.*, 1997b; Degaleesan, 1997; Chen *et al.*, 1999).

In a set of cylindrical air-water bubble columns, Degaleesan (1997), Chen *et al.* (1999), and Ong (2003) experimentally studied the time-averaged velocity and turbulence parameters of the liquid phase by using the Computer Automated Radioactive Particle Tracking (CARPT) Technique. CARPT is a non-invasive technique for tracking the trajectory of a radioactive particle (Figure 5.1a). In CARPT, one resorts to tagging the "typical fluid element" with a gamma ray source (i.e., the liquid phase is tagged with a neutrally buoyant radioactive particle). The particle location at each time instant, $x_p(t)$, can be reconstructed from a record of the gamma-ray photon counts at a number of strategically located detectors, and a pre-established calibration between the detector counts and tracer particle location. Tracer particle trajectory (Figure 5.1b) is acquired over a very long time, typically 18-20 hours, in order to collect sufficient statistics (typically, two million or more occurrences in the column). By time differencing of

successive particle positions one obtains the instantaneous Lagrangian particle velocity, $u_p(t)$, and cross-correlation of these can be used to compute the components of the turbulent eddy diffusivity tensor (Devanathan *et al.*, 1990; Yang *et al.*, 1992; Degaleesan, 1997).

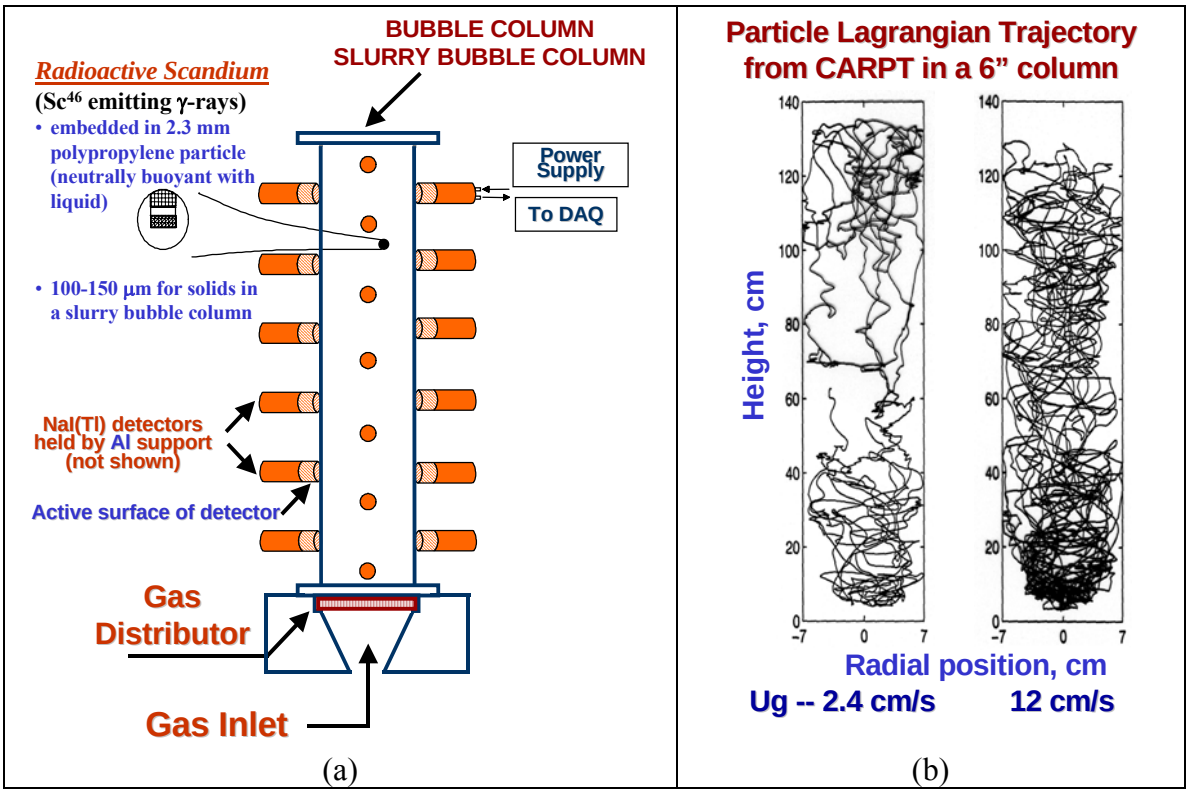

Figure 5.1 (a) Schematic diagram of the CARPT experimental setup (from Gupta, 2002) and (b) typical particle trajectory (from Degaleesan, 1997)

The time-averaged liquid velocities and turbulence parameters in the Eulerian framework, i.e. at different positions in the column, can be calculated from CARPT data provided there is sufficient data to guarantee convergent statistics (typically, two million or more occurrences in the column). The column is divided into compartments. The velocity of the particle is then assigned to that compartment which contains the mid-point of the two successive positions of the particle. In this manner instantaneous velocities are assigned to their respective compartments. Ensemble averaging is done of the velocities

in a given compartment over the number of times (repetitions) that the particle visits that compartment. The turbulence-related correlations can be calculated after the mean velocities are obtained.

In a set of cylindrical air-water and air-Therminol-glass-beads (slurry) bubble columns, Kumar (1994), Chen *et al.* (1999), Ong (2003), and Shaikh *et al.* (2003) experimentally studied the time-averaged gas holdup distribution by using Computed Tomography (CT). By placing a strong gamma-ray source in the plane of interest and a planar array of collimated scintillation detectors on the other side of the reactor, one measures attenuation in the beam of gamma radiation (Figure 5.2). The attenuation is a function of the line-averaged holdup distribution along the path of the beam. Many such "projections" are obtained at different angular orientations around the reactor. The complete set of projections is then used to back-calculate the cross-sectional distribution of densities. Since the density at any point in the cross-section is a sum of densities of individual phases weighted by their volume fractions, the cross-sectional volume fraction (holdup) distribution of a particular phase can be uniquely recovered provided only two phases are present. The total scanning time is about 2 hours, thus the scanned image provides a time-averaged cross-sectional distribution of mixture density. The results of the two-dimensional holdup distribution can be subsequently averaged azimuthally for direct comparison against a suitable simulation.

Details of the experimental setup and procedure for the particle tracking and the tomographic techniques may be found elsewhere (Devanathan *et al.*, 1990; Devanathan, 1991; Moslemian *et al.*, 1992; Yang *et al.*, 1992; Kumar *et al.*, 1995; Kumar *et al.*, 1997b; Chaouki *et al.*, 1997; Degaleesan, 1997; Roy, 2000). All the data used in this thesis for comparison with simulation came from those previous experimental studies (Kumar, 1994; Degaleesan, 1997; Chen *et al.*, 1999; Ong, 2003; Shaikh *et al.*, 2003).

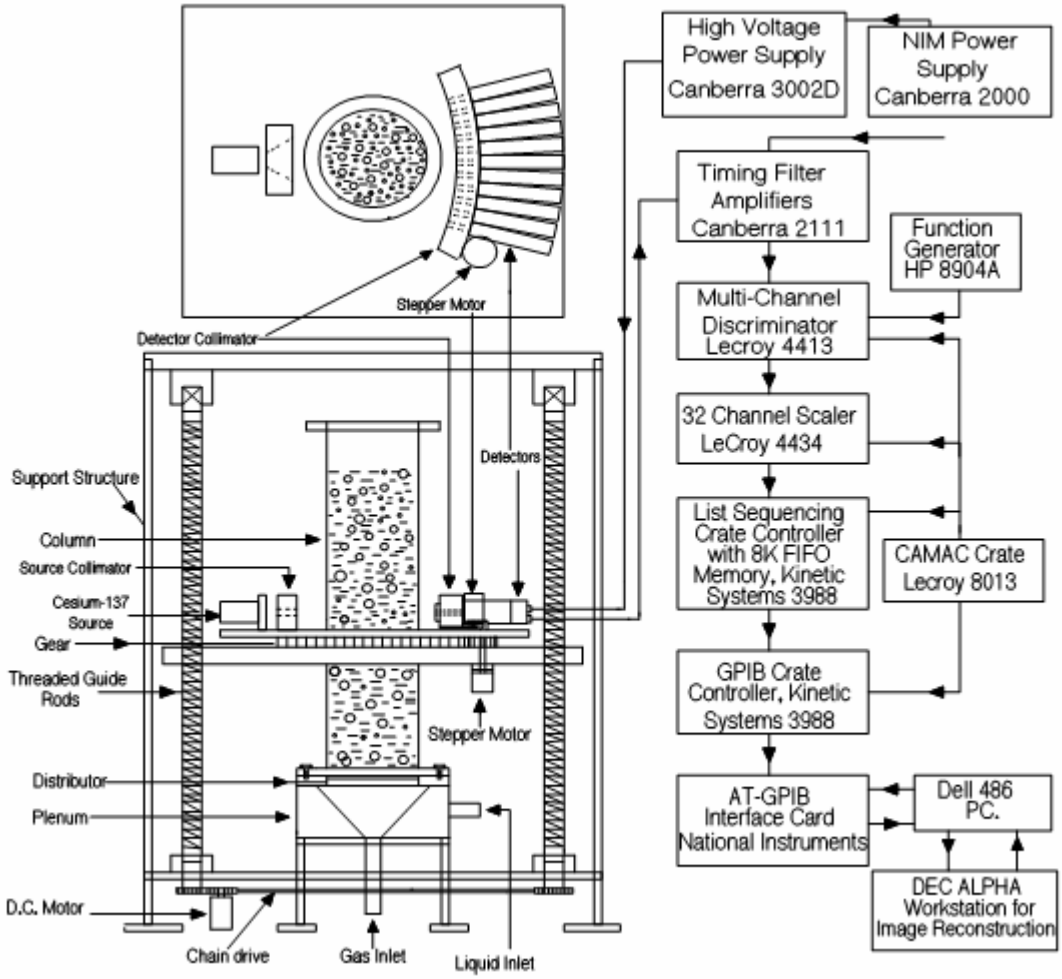

Figure 5.2 Schematic diagram of the CT setup (from Kumar, 1994).

5.2 Two-dimensional Axisymmetric Simulation

It is worth noting that the real observed bubble column flows are highly transient and turbulent with rising three-dimensional vortical bubble swarms which cause smaller bubbles and liquid to be trailed in their wakes. The flow never reaches steady-state. The axisymmetric boundary condition in 2D computations, however, causes the liquid flow to develop very quickly (5-10 s of real time) and reach its long-time "steady" pattern. Thus, the realizations of the instantaneous hydrodynamic properties cannot be captured as the instantaneous flow is never axisymmetric in reality, i.e., significant instantaneous azimuthal and radial components do exist. Besides, the time-scale of the dynamic flows

cannot be captured as well. However, the experiments had shown repeatedly (Hills, 1974; Svendsen *et al.*, 1992; Degaleesan, 1997) that, in the time-averaged sense, there is a steady axisymmetric flow pattern in a cylindrical bubble column. Therefore, it is possible that 2D axisymmetric simulation captures the essence of certain time-averaged hydrodynamic properties in bubble column flows. Since these 2D computations are so much faster to perform, we want to examine to what extent they capture the experimental evidence. Moreover, it is also important to learn the effect of different breakup and coalescence closures before one performs full 3D computations. The breakup and coalescence models implemented in the simulation are listed in Table 5.1.

Table 5.1 Implemented breakup and coalescence closures.

Case	Breakup Closure	Coalescence Closure
1	Luo and Svendsen, 1996	Chesters, 1991
2	Luo and Svendsen, 1996	Luo, 1993
3	Martínez-Bazán *et al.*, 1999a; b	Luo, 1993
4	Luo and Svendsen, 1996	Prince and Blanch, 1990

In the churn-turbulent flow regime, there are no significant gas holdup axial gradients in the fully developed region (Bukur *et al.*, 1996), which indicates that breakup and coalescence phenomena are close to equilibrium. This invariance with axial position of radial gas holdup profiles was also captured by Shollenberger *et al.* (2000), George *et al.* (2000) and Ong (2003). In contrast, the model predicted coalescence rate is about one order of magnitude higher than the predicted breakup rate calculated from the reported breakup closures.

There are a number of possible reasons for the mismatch in magnitude of model predicted breakup and coalescence rates.

1) The bubble breakup rate and daughter bubble p.d.f. measurements are done in dilute system, which may not be applicable in churn-turbulent flow regime where the gas holdup is high.

2) In this study, the energy dissipation rate obtained by the $k-\varepsilon$ model can only account for small scale energy dissipation. In other words, the predicted dissipation rate could be underpredicted. If dissipation rate, ε, increases, the model predicted breakup rate increases *linearly* with $\varepsilon^{1/3}$, the collision rate also increases *linearly* with $\varepsilon^{1/3}$, but the coalescence efficiency decreases *exponentially* with respect to $\varepsilon^{1/3}$. Thus, if the energy dissipation rate is underpredicted, then the coalescence rate is overpredicted and the breakup rate is underpredicted. In addition, as illustrated in Section 3.3.2, if bubble relative velocities difference induced collision, neglected at present, is superimposed on the turbulence induced collision, the bubble coalescence rate could decrease.

3) Moreover, the estimated breakup time scale (measured from the onset of deformation), τ_b, and coalescence time scale (measured from the instant when two bubbles collide with each other), τ_c, are higher by an order of magnitude than the time step used in simulation (~ 5 ms). Therefore, it is assumed implicitly in the simulation that the dissipation rate ε at time t to $t+\tau_b$ (or $t+\tau_c$) is the mean dissipation rate to which breaking (or coalescing) bubbles are exposed to in the turbulent flow field. Turbulence induced coalescence occurs due to eddies with sizes larger than or equal to the sizes of the colliding bubbles. The coalescence time scale however is determined by the liquid physical properties, bubble diameter and the characteristic size of the eddies that induced the collision. Therefore, the history of the dissipation rate surrounding the bubbles after this collision is not important for the coalescence rate estimation. However, this is not the case for bubble breakup rate estimation. The breakup is induced by the eddy bombardment. The bubble breakup rate is determined by all the incoming eddies reaching the bubble surface during the bubble deformation. Thus the history of dissipation rate surrounding the bubbles from the onset of bubble deformation is important. As the breakup rate is proportional to $\varepsilon^{1/3}$, due to this functional dependence the estimated breakup rate is higher if the dissipation rate history is used rather than the mean value. Using such history is only possible for Euler-

Lagrangian simulation in bubbly flow. It should be noted that we only account for the turbulence-induced coalescence. We cannot at present account for other coalescence phenomena (e.g., wake induced coalescence) due to the lack of suitable physical models. As illustrated in Section 3.3.2, if collision due to difference in bubbles relative velocities is included, the bubble coalescence rate could decrease.

If the coalescence rate is reduced by a factor of 10 in the simulation (i.e., $\Omega_B = \Omega_B^{original}$, $\Omega_C = 0.1\Omega_C^{original}$), the simulated mean bubble diameter cannot reach equilibrium in the column. Therefore, breakup rates are enhanced by a factor of 10 (i.e., $\Omega_B = 10.0\Omega_B^{original}$, $\Omega_C = \Omega_C^{original}$) in all the simulations. It is important to emphasize that this factor of ten arose as an engineering estimate and one could obtain "better" comparison against observed data by tweaking this factor. By doing so, however, one loses the predictive nature of CFD, which is one of the main purposes of numerical simulation. Thus, the factor by which breakup is multiplied is fixed at 10 for all the cases in this thesis. Most importantly, the mismatch in magnitude of available breakup and coalescence closures indicates that these closures need to be developed further.

In Figure 5.3 the computed time-and azimuthally averaged liquid axial velocity profiles, $U_z(r)$, are compared against the data obtained by CARPT for the operating conditions reported in Table 4.6. Different breakup-coalescence closures of Table 5.1 used in the computation are indicated in the legend of each figure. Wilkinson's (1991) model is used to calculate the assumed single bubble size (without BPBE implementation), which can be written as:

$$d_b = 3g^{-0.44}\sigma^{0.34}\mu_l^{0.22}\rho_l^{-0.45}\rho_g^{-0.11}U_g^{-0.02} \tag{5.1}$$

where g is gravity, σ is surface tension, μ_l is liquid phase viscosity, ρ_l and ρ_g are liquid and gas phase density, respectively, and U_g is superficial gas velocity. Thus, the simulation without BPBE remains predictive as the bubble diameter is calculated from

correlation rather than "tweaked". The compared profiles are for the middle section of the column where the mean flow is usually assumed one-dimensional.

Legend:

CARPT	Experimental data obtained via CARPT	
CT	Experimental data obtained via CT	
L-S/C	Luo and Svendsen, 1996 (Breakup)	Chesters, 1991 (Coalescence)
L-S/L	Luo and Svendsen, 1996 (Breakup)	Luo, 1993 (Coalescence)
MB/L	Martínez-Bazán *et al.*, 1999a; b (Breakup)	Luo, 1993 (Coalescence)
L-S/P-B	Luo and Svendsen, 1996 (Breakup)	Prince and Blanch, 1990 (Coalescence)
Wilkinson	Wilkinson, 1991 (Bubble Mean Diameter Correlation)	

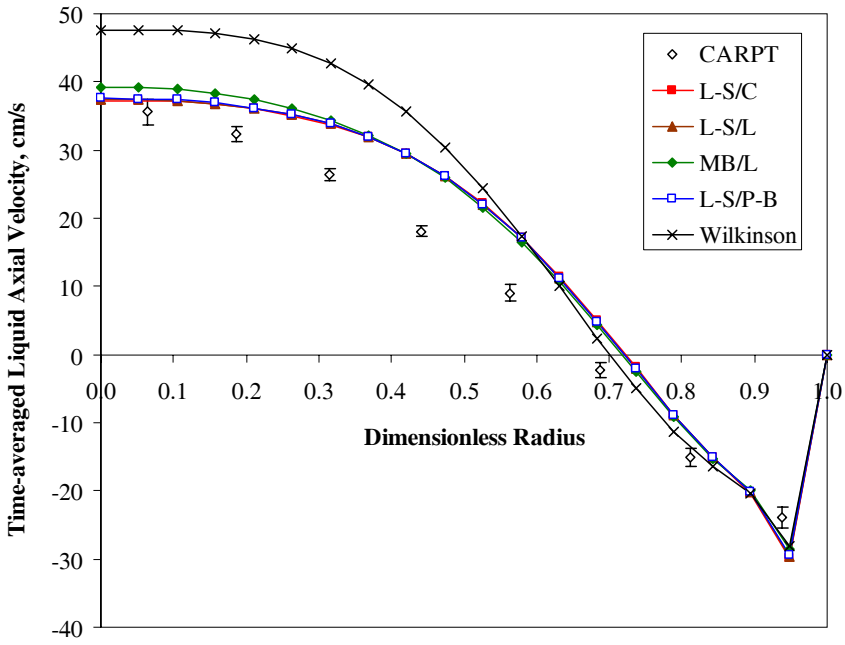

(a)

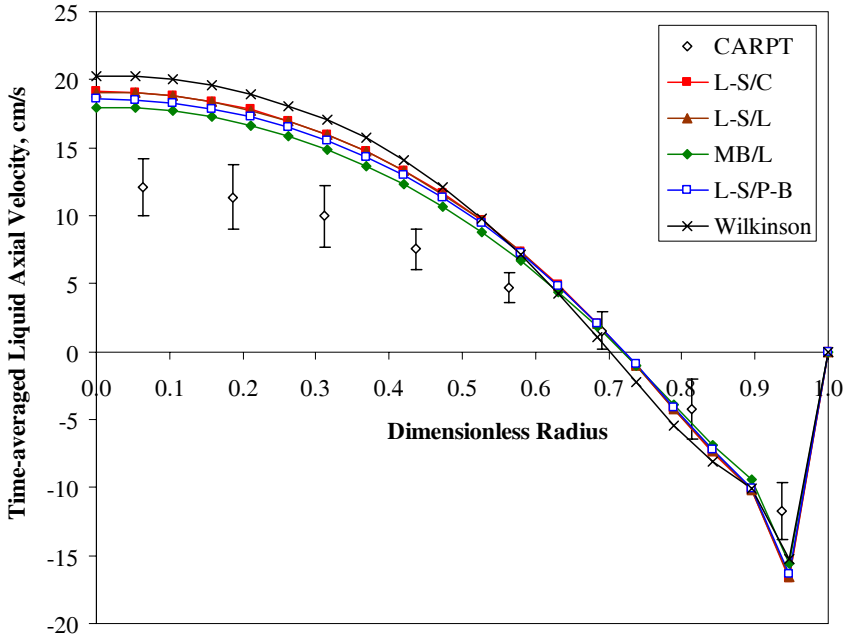
Time-averaged Liquid Axial Velocity, cm/s
Dimensionless Radius
CARPT
L-S/C
L-S/L
MB/L
L-S/P-B
Wilkinson
25
20
15
10
5
0
-5
-10
-15
-20
0.0
0.1
0.2
0.3
0.4
0.5
0.6
0.7
0.8
0.9
1.0

(b)

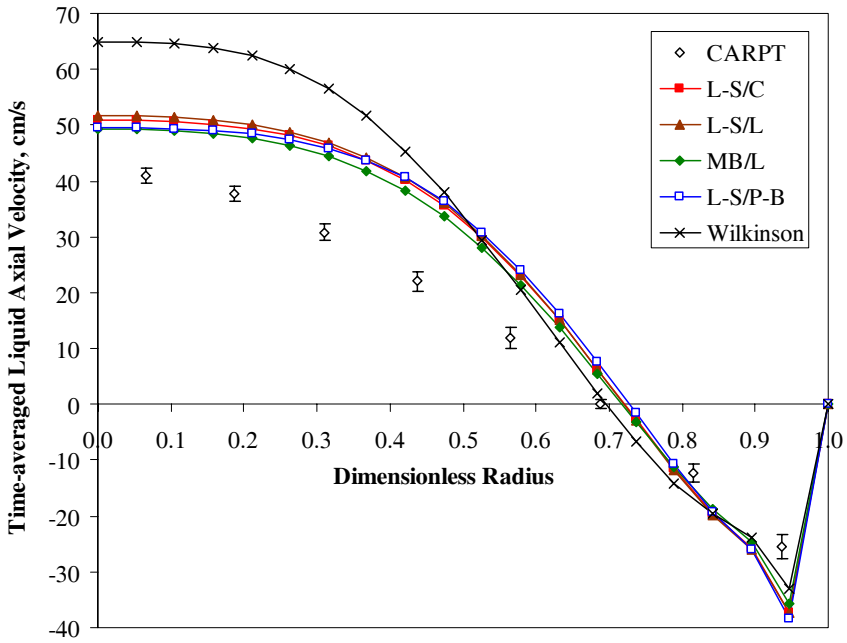
Time-averaged Liquid Axial Velocity, cm/s
Dimensionless Radius
CARPT
L-S/C
L-S/L
MB/L
L-S/P-B
Wilkinson
70
60
50
40
30
20
10
0
-10
-20
-30
-40
0.0
0.1
0.2
0.3
0.4
0.5
0.6
0.7
0.8
0.9
1.0

(c)

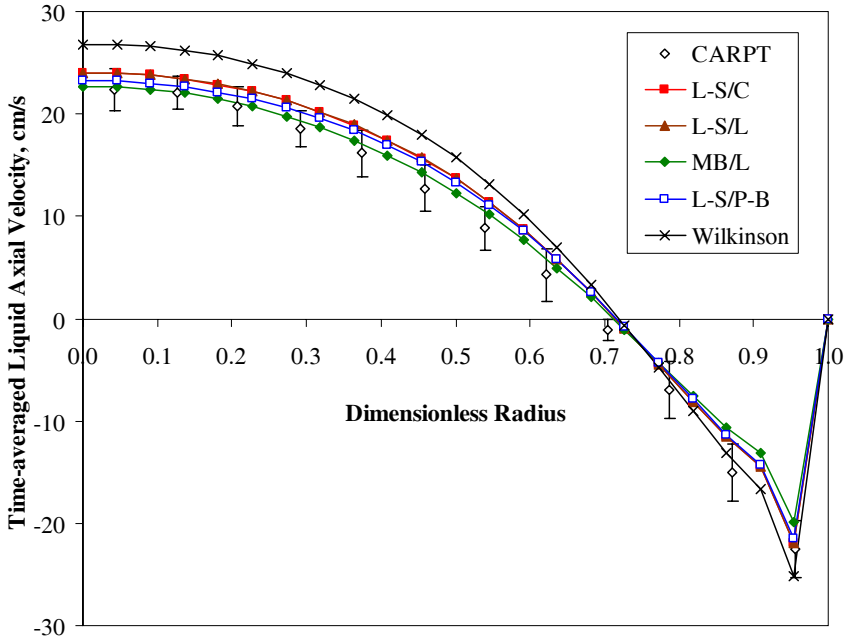

(d)

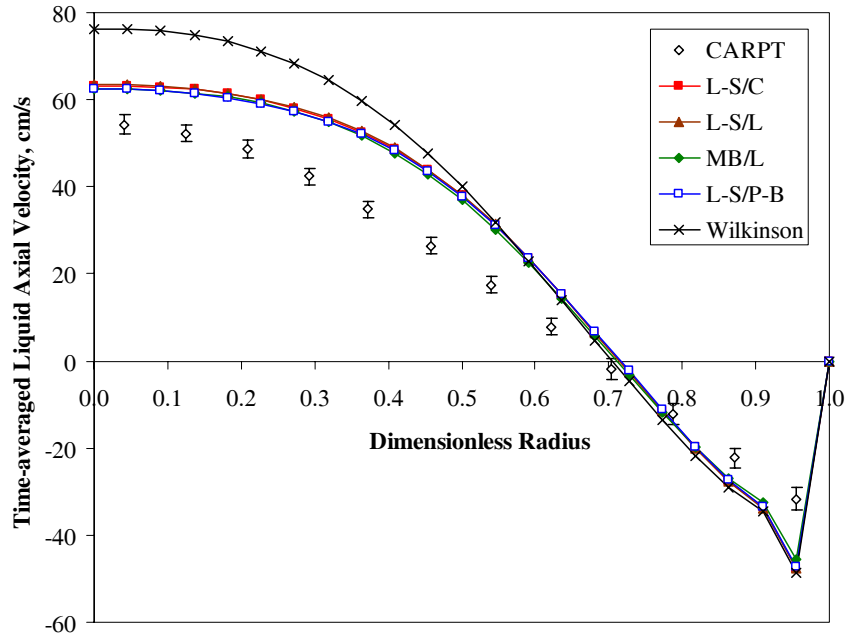

(e)

Figure 5.3 Comparison of the radial profiles of the axial liquid velocity obtained from simulations with experimental data measured by CARPT for (a) 14-cm diameter column operated at U_g = 9.6 cm/s, (b) 19-cm diameter column operated at U_g = 2.0 cm/s (c) 19-cm diameter column operated at U_g = 12.0 cm/s (d) 44-cm diameter column operated at U_g = 2.0 cm/s, (e) a 44-cm diameter column operated at U_g = 10.0 cm/s, P = 1 bar.

The general shape of the velocity profile is well captured and the discrepancy in the model predicted and CARPT-measured time-averaged axial liquid velocity diminishes as one moves radially outwards in the column. The computed time-averaged liquid velocity from the crossover point to the wall is well predicted while the experimentally observed values in the core region are overpredicted. The simulation results for large diameter column (D = 44 cm) are in better agreement with data than those for small diameter column (D = 19 cm). The observed difference between the data and predicted velocities could be due to the turbulence model (k-ε model) used in the simulation which assumes isotropic unbounded turbulence. Figure 5.3b and Figure 5.3d illustrate that, with or without bubble population balance equation implemented, the simulated liquid velocity profiles are similar in bubbly flow regime where breakup and coalescence phenomena are *not important*. In the churn-turbulent flow regime (Figure 5.3a, Figure 5.3c and Figure 5.3e) where breakup and coalescence phenomena are *important*, the liquid velocity profiles obtained from simulations with bubble population balance equation implemented are closer to data than those based on an assumed single bubble size obtained from correlation. This is especially true in the core region. However, the effect of different bubble breakup and coalescence models on the simulated liquid velocity profile is largely insignificant. In all five cases, the simulated centerline liquid velocities are over-predicted which could be due to the nature of the 2D axisymmetric simulation. As mentioned earlier, there are significant instantaneous radial and azimuthal liquid velocity components which cannot be captured in 2D axisymmetric simulation. If the pertinent physics is properly modeled, the actual instantaneous mean energy of liquid flow, which is acquired from air due to gas-liquid momentum exchange, and in reality contains contributions from axial, radial and azimuthal velocities, must be the same in 2D axisymmetric simulation which contains only contributions from the axial velocity. This implies that the axial liquid velocity in the 2D axisymmetric simulation has to be over-predicted which is what is seen in all the cases studied.

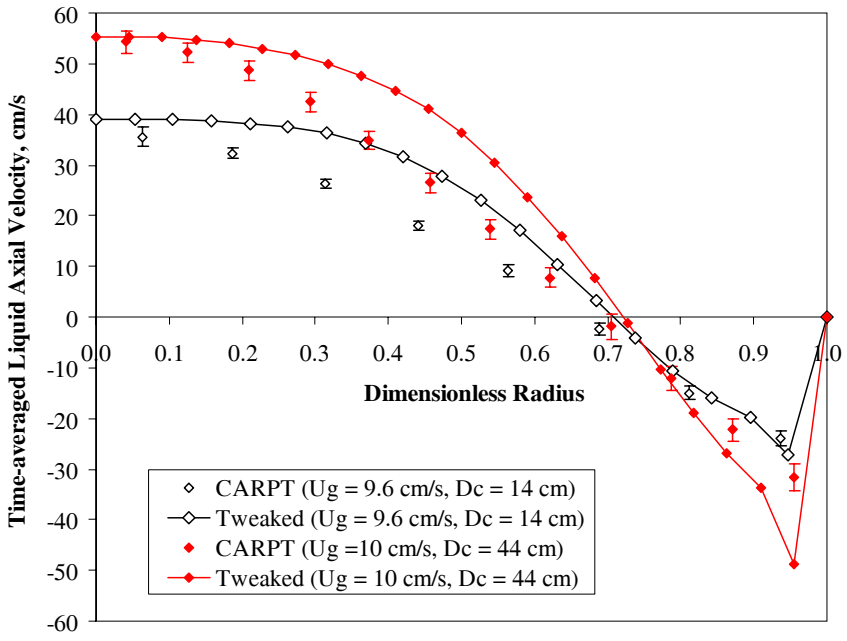

Figure 5.4 Comparison of the radial profiles of the axial liquid velocity obtained from simulations by "tweaked" mean bubble size with experimental data measured by CARPT (P = 1 bar).

One may notice that our prediction of the time-averaged liquid axial velocity that is based on the mean bubble size assumption without involving the BPBE seems worse than reported in other studies presented in the open literature. This is due to the fact that our computation based on the mean bubble size assumption remains predictive as the bubble diameter used as input is calculated from Wilkinson's (1991) correlation. In fact, one may tweak the input bubble diameter to obtain a "better" fit, as illustrated in Figure 5.4, and this adjustment of the single bubble size is what is used by other authors whether they admit to it or not. The mean bubble diameter used in Figure 5.4 is 8.5 mm, and the calculated mean bubble diameter from Wilkinson's (1991) correlation is 4.5 mm.

In Figure 5.5 the computed time-and-azimuthally averaged liquid kinetic energy (obtained by solution of the k-ε model in the simulations) profiles are compared against data obtained by CARPT. In the churn-turbulent flow regime (Figure 5.5a, Figure 5.5c and Figure 5.5e), kinetic energy profiles typically exhibit a maximum around the cross-

over point for the time-averaged liquid axial velocity, due to large gradients and large fluctuations in the liquid velocity. In the bubbly regime this effect is not very significant (because of suppressed turbulence) and the liquid turbulent kinetic energy is practically flat as a function of radius. These effects are clearly captured in the simulation results presented in Figure 5.5b and Figure 5.5d. For all the cases, the simulations with bubble population balance equation implemented give better prediction of data especially in the churn-turbulent flow regime. The impact of different breakup and coalescence closures is not significant for turbulent kinetic energy prediction. Turbulent kinetic energy obtained from the two-phase k-ε formulation arises from the turbulence microscale, while that obtained from experiments like CARPT arises from the larger scales. (For example, it is estimated that the "CARPT tracer particle" cannot respond to the turbulence fluctuations above 20-25 Hz in frequency.) It seems that a meaningful comparison of kinetic energy cannot be made as they are not of the same scale. However, as illustrated by Sanyal *et al.* (1999), in the present type of axisymmetric simulations, the "turbulent" kinetic energy (i.e., all the flow energy that is not due to the mean flow) is forced to represent the large scale turbulent kinetic energy as measured by CARPT. In other words, the 2D axisymmetric simulation imposes all the turbulence time scales smaller than the total averaging time to contribute to the turbulent kinetic energy at the "microscale" (hence, captured by the k-ε model). One also should expect a reasonable comparison of the overall kinetic energy profiles if the mean velocity profile and gas holdup profile are reasonably predicted.

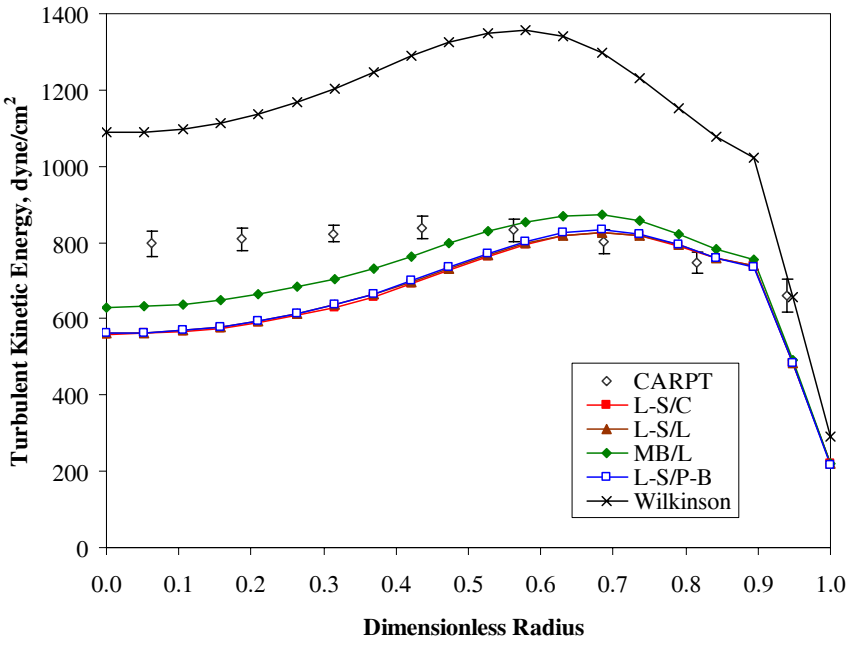
Turbulent Kinetic Energy, dyne/cm^2
Dimensionless Radius
CARPT
L-S/C
L-S/L
MB/L
L-S/P-B
Wilkinson

(a)

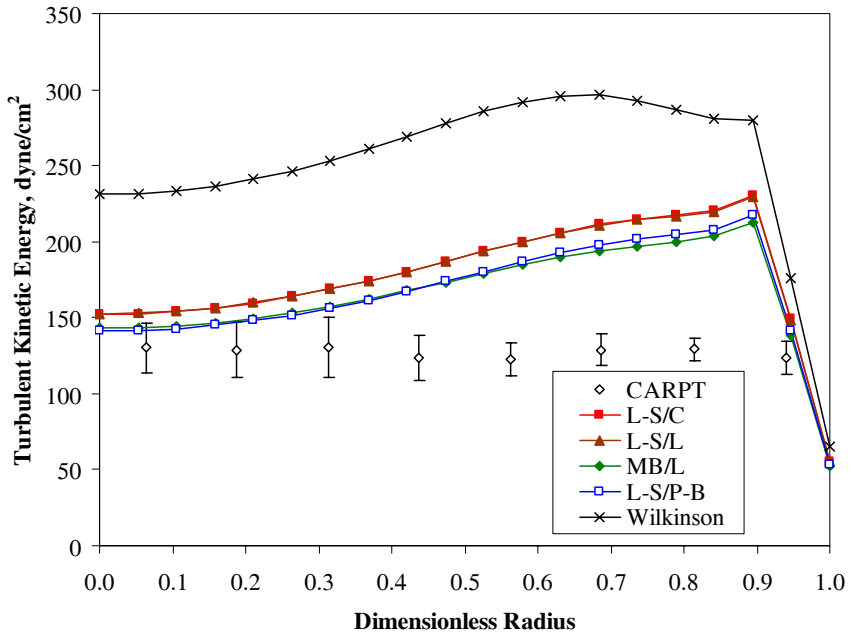
Turbulent Kinetic Energy, dyne/cm^2
Dimensionless Radius
CARPT
L-S/C
L-S/L
MB/L
L-S/P-B
Wilkinson

(b)

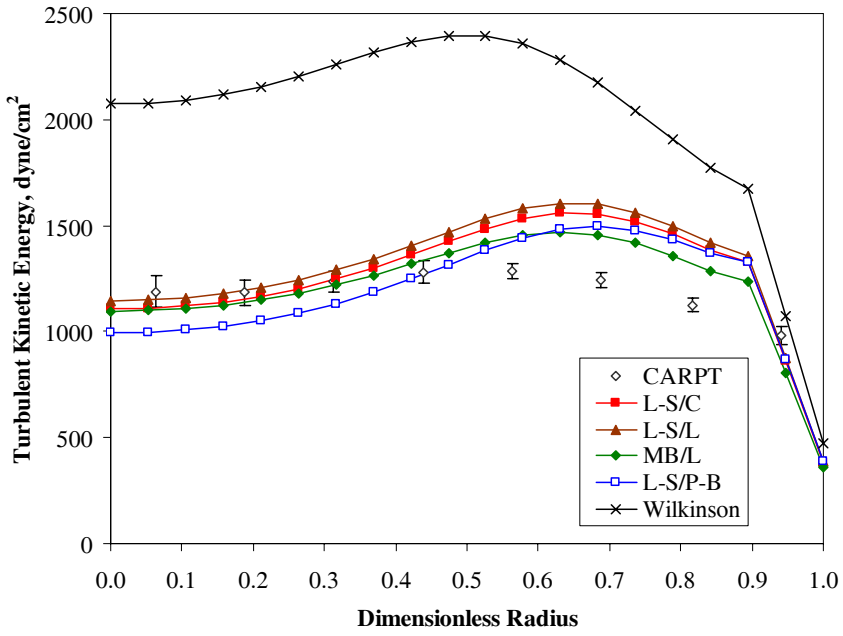
Turbulent Kinetic Energy, dyne/cm2
Dimensionless Radius
CARPT
L-S/C
L-S/L
MB/L
L-S/P-B
Wilkinson

(c)

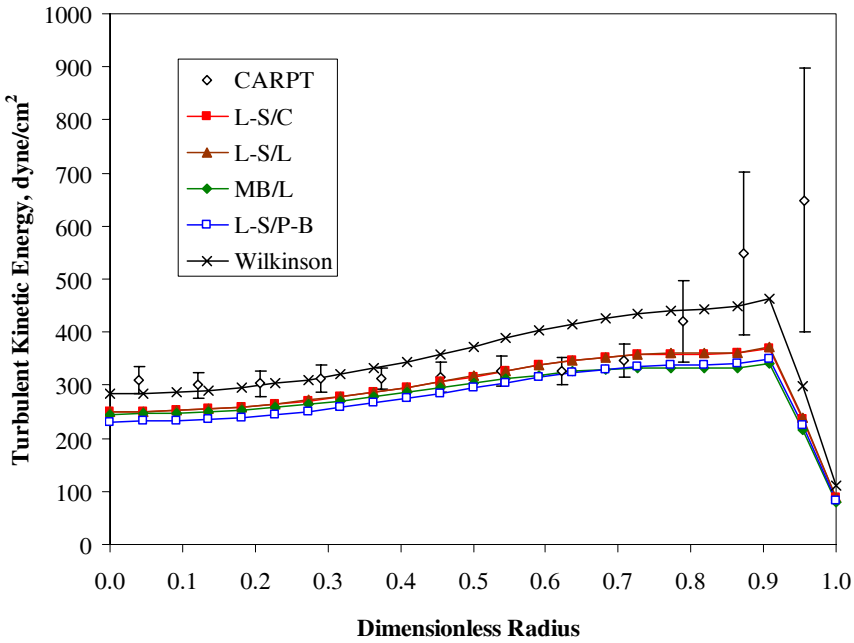
Turbulent Kinetic Energy, dyne/cm2
Dimensionless Radius
CARPT
L-S/C
L-S/L
MB/L
L-S/P-B
Wilkinson

(d)

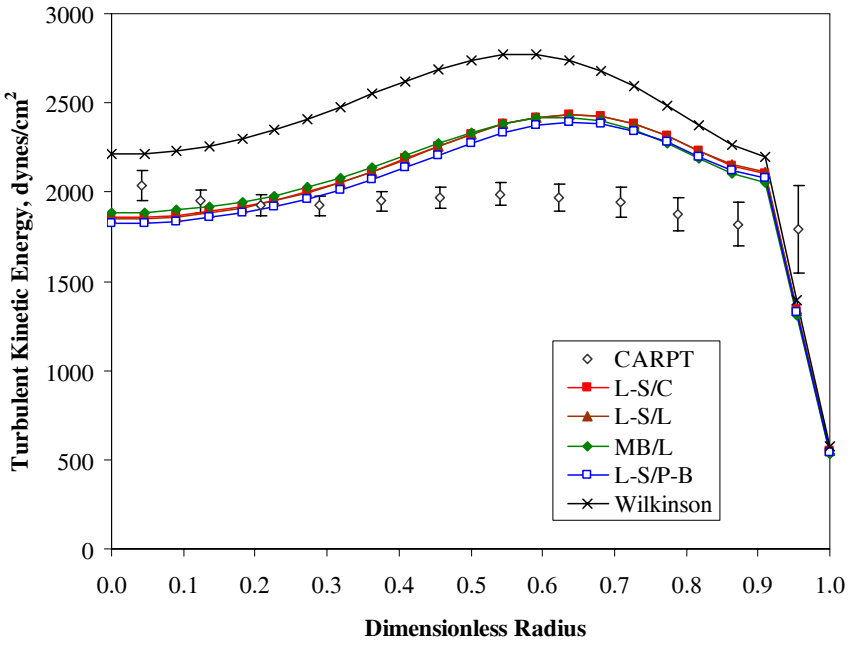

(e)

Figure 5.5 Comparison of the radial profiles of the kinetic energy obtained from simulations with experimental data measured by CARPT for (a) 14-cm diameter column operated at U_g = 9.6 cm/s, (b) 19-cm diameter column operated at U_g = 2.0 cm/s (c) 19-cm diameter column operated at U_g = 12.0 cm/s (d) 44-cm diameter column operated at U_g = 2.0 cm/s, (e) a 44-cm diameter column operated at U_g = 10.0 cm/s, P = 1 bar.

In Figure 5.6 the typical computed time-and-azimuthally averaged gas holdup profiles in churn turbulent flow regime are compared against the data obtained by Computed Tomography (CT). The assumption of cylindrical axi-symmetry in the computation prevents lateral motion of the dispersed gas phase and leads to an unrealistic gas holdup distribution wherein a maximum holdup is away from the centerline, which is also reported by other authors (e.g. Krishna *et al.*, 2000). Apparently, in order to get rid of this "hump" profile, full three-dimensional simulation may be necessary to obtain more realistic radial gas holdup profiles. The predicted gas holdup obtained from constant mean bubble size simulation is higher in the core region and lower in the wall region than that obtained from simulation with bubble population balance equation implemented. One of the reasons could be due to the fact that the local mean bubble size

in the core region is larger than in the wall region, which is captured by BPBE, as illustrated in Figure 5.7. In the core region of the bubble column, gas holdup is higher, while dissipation rate is lower, which results in larger bubbles because of the higher coalescence rate and lower breakup rate. On the other hand, gas holdup is lower while dissipation rate is higher in the wall region, which results in smaller bubbles because of the lower coalescence rate and higher breakup rate. Although the effects of breakup and coalescence closures on the predicted gas holdup, liquid axial velocity and kinetic energy are not significant, their effect on the predicted Sauter mean bubble size is apparent (see Figure 5.7).

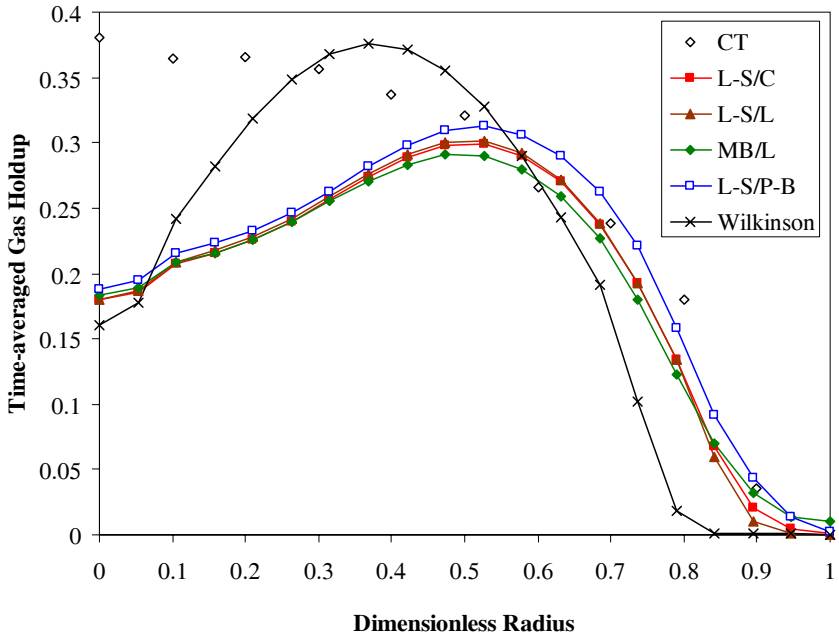

Figure 5.6 Comparison of the radial profiles of the gas holdup obtained from simulations with experimental data measured by CT for a 19-cm diameter column operated at Ug = 12.0 cm/s, P = 1 bar.

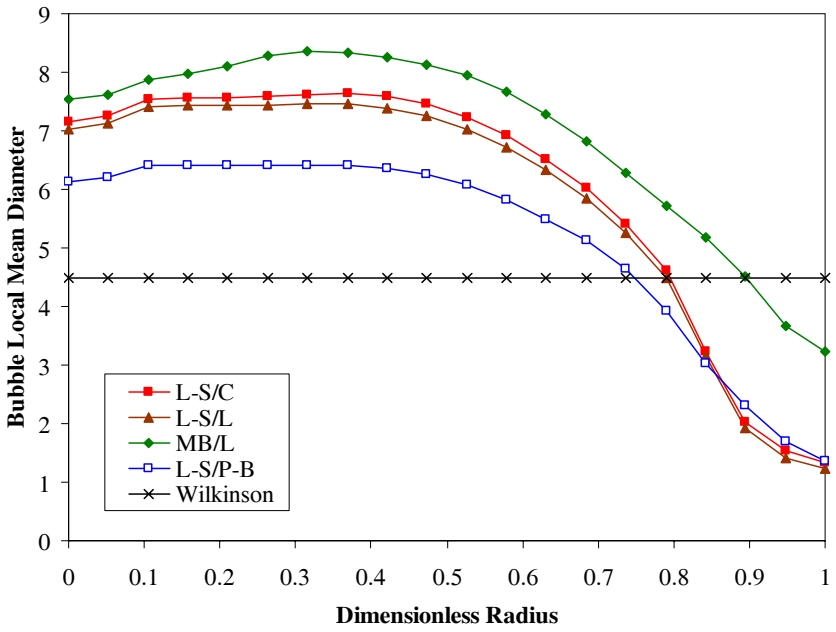

Figure 5.7 Comparison of the radial profiles of the bubble local mean diameter for a 19-cm diameter column operated at U_g = 12.0 cm/s, P = 1 bar.

In Figure 5.8, the effect of breakup and coalescence closure on the bubble volume-based p.d.f. is illustrated. It can be seen that the effect of these drastically different breakup models (Luo and Svendsen, 1996; Martínez-Bazán *et al.*, 1999a; b) are substantial. Martínez-Bazán *et al.*'s (1999a; 1999b) model produces significantly fewer smallest bubbles and more largest bubbles, and the bubble size distribution is significantly narrower as compared with Luo and Svendsen (1996). Rigorous local experiments are needed in order to test these available breakup and coalescence closures. In Figure 5.9a and Figure 5.9b the computed time averaged interfacial area density is displayed. The effect of BPBE on the computed interfacial area density, which is of great interest in bubble column industrial operation, is significant (~ 100% difference). Unfortunately, there is no experimental data available at present for the interfacial area density distribution. The significant difference between the simulated interfacial area results mentioned earlier suggests that BPBE may be necessary when gas-liquid transfer needs to be considered.

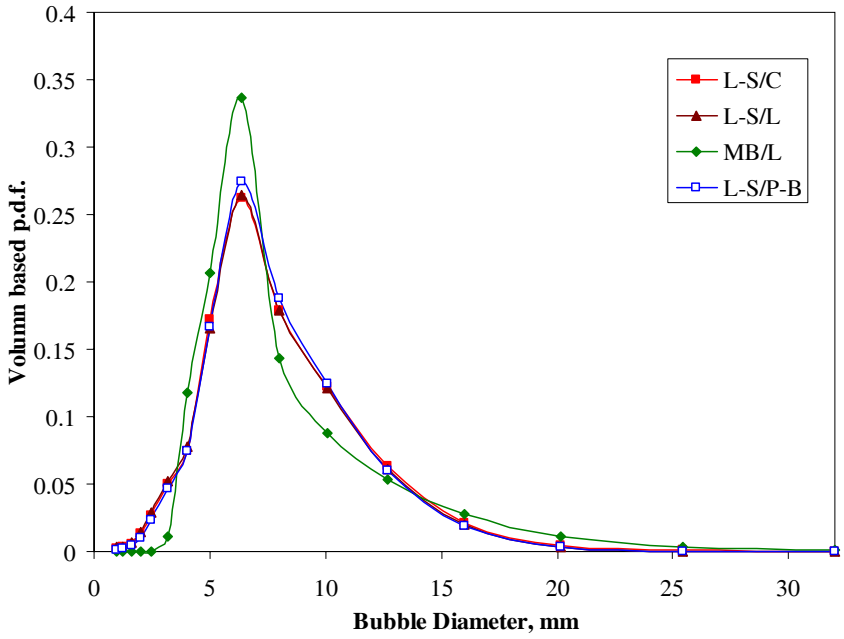

Figure 5.8 Comparison of the bubble volume-based p.d.f. for a 44-cm diameter column operated at U_g = 10.0 cm/s, P = 1 bar.

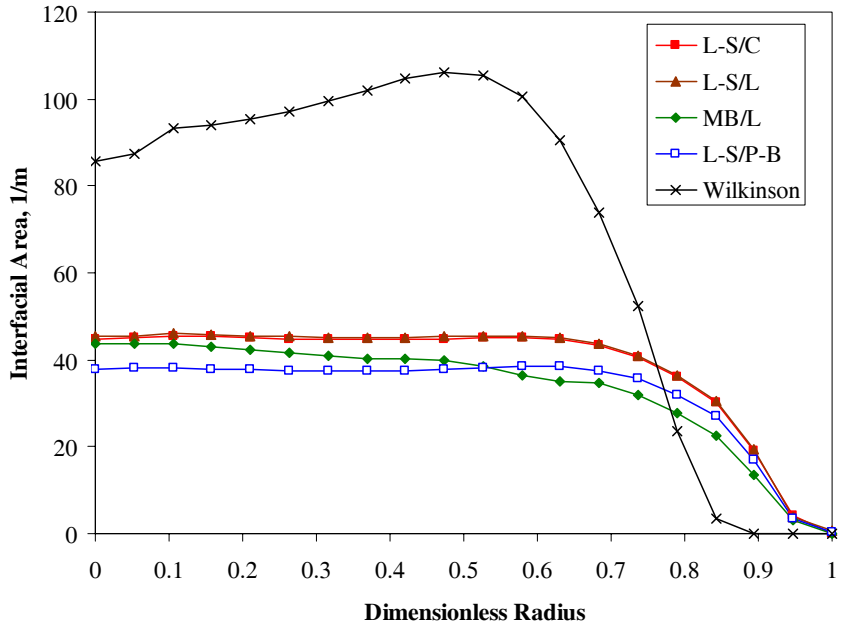

(a)

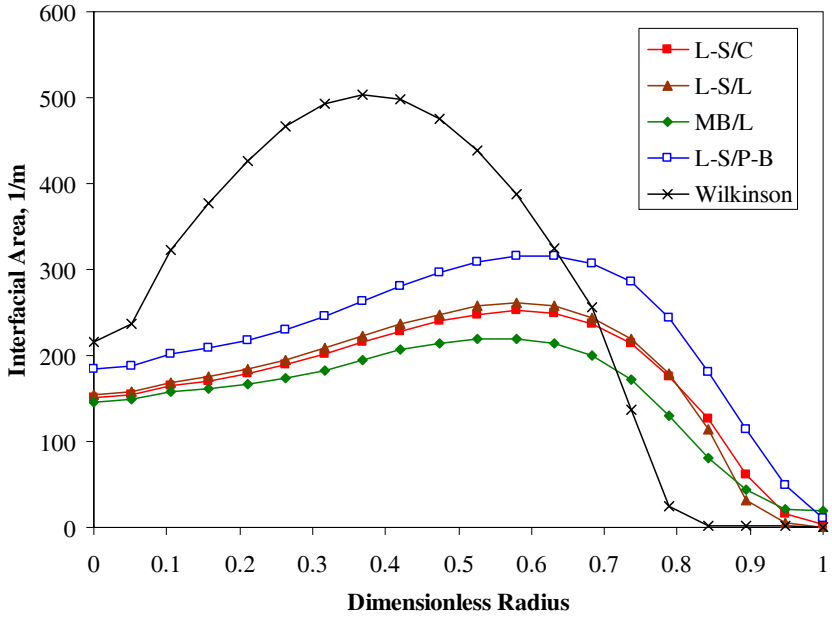

(b)

Figure 5.9 Comparison of the radial profiles of the interfacial area for a 19-cm diameter column operated at (a) U_g = 2.0 cm/s, P = 1 bar (b) U_g = 12.0 cm/s, P = 1 bar.

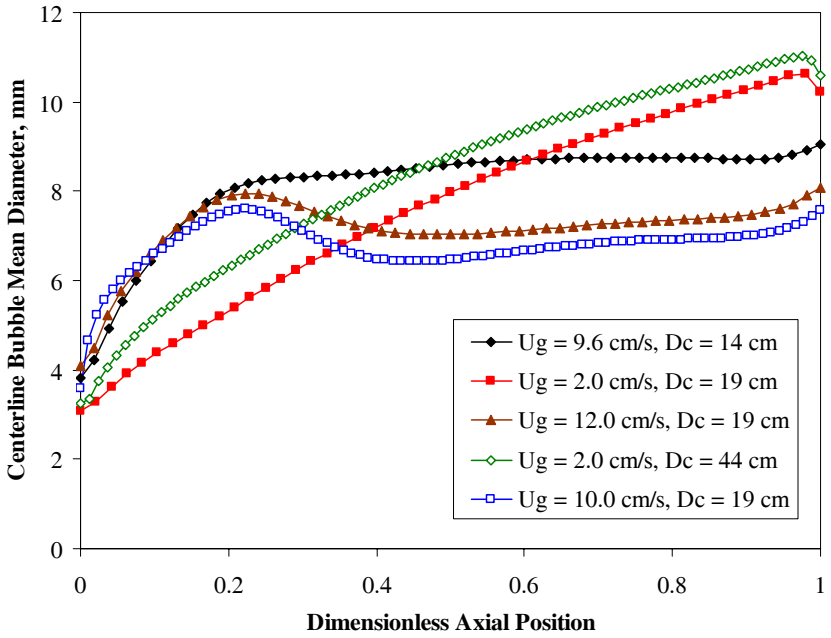

Figure 5.10 Centerline mean bubble diameter evolution.

One would expect that without well-predicted gas holdup profile, the bubble size distribution profile and Sauter mean bubble diameter cannot be accurately predicted because gas holdup is needed in the breakup and coalescence closures. However, qualitative conclusions may still be possible. In Figure 5.10 the computed evolution of the local Sauter mean bubble diameter in the centerline is illustrated. In the churn-turbulent flow regime, the Sauter mean bubble diameters are stabilized after 1 - 2 column diameters as the breakup and coalescence reach equilibrium, while this is not the case in bubbly flow. Moreover, it seems that the coalescence rates are over-predicted in the bubbly flow regime. This is expected because the bubble net birth rate is roughly proportional to $-K_1\alpha_g\varepsilon^{1/3} + K_2\varepsilon^{1/3}\exp\left(-K_3\varepsilon^{1/3}\right)\alpha_g$ according to the current breakup and coalescence models used in this work. The exponential dependence of the coalescence rate (i.e. $K_2\varepsilon^{1/3}\exp\left(-K_3\varepsilon^{1/3}\right)\alpha_g$) on the local turbulent dissipation rate leads to coalescence dominating the bubbly flow simulation. However, the current breakup and coalescence models are developed based on bubbles immersed in a highly turbulent field which may not be applicable in bubbly flow. Improved breakup and coalescence closures in bubbly flow regime need to be developed. On the other hand, as illustrated earlier, one may not need to implement BPBE in the bubbly flow regime simulation at all as the bubble size distribution is narrow and all that is needed is the prediction of mean bubble size.

In Figure 5.11a and Figure 5.11b, the evolution of cross-sectional bubble class volume based p.d.f. is presented. For churn-turbulent flow (U_g = 9.6 and 10 cm/s), the bubble class distribution stabilized after 1.5 - 3 column diameter. It seems that the bubble size distribution in bigger diameter column needs more height to reach a stable profile (60 cm in 44-cm diameter column and 40 cm in 14-cm diameter column for U_g about 10 cm/s), however, the effect is not significant.

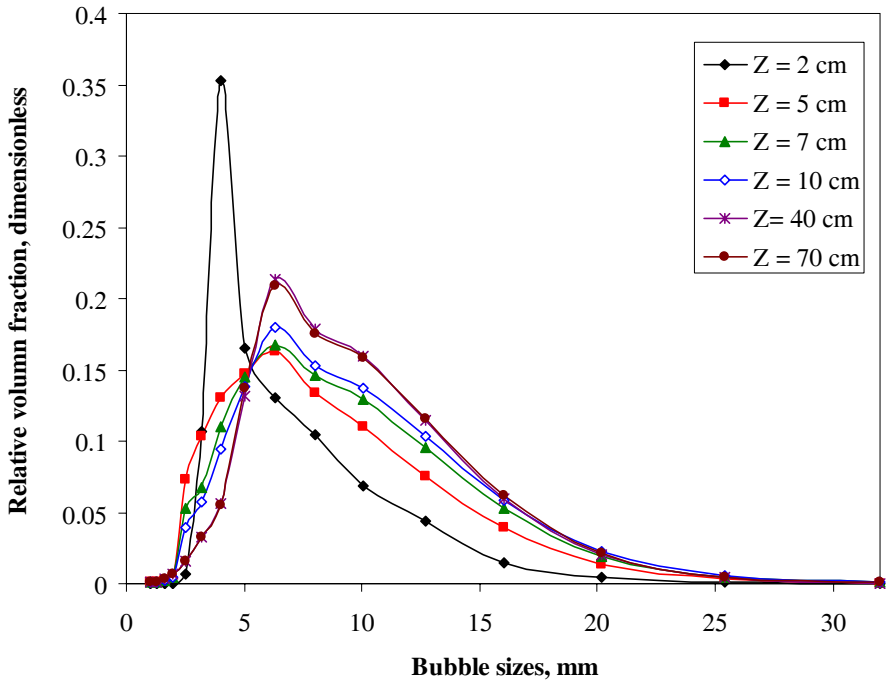

(a)

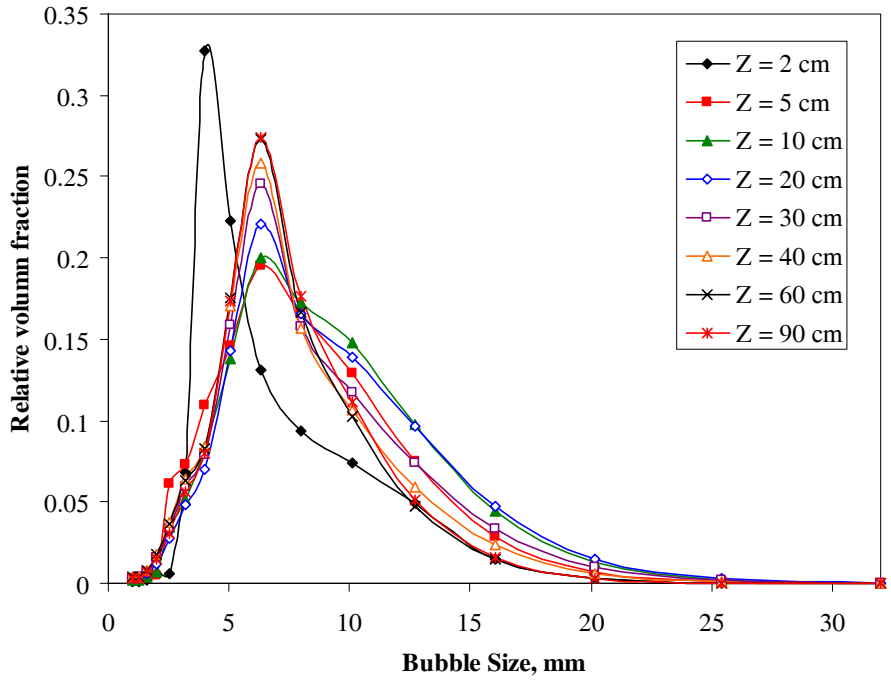

(b)

Figure 5.11 Bubble size distribution evolution along column elevation in (a) 14-cm diameter column operated at U_g = 9.6 cm/s, P = 1 bar (b) 44-cm diameter column operated at U_g = 10 cm/s, P = 1 bar

5.2.1 Summary

Reasonable agreement in trend was obtained between the experimental data and two-dimensional axisymmetric simulations for the time-averaged axial liquid velocity profiles, as well as for the kinetic energy profiles. It is found that the model predicted coalescence rate and breakup rate are out of balance by an order of magnitude (the former being the larger). To match experimental evidence the breakup rate was increased by a factor of ten. The unrealistic time-averaged gas holdup profiles arise due to the nature of two-dimensional axisymmetric simulations and suggest that full three-dimensional simulation is needed. Better agreement with data is obtained with the Bubble Population Balance Equation (BPBE) implemented, especially in the churn-turbulent flow regime, compared with the simulation using a constant mean bubble size. The difference in predicted interfacial area densities, with and without BPBE implemented, is significant. The choice of current available bubble breakup and coalescence closures does not have significant impact on the simulated results. BPBE is necessary for churn-turbulent flow simulation when interfacial area density information is important.

5.3 Three-Dimensional Simulation

From two-dimensional axisymmetric simulation, it is found that the choice of current available bubble breakup and coalescence closures does not have significant impact on the simulated results. Therefore, in the following investigations, only Luo and Svendsen's (1996) breakup and Luo's (1993) coalescence model are implemented.

During this stage of simulation, the level of the interface is monitored. An indication of the quasi-steady state is a dynamically stabilized interface. We also monitor the velocities, both for gas and liquid phase, at some representative points in the column, as indications of flow development. Generally it takes about 60 - 100 seconds for the simulation to reach the quasi-steady state depending on the superficial gas velocity as well as the diameter of the column. Once the fully developed, quasi-steady state is

reached, the time-averaged quantities are calculated. In all simulations the velocity and gas holdup fields are sampled every 0.05 - 0.1 second. To ensure the convergence of the averaged quantities the averaging processes are performed for 80 - 120 seconds. The spatial averaging is then performed along the vertical direction within the middle sections of the column.

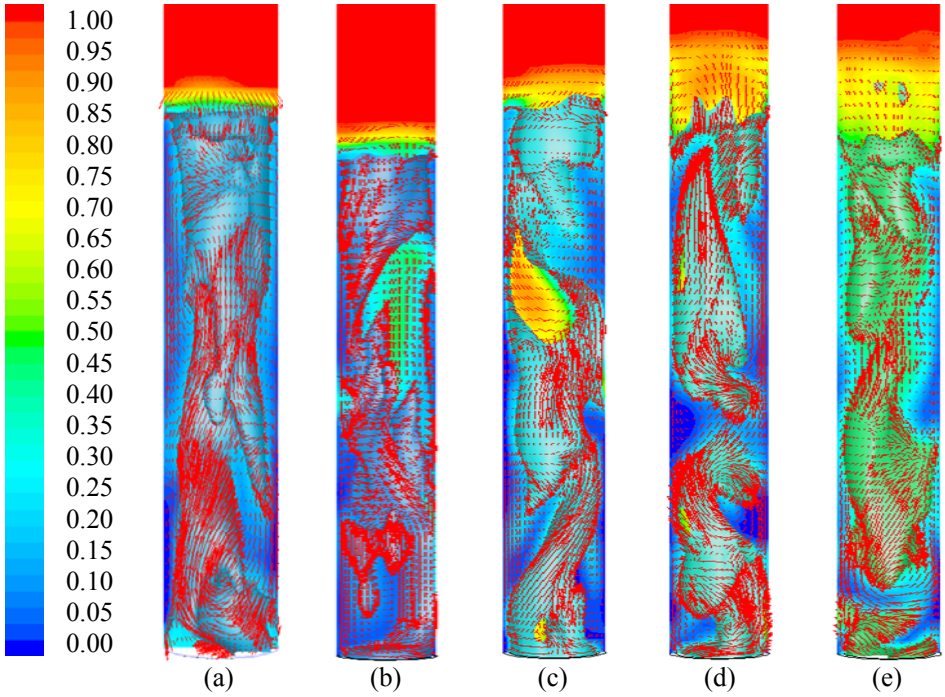

Figure 5.12 The instantaneous iso-surfaces of the gas holdup, α, in various bubble columns: (a) α = 0.2, U_g = 10.0 cm/s, (b) α = 0.13, U_g = 14.0 cm/s, (c) α = 0.28, U_g = 30.0 cm/s, P = 1 bar, (d) α = 0.35, U_g = 30.0 cm/s, P = 4 bar, (e) α = 0.44, U_g = 30.0 cm/s, P = 10 bar

Gas-liquid flow in bubble columns is highly transient and turbulent. Figure 5.12 shows the instantaneous iso-surfaces of the gas volume fraction in columns of different diameters and operated at different superficial gas velocities and/or operation pressure. The plots show the three-dimensional spiral structures and transient pockets of high gas volume fraction mixtures rising up continuously in the center region of the column, carrying the surrounding liquid phase upward at higher speeds. Figure 5.13 illustrates

typical simulated local gas holdup and liquid axial velocity time series. It can be seen that while the flow is quite chaotic the simulated gas holdup and liquid axial velocity oscillation is in-phase. The numerical predictions are further compared quantitatively with the experimental data.

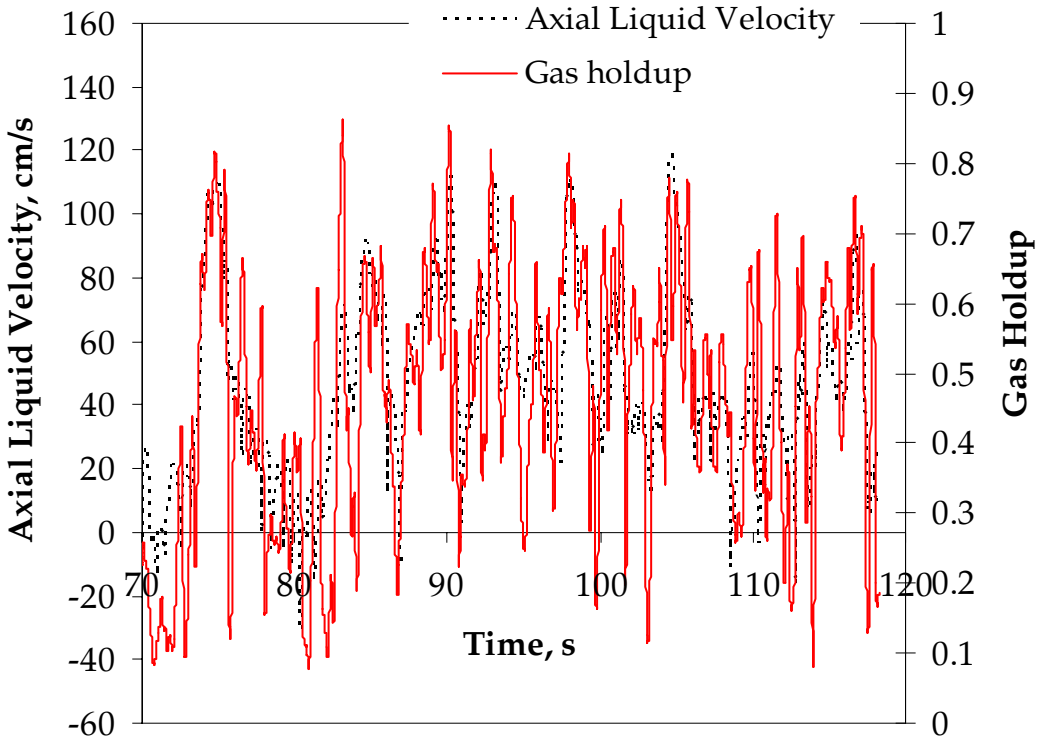

Figure 5.13 Typical simulated gas holdup and liquid axial velocity time series (D_C= 44 cm, U_g = 10.0 cm/s, P = 1 bar)

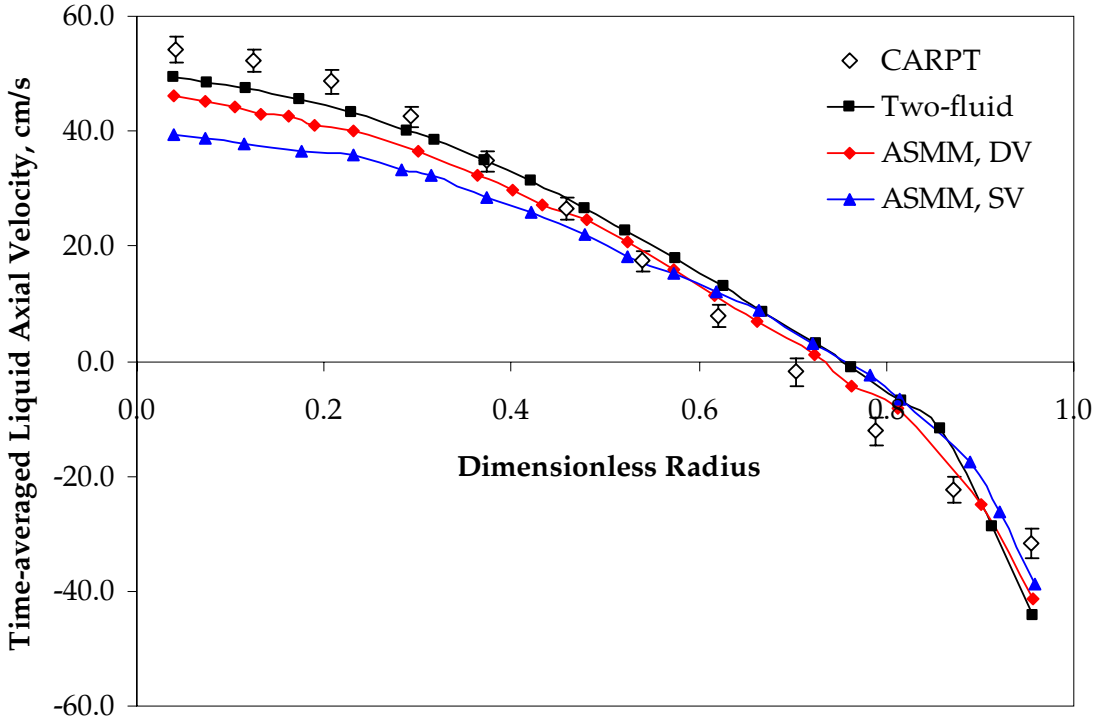

(a)

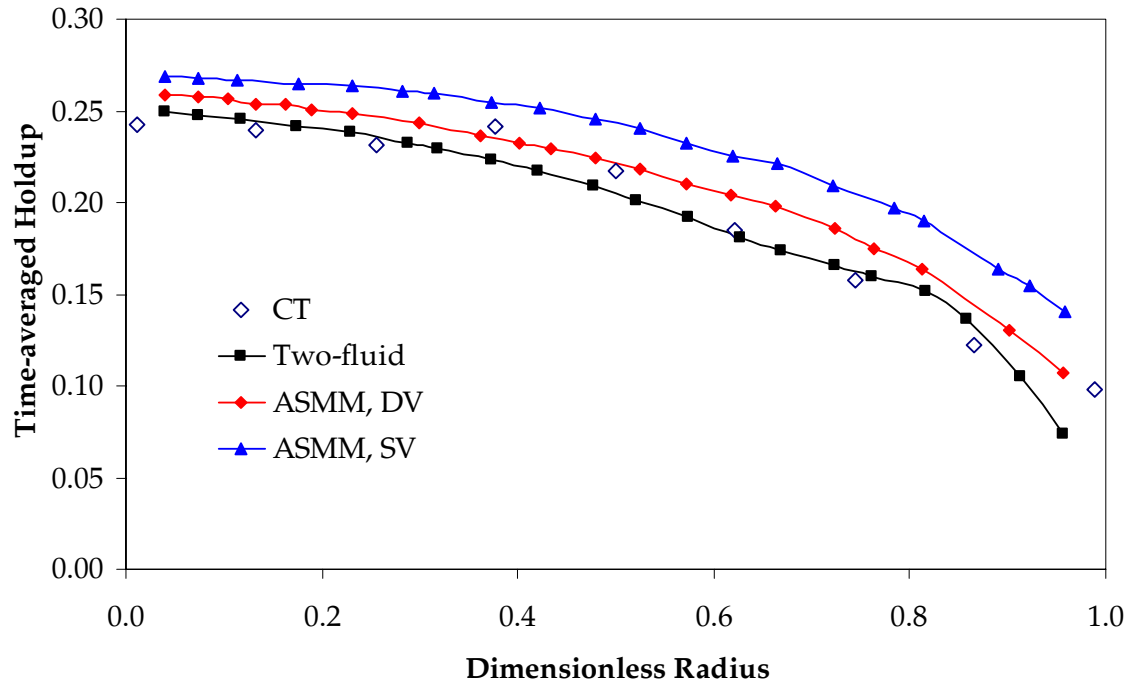

(b)

Figure 5.14 Comparison of time-averaged (a) axial liquid velocity and (b) gas holdup distribution (D_C= 44 cm, U_g = 10.0 cm/s, P = 1 bar)

Figure 5.14 shows the comparison of the simulated and experimental time-and-azimuthally averaged axial liquid (water) velocity profiles and gas holdup profile of a 44-cm diameter column at $U_g = 10\ cm/s$ superficial gas velocity. The simulated results are axially averaged in the fully developed region (from z = 89 cm to 170 cm). Three types of models (closure implementations) mentioned earlier are implemented: 1) BPBE in two-fluid model with velocities of all bubbles assumed to be locally equal to gas phase ensemble local averaged velocity; 2) BPBE in ASMM with velocities of all bubbles assumed to be locally equal to gas phase ensemble local averaged velocity (ASMM, SV); and 3) BPBE in ASMM with N+1 phases such that different size bubbles have different local velocity calculated from the ASMM (ASMM, DV). It should be noted that we only account for the turbulence-induced coalescence in this work because the turbulent induced coalescence efficiency model may not be applicable. As illustrated in Section 3.3.2, if bubble relative velocities difference induced collision is included, the bubble coalescence rate could decrease.

The simulated profiles are compared to data for the middle section of the column where the mean flow is one-dimensional. The time-and-azimuthally-averaged gas holdup profile and liquid axial velocity profile are well predicted for all three types of implementations, especially with closure 1 and 3. The choice of the multiphase flow model and of population balance closures do not have a significant effect on the simulated results as illustrated in Figure 5.14. Gas holdup radial profile prediction with closure type 3 (bubbles with different velocities in ASMM) is a little lower and closer to the observed CT data than that of closure type 2 (bubbles with identical velocity in ASMM). Time-averaged liquid velocity radial profile prediction with closure type 3 is a little steeper and closer to the CARPT data than that with closure type 2. The effect of the choice of population balance closure is not significant. Besides, it is easier to implement different drag laws and pressure effects in the two-fluid model. Therefore, in what follows, only the results of the two-fluid model are presented.

Figure 5.15 shows the comparison of the effect of BPBE on the time-averaged gas holdup and liquid velocity profile prediction. Euler-Euler two-fluid model framework is used. Wilkinson's (1991) model is used to calculate the assumed single bubble size ($d_B = 4.5$ mm). The shape of the predicted gas holdup and liquid axial velocity profile via assumed mean bubble diameter is flatter than the experimental data and the simulated results obtained from simulation with BPBE implemented. The predicted gas holdup profile with single mean bubble diameter becomes worse as one moves towards the wall region, and the liquid axial velocity profile becomes worse as one moves towards the core region. Previous investigations (e.g. Krishna *et al.*, 2000) also shown that the gas holdup and liquid axial velocity profile cannot be predicted well simultaneously by two-fluid model with assumed mean bubble diameter.

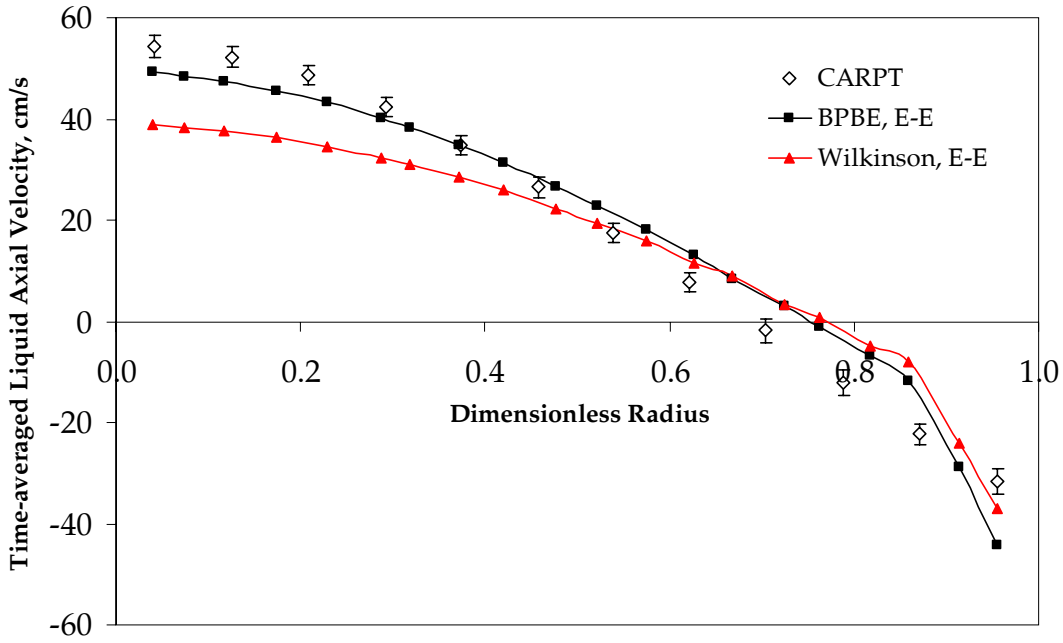

(a)

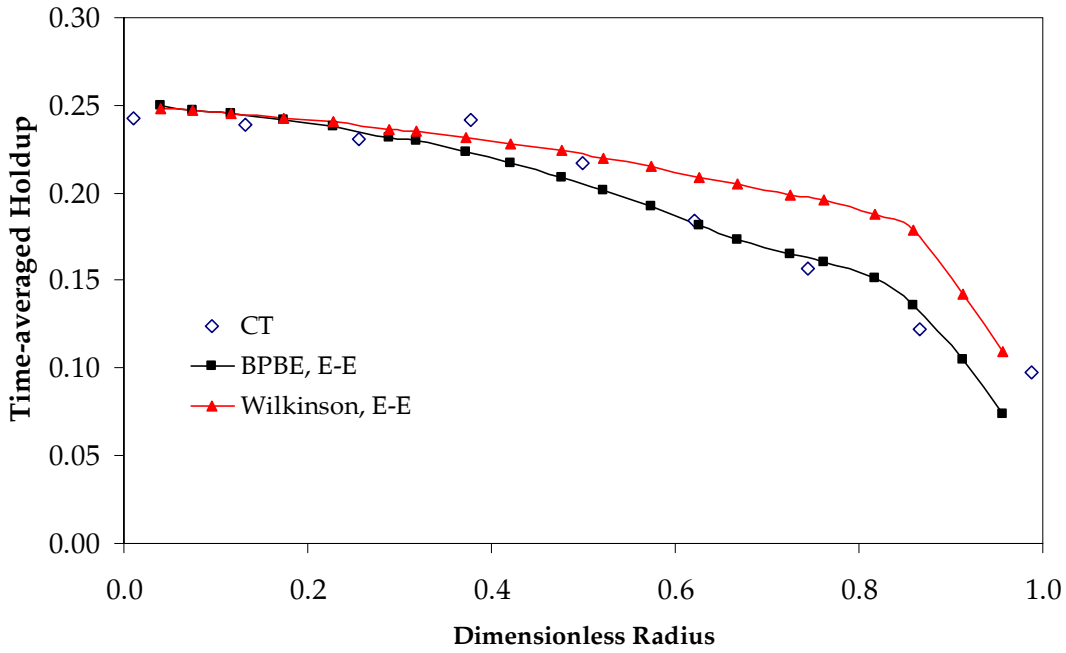

(b)

Figure 5.15 Effect of BPBE on the prediction of (a) axial liquid velocity and (b) gas holdup distribution for a 44-cm diameter column operated at Ug = 10.0 cm/s, P = 1 bar.

In the open literature, the simulated liquid axial velocity radial profiles are normally shown without being given exact axial locations, and are believed to reach a plateau in the fully developed region. For two-dimensional axisymmetric simulation, such perfectly flat plateau does exist as illustrated in Figure 5.16a. However, such plateau is not found in three dimensional simulation. Moreover, the liquid axial velocity evolution trend obtained from 2D and 3D simulation are significantly different. Before reaching the plateau, the liquid axial velocity obtained from 2D simulation exhibits a strong overshoot which was not observed experimentally (Degaleesan, 1997), while the trend obtained from 3D simulation qualitatively agrees with the experimental observations (e.g. Figure 5.17). The 2D simulation overpredicted liquid axial velocity at the centerline in the fully developed region by about 5% and 3D simulation underpredicted it by about 5%. As mentioned earlier in previous section, the 2D axi-symmetric simulation causes the liquid flow to develop very quickly (5-10 s of real time)

and reach its long-time "steady" pattern without lateral motion. Thus the momentum carried by gas phase can be transferred in axial direction only. In addition, the gas holdup predicted by 2D axi-symmetric simulation is higher in the center region, and lower in the wall region, than that predicted by 3D simulation. These two factors (momentum transfer and buoyancy) result in higher liquid axial velocity prediction than obtained in 3D simulation. Figure 5.16b illustrates the time-averaged liquid axial velocity profile evolution in the fully developed region obtained from the 3D simulation. The variation is not significant (around ±5%), while the trend is apparent. Similarly for the simulated gas holdup profile, there is small variation (around ±5%) at different axial locations in the fully developed region, as illustrated in Figure 5.18.

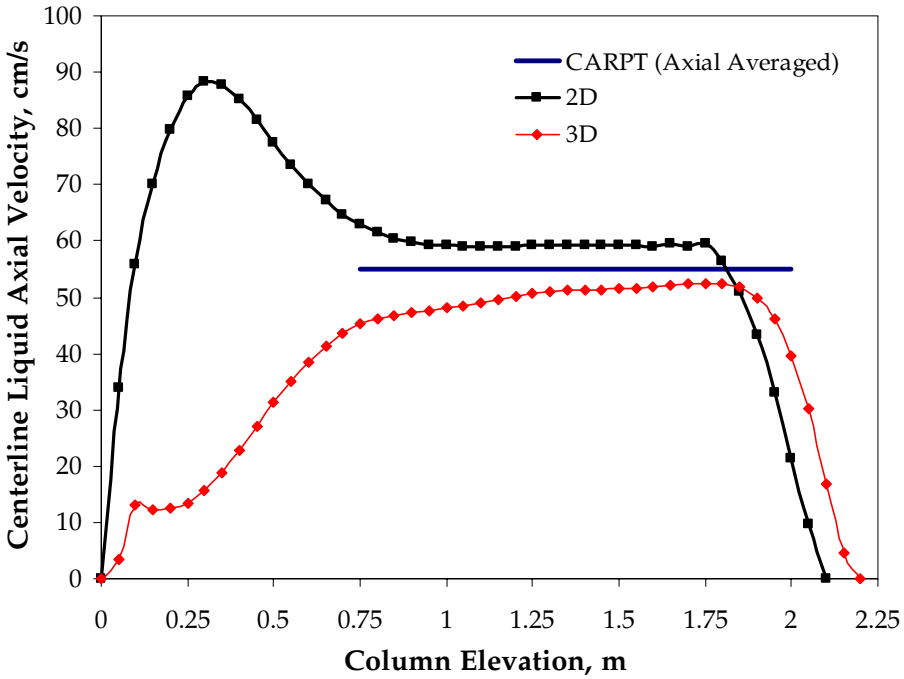

(a)

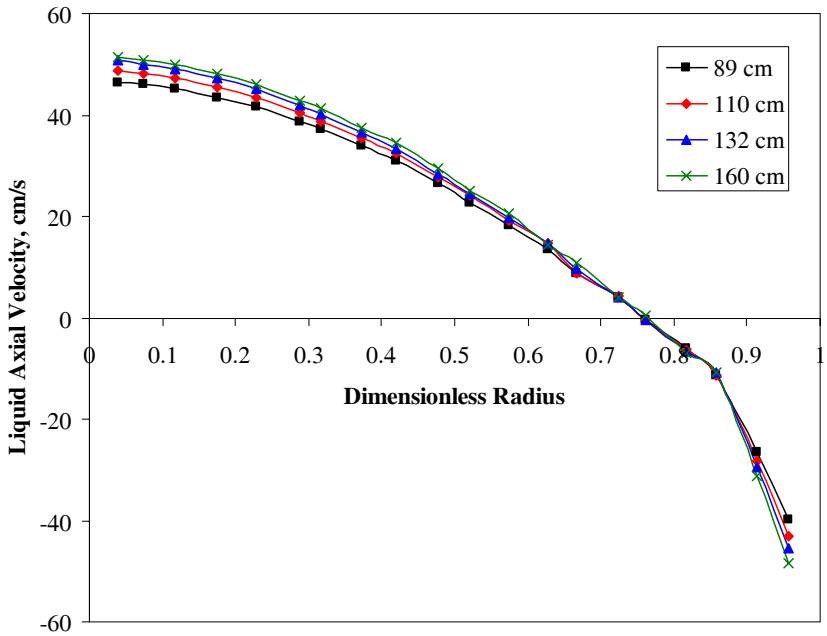

(b)

Figure 5.16 Time-averaged liquid axial velocity profile evolution

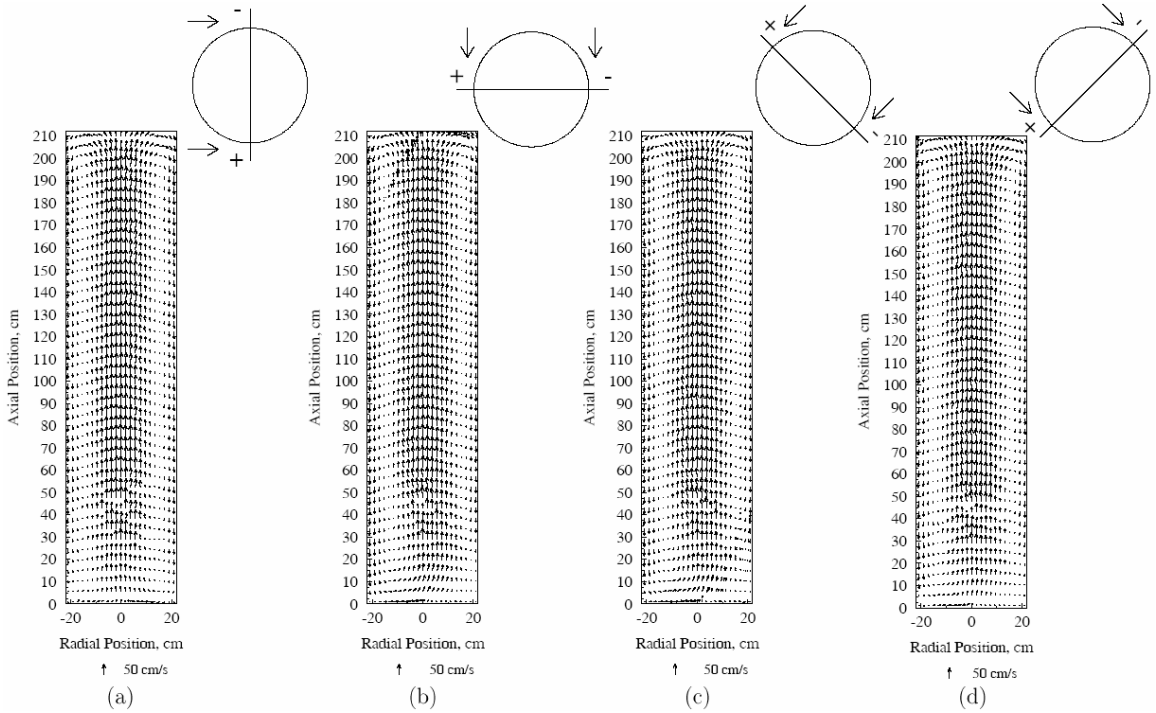

Figure 5.17 Velocity vector plot for D_C = 44 cm, U_g = 10.0 cm/s, P = 1 bar (from Degaleesan, 1997)

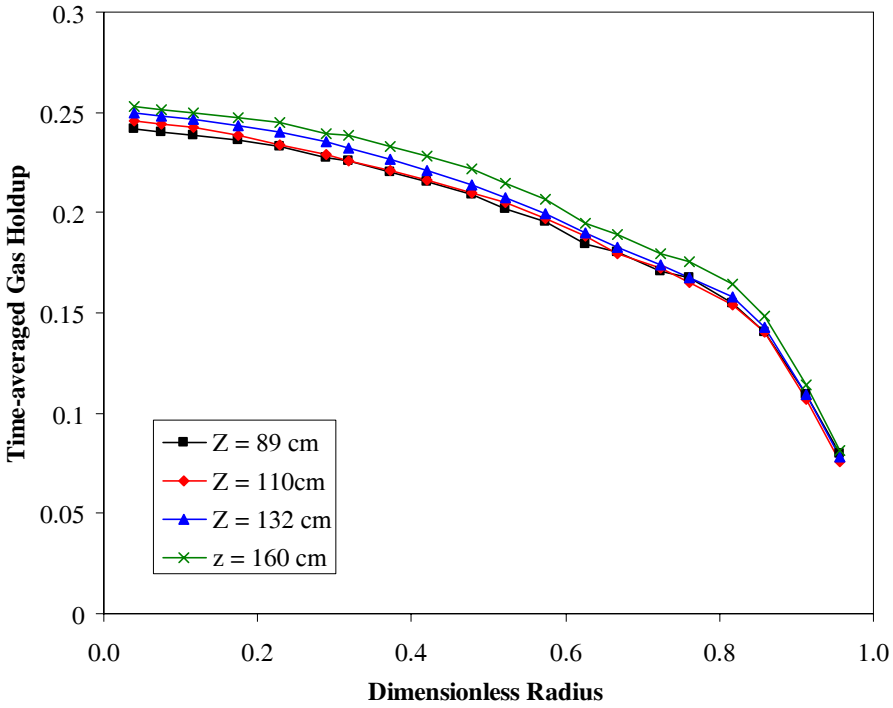

Figure 5.18 Time-averaged gas holdup profile evolution

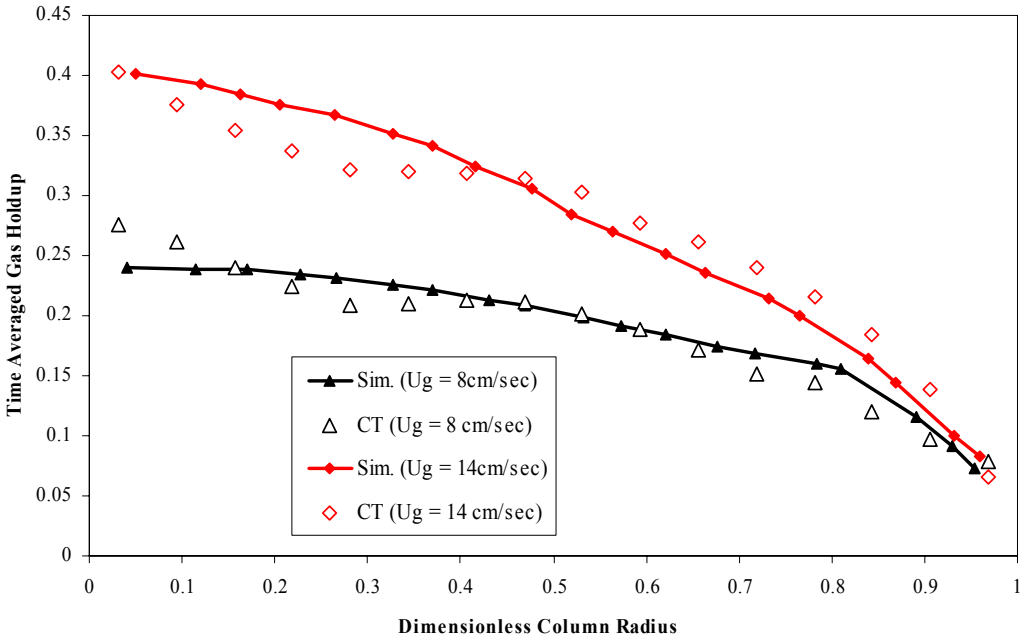

Figure 5.19 Comparison of time-averaged gas holdup profile of Air-Therminol-glass beads system

Figure 5.19 shows the time-and-azimuthally averaged gas holdup profile in a 16.2-cm diameter column operated at $U_g = 8$ and 14 cm/s in an air-therminol-glass beads (150 μm) slurry system. The solids loading is 9.1%. The slurry phase is assumed to be pseudo-homogeneous, thus two-phase (air and slurry) flow rather than three-phase (air, therminol and glass beads) flow is simulated. The apparent viscosity of the slurry phase is calculated by Einstein's viscosity for dilute suspension:

$$\mu^* = \mu\left(1+\frac{5}{2}\alpha_s + O\left(\alpha_s^2\right)\right) \approx 1.08 \text{ cP} \tag{5.2}$$

The slurry density is calculated as

$$\rho^* = \alpha_s\rho_s + \left(1-\alpha_s\right)\rho_t \approx 1015 \ kg/m^3 \tag{5.3}$$

and the slurry phase surface tension is estimated as Therminol surface tension (17 dyne/cm). The apparent density and viscosity of the slurry mixture are close to water, while its surface tension is much lower than that of water. The gas holdup profile is well predicted for both superficial gas velocity conditions.

In Figure 5.20, the time and azimuthally-averaged liquid axial velocity and the phase-weighted liquid axial velocity are compared against each other as well as to CARPT data for the 44-cm column operated at $U_g = 10 \ cm/s$. The phase-weighted liquid axial velocity is defined as

$$\widetilde{u_{lz}\left(\mathbf{x}\right)}^t = \frac{\overline{u_{lz}\left(\mathbf{x}\right)\alpha_l\left(\mathbf{x}\right)}^t}{\overline{\alpha_l\left(\mathbf{x}\right)}^t} \tag{5.4}$$

where u_{lz} is liquid axial velocity, α_l is liquid holdup, $\mathbf{x}$ is the position vector, $\overline{f\left(\mathbf{x}\right)}^t$ is the time-averaged value of the time series $f\left(\mathbf{x},t\right)$,

$$\overline{f\left(\mathbf{x}\right)}^t = \int_\tau^{\tau+T} f\left(\mathbf{x},t\right)dt \Big/ T \tag{5.5}$$

and

$$f(\mathbf{x},t) = \overline{f(\mathbf{x})}^{t} + f'(\mathbf{x},t) \tag{5.6}$$

Equation (5.4) can be rewritten as

$$\overline{\alpha_l(\mathbf{x})}^{t}\,\widetilde{u_{lz}(\mathbf{x})}^{t} = \overline{\alpha_l(\mathbf{x})u_{lz}(\mathbf{x})}^{t} \tag{5.7}$$

It should be noted that the cross-sectional integral of the product of the time-averaged liquid axial velocity and the time-averaged liquid holdup is *not* equal to zero. The continuity equation for batch liquid requires:

$$\begin{aligned}\left\langle \overline{\alpha_l(r,\theta,Z)}^{t}\,\widetilde{u_{lz}(r,\theta,Z)}^{t} \right\rangle &\equiv \left\langle \overline{\alpha_l(r,\theta,Z)u_{lz}(r,\theta,Z)}^{t} \right\rangle \quad \text{(From equation 5.6)} \\ &= \overline{U_{sup}}^{t} \quad (\because \text{ Continuity}) \\ &= 0 \quad (\because \text{ Batch liquid})\end{aligned} \tag{5.8}$$

where $\langle\ \rangle$ is cross-sectional integral at given elevation.

$$\left\langle f(r,\theta,Z) \right\rangle = 2\int_0^1 \xi f d\xi \qquad \text{at } z = Z \tag{5.9}$$

This leads to

$$\begin{aligned}\left\langle \overline{\alpha_l(x,y,Z)u_{lz}(x,y,Z)}^{t} \right\rangle &= \left\langle \overline{\alpha_l(x,y,Z)}^{t}\,\overline{u_{lz}(x,y,Z)}^{t} \right\rangle \\ &\quad + \left\langle \overline{\alpha_l'(x,y,Z)u_{lz}'(x,y,Z)}^{t} \right\rangle\end{aligned} \tag{5.10}$$

thus

$$\left\langle \overline{\alpha_l(x,y,Z)}^{t}\,\overline{u_{lz}(x,y,Z)}^{t} \right\rangle = -\left\langle \overline{\alpha_l'(x,y,Z)u_{lz}'(x,y,Z)}^{t} \right\rangle \neq 0 \tag{5.11}$$

where α_l' and u_{lz}' are the gas holdup and liquid axial velocity fluctuations with respect to their long-time average value, respectively. From the simulated results, as shown in Figure 5.20, the difference between the time-averaged liquid velocity $\overline{u_{lz}}^{t}$ and phase-weighted liquid time-averaged velocity $\widetilde{u_{lz}}^{t}$ is small. Thus, liquid holdup and velocity cross-correlation is not significant for the 44-cm diameter column operated at

$U_g = 10\ cm/s$ superficial gas velocity. The simulated time-averaged liquid velocity, $\overline{u_{lz}}^{t}$, are higher than phase-weighted liquid time-averaged velocity, $\widetilde{u_{lz}}^{t}$, throughout the column, which indicates that the correlation between liquid holdup and axial velocity, $\left\langle \overline{\alpha_l' u_{lz}'}^{t} \right\rangle_s$, is negative. In other words, the correlation between *gas* holdup and *liquid* axial velocity, $\left\langle \overline{\alpha_g' u_{lz}'}^{t} \right\rangle_s$, is positive as $\alpha_g = 1 - \alpha_l$. This is consistent with the simulated time series of local gas holdup and liquid axial velocity, which are in-phase as illustrated in Figure 5.13. The difference becomes smaller as one moves towards the wall region, where gas holdup is lower and its fluctuation is not significant.

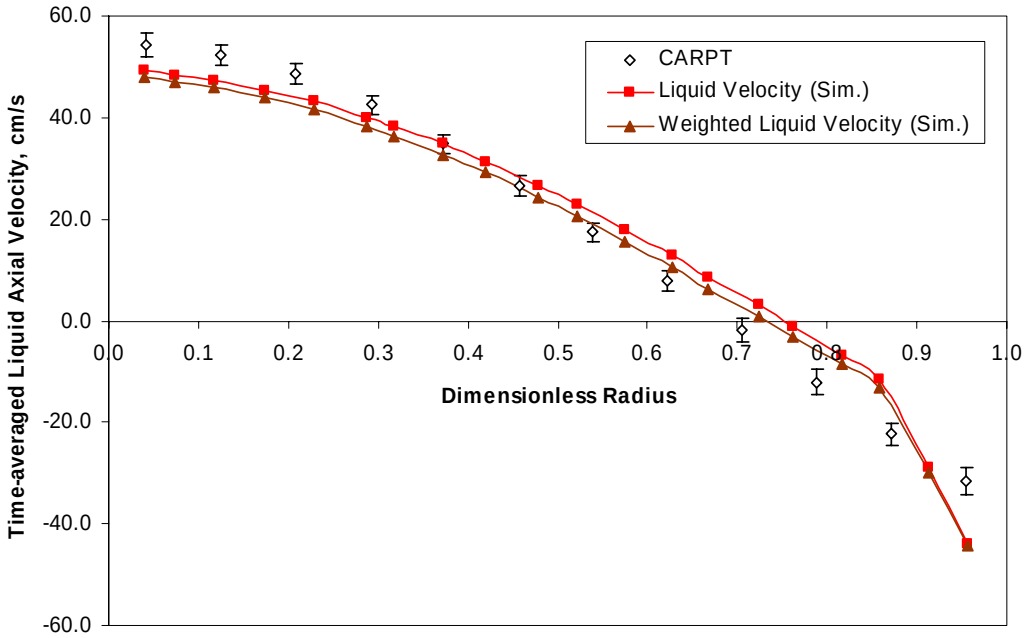

Figure 5.20 Comparison of time-averaged and liquid holdup weighted liquid axial velocity profile (D_C = 44 cm, U_g = 10 cm/s, P = 1 bar)

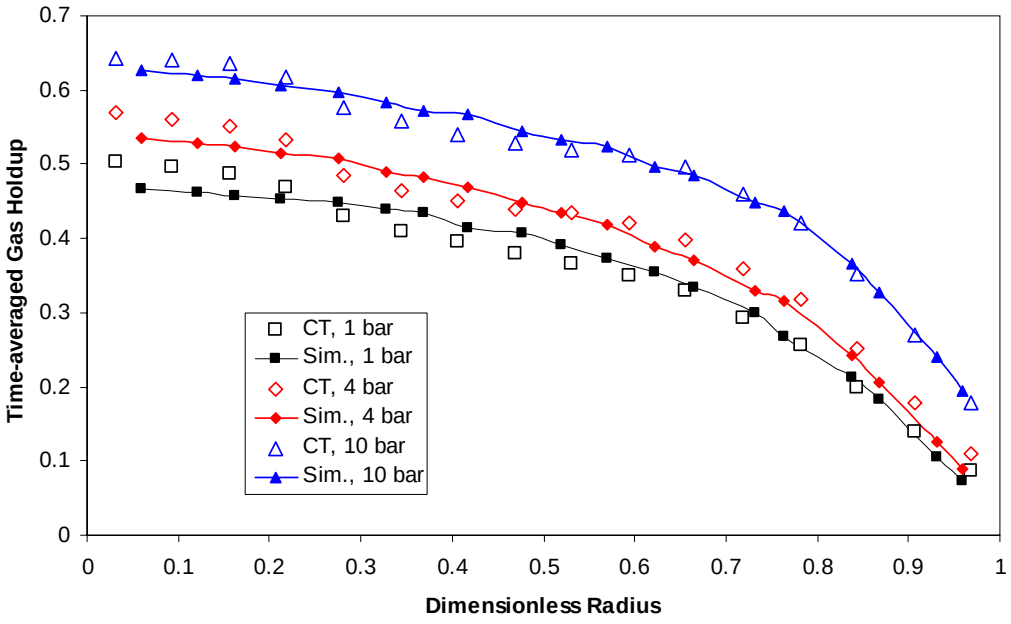

Figure 5.21 Comparison of time-averaged gas holdup profile (D_C = 16.2 cm, U_g = 30 cm/s, P = 1, 4, and 10 bar)

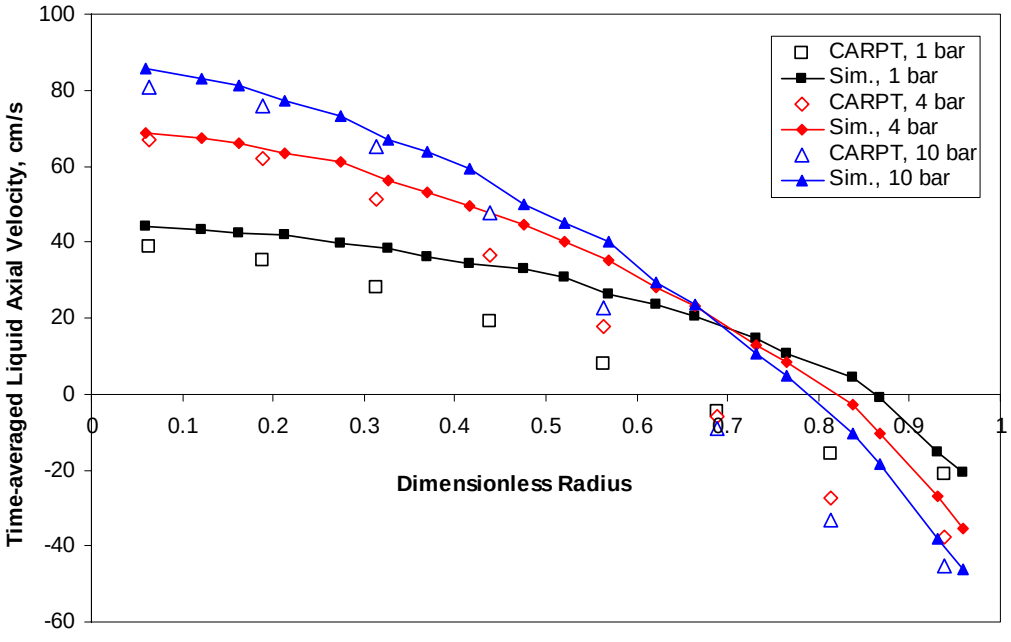

(a)

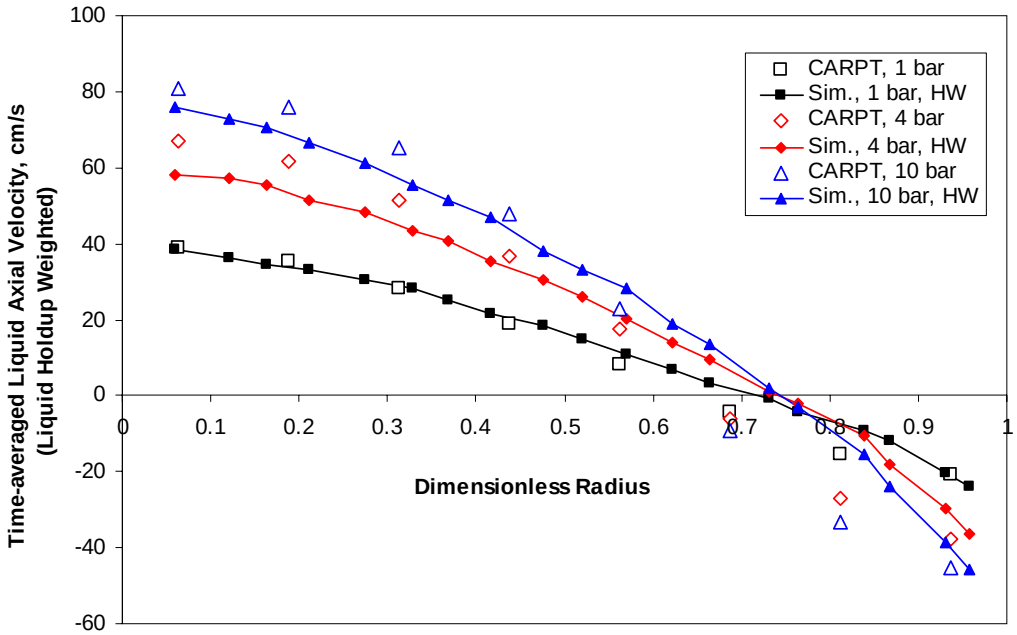

(b)

Figure 5.22 Comparison of liquid axial velocity profile for air-water bubble column. D_C = 16.2 cm, U_g = 30.0 cm/s, P = 1, 4, 10 bar .(a) Time averaged (b) Time-averaged and liquid holdup weighted

In Figure 5.21, the simulated time and azimuthally-averaged gas holdup profiles, in a 16.2-cm diameter air-water bubble column operated at $U_g = 30\ cm/s$ superficial gas velocity at 1, 4 and 10 bars, are compared with CT experiments. The simulated results predict the gas holdup distribution well for all the operating pressures. One should note that in order to accomplish this favorable comparison we needed to weight the drag force by $\left(\rho_g/\rho_{g,1atm}\right)^{0.25}$ as indicated in Chapter 4. It seems that this density correction factor used in this work, $\left(\rho_g/\rho_{g,1atm}\right)^{0.25}$, could be a good scaling factor for engineering purposes. The usefulness of this correction factor needs to be investigated further.

Figure 5.22 shows the time-and-azimuthally averaged axial liquid (water) velocity profiles and holdup weighted liquid (water) velocity profile in a 16.2-cm diameter column at $U_g = 30\ cm/s$ superficial gas velocity and operated at 1, 4, and 10 bars,

respectively. From Figure 5.22, it is evident that the cross-sectional integral of the product of simulated time-averaged liquid axial velocity and time-averaged liquid holdup, $\left\langle \overline{\alpha_l}\ \overline{u_{lz}} \right\rangle_s$, has positive values as the simulated time-averaged liquid axial velocity is higher than time-averaged and liquid-holdup weighted liquid velocity. In contrast, the cross-sectional integral of the product of experimental time-averaged liquid axial velocity and time-averaged liquid holdup, $\left\langle \overline{\alpha_l}\ \overline{u_{lz}} \right\rangle_e$, has negative values (Ong, 2003). This mass "imbalance" is negligible in 2D axisymmetric simulation (Chen *et al.*, 2003) because the axisymmetric boundary condition in 2D computations causes the liquid flow to develop very quickly (5-10 s of real time) and reach its long-time "steady" pattern (Sanyal *et al.*, 1999; Chen *et al.*, 2003). In other words, the fluctuation of liquid holdup and axial velocity is artificially eliminated in such simulation. However, in reality and in 3D simulations, such fluctuations can be significant at high superficial gas velocities (e.g., 30 cm/s). Figure 5.23 illustrates the model calculated cross-correlation of the liquid holdup and axial velocity, $-\overline{\alpha_l' u_{lz}'}$. The predicted magnitude of the liquid velocity and holdup cross-correlation increases with the gas superficial velocity, while it decreases with the operating pressure.

From the simulation, $\left\langle \overline{\alpha_l' u_{lz}'} \right\rangle_s$ is negative which appears to be reasonable. Bubble column flow is buoyancy driven, gas controls its hydrodynamics and momentum is transferred from the faster, upward moving, gas phase to the slower liquid phase. As a result, the time series of local gas holdup and liquid axial velocity should be in-phase. In other words, when $\alpha_g\left(\mathbf{x}, t = t_1\right) > \overline{\alpha_g}\left(\mathbf{x}\right)$, the gas pocket will, most likely, bring liquid upward at a higher velocity than $\overline{u_{lz}}\left(\mathbf{x}\right)$ (see Figure 5.13). Thus, if $\alpha_g' > 0$ ($\alpha_l' < 0$), then $u_{lz}' > 0$ thus $\alpha_l' u_{lz}' < 0$ (and $\overline{\alpha_l' u_{lz}'} < 0$) throughout the column, which is computed by the simulation and presented in Figure 5.20, Figure 5.22, Figure 5.23 and Table 5.2. Moreover, the magnitude of $\left\langle \overline{\alpha_l' u_{lz}'} \right\rangle_s$ decreases with the operating pressure which

suppresses the chaotic nature of bubble column flows, as evident from in Table 5.2 and Figure 5.23 as well.

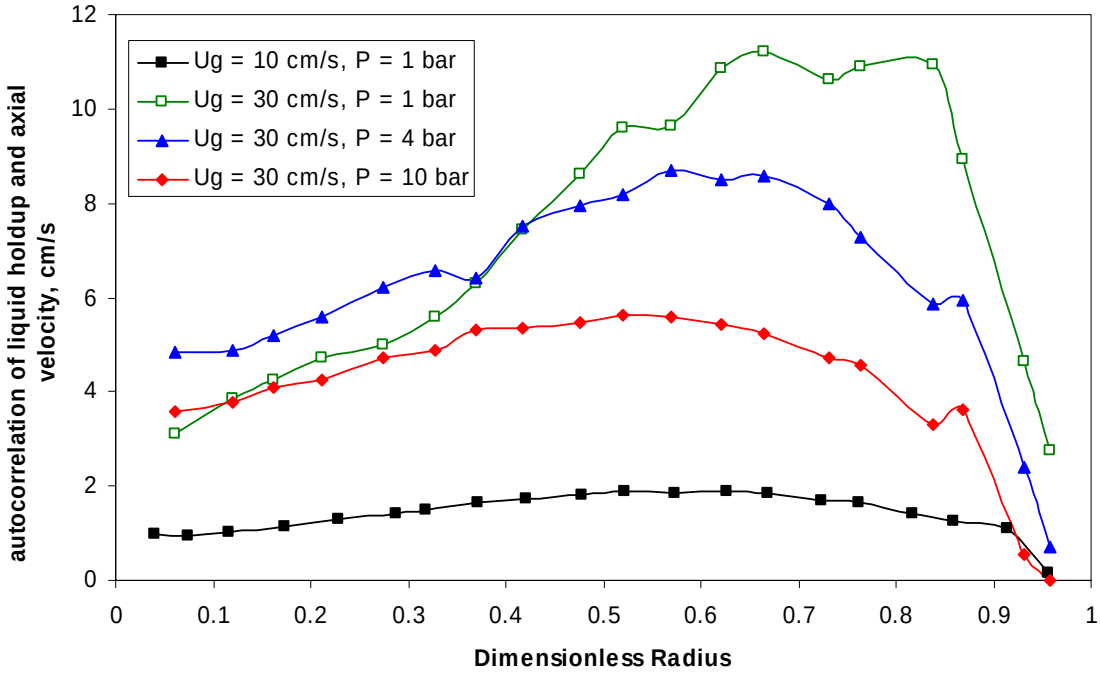

Figure 5.23 Cross correlation radial distribution of the liquid holdup and axial velocity, $\overline{-\alpha_l' u_{lz}'}$

Table 5.2 Overall liquid continuity for air-water bubble column: D_C = 16.2 cm and U_g = 30.0 cm/s

	$\langle \overline{\alpha_l}\ \overline{u_{lz}} \rangle,\ cm/s$	
	Exp.	Sim.
P = 1 bar	-3.3	6.8
P = 4 bar	-5.3	5.4
P = 10 bar	-6.7	2.7

However, the above analysis and simulation results are not in agreement with the data obtained from CT and CARPT, from which $\left\langle \overline{\alpha_l' u_{lz}'} \right\rangle_e$ is indirectly estimated to be positive, suggesting that higher local instantaneous gas holdup is correlated with lower

local liquid axial velocity. Moreover, the magnitude of $\left\langle \overline{\alpha_l' u_{lz}'} \right\rangle_e$ observed from experiments increases with the operating pressure, which suggests that higher operating pressure may *promote* the chaotic flow in bubble column. The experimental mass "imbalance" resulting from the average up-flow and down-flow rate shows little dependence on the operating pressure, while the operating pressure has a significant effect on simulated results as shown in Table 5.2. This discrepancy at the moment cannot be resolved and needs to be investigated in the future.

In most current applications of bubble column CFD modeling, the full-scaled simulations (i.e., multiphase reacting flow simulations) are out of reach due to computational cost (20-30 scalar transport equation may need to be solved) and instability, which arises from the non-linear reaction rates (appear in source term of scalar transport equation) and complicated reaction network. Thus CFD is mainly used to provide the needed fluid dynamics to models ranging from single parameter axial dispersion model to two dimensional convection with eddy diffusion model (Degaleesan, 1997; Degaleesan *et al.*, 1997; Degaleesan and Dudukovic, 1998). In these reactor models, the preservation of the continuity condition for the gas and liquid phase is imperative. Moreover, it is the liquid flux, rather than liquid holdup or velocity itself, that matters in bubble column reactor modeling. Thus the holdup weighted liquid (water) velocity profile, $\widetilde{u_{lz}}(r)$, which satisfies the continuity equation, may need to be used for such purposes.

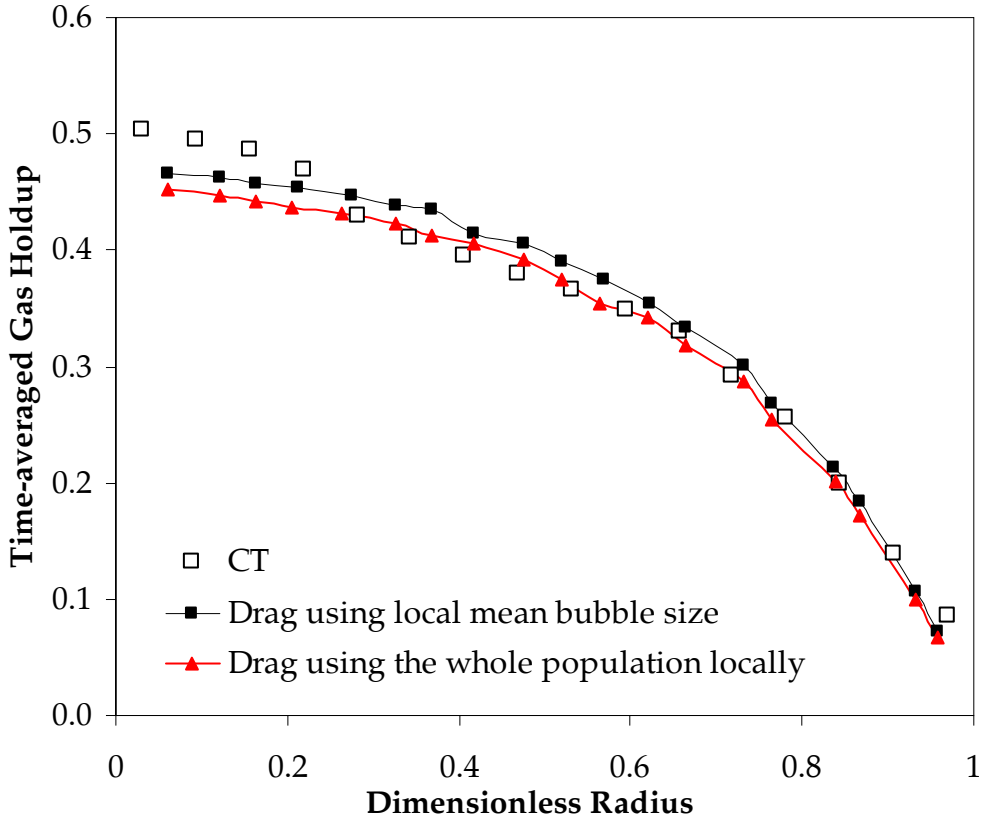

Figure 5.24 Effect of using the whole population locally on calculating drag and in using local mean bubble size (D_C = 16.2 cm, U_g = 30.0 cm/s, P = 1 bar)

In this study, the drag force is calculated based on local mean bubble size (Equation (4.4)) obtained from bubble population distribution. The drag force can also be calculated from the whole local bubble population as:

$$\mathbf{M}_d = \frac{3}{4}\alpha_l \rho_l \left(\rho_g / \rho_{g,1atm}\right)^{0.25} \left|\mathbf{u}_l - \mathbf{u}_g\right| \left(\mathbf{u}_l - \mathbf{u}_g\right) \sum_{i=1}^{N} \alpha_i \frac{C_{D,i}}{d_i} \tag{5.12}$$

$$C_{D,i} = \begin{cases} 24\left(1 + 0.15 Re_i^{0.687}\right)/Re_i & Re_i \le 1000 \\ 0.44 & Re_i > 1000 \end{cases}, \quad Re_i = \frac{d_i \left|\mathbf{u}_l - \mathbf{u}_g\right| \rho_l}{\mu_l} \tag{5.13}$$

where α_i is the holdup of i[th] bubble class and $\sum_{i=1}^{N} \alpha_i = \alpha_g$, d_i is diameter of i[th] bubble class, and $C_{D,i}$ is the local drag coefficient for i[th] bubble class, and Re_i is i[th] bubble class local Reynolds number. The effect of these two drag force calculation method on the gas holdup prediction is not negligible as illustrated in Figure 5.24.

In addition to the mean axial liquid velocity profile, the intensities of fluctuations about the mean values are also provided by the CARPT experiments. Conventionally, these quantities, $\langle u_z' u_z' \rangle$, $\langle u_r' u_r' \rangle$ and $\langle u_\theta' u_\theta' \rangle$, as expressed in cylindrical coordinates, are called turbulence intensities. (Such a name may not be appropriate for the fluctuations due to the periodic and/or quasi-periodic large-scale motions, which are usually not considered turbulence, are included in these correlations. Nevertheless, the definition, mathematically, is clear.). The characteristics of the liquid phase motion are revealed, at first level, by these correlations.

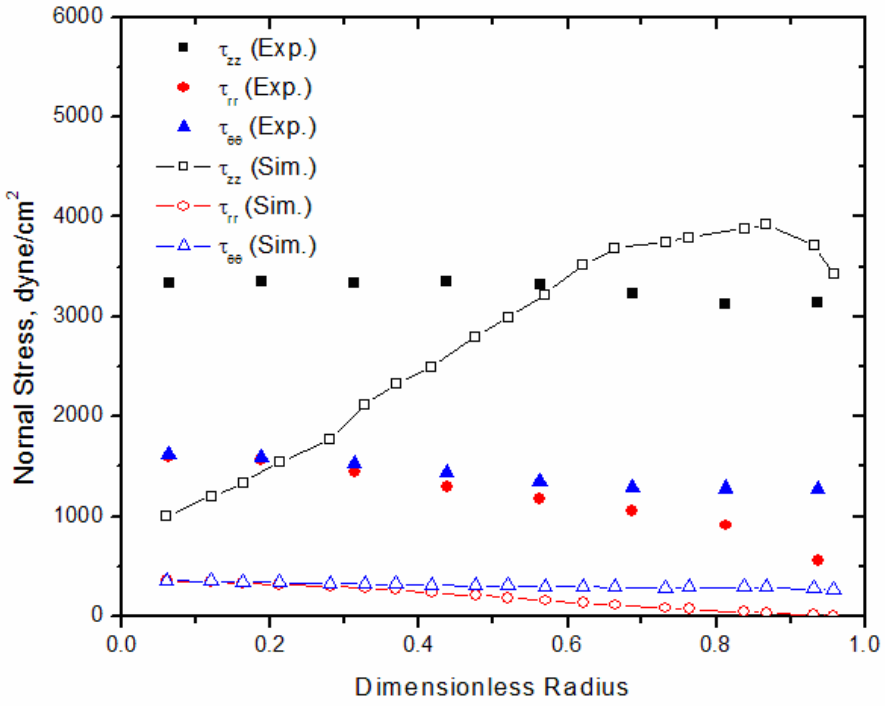

(a)

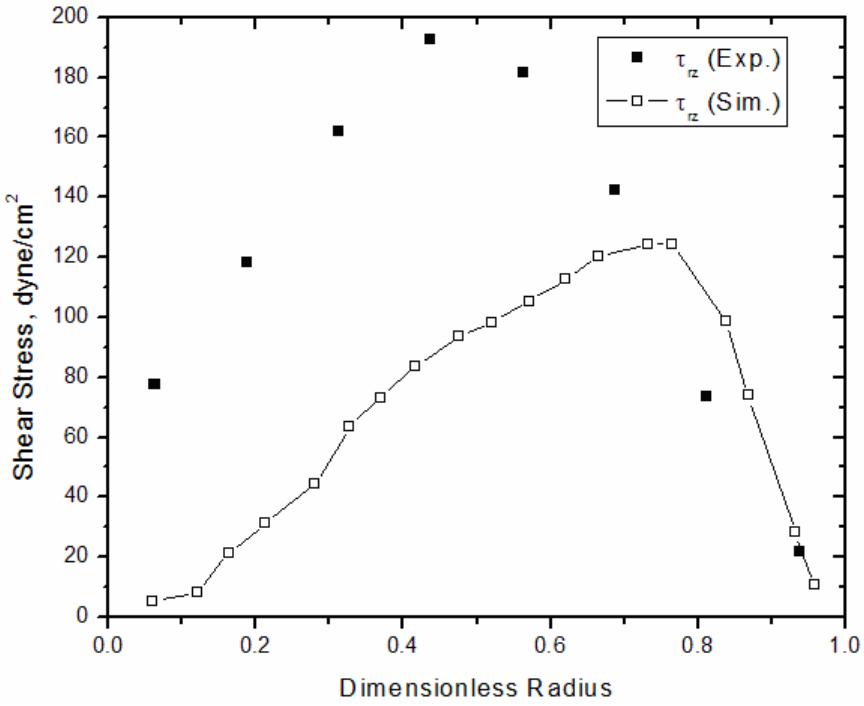

(b)

Figure 5.25 Comparison of the intensity of liquid turbulent (a) normal stress and (b) shear stress obtained from simulations with experimental data for air-water bubble column: Dc = 16.2 cm, Ug = 30.0 cm/s, P = 1 bar.

Figure 5.25a compares the radial distribution of the liquid velocity autocorrelations calculated from the simulation, for a 16.2-cm diameter air-water bubble column operated at 30 cm/s superficial gas velocity and 1 bar, and those obtained from CARPT measurements. As expected, the values of the fluctuations in the axial direction are much stronger than in the radial and angular directions. For the radial and angular normal stress, the numerical values are significantly lower than the experimental data. This is due to model's inability of resolving all the fluctuations as the turbulence level is enhanced by increasing the superficial gas velocity. For the axial normal stress, although the discrepancy between the simulated results and the experimental data is still significant, the relative difference is not as large as that for the radial and angular normal stress, and the difference becomes smaller as one moves towards the wall. In Figure 5.25b, the liquid turbulent shear stress obtained from simulations are compared with experimental data. Similar to the prediction of normal stress in radial direction, the simulation

significantly underpredicts the turbulent shear stress. Similar behavior was found in other simulations in this work. This comparison indicates and confirms that the present numerical model, although it can resolve the fluctuating liquid velocity in the bubbly flow regime, is not able to fully resolve the fluctuating liquid velocity in the churn-turbulent flow regime (Pan and Dudukovic, 2001).

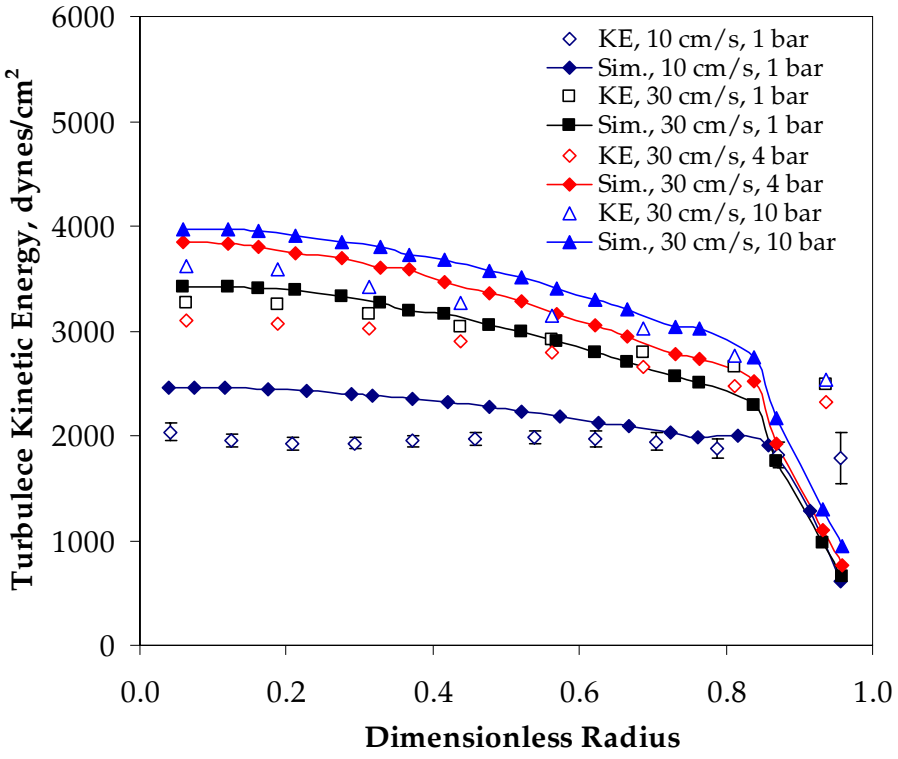

Figure 5.26 Comparison of the liquid turbulent kinetic energy obtained from simulations with experimental data for columns of different diameter and operated in the churn turbulent regime.

Although the "turbulent" shear stress cannot be accurately predicted, the "turbulent" kinetic energy obtained from the k-ε model agrees reasonably well with the experimental data as shown in Figure 5.26. One should note that in contrast to smaller diameter columns and operated at lower superficial gas velocity (e.g. D_C = 14 cm, U_g = 9.6 cm/s and D_C = 19 cm, U_g = 12.0 cm/s), where kinetic energy profiles typically exhibit a maximum around the cross-over point for the time-averaged liquid axial velocity

(Degaleesan, 1997; Chen *et al.*, 2003), such peak does not exist in bigger columns ($D_C = 44$ cm) or at higher superfical gas velocity ($U_g = 30$ cm/s).

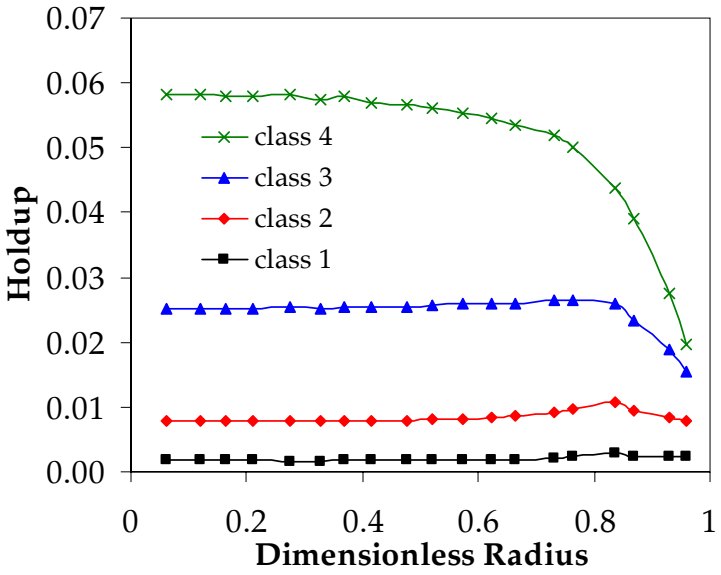

(a)

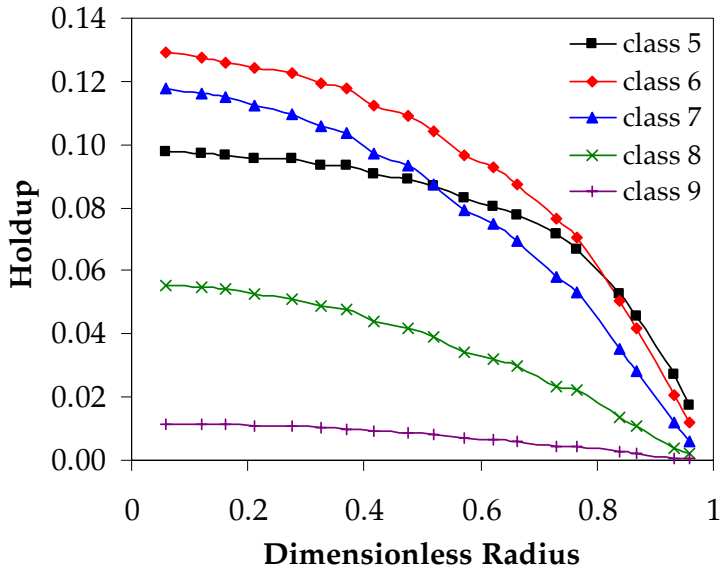

(b)

Figure 5.27 Time-averaged bubble class holdup profile (D_C = 16.2 cm, U_g = 30.0 cm/s, P = 1 bar)

Figure 5.27 shows the simulated time and azimuthally-averaged volume fraction profiles for different diameter bubbles in a 16.2-cm diameter air-water bubble column operated at 30 cm/s superficial gas velocity and 1 bar. The volume fraction of small bubbles ($d \le 4\ mm$) is uniformly distributed, especially for tiny bubbles ($d < 2.5\ mm$). For large bubbles, however, the volume fraction distribution is parabolic as shown in Figure 5.27b. In Figure 5.28, the effects of operating pressure and gas superficial velocity on medium diameter bubbles are illustrated. The radial holdup distributions of such bubbles are more uniform at higher pressure (10 bars) than at lower pressure (1 bar), which indicates that the simulation correctly captured the pressure effect on bubble column flow which pushes the churn-turbulent flow toward bubbly flow when pressure is increased.

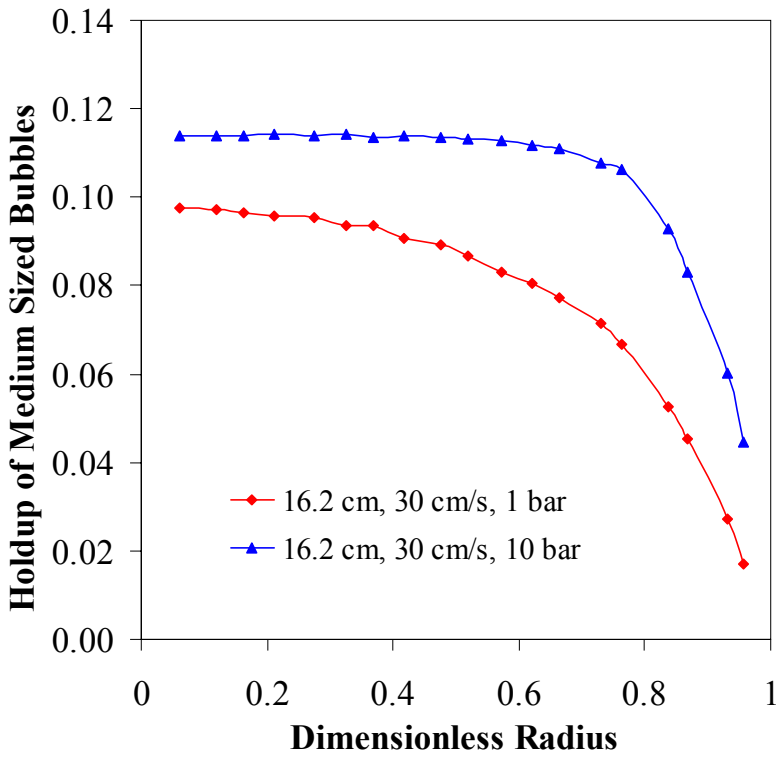

Figure 5.28 Effect of operating pressure on medium size bubbles ($d = 6.35\ mm$)

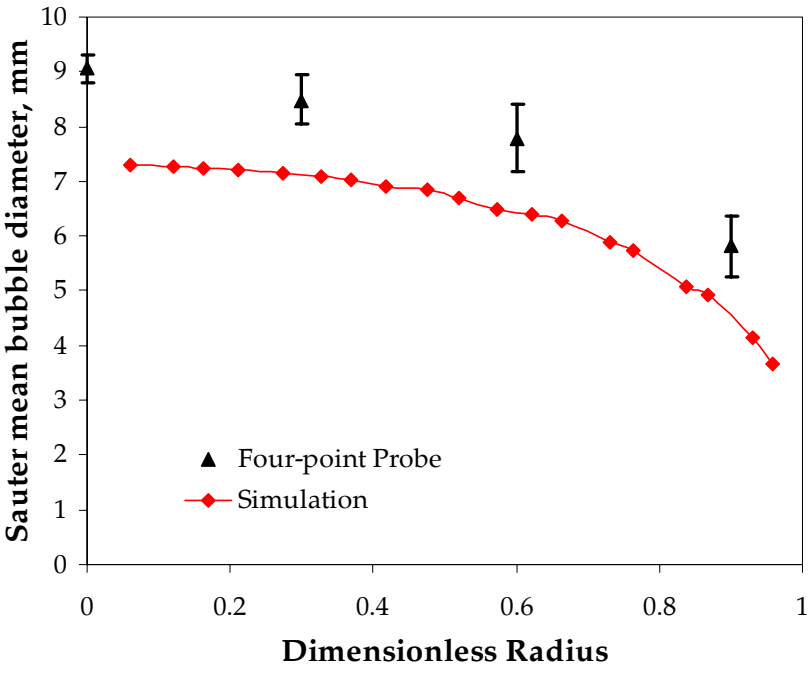

(a)

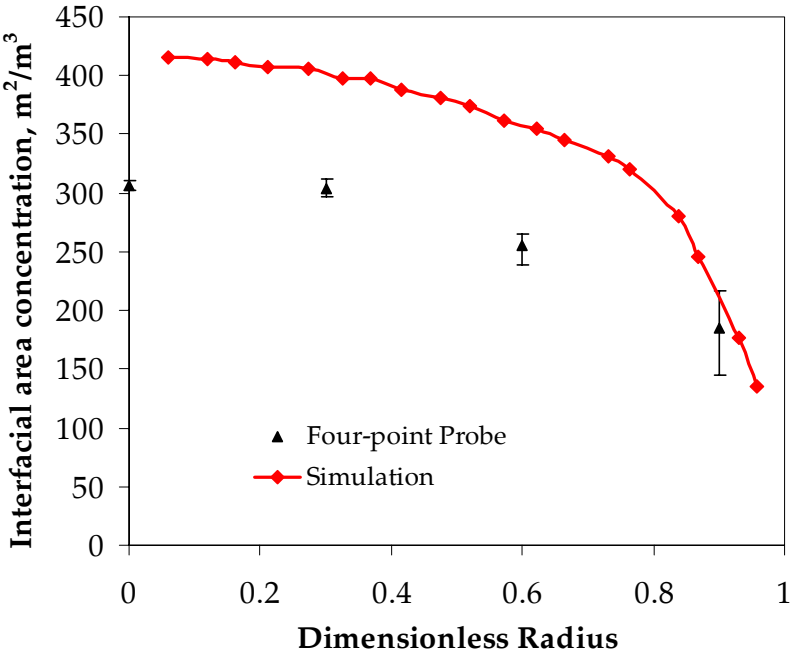

Figure 5.29 Comparison of the radial profiles of the (a) bubble Sauter mean diameter and (b) interfacial area concentration obtained from simulation with experimental data measured by four-point optical probe for 16.2-cm diameter column operated at U_g = 30.0 cm/s.

In Figure 5.29, the radial profiles of the bubble Sauter mean diameter and interfacial area per unit volume obtained from simulation are compared with experimental data measured by four-point optical probe. The simulated Sauter mean diameter profile underestimated the experimental data (Xue, 2004) by about 20%, and the simulated interfacial area per unit volume overestimated the experimental data (Xue, 2004) by 30-40%.

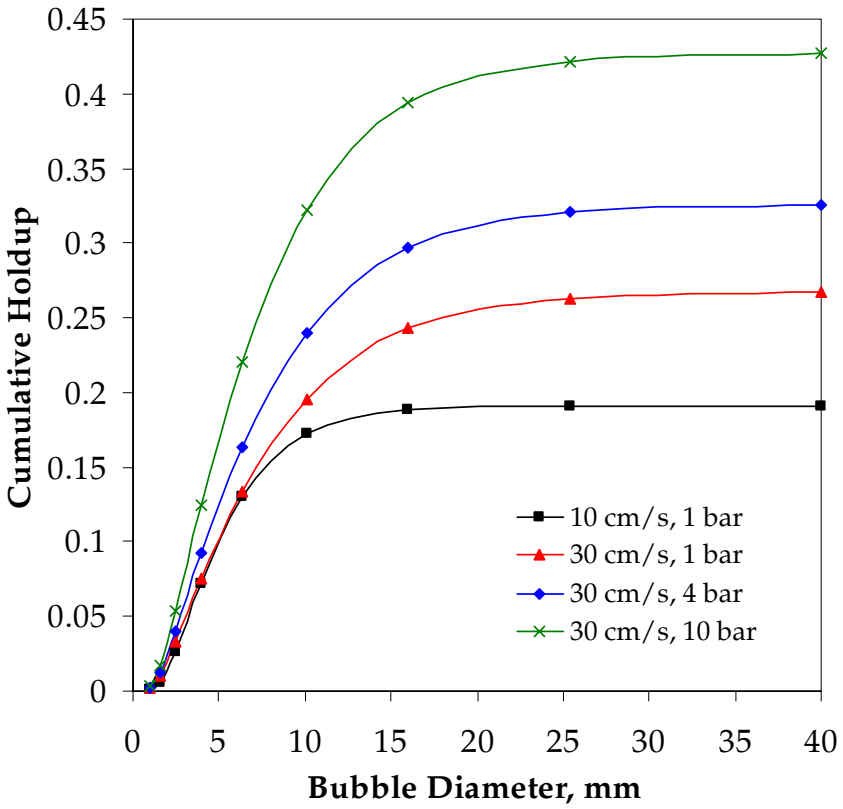

Figure 5.30 Overall bubble classes cumulative holdup

In Figure 5.30, the simulated cumulative bubble volume fraction is given. The summation of the volume fraction of all bubble classes is equal to the simulated gas holdup, thus if the simulated overall gas holdup is underestimated, the cumulative bubble volume fraction will most likely be underestimated as well. Similarly, if the simulated overall gas holdup is overestimated, the cumulative bubble volume fraction will also be

most likely overestimated. Thus, for fair comparison, each bubble class volume fraction needs to be weighted against the experimental gas holdup. This weighting procedure can be written as:

$$\bar{\alpha}_{i,adj} = \bar{\alpha}_{i,sim} \frac{\bar{\alpha}_{g,\exp}}{\bar{\alpha}_{g,sim}} \tag{5.14}$$

Here, we made the assumption that the increase/decrease of overall gas holdup would not change the bubble volume fraction based distribution. As the relative error of the simulation against the experimental overall gas holdup, as well as the adjusting factor, is small (see Table 4.7), it may be a valid assumption. It can be seen that the cumulative volume fraction of smaller bubbles (up to 6.4 mm) does not change with the superficial gas velocity (10 and 30 cm/s) while it increases with respect to the operating pressure, which is in line with the two-bubble-class hypothesis (e.g., Krishna and Ellenberger, 1996). Nevertheless, a bimodal bubble size distribution is not found in the simulation as shown in Figure 5.31. The operating pressure does not have a noticeable effect on the simulated bubble size distribution, which results from breakup and coalescence closures used in this work which do not take the pressure effect into account. The superficial gas velocity has little effect on volume fraction of small bubbles (1 and 1.6 mm), while such effect becomes pronounced for larger bubbles. The bubble size distribution becomes wider and the Sauter mean bubble diameter becomes larger as the superficial gas velocity increase. The simulation suggests that although the volume fraction of small bubbles may not change with respect to the superficial gas velocity in churn-turbulent flow regime, the bubble size distribution remains single modal and simply becomes wider and moves towards larger bubble diameter when superficial gas velocity increases. This is in line with observations reported by Fan *et al.* (1999) in high pressure small diameter column. Bimodal bubble size distribution postulated by Krishna and Ellenberger (1996) is not seen in any of our simulations or in data by Fan *et al.* (1999).

Table 5.3 Physical properties

Liquid (Slurry) phase	Density, kg m^{-3}	Viscosity, cp	Surface tension, N/m
Water	1000	1.0	0.072
Therminol-Glass beads (9.1 % solids loading)	1015	1.08	0.017

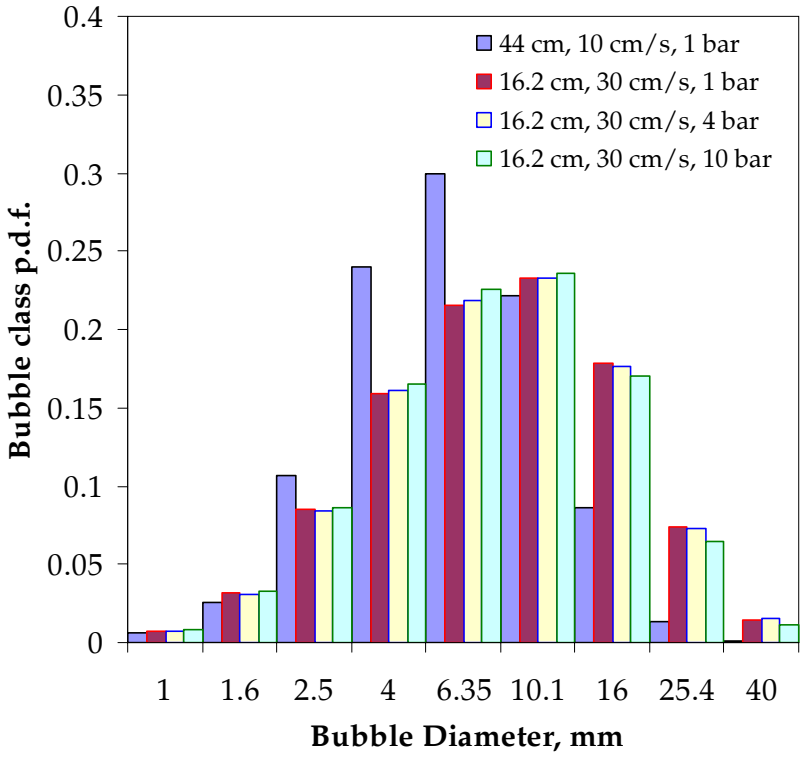

Figure 5.31 Bubble classes holdup-based probability distribution

The bubble class holdup-based probability function is illustrated in Figure 5.32 for air-water bubble column (Ug = 10 cm/s) and air-Therminol-glass beads slurry bubble column (Ug = 8 cm). The physical properties of liquid (slurry) phase for these two columns are listed in Table 5.3, and the operating conditions are listed in Table 5.4. The major difference in these two systems is the surface tension of the liquid (slurry). The simulated overall gas holdup for these two columns are about the same. However, the

bubble class holdup-based probability density function for these two systems, as expected, is significantly different because of the difference in the liquid (slurry) phase surface tension. There are many more smaller bubbles in the air-Therminol-glass beads slurry bubble column than in the air-water bubble column operated at similar superficial gas velocity, and this is captured by the simulation.

Table 5.4 Operation condition

D_C, cm	U_g, cm/s	System	Overall Gas Holdup (Sim.)
16.2	8	Air-Therminol	0.165
44	10	Air-Water	0.162

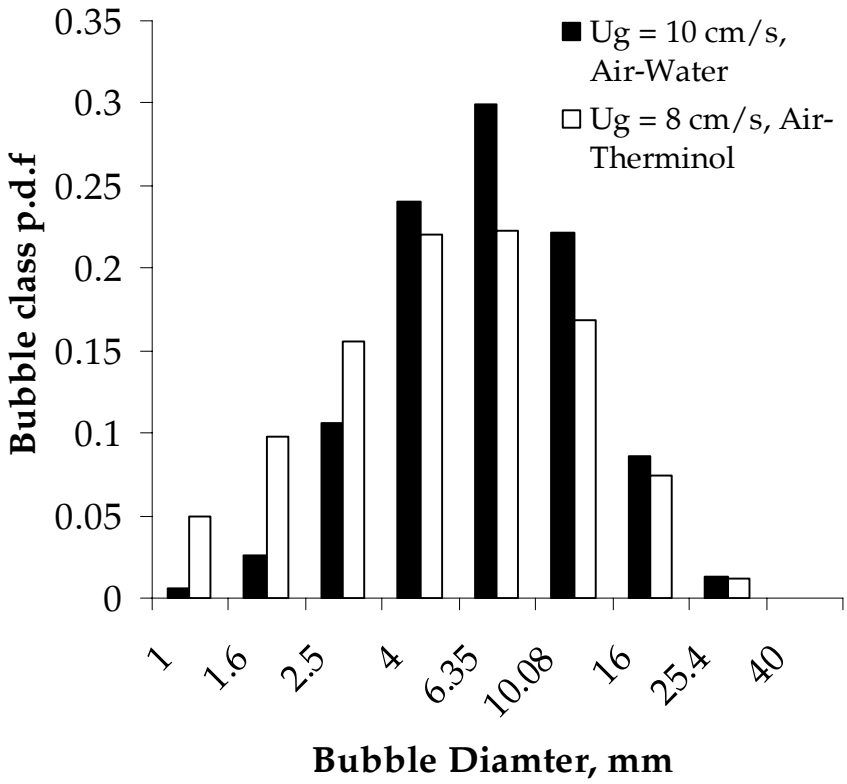

Figure 5.32 Surface tension effect on bubble holdup-based probability distribution.

5.3.1 Results and Conclusions

The numerical simulation of the transient gas-liquid flow in three-dimensional cylindrical bubble columns using the Euler-Euler two-fluid model (TFM) and the ASMM with BPBE implemented is able to capture the dynamic features of the large-scale structures. The time-averaged liquid velocity field exhibits single loop axi-symmetric re-circulation pattern in the middle section of the column. Such flow pattern had been confirmed experimentally by the liquid velocity measurements, which used Computer Automated Radioactive Particle Tracking technique, in various columns operating at churn turbulent flow conditions. The evidence, both numerical and experimental, supports the assumption of one-dimensionality within the middle section of the column of the time-averaged velocity profile, in the sense of time- and azimuthal-averaging, and in turn the use of one-dimensional re-circulation model widely adopted in engineering applications (Degaleesan *et al.*, 1996b; Degaleesan *et al.*, 1997; Gupta *et al.*, 2001a). Quantitative comparisons with the experimental (CT/CARPT) data demonstrate that, by applying inter-phase momentum transfer, modified $k-\varepsilon$ turbulence model in the liquid phase, and the BPBE for the bubble size prediction, the two-fluid and ASMM simulations are able to provide satisfactory mean axial liquid velocity and gas holdup profile for columns operated over a wide range of superficial velocity, operating pressure, physical properties, and column diameter. By comparing the computed and experimentally determined turbulence intensities (auto correlations of the liquid velocity fluctuations) and the Reynolds shear stress (cross correlation of the liquid velocity fluctuations), we find that for columns operating in the churn turbulent regime the velocity field cannot be fully resolved which results in a underestimated prediction of the fluctuations related mean quantities. The simulation correctly captured qualitatively the elevated pressure effect on bubble column flows which pushes the churn-turbulent flow towards bubbly flow when pressure is increased, and suggests that although the volume fraction of small bubbles may not change with respect to the superficial gas velocity in churn-turbulent flow regime, the bubble size distribution still remains single modal but becomes wider and moves towards larger bubble diameter when superficial gas velocity is increased.

For truly predictive results in simulation of gas-liquid flows in churn turbulent regime one needs to continue exploring the models for momentum exchange, bubble breakup/coalescence, and the models for multiphase turbulence.

Chapter 6
Numerical Tracer and Particle Tracking

6.1 Introduction

One of the primary tasks in the current methodology of bubble column design involves description of the degree of mixing of each of the involved phases (e.g., axial dispersion model), which is subsequently used along with reaction kinetics to estimate the reactor performance *viz.* the conversion, yield and selectivity. The advantages of using phenomenological models, using parameters obtained from transient fluid dynamic models of the column, have been demonstrated (Degaleesan *et al.*, 1996b; Degaleesan, 1997; Gupta *et al.*, 2001a). Thus, the time-dependent velocity field is needed for calculating the convection and turbulent dispersion of the passive scalar in the liquid and/or gas phase.

One of the major objectives of our ongoing modeling and dynamic simulation of bubble column flow is to study the liquid/gas dispersion and mixing. The widely used one-dimensional axial dispersion model requires the effective axial dispersion coefficient for which no suitable accurate correlation has been found to date. On the other hand the two dimensional convective-diffusive model requires axial and radial eddy diffusivities and the liquid velocity profile. It was demonstrated that such a model, with the velocity profile and eddy diffusivity values provided from the Computer Automated Radioactive Particle Tracking (CARPT) studies, can predict well the independently measured liquid tracer exit age density function (Degaleesan *et al.*, 1996b; Degaleesan *et al.*, 1997) in bubble column of the same size. This implies that such a model can accurately predict

reactor performance of such a bubble column for the first order reaction schemes and is a model of choice for mildly nonlinear reactions. However, the parameters of the model need to be supplied which, if based on experimentation, is a very expensive and tedious proposition. Therefore, we attempt here to obtain the modeled parameters by three-dimensional numerical simulation of the flow field and tracer spreading. In the present study, we verify the capability of the dynamic tracer simulation for the evaluation of the averaged liquid turbulent diffusivity.

6.2 Computational Models

Before a tracer simulation is started, one needs to generate a fully developed turbulent liquid/gas velocity field inside the bubble column. The two-fluid model, with bubble population balance equation implemented, is adopted to dynamically simulate the buoyancy driven flow. The details of the model and implementation have been illustrated in Chapter 4 and Chapter 5.

6.3 Numerical Tracer Experiment

The three dimensional dynamic simulations for the cylindrical bubble columns operated at various conditions can then be performed by using FLUENT, in which the Euler-Euler model is implemented. Such simulations generate fully developed flow fields, i.e. $\mathbf{u}_l(\mathbf{x},t)$, $\mathbf{u}_g(\mathbf{x},t)$, $\alpha_g(\mathbf{x},t)$ and $\alpha_l(\mathbf{x},t)$. The tracer simulations can then be started. If we use some type of passive scalar, say C, as the local tracer concentration for the liquid phase, the convection-diffusion equation for C is given by

$$\frac{\partial \alpha_l C}{\partial t} + \nabla \cdot \left[\alpha_l \mathbf{u}_l C\right] = D_m^l \nabla^2 C \qquad (6.1)$$

in which D_m^l is the molecular diffusivity, α_l is liquid holdup and $\mathbf{u}_l$ is liquid velocity vector. Similarly the governing equation for the gas tracer is written as,

$$\frac{\partial \alpha_g S}{\partial t} + \nabla \cdot \left[\alpha_g \mathbf{u}_g S \right] = D_m^g \nabla^2 S \tag{6.2}$$

where we use S to denote the local gas phase tracer concentration. These equations, i.e. Equation (6.1) and (6.2), which are also implemented, are then solved, together with the Euler-Euler model equations, to generate the tracer concentration as a function of time and location in the column, $C(\mathbf{x},t)$ and $S(\mathbf{x},t)$, for the liquid and gas phase, respectively. Since in bubble columns the dispersion of passive scalars are dominantly controlled by turbulence, the molecular diffusivities, D_m^l and D_m^g, can be taken as negligible and thus are given zero value during the simulations. It should be emphasized here that during the tracer simulation the fluid dynamic equations are still being solved continuously. Since the tracers are passive scalars, their existence in the column, either in liquid phase or in gas phase, do not change the fluid dynamics at all.

Assuming axisymmetric flow filed in a bubble column and neglecting the molecular diffusivity, Equation (6.1) can be convert into the following form, in terms of cylindrical coordinates,

$$\frac{\partial \alpha_l C}{\partial t} + \frac{1}{r}\frac{\partial \alpha_l r u_r C}{\partial r} + \frac{\partial \alpha_l u_z C}{\partial z} = \frac{1}{r}\frac{\partial}{\partial r}\left[D_{rr}\alpha_l r \frac{\partial C}{\partial r} \right] + \frac{\partial}{\partial z}\left[D_{zz}\alpha_l \frac{\partial C}{\partial z} \right] \tag{6.3}$$

where α_l is liquid holdup, u_r, u_z are liquid velocity component in r and z direction, and C is tracer concentration within liquid phase, respectively. The coefficients, D_{zz} and D_{rr} represent the axial and radial liquid turbulent eddy diffusivities, respectively. They are related to the liquid turbulent transport by the following assumptions:

$$u_z' C' = -D_{zz} \frac{\partial C}{\partial z} \tag{6.4}$$

$$u_r' C' = -D_{rr} \frac{\partial C}{\partial r} \tag{6.5}$$

Equation (6.3) represents the averaged balance equation for the non-volatile (passive) species, and is a transient two-dimensional convection-diffusion equation. The phasic averaging that has been performed (see Degaleesan, 1997) to arrive at this equation

(Equation (6.3)) refers to any time interval, which may be small or large. In the two dimensional convective-diffusive model, long-time averaged velocity and holdup profile are used. It is assumed that the eddy diffusivity associated with the small scale fluctuation, which cannot be capture by the CFD simulation, is less important and can be neglected compared to the eddy diffusivity associated with the large scale fluctuation. Based on the computed transient flow field and concentration field, and long-time averaged flow field, the turbulent diffusivity, D_{zz} and D_{rr}, can be obtained.

Performing a volume integration of the above equation over a section of the column, one gets,

$$\iint \frac{\partial \alpha_l C}{\partial t} dsdz + \iint \frac{\partial}{\partial z}(\alpha_l u_z C) dsdz = \iint \frac{\partial}{\partial z}\left(D_{zz} \alpha_l \frac{\partial C}{\partial z} \right) dsdz \tag{6.6}$$

in which $\int ds$ represents the area integration over the column's cross-section. The term involving the radial turbulent eddy diffusivity, D_{rr}, vanishes since the boundary condition of zero flux in radial direction at $r = R$, is imposed. The axial turbulent eddy diffusivity, D_{zz}, may be a function of r. The volume-averaged axial turbulent eddy diffusivity, however, can be defined as

$$\overline{D}_{zz} = \frac{\iint \frac{\partial \alpha_l C}{\partial t} dsdz + \iint \frac{\partial}{\partial z}(\alpha_l u_z C) dsdz}{\iint \frac{\partial}{\partial z}\left(\alpha_l \frac{\partial C}{\partial z} \right) dsdz} \tag{6.7}$$

If the integration along the axial direction, z, extends from z_1 to z_2, as indicated in Figure 6.1, Equation (6.7) can be further written as

$$\overline{D}_{zz} = \frac{\iint \frac{\partial \alpha_l C}{\partial t} dsdz + \int \left[(\alpha_l u_z C)_{z2} - (\alpha_l u_z C)_{z1} \right] ds}{\int \left[\left(\alpha_l \frac{\partial C}{\partial z} \right)_{z2} - \left(\alpha_l \frac{\partial C}{\partial z} \right)_{z1} \right] ds} \tag{6.8}$$

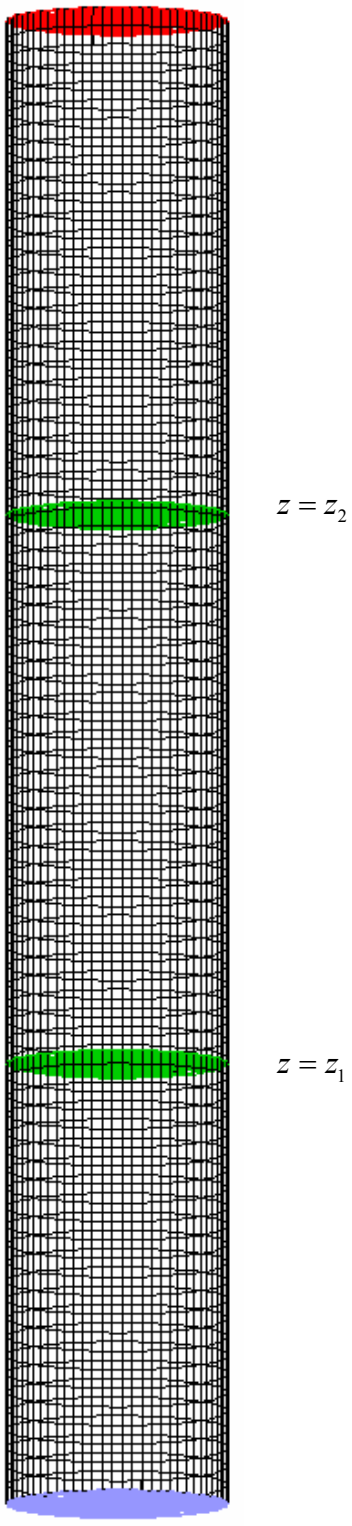

Figure 6.1 Computational mesh system for tracer simulation in bubble columns

Notice that $\overline{D}_{zz}$ in Equation (6.8) is still a function of time. Like in ensemble-averaging, $\overline{D}_{zz}$, which is now a volume-averaged quantity, should be further averaged over time to obtained the long-time averaged turbulent eddy diffusivity. In the dynamic simulations presented here, the FLUENT code outputs the time-dependent results every Δt seconds. Usually the tracer simulations for a 44-cm diameter column operated at 10.0 cm/s superficial gas velocity lasts about 20 to 30 seconds. For this particular case, as shown by the results which are discussed later, the liquid tracer concentration reaches a nearly uniform distribution at about 15 seconds after the tracer-injection. The time interval for output, Δt, is set to 0.1 second. The averaged turbulent eddy diffusivity, $\langle D_{zz} \rangle$, is therefore calculated as,

$$\langle D_{zz} \rangle = \frac{1}{N} \sum_{n=1}^{N} \overline{D}_{zz}(t_0 + n\Delta t) \tag{6.9}$$

where t_0 denotes the time when the tracer is injected into the column and $N\Delta t$ represents the total time of the tracer simulation. Both Δt and N are adjustable according to the flow conditions and column geometry.

6.4 Numerical Particle Tracking Experiment

The dispersion of passive scalars by continuous motion in turbulent flows evolved as a major filed of research, particularly during the recent years, due to industrial and environmental issues of utmost importance related to the energy crisis, pollution spreading and the need to improve plant design for two- or multi-phase flow processes. In the design of bubble column reactors, liquid phase mixing is one of the important factors that not only governs the residence time distribution of the liquid, but also affects that of the gas phase, and in addition, determines the mean driving force for mass transfer. As is well known, turbulence largely enhances the transport and mixing of any passive scalar released to a continuous material phase. The rates of transfer and mixing in the presence of turbulence are orders of magnitude larger than the rates due to molecular transport

alone. The most common method of dealing with equations governing turbulent flow is by treating the diffusive nature of turbulence via the introduction of a turbulent diffusivity for a given quantity. This is usually done using the gradient model, based on the well-known Boussinesq's hypothesis, which represent the correlations between the fluctuating velocity vector and scalar, i.e. $\overline{v_i' C'}$ with the product of eddy diffusivity and the ensemble averaged concentration. With a suitable diffusivity, such a model appears in the averaged mass balance equation as a diffusive term. However, the turbulent eddy diffusivity that appears in the resulting equations is itself unknown and needs to be modeled. This approach was introduced in the previous section by equation (6.4) and (6.5).

While molecular diffusivity is caused by the Brownian motion of molecules, the turbulent eddy diffusivity is naturally related to the Lagrangian turbulent motion of fluid particles. Measurements and simulations of fluid particle's velocities and trajectories, in a Lagrangian framework, are therefore needed for the study of the turbulent eddy diffusivity. The Computer Automated Radioactive Particle Tracking (CARPT) technique is capable of recording the Lagrangian trajectory of a tracer particle traveling through the entire column in a reasonable period of time. The Lagrangian turbulent eddy diffusivities are then directly evaluated from such data. Similarly, numerical particle tracking can be performed in a velocity field generated by the dynamic simulations of the transient gas-liquid flow in bubble columns. The numerical particle trajectories can then also be used to calculate the Lagrangian turbulent eddy diffusivities. In this sense there is no difference between the CARPT data and the data from numerical particle tracking.

However, there has been no generally established relationship that relates the eddy diffusivities, arising from the Boussinesq's gradient approximation, with the turbulent eddy diffusivities defined in the Lagrangian framework. In an isotropic and homogeneous turbulence field, it has been shown, by using scale arguments and by comparing the probability distribution function for the spread of particles with the solution of the turbulent convective diffusion equation, that the diffusivity appearing in

the convection-diffusion equation can be approximated by the Lagrangian based turbulent eddy diffusivities (Tenneke and Lumley, 1972). Even without such a relation, the Lagrangian information deduced from a CARPT experiment directly reveals the characteristics of the dispersion process in the liquid phase and can be utilized to study and model the effect of fluid dynamics on liquid phase mixing in bubble columns.

In this chapter we evaluate the Lagrangian turbulent eddy diffusivity in bubble columns by utilizing the numerical particle tracking. We compare the diffusivities from CARPT measurement with the ones from numerical simulation. Such comparison also serves as a validation of the numerical predictions arising from the two-fluid simulation of bubble column hydrodynamics. As stated earlier, we have completed the three-dimensional dynamic simulations for bubble columns of three sizes and operated at different superficial gas velocities and compared the time-averaged quantities with the data from CARPT experiments. From these simulations, we choose one case for particle tracking simulation: 44-cm diameter column operated at superficial gas velocity of 10 cm/s. The simulations start from fully developed flow fields. Unlike the CARPT experiment, where the technique is able to follow a single tracer particle only, numerically, there is no limit on the number of particles that can be traced simultaneously. Typically, 1440 initially randomly seeded particles are followed in a simulation. The dynamic simulation of the fluid flow field continues while the particle-tracking is being performed. For the cases reported here the simulation ran 60 seconds and the sampling frequency for the particle trajectory was 50 Hz. The numerical particle tracking experiment thus records 4,320,000 particle occurrences, which is about the same as in a CARPT experiment. CARPT data processing algorithm (Degaleesan, 1997) is used to obtain the turbulent eddy diffusivity. The equations are listed in Table 6.1.

Table 6.1 Turbulent eddy diffusivity calculation

$$D_{ij}(\tau) \equiv \frac{1}{2}\frac{d}{d\tau}\overline{\{x_i(\tau+t)-x_i(t)\}\{x_i(\tau+t)-x_i(t)\}}$$

$$D_{rr} = \overline{u_x \Delta x \cos^2\theta} + \overline{u_y \Delta y \sin^2\theta} + \overline{\cos\theta \sin\theta (u_y \Delta x + u_x \Delta y)}$$

$$D_{zz} = \overline{u_z' \Delta z'}$$

$$\Delta x = x(\tau+t) - x(t); \quad \Delta y = y(\tau+t) - y(t); \quad \Delta z' = z'(\tau+t) - z'(t);$$

$$u_x = u_x(\tau+t); \quad u_y = u_y(\tau+t); \quad u_z' = u_z'(\tau+t);$$

$$\cos\theta = \frac{x(\tau+t)}{\sqrt{x^2(\tau+t)+y^2(\tau+t)}}; \qquad \sin\theta = \frac{y(\tau+t)}{\sqrt{x^2(\tau+t)+y^2(\tau+t)}}$$

$$u_z'(\tau+t) = u_z(\tau+t) - U_z[r(t+\tau)]; \quad r = \sqrt{x^2(t+\tau)+y^2(t+\tau)}$$

$$z'(t) = \int_0^t u_z'(s)ds$$

6.5 Results and Discussions

To ensure an accurate evaluation of the eddy dispersion coefficients, the numerical tracer simulation can only be started when the flow field of the column reaches a statistically quasi-steady state. Since the tracer dispersion in the axial direction is largely controlled by the mean axial momentum and its fluctuation, we calculated the time- and azimuthal-averaged profiles of the liquid axial velocity, $\langle u_z \rangle$, and the axial turbulence intensity, $\langle u_z' u_z' \rangle$. Pan (1999) conducted numerical tracer experiment in bubbly flow and the predicted cross-sectional axial eddy diffusivity compared well with the experimental data obtained via CARPT (Table 6.2). In this study, we focused on eddy diffusivity prediction in the churn-turbulent flow regime. The numerical tracer experiments were conducted for the 44-cm diameter column operated at U_g = 10 cm/s and 16.2-cm diameter column operated at U_g = 30 cm/s.

Table 6.2 Predicted axial eddy diffusivity in bubbly flow

D_C (cm)	U_g (cm/s)	Computed $\langle D_{zz} \rangle$ (cm^2/sec)	$\langle D_{zz} \rangle$ (cm^2/sec)	
			Sparger 6A	Sparger 6B
14	2.4	72	48	75

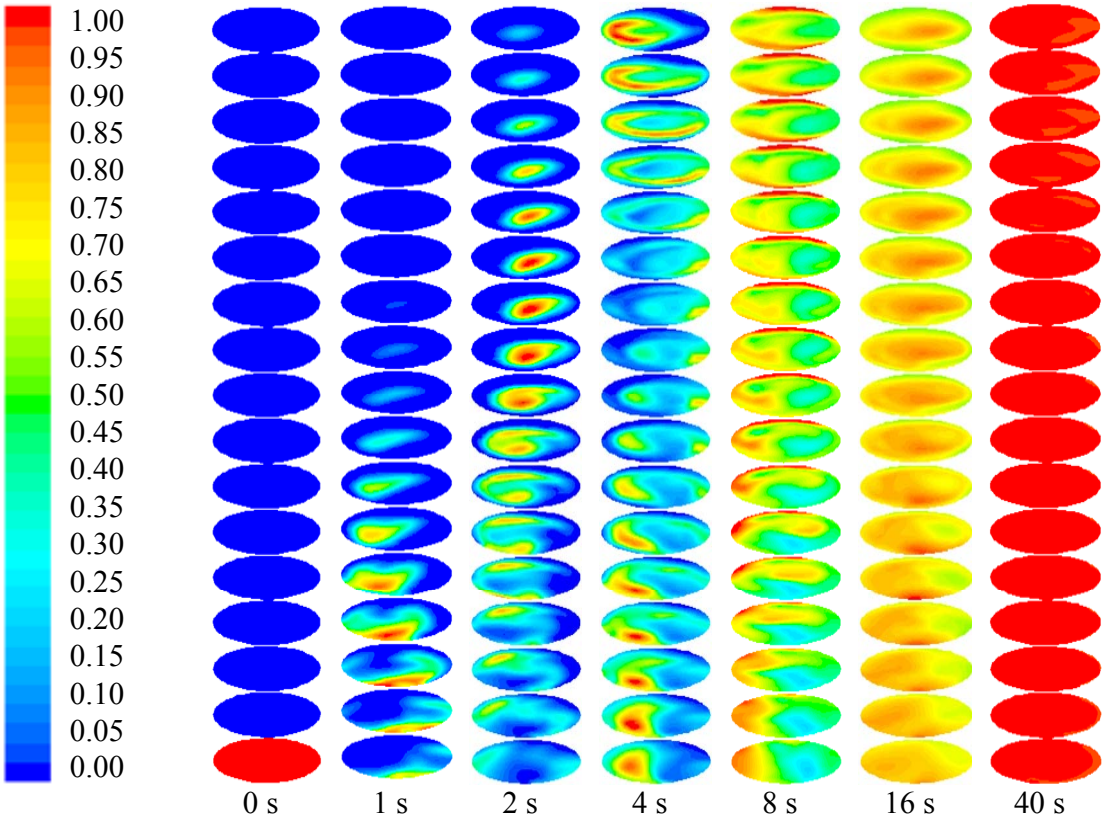

Figure 6.2. Time evolution of the liquid tracer concentration inside a 44-cm diameter column at U_g=10 cm/s.

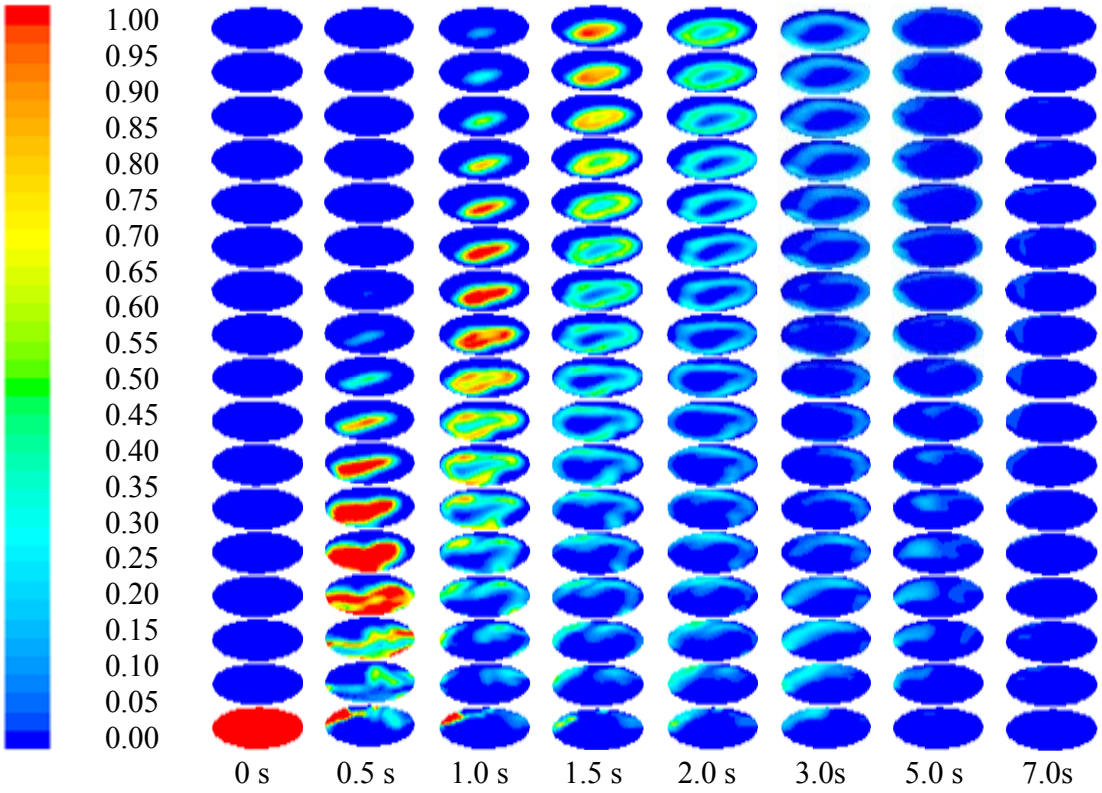

Figure 6.3. Time evolution of the gas tracer concentration inside a 44-cm diameter column at U_g = 10 cm/s.

Figure 6.2 shows the time evolution of liquid tracer concentration in the 44-cm diameter column operated at superficial gas velocity of 10 cm/s. The tracer concentration contour plots are normalized against the maximum value in the column at given time, respectively, for better illustration. An impulse of tracer is injected at the center of the column (r=0) and close to the bottom (z=3 cm). The injection is made when the flow field reaches the fully developed state. Due to liquid recirculation, i.e. batch flow, the liquid tracer cannot escape the column. The tracer concentration, therefore, eventually approaches a uniform pattern. On the other hand, the gas tracer, as shown in Figure 6.3, eventually exits the column. One can also observe the downwards dispersion of the gas tracer due to the carrying of gas bubbles by liquid back flow near the wall region.

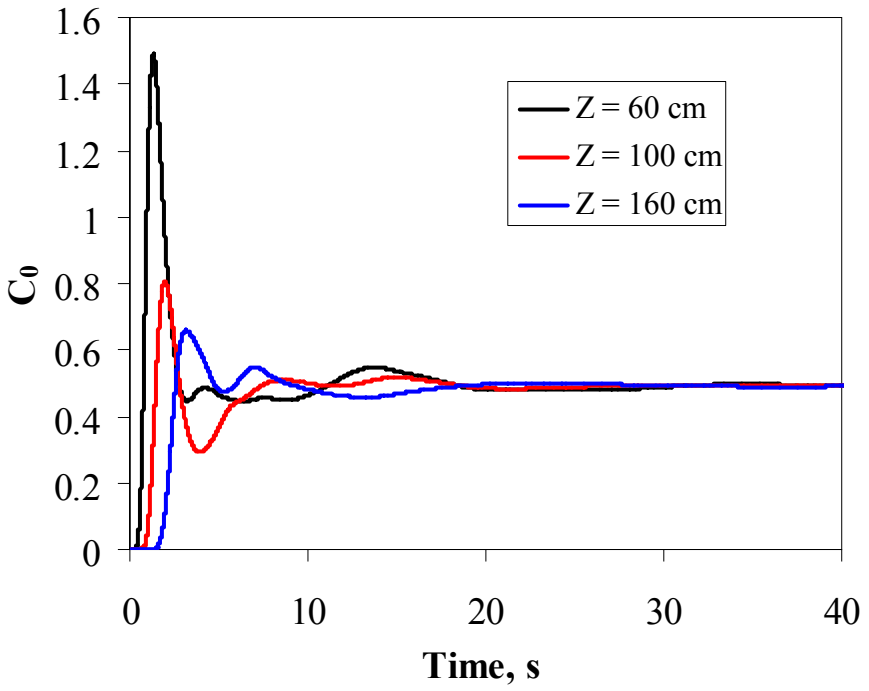

Figure 6.4. Numerical detector responses for liquid tracer injection at z = 3 cm, in a 44-cm column operated at U_g=10 cm/s.

Figure 6.4 displays the liquid tracer concentrations observed at different axial locations as functions of time. C_0 is proportional to the cross-section average concentration and is defined as,

$$C_0(z) \equiv \int C ds \tag{6.10}$$

where the area integral, $\int (\ ) ds$, is taken over the cross-section at a axial location, z, and ds is the element of area. It can be seen that at the time of 15 seconds after the tracer injection, there is still a spatial non-uniformity of tracer distribution. The complete simulation indicates that after about 18 seconds the tracer concentration field reaches uniform distribution along the z direction. From this simulation the liquid velocity, liquid holdup, tracer concentration and the spatial gradient of the tracer concentration are sampled every 0.1 second. The averaged axial turbulent eddy diffusivity is calculated by using Equation (6.8) and (6.9). This result is listed in Table 6.3, in which the

experimentally measured values of eddy diffusivity obtained by CARPT are also listed. The calculated turbulent eddy diffusivity overpredicts the experimental data within 50%.

Table 6.3 Predicted axial eddy diffusivity in churn-turbulent flow.

D_C (cm)	U_g (cm/s)	$\langle D_{zz} \rangle_{sim}$ (cm^2/sec)		$\langle D_{zz} \rangle_{\exp}$ (cm^2/sec)
		Numerical Tracer	Particle Tracking	
44	10	702	809	550
16.2	30	519		350

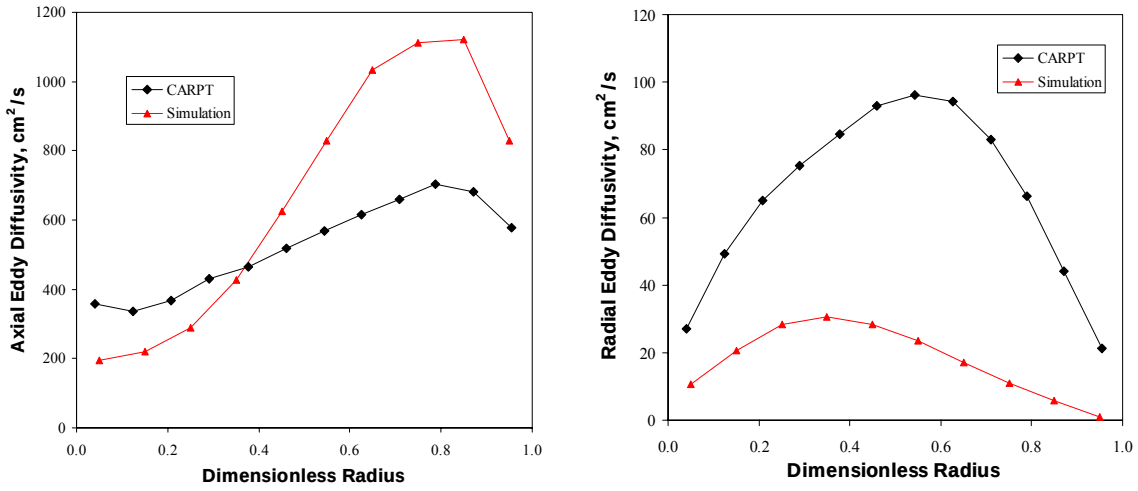

(a) (b)

Figure 6.5 Comparison of Eddy diffusivity radial profile (D_C = 44 cm, U_g = 10 cm/s, P = 1 bar).

Figure 6.5 compares the simulated D_{zz} and D_{rr} radial profile with those evaluated from CARPT data for the 44-cm diameter column operated at superficial gas velocity of 10 cm/s. Similar to the shear stress prediction, the simulated results qualitatively agree with the experimental observations in shape. The axial eddy diffusivity in the center region is under-predicted while it is over-predicted in the wall region. The radial eddy diffusivity is significantly under-estimated. The cross-sectional averaged axial eddy diffusivity is over-predicted by about 47%, and the cross-sectional averaged radial eddy

diffusivity is under-predicted by about 84%. The difference between the predicted cross-sectional averaged axial eddy diffusivity by numerical tracer experiment and by numerical particle tracking is about 15%. Clearly the CFD model needs to be improved further for the prediction of instantaneous quantities (fluctuation), especially in the horizontal plane. This is necessary to provide more accurate eddy diffusivity estimation and accomplish closure of the $\overline{v_i' C'}$ terms, that appear in the tracer species balance equation for liquid phase, in modeling liquid mixing in bubble columns using the gradient diffusion model. From a practical point of view, most proposed models are 1-D models, such as the cross flow with recycle ad dispersion model (Degaleesan *et al.*, 1996b) and gas-liquid recirculation model (Gupta *et al.*, 2001b), and only the overall axial and radial eddy diffusivities in upflow and downflow region, and radial eddy diffusivities at the cross-over point ($r/R \sim 0.7$), are of interest. The overall axial eddy diffusivities in upflow and downflow region, as illustrated, can be estimated by the three dimensional dynamic simulations, while the radial eddy diffusivity prediction needs significant improvements. The time scales for convection and dispersion in a 44-cm diameter column operated at Ug=10 cm/s are illustrated in Table 6.4. Clearly, the bubble column flow is convection dominated flow, and the simulation can predict the convection well, and predict axial dispersion with certain degree of accuracy, while underpredict the radial dispersion by a factor of six.

Table 6.4 Time scales for convection and dispersion in a 44-cm diameter column operated at U_g=10 cm/s.

Time-scale (s)	Experimental	Numerical
Convection $\tau_L = L/u_{L,0}$	8.7	9.6
Axial Dispersion $\tau_{LD} = L^2/D_{zz}$	80	63
Radial Dispersion $\tau_{RD} = R^2/D_{rr}$	7.6	48

6.6 Summary

The methodologies for numerical tracer and numerical particle tracking experiment are illustrated. The fully developed three dimensional flow field obtained from numerical simulation (Chapter 4) can be used for such purpose. CFD model currently cannot fully resolve the fluctuating liquid velocity, especially in the horizontal plane, in the churn-turbulent flow regime, thus the radial turbulent eddy diffusivity is significantly under-estimated. Nevertheless, the axial turbulent eddy diffusivity can be estimated by the three dimensional dynamic simulations with reasonable accuracy.

Chapter 7
Conclusions and Recommendations

7.1 Conclusions

In this work, we incorporated the known breakup and coalescence models via the bubble population balance equation (BPBE) into the Euler-Euler model and ASMM to improve the gas holdup, liquid velocity, surface area per unit volume and Sauter mean bubble size prediction in the churn-turbulent flow regime. It should be noted that much of the physics is uncertain in this complicated flow regime. The previous BPBE implementations are few and focused on bubbly flow, where bubble breakup and coalescence effects on holdup and velocity distributions are marginal. In this work, we systematically investigated the effect of incorporating BPBE in CFD simulation of both bubbly and churn-turbulent flow. Quantitative comparison of model predictions was performed with experimental data whenever possible. The following conclusions were reached:

Two-dimensional axisymmetric simulation of gas-liquid bubble column flow can provide reasonable agreement with experimental data for the time-averaged axial liquid velocity profiles, as well as for the kinetic energy profiles. However, this requires that the model predicted breakup rate be increased by a factor of ten to match the coalescence rate in order to establish the experimentally observed invariance with axial position of radial gas holdup profile in the fully developed region (about two column diameters above the sparger).

There are a number of possible reasons for the mismatch in magnitude of model predicted breakup and coalescence rates.

1) The bubble breakup rate and daughter bubble p.d.f. measurements are done in dilute systems, and may not be applicable in churn-turbulent flow regime where gas holdup is high.

2) In this study the energy dissipation rate is obtained by the $k-\varepsilon$ model and only accounts for small scale energy dissipation. In other words, the predicted dissipation rate, ε, is underpredicted. The model predicted breakup rate increases linearly with $\varepsilon^{1/3}$, the collision rate also increases linearly with $\varepsilon^{1/3}$, but the coalescence efficiency decreases exponentially with $\varepsilon^{1/3}$. Thus, if the energy dissipation rate is underpredicted, then the coalescence rate may be overpredicted and the breakup rate is underpredicted. In addition, as illustrated in Section 3.3.2, if collision of bubbles due to relative velocities difference, neglected at present, is superimposed on the turbulence induced collision, the bubble coalescence rate would decrease because the coalescence efficiency decreases as the bubble collision speed increases.

3) The estimated breakup time (measured from the onset of bubble deformation to the time of actual breakup), τ_b, and coalescence time (measured from the instant when two bubbles collide with each other to the time when they unite into one bubble), τ_c, are larger by an order of magnitude than the time step used in the simulation (~ 5 ms). Therefore, it is assumed implicitly in the simulation that the dissipation rate ε at time t to $t+\tau_b$ (or $t+\tau_c$) is the mean dissipation rate to which breaking (or coalescing) bubbles are exposed to in the turbulent flow field. Turbulence induced coalescence occurs due to eddies with sizes larger than or equal to the sizes of the colliding bubbles. The coalescence time scale however is determined by the liquid physical properties, bubble diameter and the characteristic size of the eddies that induced the collision. Therefore, the history of the dissipation rate surrounding the bubbles after this collision is not important for the coalescence rate estimation. However, this is not the case for bubble breakup rate estimation. The breakup is induced by the eddy bombardment. The bubble breakup rate is determined by all the incoming eddies reaching the bubble

surface during the bubble deformation. Thus, the history of dissipation rate surrounding the bubbles from the onset of bubble deformation is important. As the breakup rate is proportional to $\varepsilon^{1/3}$, due to this functional dependence the estimated breakup rate is higher if the dissipation rate history is used rather than the mean value. Using such history is only possible for Euler-Lagrangian simulation in bubbly flow. It should be noted that we only account for the turbulence-induced coalescence. We cannot at present account for other coalescence phenomena (e.g., wake induced coalescence) due to the lack of suitable physical models. As illustrated in Section 3.3.2, if collision due to difference in bubbles relative velocities is included, the bubble coalescence rate could decrease.

Due to the nature of two-dimensional axisymmetric simulations, the unrealistic time-averaged gas holdup profiles arises, which suggests that full three-dimensional simulation is needed to capture the gas-holdup profile. Better agreement with data is obtained with the Bubble Population Balance Equation (BPBE) implemented, especially in the churn-turbulent flow regime, compared with the simulation using a constant mean bubble size. The difference in predicted interfacial area densities, with and without BPBE implemented, is significant. The choice of currently available bubble breakup and coalescence closures does not have significant impact on the simulated results. BPBE is necessary for churn-turbulent flow simulation when interfacial area density information is important.

The widely used drag force formulation (e.g., Schiller and Naumann, 1935; Ishii and Zuber, 1979; Tsuchiya *et al.*, 1997) , does not account for the effect of elevated pressure. Krishna and van Baten (2001a) proposed in the drag formulation as density correction factor, the ratio of gas density at operating and atmospheric pressure, $\rho_g / \rho_{g,1atm}$. However, the introduction of such a correction factor significantly over-predicted the overall gas holdup at higher superficial velocity and higher pressure (e.g., $U_g = 30\ cm/s, P = 0.6\ MPa$). For that reason, the density correction factor is

reduced in this study to $\left(\rho_g / \rho_{g,1atm}\right)^{0.25}$. Although there is not enough experimental data to draw a conclusion regarding the exponent in this density correction factor, it is found that the exponent of 0.25 works well in this study.

The shape of the predicted gas holdup and liquid axial velocity profile via assumed mean bubble diameter in 3D simulation is flatter than the experimental data. In contrast the simulated results obtained from simulation with BPBE implemented are in good agreement with data. The predicted gas holdup profile with single mean bubble diameter becomes worse as one moves towards the wall region, and the predicted liquid axial velocity profile becomes worse as one moves towards the core region.

The numerical simulation of the transient gas-liquid flow in three-dimensional cylindrical bubble columns using the Euler-Euler two-fluid model (TFM) and the ASMM with BPBE implemented is able to capture the dynamic features of the large-scale structures. The time-averaged liquid velocity field exhibits a single loop axisymmetric recirculation pattern in the middle section of the column. Such flow pattern had been confirmed experimentally by the liquid velocity measurements, which used Computer Automated Radioactive Particle Tracking technique, in various columns operating at churn turbulent flow conditions. The evidence, both numerical and experimental, supports the assumption of one-dimensionality of the time-averaged velocity profile, in the sense of time- and azimuthal-averaging, within the middle section of the column and in turn the use of one-dimensional re-circulation model widely adopted in engineering applications (Degaleesan *et al.*, 1996b; Degaleesan *et al.*, 1997; Gupta *et al.*, 2001a). Quantitative comparisons with the experimental (CT/CARPT) data demonstrate that, by applying inter-phase momentum transfer, modified $k-\varepsilon$ turbulence model in the liquid phase, and the BPBE for the bubble size prediction, the two-fluid and ASMM simulations are able to provide satisfactory mean axial liquid velocity and gas holdup profile for columns operated over a wide range of superficial velocity, operating pressure, physical properties, and column diameter. In this study, the drag force is calculated based on local mean bubble size obtained from the local bubble population distribution. The drag force

can also be calculated from the whole local bubble population. The effect of these two different drag force calculation methods on the simulated results is not significant. By comparing the computed and experimentally determined turbulence intensities (auto correlations of the liquid velocity fluctuations) and the Reynolds shear stress (cross correlation of the liquid velocity fluctuations), we find that, for columns operating in the churn turbulent regime, the velocity field cannot be fully resolved which results in a underestimated prediction of the fluctuations related mean quantities. The simulation correctly captured qualitatively the elevated pressure effect on bubble column flows, which pushes the churn-turbulent flow towards bubbly flow when pressure is increased. It suggests that the volume fraction of small bubbles does not change with respect to the superficial gas velocity in churn-turbulent flow regime. The bubble size distribution remains single modal but becomes wider and moves towards larger bubble diameter when superficial gas velocity is increased. For truly predictive results in simulation of gas-liquid flows in churn turbulent regime one needs to continue exploring the models for momentum exchange, bubble breakup/coalescence, and the models for multiphase turbulence.

In this study, the virtual mass and lift force are neglected. The virtual mass was neglected by most authors or found to be negligible in Euler-Euler simulation, and in the churn-turbulent flow regime, large bubbles do not have a closed wake and the concept of added mass is not applicable (Sankaranarayanan and Sundaresan, 2002; Tomiyama *et al.*, 2002). The main reason for neglecting lift forces is that the lift force due to bubble deformation in strong shear flow fields, which is the most important and relevant lateral force in gas-liquid flow, has not been well modeled and is not available even for a single bubble. In the literature (Sankaranarayanan and Sundaresan, 2002) the lift force coefficient is not only related to the bubble diameter, but also to the local shear stress field to which the bubble is exposed. Moreover, a negative lift force coefficient is reported for large bubbles and in strong shear fields (Kumar, 1994). Another reason is that the lift force is less important in magnitude than the drag force. However, it should

be noted that the lift force component in the horizontal plane may not be negligible in a region of large velocity gradient.

From the computed flow field, the magnitude of virtual mass and lift force in the churn-turbulent flow regime can be estimated. If the lift force coefficient and virtual mass coefficient are both equal to 0.5, then the calculated drag force is about one order of magnitude larger than the virtual mass force in all direction (r, θ, z). In the axial direction, the drag force is at least two orders of magnitude larger than the lift force. In the horizontal plane, the calculated drag force is about the same in magnitude as the lift force. It should be noted that the above estimates are based on computed instantaneous velocities which are underestimated by about a factor of three compared to experimental values. Hence, predicted radial and azimuthal liquid normal stresses are also underpredicted by a factor of ten. The instantaneous gas velocity and slip velocity in the horizontal plane may also be underestimated by a similar factor. Thus, the drag force, $\mathbf{M}_d = \frac{3}{4}\alpha_g \alpha_l \frac{\rho_l}{d_b} C_D \left|\mathbf{u}_l - \mathbf{u}_g\right| \left(\mathbf{u}_l - \mathbf{u}_g\right)$, in the horizontal plane may still be the dominant force, if the computed slip velocity in the horizontal plane, $\left(\mathbf{u}_l - \mathbf{u}_g\right)_{r,\theta}$, is underestimated by a factor of three. The lift force may be important as well. It should be emphasized that the above order of magnitude analysis of the different forces rests on the assumption $C_L = 0.5$, which may not be true in churn-turbulent flow regime. Moreover, it is found experimentally (e.g., Kumar and Ramkrishna, 1996b) that the gas holdup radial profile can be expressed as:

$$\varepsilon_G\left(\xi\right) = \bar{\varepsilon}_G \left(\frac{m+2}{m+2-2c}\right)\left(1 - c\xi^m\right) \tag{7.1}$$

where m is an indication of steepness of the gas holdup profile. In churn-turbulent flow regime (e.g., $U_g = 30$ cm/s). Most experimental data indicates m = 2 while m ≈ 3 by the 3D simulation in this work. This suggests that incorporation of BPBE itself may not be enough for accurate gas holdup distribution prediction, and inclusion of radial lateral force may still be needed.

The procedure for numerical tracer and numerical particle tracking experiment are illustrated. The fully developed three dimensional flow field obtained from numerical simulation can be used for such purpose. CFD models currently cannot fully resolve the fluctuating liquid velocity, especially in the horizontal plane, in the churn-turbulent flow regime, thus the radial turbulent eddy diffusivity is significantly under-estimated, by about a factor of six. In contrast, the axial turbulent eddy diffusivity can be estimated by the three dimensional dynamic simulations with reasonable accuracy. For reactor modeling, convective and axial dispersion time scales are thus predicted correctly, improvement is needed for the radial dispersion time scale.

7.2 Recommendations

Suggestions for extending the work conducted in different parts of this study are listed below:

- It should be noted that the density correction factor used in this study, $\left(\rho_g / \rho_{g,1atm}\right)^{0.25}$, is an engineering estimate. It needs to be validated with more experimental data or based on theoretical calculations.

- The fluctuating velocity components are not well captured in this work. In order to capture better the small scale structure in bubble column flows, Large Eddy Simulation (LES) is desirable.

- The mismatch in order of magnitude of current breakup and coalescence closures, which is found in this work, suggests that new breakup and coalescence closures are needed.

- In this study, the virtual mass force and the lift force are neglected as in line with the work of most other investigators. Although the physics is uncertain, from

engineering point of view, it is desirable to study the effect of these two forces on the simulated results in churn-turbulent flow.

- It may be desirable to implement more recent BPBE solution methods, such as the moving pivot technique (Ong, 2003) for improved accuracy.

- As the velocity and holdup evolution in 2D and 3D simulation are significantly different, it is desirable to confirm whether the effect of different breakup and coalescence closures are also insignificant for 3D simulation as they were shown in the 2D simulation.

- A more rigorous validation of the BPBE model, breakup and coalescence closures is needed. Although it is very difficult, if not impossible, to obtain bubble size distribution data in churn-turbulent flow experimentally, via the four-point optical probe, the bubble chord-length distribution can be obtained and can serve as a valuable validation for the BPBE model. Moreover, there is no gas phase axial velocity data available in the open literature at present. Such data obtained from the four-point probe can not only validate general multiphase CFD models, but also provide needed information, together with the CARPT technique, for drag force formulation under churn-turbulent flow regime and/or at elevated pressure.

- The computed correlation between liquid holdup and liquid axial velocity, $\left\langle \overline{\alpha_l' u_{lz}'}^{t} \right\rangle_s$, as illustrated in Chapter 5, suggests that higher local instantaneous gas holdup is correlated with higher local liquid axial velocity. Moreover, the magnitude of $\left\langle \overline{\alpha_l' u_{lz}'}^{t} \right\rangle_s$ decreases with the operating pressure, which suggests that higher operating pressure suppresses chaotic flow in bubble columns. The opposite sign for the liquid holdup and liquid velocity correlation, $\left\langle \overline{\alpha_l' u_{lz}'}^{t} \right\rangle_e$, is obtained from the CARPT-CT data (Ong, 2003). This leads the conclusion that high gas holdup

correlates with low liquid velocities which is not supported by other evidence. Moreover, the magnitude of the experimental data based $\left\langle \overline{\alpha_l' u_{lz}'}^{t} \right\rangle_e$ increases with pressure, implying that chaotic behavior is promoted by higher pressure. This calls for reexamination of experimental data. CARPT-CT measurements on the same column at different gas velocities should be performed. The effect of the material of the column wall and the effect of particle settling velocity (e.g., use of different size tracer particle) on the results should be carefully examined.

References

Abou-Arab, T. W. (1986). Turbulence models for two-phase flows. *Gas-Liq. Flows*, **3**, 863-907.

Adkins, D. R., Shollenberger, K. A., O'Hern, T. J. and Torczynski, J. R. (1996). Pressure effects on bubble column flow characteristics. *ANS Proceedings*, **9**, 318-325.

Anderson, K. G. and Rice, R. G. (1989). Local turbulence model for predicting circulation rates in bubble columns. *AIChE J.*, **35**, 514-518.

Batchelor, G. K. (1956). *The Theory of Homogeneous Turbulence*, Cambridge University Press.

Batchelor, G. K. (1987). The stability of a large gas bubble rising through liquid. *J. Fluid Mech.*, **184**, 399.

Becker, S., De Bie, H. and Sweeney, J. (1999). Dynamic flow behavior in bubble column. *Chem. Eng. Sci.*, **54**, 4929-4936.

Becker, S., Sokolichin, A. and Eigenberger, G. (1994). Gas-liquid flow in bubble columns and loop reactors: Part II: Comparison of detailed experiments and flow simulation. *Chem. Eng. Sci.*, **49**(24B), 5747-5762.

Bhavaraju, S. M., Russell, T. W. F. and Blanch, H. W. (1978). The design of gas sparger devices for viscous liquid systems. *AIChE J.*, **14**, 3.

Biesheuvel, A. and Spoelstra, S. (1989). The added mass coefficient of a dispersion of spherical gas bubbles in liquid. *Int. J. Multiphase Flow*, **15**, 911.

Bilicki, Z. and Kestin, J. (1987). Transition criteria for two-phase flow pattern in vertical upward flow. *Int. J. Multiphase Flow*, **13**(3), 283.

Borchers, O., Busch, C., Sokolichin, A. and Eigenberger, G. (1999). Applicability of the standard k-e turbulence model to the dynamic simulation of bubble columns. Part II: Comparison of detailed experiments and flow simulations. *Chem. Eng. Sci.*, **54**, 5927-5935.

Brackbill, J. U., Kothe, D. B. and Zemach, C. (1992). A continuum method for modeling surface tension. *Journal of Computational Physics*, **100**(2), 335-54.

Bukur, D. B., Daly, J. G. and Patel, S. A. (1996). Application of -ray attenuation for measurement of gas holdups and flow regime transitions in bubble columns. *Ind. Eng. Chem. Res.*, **35**, 70.

Bunner, B. and Tryggvason, G. (1999). Direct numerical simulations of three-dimensional bubbly flows. *Physics of Fluids*, **11**(8), 1967-1969.

Bunner, B. and Tryggvason, G. (2002). Dynamics of homogeneous bubbly flows Part 1. Rise velocity and microstructure of the bubbles. *J. Fluid Mech.*, **466**, 17-52.

Burns, L. F. and Rice, R. G. (1997). Circulation in bubble columns. *AIChE Journal*, **43**(6), 1390-1402.

Buwa, V. V. and Ranade, V. V. (2002). Dynamics of gas-liquid flow in a rectangular bubble column experiments and single/multi-group CFD simulations. *Chem. Eng. Sci.*, **57**(22-23), 4715-4736.

Campos, F. B. and Lage, P. L. C. (2003). A numerical method for solving the transient multidimensional population balance equation using an Euler–Lagrange formulation. *Chem. Eng. Sci.*, **58**(12), 2725 – 2744.

Cartellier, A. (1992). Simultaneous void fraction measurement, bubble velocity, and size estimate using a single optical probe in gas-liquid two-phase flows. *Rev. Sci. Instrum.*, **63**(11), 5442-5453.

Chabot, J. and De Lasa, H. I. (1993). Gas holdup and bubble characteristics in a bubble column operated at high temperature. *Ind. Eng. Chem. Res.*, **32**, 2595-2601.

Chaouki, J., Larachi, F. and Dudukovic, M. P. (1997). Non-invasive monitoring of multiphase flows, Elsevier**:** 585 pp.

Chatzi, E., Garrielides, A. D. and Kiparissides, C. (1989). Generalized model for prediction of the steady-state drop size distributions in batch stirred vessels. *Ind. Eng. Chem. Res.*, **28**, 1704.

Chatzi, E. and Kiparissides, C. (1992). Dynamic simulation of bimodal drop size distribution in low-coalescence batch dispersion systems. *Chem. Eng. Sci.*, **47**, 445.

Chen, J., Li, F., Degaleesan, S., Gupta, P., Al-Dahhan, M. H., Dudukovic, M. P. and Toseland, B. A. (1999). Fluid dynamic parameters in bubble columns with internals. *Chem. Eng. Sci.*, **54**(13-14), 2187-2197.

Chen, J. J. J., Jamialahmadi, M. and Li, S. M. (1989). Effect of liquid depth on circulation in bubble columns. *Chem. Eng. Res. Design*, **67**, 203-207.

Chen, P., Sanyal, J. and Dudukovic, M. P. (2003). Numerical simulation of bubble columns flows: Effect of different breakup and coalescence closures. *Chem. Eng. Sci.*, submitted.

Chen, R. C. and Fan, L. S. (1992). Particle image velocimetry for characterizing the flow structure in three-dimensional gas-liquid-solid fluidized beds. *Chem. Eng. Sci.*, **47**, 3615-3622.

Chen, R. C., Reese, J. and Fan, L. S. (1994). Flow structure in a three-dimensional bubble column and three-phase fluidized bed. *AIChE J.*, **40**, 1093-1104.

Chesters, A. K. (1991). The modeling of coalescence processes in fluid-liquid dispersions. *Trans. Inst. Chem. Eng.*, **69**, 259-270.

Choi, K. H. and W. K., L. (1990). Comparison of probe methods for measurement of bubble properties. *Chem. Eng. Comm.*, **91**, 35-47.

Chung, J. N. and Troutt, T. R. (1988). Simulation of particle dispersion in an axisymmetric jet. *J. Fluid Mech.*, **186**, 199-222.

Clift, R., Grace, J. R. and Weber, M. E. (1978). *Bubbles, Drops and Particles*. New York, Academic Press.

Cohen, R. D. (1991). Shattering of a Liquid Drop due to Impact. *Proc. Roy. Soc. London. Ser. A*, **435**, 483.

Colella, D., Vinci, D., Bagatin, R., Masi, M. and Bakr, E. A. (1999). A study on coalescence and breakage mechanism in three different bubble columns. *Chem. Eng. Sci.*, **54**, 4767-4778.

Coulaloglou, C. A. and Tavlarides, L. L. (1977). Description of interaction processes in agitated liquid-liquid dispersions. *Chem. Eng. Sci.*, **32**, 1289.

Crowe, C. T., Troutt, T. R. and Chung, J. N. (1996). Numerical models for two-phase turbulent flows. *Ann. Rev. Fluid Mech.*, **28**, 11-43.

Deckwer, W. D. and Schumpe, A. (1987). Bubble columns - the state of the arts and current trends. *Int. Chem. Eng.*, **27**, 405-422.

Degaleesan, S. (1997). *Fluid dynamic measurements and modeling of liquid mixing in bubble columns*. D.Sc. Thesis, Washington University, St Louis.

Degaleesan, S. and Dudukovic, M. P. (1998). Liquid backmixing in bubble columns and the axial dispersion coefficient. *AIChE J.*, **44**(11), 2369-2378.

Degaleesan, S., Dudukovic, M. P., Bhatt, B. L. and Toseland, B. A. (1996a). *Slurry bubble column hydrodynamics: Tracer studies of the La Porte AFDU reactor during methanol synthesis*, Fourth quarterly report for Contract DOE-FC 2295 PC 95051.

Degaleesan, S., Dudukovic, M. P., Toseland, B. A. and Bhatt, B. L. (1997). A two-compartment convective-diffusion model for slurry bubble column reactors. *Ind. Eng. Chem. Res.*, **36**(11), 4670-4680.

Degaleesan, S., Roy, S., Kumar, S. B. and Dudukovic, M. P. (1996b). Liquid mixing based on convection and turbulent dispersion in bubble columns. *Chem. Eng. Sci.*, **51**(10), 1967-1976.

Delnoij, E., Kuipers, J. A. M. and van Swaaij, W. P. M. (1997a). Dynamic simulation of gas-liquid two-phase flow: Effect of column aspect ratio on the flow structure. *Chem. Eng. Sci.*, **52**(21), 3759-3772.

Delnoij, E., Kuipers, J. A. M. and Van Swaaij, W. P. M. (1999). A three-dimensional CFD model for gas-liquid bubble columns. *Chem. Eng. Sci.*, **54**, 2217-2226.

Delnoij, E., Lammers, F. A., Kuipers, J. A. M. and van Swaaij, W. P. M. (1997b). Dynamic simulation of dispersed gas-liquid two-phase flow using a discrete bubble model. *Chem. Eng. Sci.*, **52**(9), 1429-1458.

Delnoij, E., M., K. J. A. and M., v. S. W. P. (1997c). Computational fluid dynamics applied to gas-liquid contactors. *Chem. Eng. Sci.*, **52**(21), 3623-3638.

Devanathan, N. (1991). *Investigation of liquid hydrodynamics in bubble columns via computer automated radioactive particle tracking (CARPT)*. D.Sc. Thesis, Washington University, St Louis.

Devanathan, N., Dudukovic, M. P., Lapin, A. and Luebbert, A. (1995). Chaotic flow in bubble column reactors. *Chem. Eng. Sci.*, **50**(16), 2661-2667.

Devanathan, N., Moslemian, D. and Dudukovic, M. P. (1990). Flow mapping in bubble columns using CARPT. *Chem. Eng. Sci.*, **45**, 2285-2291.

Dickin, F. J., Williams, R. A. and Beck, M. S. (1993). Determination of composition and motion of multicomponent mixtures in process vessels using electrical impedance tomography-I. Principles and process engineering applications. *Chem. Eng. Sci.*, **48**(10), 1883-1897.

Doubliez, L. (1991). The drainage and rupture of a non-foaming liquid "lm formed upon bubble impact with a free surface. *Int. J. Multiphase Flow*, **17**(6), 783-803.

Drew, D. A. (1983). Mathematical modeling of two-phase flow. *Ann. Rev. Fluid Mech.*, **15**, 261-291.

Drew, D. A., Cheng, L. and Lahey R. T., J. (1979). The analysis of virtual mass effects in two-phase flow. *Int. J. Multiphase Flow*, **5**, 233-242.

Drew, D. A. and Lahey, R. T., Jr. (1987). The virtual mass and lift force on a sphere in rotating and straining inviscid flow. *Int. J. Multiphase Flow*, **13**(10), 113-121.

Drew, D. A. and Passmann, S. L. (1999). *Theory of Multicomponent Fluids*. New York, Springer.

Dudukovic, M. P., Degaleesan, S., Gupta, P. and Kumar, S. B. (1997). Fluid dynamics in churn-turbulent bubble columns: Measurements and modeling. *1997 ASME Fluid Engineering Division Summer Meeting*.

Duineveld, P. C. (1994). *Bouncing and coalescence of two bubbles in water*. D.Sc. Thesis, University of Twente, The Netherlands.

Elghobashi, S. E. and Abou-Arab, T. W. (1983). A Two-equation turbulence model for two-phase flows. *Phys. Fluids*, **26**(4), 931-938.

Esmaeeli, A. and Tryggvason, G. (1996). An inverse energy cascade in two-dimensional, low Reynolds number bubbly flows. *J. Fluid Mech.*, **314**, 313-345.

Esmaeeli, A. and Tryggvason, G. (1999). Direct numerical simulations of bubbly flows. Part II - moderate Reynolds number arrays. *J. Fluid Mech.*, **385**, 325-358.

Fan, L.-S., Yang, G. Q., Lee, D. J., Tsuchiya, K. and Luo, X. (1999). Some aspects of high-pressure phenomena of bubbles in liquids and liquid-solid suspensions. *Chem. Eng. Sci.*, **54**, 4681-4709.

George, D. L., Shollenberger, K. A. and Torczynski, J. R. (2000). *Sparger effect on gas volume fraction distributions in vertical bubble-column flows as measured by gamma-densitometry tomography*. ASME 2000 Fluids Engineering Division Summer Meeting, Boston, MA.

Grace, J. R., Wairegi, T. and Brophy, J. (1978). Break-up of drops and bubbles in stagnant media. *Can. J. Chem. Eng.*, **56**, 3.

Grienberger, J. and Hofmann, H. (1992). Investigations and modeling in bubble columns. *Chem. Eng. Sci.*, **47**, 2215-2221.

Gupta, P. (2002). *Churn-Turbulent bubble columns experiments and modeling*. D.Sc. Thesis, Washington University, Saint Louis.

Gupta, P., Al-Dahhan, M. H., Dudukovic, M. P. and Toseland, B. A. (2001a). Comparison of single- and two-bubble class gas-liquid recirculation models - application to pilot-plant radioactive tracer studies during methanol synthesis. *Chem. Eng. Sci.*, **56**(3), 1117-1125.

Gupta, P., Ong, B., Al-Dahhan, M. H., Dudukovic, M. P. and Toseland, B. A. (2000). Hydrodynamics of churn turbulent bubble columns: Gas-liquid recirculation and mechanistic modeling. *Catalysis Today*, **2253**, 1-17.

Gupta, P., Ong, B., Al-Dahhan, M. H., Dudukovic, M. P. and Toseland, B. A. (2001b). Hydrodynamics of churn turbulent bubble columns: Gas-liquid recirculation and mechanistic modeling. *Catal. Today*, **64**(3-4), 253-269.

Hagesaether, L., Jackson, N. B. and Svendsen, H. F. (2002a). A model for turbulent binary breakup of dispersed fluid particles. *Chem. Eng. Sci.*, **57**, 3251-3267.

Hagesaether, L., Jakobsen, H. A. and Svendsen, H. F. (2000). A coalescence and breakup module for implementation in CFD codes. *Comput.-Aided Chem. Eng.*, **8**, 367-372.

Hagesaether, L., Jakobsen, H. A. and Svendsen, H. F. (2002b). Modeling of the dispersed-phase size distribution in bubble columns. *Industrial & Engineering Chemistry Research*, **41**(10), 2560-2570.

Hesketh, R. P., Etchells, A. W. and Russell, T. W. F. (1991). Experimental observations of bubble breakage in turbulent flows. *Ind. Eng. Chem. Res.*, **30**, 845.

Hibiki, T. and Ishii, M. (2000). Two-group interfacial area transport equations at bubbly-to-slug flow transition. *Nucl. Eng. Des.*, **202**, 39-76.

Hibiki, T., Mi, Y., Situ, R. and Ishii, M. (2003). Interfacial area transport of vertical upward bubbly two-phase flow in an annulus. *International Journal of Heat and Mass Transfer*, **46**(25), 4949-4962.

Hills, J. H. (1974). Radial non-uniformity of velocity and voidage in a bubble column. *Trans IChemE*, **52**, 1-9.

Hinze, J. O. (1955). Fundamentals of the hydrodynamics mechanism of splitting in dispersion process. *AIChE J.*, **1**, 289.

Hirt, C. W. and Nichols, B. D. (1981). Volume of fluid (VOF) method for the dynamics of free boundaries. *Journal of Computational Physics*, **39**, 201.

Hoomans, B. P. B. (2000). *Granular dynamics of gas solid two phase flow*. D.Sc. Thesis, Universiteit Twente, Twente, Netherlands.

Hoomans, B. P. B., Kuipers, J. A. M., Briels, W. J. and Swaaij, W. P. M. (1996). Discrete particle simulation of bubble and slug formation in a two dimensional gas-fluidised bed: A hard sphere approach. *Chem. Eng. Sci.*, **51**, 99.

Ishii, M., Sun, X. and Kim, S. (2003). Modeling strategy of the source and sink terms in the two-group interfacial area transport equation. *Annals of Nuclear Energy*, **30**(13), 1309-1331.

Ishii, M. and Zuber, N. (1979). Drag coefficient and relative velocity in bubbly, droplet or particulate flows. *AIChE J.*, **25**(5), 843-855.

Jacqmin, D. (1999). Calculation of two-phase Navier-Stokes flows using phase-field modeling. *J. Comput. Phys.*, **155**, 96-127.

Jakobsen, H. A. (1993). *On the modelling and simulation of bubble column reactors using two-fluid model*. D.Sc. Thesis, NTH, Trondheim.

Jakobsen, H. A. (2001). Phase distribution phenomena in two-phase bubble column reactors. *Chem. Eng. Sci.*, **56**, 1049-1056.

Jakobsen, H. A., Sannaes, B. H., Grevskott, S. and Svendsen, H. (1997). Modelling of vertical bubble-driven flows. *Ind. Eng. Chem. Res.*, **36**, 4052-4074.

Jakobsen, H. A., Svendsen, H. and Hjarbo, K. W. (1993). On the prediction of local flow structures in internal loop and bubble column reactors using a two-fluid model. *Comp. Chem. Eng.*, **17S**, S531-S536.

Johansen, S. T. (1990). *On the modeling of disperse two phase flows*. D.Sc. Thesis, NTH, Trondheim.

Johansen, S. T. and Boysan, F. (1988). Fluid dynamics in bubble stirred ladles: Part II. Mathematical modeling. *Metallurg. Trans. B*, **19**(B), 755.

Johansen, S. T., Boysan, F. and Ayers, W. H. (1987). Mathematical modeling of bubble driven flows in metallurgical process. *Appl. Sci. Research*, **44**, 197-207.

Johnson, A. A. and Tezduyar, T. E. (1997). 3D simulation of fluid-particle interactions with the number of particles reaching 100. *Comput. Methods Appl. Mech. Engng.*, **145**, 301-321.

Kantak, M. V., Hesketh, R. P. and Kelkar, B. G. (1995). Effect of gas and liquid properties on gas phase dispersion in bubble columns. *Chemical Engineering Journal (Lausanne)*, **59**(2), 91-100.

Kariysaki, A. (1987). Behaviour of a single gas bubble in a liquid flow with a linear velocity profile. *Proceedings of the ASME-JSME Thermal Eng. Joint Conference*, **New York**, 261-267.

Kirkpatrick, R. D. and Lockett, M. J. (1974). The Influence of approach velocity on bubble coalescence. *Chem. Eng. Sci.*, **29**, 2363.

Kitscha, J. and Kocamustafaogullari, G. (1989). Criteria for fluid particles. *Int. J. Multiphase Flow*, **15**, 573.

Kocamustafaogullari, G. and Ishii, M. (1995). Foundation of the interfacial area transport equation and its closure relations. *Int. J. Heat Mass Transfer*, **38**, 481.

Konno, M., Aoki, M. and Saito, S. (1983). Scale-effect on breakup process in liquid-liquid agitated tanks. *J. Chem. Eng. Japan*, **16**, 312.

Krahn, E. (1956). Negative Magnus force. *J. Aero. Sci.*, **23**, 377-378.

Krishna, R. and Ellenberger, J. (1996). Gas holdup in bubble column reactors operating in the churn-turbulent flow regime. *AIChE J.*, **42**, 2627-2634.

Krishna, R., Ellenberger, J. and Sie, S. T. (1996). Reactor development for conversion of natural gas to liquid fuels: a scale-up strategy relying on hydrodynamic analogies. *Chem. Eng. Sci.*, **51**(10), 2041-2050.

Krishna, R., Urseanu, M. I., van Baten, J. M. and Ellenberger, J. (1999). Influence of scale on the hydrodynamics of bubble columns operating in the churn-turbulent regime: Experiments vs. Eulerian simulations. *Chem. Eng. Sci.*, **54**, 4903-4911.

Krishna, R. and Van Baten, J. M. (1999). Simulating the motion of gas bubbles in a liquid. *Nature (London)*, **398**(6724), 208.

Krishna, R. and van Baten, J. M. (2001a). Eulerian simulations of bubble columns operating at elevated pressures in the churn turbulent flow regime. *Chemical Engineering Science*, **56**(21-22), 6249-6258.

Krishna, R. and van Baten, J. M. (2001b). Scaling up bubble column reactors with the aid of CFD. *Trans IChemE.*, **79**(A).

Krishna, R., van Baten, J. M. and Urseanu, M. I. (2000). Three-phase Eulerian simulations of bubble column reactors operating in the churn-turbulent regime: a scale up strategy. *Chem. Eng. Sci.*, **55**(16), 3275-3286.

Krishna, R., van Baten, J. M. and Urseanu, M. I. (2001a). Scale effects on the hydrodynamics of bubble columns operating in the homogeneous flow regime. *Chem. Eng. Technol.*, **24**(5), 451-458.

Krishna, R., van Baten, J. M., Urseanu, M. I. and Ellenberger, J. (2001b). Design and scale up of a bubble column slurry reactor for Fisher-Tropsch synthesis. *Chem. Eng. Sci.*, **56**, 537-545.

Kuboi, R., Komasawa, I. and Otake, T. (1972). Behavior of Dispersed particles in turbulent liquid flow. *J. Chem. Eng. Japan*, **5**, 349.

Kuipers, J. A. M. and Swaaij, v. (1998). Computational fluid dynamics applied to chemical reaction engineering. *Adv. Chem. Eng.*, **24**, 227-328.

Kumar, S. and Ramkrishna, D. (1996a). On the solution of population balance equations by discretization-I. A fixed pivot technique. *Chem. Eng. Sci.*, **51**, 1311.

Kumar, S. and Ramkrishna, D. (1996b). On the solution of population balance equations by discretization-II. A moving pivot technique. *Chem. Eng. Sci.*, **51**, 1333.

Kumar, S. B. (1994). *Computed tomographic measurements of void fraction and modeling of the flow in bubble columns*. D.Sc. Thesis, Florida Atlantic University, Boca Raton, Florida, USA.

Kumar, S. B., Devanathan, N., Moslemian, D. and Dudukovic, M. P. (1994). Effect of scale on liquid recirculation in bubble columns. *Chem. Eng. Sci.*, **49**(24B), 5637-5652.

Kumar, S. B., Dudukovic, M. P. and Toseland, B. A. (1997a). Measurement techniques for local and global fluid dynamic quantities in two and three phase systems. *Non-Invasive Monitoring of Multiphase Flows*. J. Chaouki, F. Larachi and M. P. Dudukovic. Amsterdam, The Netherlands, Elsevier**:** 1-45.

Kumar, S. B., Moslemian, D. and Dudukovic, M. P. (1995). A gamma-ray tomographic scanner for imaging voidage distribution in two-phase systems. *Flow Meas. Instrum.*, **6**(1), 61-73.

Kumar, S. B., Moslemian, D. and Dudukovic, M. P. (1997b). Gas-holdup measurements in bubble columns using computed tomography. *AIChE J.*, **43**(6), 1414-1425.

Lahey, R. T. (1990). The analysis of phase separation and phase distribution phenomena using two-fluid model. *Adv. Nucl. Eng. Design*, **122**, 17.

Lain, S., Broder, D. and Sommerfeld, M. (1999). Experimental and numerical studies of the hydrodynamics in a bubble column. *Chem. Eng. Sci.*, **54**, 4913-4920.

Lapin, A. and Lübbert, A. (1994a). Dynamic simulation of the two-phase flow mixing in bubble columns. *Inst. Chem. Eng., Symp. Ser.*, **136**, 365-373.

Lapin, A. and Lübbert, A. (1994b). Numerical simulations of the dynamics of two-phase gas-liquid flows in bubble columns. *Chem. Eng. Sci.*, **49**(21), 3661-3674.

Lapin, A., Maul, C., Junghans, K. and Lubbert, A. (2001). Industrial-scale bubble column reactors: gas-liquid flow and chemical reaction. *Chem. Eng. Sci.*, **56**, 239-246.

Lapin, A., Paaschen, T., Junghans, K. and Lubbert, A. (2002). Bubble column fluid dynamics, flow structures in slender columns with large-diameter ring-spargers. *Chem. Eng. Sci.*, **57**, 1419-1424.

Larachi, F., Kennedy, G. and Chaouki, J. (1994). A gamma-ray detection system for 3D particle tracking in multiphase reactors. *Nuclear Instruments and Methods in Physics Research A*, **338**, 568-576.

Lathouwers, D. (1999). *Modelling and simulation of turbulent bubbly flow*. D.Sc. Thesis, Technische Universiteit Delf, The Netherlands.

Launder, B. E. and Spalding, D. B. (1974). *Mathematical Models of Turbulence*. London, Academic Press.

Lee, C., -H.;, Erickson, L. E. and Glasgow, L. A. (1987a). Bubble breakup and coalescence in turbulent gas-liquid dispersion. *Chem. Eng. Comm.*, **59**, 65.

Lee, C., -H.;, Erickson, L. E. and Glasgow, L. A. (1987b). Dynamics of Bubble Size Distribution in Turbulent Gas-Liquid Dispersion. *Chem. Eng. Comm.*, **61**, 181.

Lehr, F. and Mewes, D. (2001). A transport equation for the interfacial area density applied to bubble columns. *Chem. Eng. Sci.*, **56**, 1159-1166.

Levich, V. G. (1962). *Physiochemical Hydrodynamics*. Englewood Cliffs, NJ, Prentice Hall.

Limtrakul, S. (1996). *Hydrodynamics of liquid fluidized beds and gas - liquid fluidized beds*. D.Sc. Thesis, Washington University, St. Louis.

Lin, J. S., Chen, M. and Chao, B. T. (1985). A novel radioactive particle tracking facility for measurement of solids motion in gas fluidized beds. *AIChE J.*, **31**, 465-473.

Lin, T.-J., Tsuchiya, K. and Fan, L.-S. (1998). Bubble flow characteristics in bubble columns at elevated pressure and temperature. *AIChE J.*, **44**, 545.

Liu, H., Zhang, Z. and Qiu, C. (1998). Buoyancy driven circulation in bubble columns: Alternative analysis. *AIChE J.*, **44**(11), 2561-2564.

Lo, S. (1998). Application of population balance to CFD modeling of bubbly flows via the MUSIG model, AEAT-1096, CFX International, AEA Technology, UK.

Luo, H. (1993). *Coalescence, breakup and liquid circulation in bubble column reactors*. D.Sc. Thesis, Norwegian Institute of Technology.

Luo, H. and Svendsen, H. F. (1996). Theoretical model for drop and bubble breakup in turbulent dispersions. *AIChE J.*, **42**, 1225-1233.

Luo, X., Lee, D. J., Lau, R., Yang, G. and Fan, L. S. (1999). Maximum stable bubble size and gas holdup in high-pressure slurry bubble columns. *AIChE J.*, **45**(4), 665-680.

Magnus, G. (1853). Ueber die Abweichung der Geschosse, und: Ueber eine auffallende Erscheinung bei rotirenden Korpern. *Anal. Phys. Chem.*, **88**(1), 1-29.

Martínez-Bazán, C., Montañéz, J. L. and Lasheras, J. C. (1999a). On the breakup of an air bubble injected into a fully developed turbulent flow. Part 1: Breakup frequency. *J. Fluid Mech.*, **401**, 157.

Martínez-Bazán, C., Montañéz, J. L. and Lasheras, J. C. (1999b). On the breakup of an air bubble injected into a fully developed turbulent flow. Part 2: Size PDF of the resulting daughter bubbles. *J. Fluid Mech.*, **401**, 183.

Mashelkar, R. A. (1970). Bubble columns. *Brit. Chem. Eng.*, **15**(10), 1297-1304.

Michele, V. and Hempel, D. C. (2002). Liquid flow and phase holdup-measurement and CFD modeling for two- and three-phase bubble columns. *Chem. Eng. Sci.*, **57**, 1899-1908.

Miyahara, T., Matsuba, Y. and Takahashi, T. (1983). The size of bubbles generated from perforated plates. *Int. Chem. Eng.*, **23**(3), 517.

Miyahara, T., Tsuchiya, K. and Fan, L. S. (1991). Effect of turbulence wake on bubble-bubble interactions in a gas-liquid-solid fluidized bed. *Chem. Eng. Sci.*, **46**, 2368.

Moslemian, D., Devanathan, N. and Dudukovic, M. P. (1992). Radioactive particle tracking technique for investigation of phase recirculation and turbulence in multiphase systems. *Rev.Sci. Instrum.*, **63**(10), 4361-4372.

Mudde, R. F., Groen, J. S. and Van Den Akker, H. E. A. (1997a). Liquid velocity field in a bubble column: LDA Experiments. *Chem. Eng. Sci.*, **52**(21/22), 4217-4224.

Mudde, R. F., Lee, D. J., Reese, J. and Fan, L. S. (1997b). Role of coherent structures on Reynolds stresses in a 2-D bubble column. *AIChE J.*, **43**(4), 913-926.

Mudde, R. F. and Saito, T. (2001). Hydrodynamical similarities between bubble column and bubbly pipe flow. *J. Fluid Mech.*, **437**, 203-228.

Mudde, R. F. and Simonin, O. (1999). Two- and three- dimensional simulations of a bubble plume using a two-fluid model. *Chem. Eng. Sci.*, **54**, 5061-5069.

Mudde, R. F. and Van Den Akker, H. E. A. (2001). 2D and 3D simulations of an internal airlift loop reactor on the basis of a two-fluid model. *Chemical Engineering Science*, **56**(21-22), 6351-6358.

Myers, K. J., Dudukovic, M. P. and Ramachandran, P. A. (1987). Modelling churn-turbulent bubble columns - I. Liquid-phase mixing. *Chem. Eng. Sci.*, **42**(10), 2301-11.

Nambiar, D. K. R., Kumar, R., Das, T. R. and Gandhi, K. S. (1992). A new model for the breakage frequency of drops in turbulent stirred dispersions. *Chem. Eng. Sci.*, **47**, 2989.

Narsimhan, G., Gupta, J. P. and Ramkrishna, D. (1979). A model for transitional breakage probability of droplets in agitated lean liquid-liquid dispersion. *Chem. Eng. Sci.*, **34**, 257.

Nevers, N. and Wu, J.-L. (1971). Bubble coalescence in viscous fluids. *AIChE J.*, **17**, 182.

Novikov, E. A. and Dommermuth, D. G. (1997). Distribution of droplets in a turbulent spray. *Phys. Rev. E.*, **56**, 5479.

Oey, R. S., Mudde, R. F., Portela, L. M. and van den Akker, H. E. A. (2001). Simulation of a slurry airlift using a two-fluid model. *Chem. Eng. Sci.*, **56**, 673-681.

Oey, R. S., Mudde, R. F. and Van den Akker, H. E. A. (2003). Sensitivity study on Interfacial closure laws in Two-Fluid Bubbly flow simulations. *AIChE J.*, **49**(7), 1621-1636.

Olmas, E., Gentric, C., Vial, C., Wild, G. and Midoux, N. (2001). Numerical simulation of multiphase flow in bubble column reactors: Influence of bubble coalescence and break-up. *Chem. Eng. Sci.*, **56**, 6359-6365.

Ong, B. (2003). *Experimental investigation of bubble column hydrodynamics - Effect of elevated pressure and superficial gas velocity*. D.Sc. Thesis, Washington University, Saint Louis, USA.

Otake, T., Tone, S., Nakao, K. and Mitsuhashi, Y. (1977). Coalescence and breakup of bubbles in liquids. *Chem. Eng. Sci.*, **32**, 377.

Padial, N. T., Vanderheyden, W. B., Rauenzahn, R. M. and Yarbro, S. L. (2000). Three-dimensional simulation of a three-phase draft-tube bubble column. *Chem. Eng. Sci.*, **55**, 3261-3273.

Pan, Y. (1999). *Dynamic Simulation of Tracer Dispersion in Bubble Columns*. Nineteenth quarterly report for Contract DOE-FC 2295 PC 95051.

Pan, Y. and Dudukovic, M. P. (2000). *Mean Axial Liquid Velocity Profiles in Bubble Columns — Numerical versus CARPT*, CREL Annual Meeting.

Pan, Y. and Dudukovic, M. P. (2001). *CFD simulations of a bubble column--2D versus 3D*. 6th World Congress of Chemical Engineering, Melbourne, Australia.

Pan, Y., Dudukovic, M. P. and Chang, M. (1999). Dynamic simulation of bubbly flow in bubble columns. *Chem. Eng. Sci.*, **54**, 2481-2489.

Pan, Y., Dudukovic, M. P. and Chang, M. (2000). Numerical investigation of gas-driven flow in 2-D bubble columns. *AIChE J.*, **46**(3), 434-449.

Pfleger, D. and Becker, S. (2001). Modelling and simulation of the dynamic flow behaviour in a bubble column. *Chem. Eng. Sci.*, **56**, 1737-1747.

Pfleger, D., Gomes, S., Gilbert, N. and Wagner, H. G. (1999). Hydrodynamics simulations of laboratory scale bubble columns fundamental studies of the Eulerian-Eulerian modelling approach. *Chem. Eng. Sci.*, **54**, 5091-5099.

Prince, M. J. and Blanch, H. W. (1990). Bubble coalescence and break-up in air-sparged bubble columns. *AIChE J.*, **36**(10), 1485.

Prince, M. J., Walters, S. and Blanch, H. W. (1989). Bubble breakup in air-sparged biochemical reactors. *In Bioprocess Engineering: The First Generation (Edited by Ghose, T. K.)***:** 160.

Rafique, M., Chen, P. and Dudukovic, M. (2004). Computational modeling of gas-liquid flow in bubble columns. *Rev. Chem. Eng.*, **accepted**.

Ramkrishna, D. (2000). *Population Balances: Theory and Applications to Particulate Systems in Engineering*, Academic Press.

Ranade, V. V. (1992). Flow in bubble columns: Some numerical experiments. *Chem. Eng. Sci.*, **47**, 1857.

Ranade, V. V. (1997). Modeling of turbulent flow in a bubble column reactor. *TransIChemE.*, **75A**, 14-23.

Ranade, V. V. and Tayalia, Y. (2001). Modelling of fluid dynamics and mixing in shallow bubble column reactors: influence of sparger design. *Chem. Eng. Sci.*, **56**, 1667-1675.

Ranade, V. V. and Van der Akker, H. E. A. (1994). A computational snap-shot of gas-liquid flow in baffled stirred vessels. *Chem. Eng. Sci.*, **49**, 5175-5192.

Rice, G. R. and Geary, N. W. (1990). Prediction of liquid circulation in viscous bubble columns. *AIChE J.*, **36**(9), 1339-1348.

Ross, S. L., Verhoff, F. H. and Curl, R. L. (1978). Droplet breakage and coalescence processes in an agitated dispersion Part 2: Measurement and interpretation of mixing experiments. *Ind. Eng. Chem. Fund.*, **17**, 101.

Roy, S. (2000). *Quantification of two-phase flow in liquid-solid risers*. D.Sc. Thesis, Washington University, Saint Louis.

Rubinow, S. I. and Keller, J. B. (1961). The transverse force on a spinning sphere moving in a viscous fluid. *Fluid. Mech.*, **11**, 447.

Saffman, P. G. (1965). The lift on a small sphere in a slow shear flow. *J. Fluid Mech.*, **22**, 385.

Saffman, P. G. and Turner, J. S. (1956). On the collision of drops in turbulent clouds. *J. Fluid Mech.*, **1**, 16.

Sankaranarayanan, K. and Sundaresan, S. (2002). Lift force in bubbly suspensions. *Chem. Eng. Sci.*, **57**, 3521-3542.

Sanyal, J., Vasques, S., Roy, S. and Dudukovic, M. P. (1999). Numerical simulations of gas-liquid dynamics in cylindrical bubble column reactors. *Chem. Eng. Sci.*, **54**, 5071-5084.

Sato, Y., Sadatomi, M. and Sekoguchi, K. (1981a). Momentum and heat transfer in two-phase bubble flow, Part 1: Theory. *Int. J. Multiphase Flow*, **7**, 167-177.

Sato, Y., Sadatomi, M. and Sekoguchi, K. (1981b). Momentum and heat transfer in two-phase bubble flow, Part 2: A comparison between experimental data and theoretical calculations. *Int. J. Multiphase Flow*, **7**, 179-190.

Saxena, S. C. (1995). Bubble column reactors and Fischer-Tropsch synthesis. *Catal. Rev. Sci. Eng.*, **37**, 227-309.

Scardovelli, R. and Zaleski, S. (1999). Direct numerical simulation of free-surface and interfacial flow. *Ann. Rev. Fluid Mech.*, **31**, 567-603.

Schiller, L. and Naumann, Z. (1935). *Z. Ver. Deutsch. Ing.*, 77-318.

Schlueter, S. (1995). Simulation of bubble column reactors with the BCR computer code. *Chem. Eng. Process.*, **34**(2), 127-136.

Schlueter, S., Steiff, A. and Weinspach, P. M. (1992). Modeling and simulation of bubble column reactors. *Chem. Eng. Process.*, **31**(2), 91-117.

Schrage, D. S., Feke, D. L. and Kamotani, Y. (2001). An analytical model of the dynamic lift experienced by a bubble moving off-angle to an inviscid flow field with vorticity. *Chem. Eng. Sci.*, **56**, 3671-3681.

Shah, Y. T., Kelkar, B. G., Godbole, S. P. and Deckwert, W. D. (1982). Design parameters estimations for bubble column reactor. *AIChE J.*, **28**, 353-379.

Shaikh, A., Rados, N. and Al-Dahhan, M. H. (2003). *Phase distribution in a high pressure slurry bubble column via computed tomography*. Proceedings of Middle East Petrotech Conference 2003.

Shinnar, R. (1961). On the behaviour of liquid dispersion in mixing vessels. *J. Fluid Mech.*, **10**, 259.

Shollenberger, K. A., George, D. L. and Torczynski, J. R. (2000). *Effect of Sparger Geometry on Gas-Volume-Fraction in Bubble-Column Flows Measured by Gamma-Densitometry Tomography (GDT)*. Sandia National Laboratories.

Shollenberger, K. A., Torczynski, J. R., Adkins, D. R., O'Hern, T. J. and Jackson, N. B. (1997). Gamma-densitometry tomography of gas holdup spatial distribution in industrial-scale bubble columns. *Chem. Eng. Sci.*, **52**(13), 2037-2048.

Sokolichin, A. and Eigenberger, G. (1994). Gas-liquid flow in bubble columns and loop reactors: Part I. Detailed modelling and numerical simulation. *Chem. Eng. Sci.*, **49**(24B), 5735-5746.

Sokolichin, A. and Eigenberger, G. (1999). Applicability of the standard k-ε turbulence model to the dynamic simulation of bubble column. Part I: Detailed numerical simulations. *Chem. Eng. Sci.*, **54**, 2273-2284.

Sokolichin, A., Eigenberger, G., Lapin, A. L. and Lubbert, A. (1997). Dynamic simulation of gas-liquid two-phase flows - Euler/Euler versus Euler/Lagrange. *Chem. Eng. Sci.*, **52**, 611-626.

Stewart, C. W. (1995). Bubble interaction in low-viscosity liquids. *Int. J. Multiphase Flow*, **21**(6), 1037.

Stone, H. A. (2000). Philip Saffman and viscous flow theory. *J. Fluid Mech.*, **409**, 165-183.

Sussman, M., Smereka, P. and Osher, S. (1994). A level set approach for computing solutions to incompressible two-phase flows. *J. Comput. Phys.*, **114**, 146-159.

Svendsen, H. F., Jakobsen, H. A. and Torvik, R. (1992). Local flow structure in internal loop and bubble column reactors. *Chem. Eng. Sci.*, **47**(13/14), 3297-3304.

Swanson, W. M. (1961). The Magnus force: A summary of investigations to date. *Transaction of the ASME Journal of Basic Engineering*, 461-470.

Swift, D. L. and Friedlander, S. K. (1964). The coagulation of hydrosols by Brownian motion. *J. Colloid Sci.*, **19**, 621.

Takagi, S. and Matsumoto, Y. (1996). *Three-dimensional deformation of a rising bubble*. Proc. German-Japanese symp. on multiphase flow KfK 5389, p. 499.

Taneda, S. (1957). Negative Magnus effect. *Republic Research Institution of Mechanics (Kyushu)*, **5**, 123-128.

Tchen, C. M. (1947). *Mean value and correlation problems connected with the motion of small particles suspended in a turbulent fluid*. D.Sc. Thesis, TU, Delft, The Netherlands.

Thakre, S. S. and Joshi, J. B. (1999). CFD simulation of bubble column reactors: importance of drag force formulation. *Chem. Eng. Sci.*, **54**, 5055-5060.

Thomas, N. H., Auton, T. R., Sene, K. and Hunt, J. C. R. (1983). Entrapment and transport of bubbles by transient large eddies in multiphase turbulent shear flows. *Phys. Model. Multiphase Flow*, **169**.

Tomiyama, A., Kataoka, I. and Sakaguchi, T. (1995a). Drag coefficients of bubbles (first report, drag coefficient of a single bubble in a stagnant liquid). *Nippon Kikai Gakkai Ronbunshu B Hen*, **61**(587), 2357.

Tomiyama, A., Sou, A., Zun, I., Kanami, N. and Sakaguchi, T. (1995b). *Effect of Eotvos number and dimensionless liquid volumetric flux on lateral motion of a bubble in a laminar duct flow*. 2nd Int. Conf. Multiphase Flow, Kyoto.

Tomiyama, A., Tamai, H., Zun, I. and Hosokawa, S. (2002). Transverse migration of single bubbles in simple shear flows. *Chem. Eng. Sci.*, **57**, 1849-1858.

Torvik, R. (1990). *Investigations of two- and three-phase bubble columns*. D.Sc. Thesis, NTH, Trondheim.

Torvik, R. and Svendsen, H. F. (1990). Modeling of slurry reactors: A fundamental approach. *Chem. Eng. Sci.*, **45**, 2325.

Tsouris, C. and Tavlarides, L. L. (1994). Breakage and coalescence model for drops in turbulent dispersion. *AIChE J.*, **40**, 395.

Tsuchiya, K., Furumoto, A., Fang, L. S. and Zhang, J. (1997). Suspension viscosity and bubble rise velocity in liquid-solid fluidized beds. *Chem. Eng. Sci.*, **52**, 3053-3066.

Tsuchiya, K., Miyahara, T. and Fan, L. S. (1989). Visualization of bubble-wake interactions for a stream of bubble in a two-dimensional liquid-solid fluidized bed. *Int. J. Multiphase Flow*, **15**, 35.

Tzeng, J. W., Chen, R. C. and Fan, L. S. (1993). Visualization of flow characteristics in a 2-D bubble column and three-phase fluidized bed. *AIChE J.*, **39**, 733-744.

Ueyama, K. and Miyauchi, T. (1979). Properties of recirculating turbulent two phase flow in gas bubble columns. *AIChE J.*, **25**, 258-266.

Unverdi, S. O. and Tryggvason, G. (1992). A front-tracking method for viscous, incompressible, multi-fluid flows. *J. Comput. Phys.*, **100**, 25-37.

Valentas, K., Bilous, O. and Amundson, N. (1966). Analysis of breakage in dispersed phase systems. *Ind. Eng. Chem. Fund.*, **5**, 271.

van Baten, J. M. and Krishna, R. (2001). Eulerian simulations for determination of the axial dispersion of liquid and gas phases in bubble columns operating in the churn-turbulent regime. *Chem. Eng. Sci.*, **56**(2), 503-512.

Van Doormal, J. and Raithby, G. D. (1984). Enhancement of the SIMPLE method for predicting incompressible flows. *Num. Heat Transfer*, **7**, 147-163.

van-Baten, J. M. and Krishna, R. (2001). Eulerian simulations for determination of the axial dispersion of liquid and gas phases in bubble columns operation in the churn-turbulent regime. *Chem. Eng. Sci.*, **56**, 503-512.

Vasquez, S. A. and Ivanov, V. A. (2000). *A Phase Coupled Method for Solving Multiphase Problems on Unstructured Meshes*. ASME FEDSM'00: ASME 2000 Fluids Engineering Division Summer Meeting, Boston.

Wallis, G. B. (1969). *One dimensional two phase flow*. New York, McGraw Hill.

Wang, Q. (1996). *Modeling of gas and liquid phase mixing with reaction in bubble column reactors*. M.S. Thesis, Washington University, St. Louis.

Warsito, W. and Fan, L. S. (2001). Neural network based multi-criterion optimization image reconstruction technique for imaging two- and three-phase flow systems using electrical capacitance tomography. *Meas. Sci. Technol.*, **12**, 2198-2210.

Webb, C., Que, F. and Senior, P. R. (1992). Dynamic simulation of gas-liquid dispersion behaviour in a 2-D bubble column using a graphics mini-supercomputer. *Chem. Eng. Sci.*, **47**(13/14), 3305-3312.

Wilkinson, P. and van Dierendonck, L. L. (1990). Pressure and gas density effects on bubble break-up and gas holdup in bubble columns. *Chem. Eng. Sci.*, **45**(8), 2309.

Wilkinson, P. M. (1991). *Physical aspects and scale-up of high pressure bubble columns*. D.Sc. Thesis, University of Groningen, The Netherlands.

Wilkinson, P. M., Haringa, H. and Van Dierendonck, F. P. A. S. L. (1993). Liquid mixing in a bubble column under pressure. *Chemical Engineering Science*, **48**(10), 1785-91.

Wu, Q., Kim, S., Ishii, M. and Beus, S. G. (1998). One-group interfacial area transport in vertical bubbly flow. *Int. J. Heat Mass Transfer*, **41**, 1103.

Xue, J. (2002). Proposal of PhD thesis.

Xue, J. (2004). *CREL group meeting*.

Yabe, T. (1997). *Interface capturing and universal solution of solid, liquid and gas by CIP method*. Proc. High-Performance Computing of Multi-Phase Flow, Tokyo.

Yang, Y. B., Devanathan, N. and Dudukovic, M. P. (1992). Liquid backmixing in bubble columns. *Chem. Eng. Sci.*, **47**, 2859-2864.

Yang, Y. B., Devanathan, N. and Dudukovic, M. P. (1993). Liquid backmixing in bubble columns via computer-automated radioactive particle tracking (CARPT). *Experiments in Fluids*, **16**(1), 1-9.

Yao, B. P., Zheng, C., Gasche, H. E. and Hoffman, H. (1991). Bubble behaviour and flow structure of bubble column. *Chem. Eng. Proc.*, **29**, 67-75.

Zehner, P. (1989). *Dechema Monog.*, **114**, 215.

Zhang, D. Z. and Prosperetti, A. (1994). Ensemble phase-averaged equations for bubbly flows. *Phys. Fluids*, **6**(9), 2956-2970.

Zhang, D. Z. and Prosperetti, A. (1997). Momentum and energy equations for disperse two-phase flows and their closure for dilute suspensions. *Int. J. Multiphase Flow*, **23**(3), 425-453.

Zhao, Y., Schehl, R. R., Anderson, R. R. and Chi, R. D. (1987). A multicomponent axial dispersion model of bubble column slurry reactor for the Fischer-Tropsch synthesis. *Huaxue Fanying Gongcheng Yu Gongyi*, **3**(2), 22-33.

Vita

Name Peng Chen

Degrees

B. Eng. Organic Chemical Engineering, July 1995
Tianjin University, China

M. Eng. Biochemical Engineering, March 1998
Zhejiang University, China

D.Sc. Chemical Engineering, May 2004
Washington University, St. Louis, MO, USA.

Professional Societies American Institute of Chemical Engineers

Publications

"Three dimensional simulation of bubble columns flows with bubble coalescence and breakup", Chen, P., Sanyal, J., and Dudukovic', M. P., *AICHE J.*, submitted, 2004

"CFD Modeling of Bubble Columns Flows : Implementation of Population Balance", Chen, P., Sanyal, J., and Dudukovic', *ISCRE-18*, submitted, 2004

"Hydrodynamics of Slurry Bubble Column during Dimethyl Ether (DME) Synthesis: Gas-Liquid Recirculation Model and Radioactive Tracer Studies", Chen, P., Gupta, P, Dudukovic', M. P., and Toseland, B. A., *Ind. Eng. Chem. Res.*, submitted, 2004

"Radioactive Tracer Studies in Bubble Column for Dimethyl Ether (DME) Synthesis", Chen, P., Gupta, P, Dudukovic', M. P., and Toseland, B. A., *TRACER 3 Conference on TRACERS AND TRACING METHOD*S, 2004

"Effect of different breakup and coalescence closures on bubble column CFD simulation", Chen, P., Sanyal, J., and Dudukovic', M. P., *3rd International Symposium on Two-Phase Flow Modeling and Experimentation*, 2004

"Numerical simulation of bubble columns flows: Effect of different breakup and coalescence closures", Chen, P., Sanyal, J., and Dudukovic', M. P., *Chem. Eng. Sci.*, submitted, 2003

"Computational modeling of gas-liquid flow in bubble columns", Rafique, M., Chen, P., and Dudukovic', M. P., *Reviews in Chemical Engineering*, accepted, 2004

May, 2004